Title

Integrated Experimental and Modeling Tools for Probing Microstructural Changes of Polymers and Wormlike Micelles under Flow

Permalink

https://escholarship.org/uc/item/67j2w74f

Author

Zhang, Jiamin

Publication Date

2021

Peer reviewed|Thesis/dissertation

University of California
Santa Barbara

Integrated Experimental and Modeling Tools for Probing Microstructural Changes of Polymers and Wormlike Micelles under Flow

A dissertation submitted in partial satisfaction
of the requirements for the degree

Doctor of Philosophy
in
Chemical Engineering

by

Jiamin Zhang

Committee in charge:

Professor Matthew E. Helgeson, Co-Chair
Professor L. Gary Leal, Co-Chair
Professor M. Scott Shell
Professor Philip A. Pincus
Professor Zvonimir Dogic

September 2021

The Dissertation of Jiamin Zhang is approved.

Professor M. Scott Shell

Professor Philip A. Pincus

Professor Zvonimir Dogic

Professor L. Gary Leal, Committee Co-Chair

Professor Matthew E. Helgeson, Committee Co-Chair

August 2021

Integrated Experimental and Modeling Tools for Probing Microstructural Changes of Polymers and Wormlike Micelles under Flow

by

Jiamin Zhang

Acknowledgements

First and foremost, I want to thank my advisors, Professor Matt Helgeson and Professor Gary Leal. I feel so thankful and fortunate to be your student. Thank you for your constant patience, support, and encouragement throughout the past five years. I will deeply cherish your enthusiasm for research, heart-felt support for students, and scientific rigor as I continue my academic journey and pass on your kindness to the students I will teach and mentor in the future. I also want to thank my committee, Professor Scott Shell, Professor Fyl Pincus, and Professor Zvonimir Dogic for your support and guidance through my dissertation. Fyl, thank you for taking the time to mentor me even though I wasn't your student. I've thoroughly enjoyed all of our conversations and thank you for helping me make breakthroughs in my research projects.

I also want to thank my mentors both at UCSB and at Cornell. Professor Abe Stroock, Eugene, and Olivier, thank you for being my research mentors for three years at Cornell and inspiring me to continue doing research in grad school. Professor Duncan, thank you for the care and support you have shown to all of your students. Taking your class in freshman year and being a TA for you in my senior year helped me realize how much I want to pursue a career in teaching and to make a positive impact on future generations of students. When I started my journey in grad school, I had amazing mentors in the Helgeson and Leal groups. Peng, Alexandra, and Joe, thank you for taking the time to mentor me and always patiently answering my questions even after you graduated from UCSB.

This dissertation would not have been possible without my talented and hardworking collaborators. I want to especially thank Greg Smith, Patrick Corona, Andres Jurzyk, Anukta Datta, and Professor Patrick Underhill. Much of the work benefited from having access to neutron beamline at NIST. I want to thank our collaborators and instrument

scientists: Katie Weigandt, Ryan Murphy, and Yun Liu.

I cannot go through this long, challenging, but rewarding journey without the unconditional love, support, and constant encouragement of my family and friends. I want to thank all of my friends both at UCSB and afar, for making the last 5 years so enjoyable. I want to especially thank Nicole, Mariah, Chelsea, Pauline, Mike, Laura, and Jess for supporting me when I needed support the most. I have been extremely lucky to have two families. My host family in senior year of high school has become my American family throughout the years. Dr. Fowler, Mrs. Fowler, and Shannon, thank you for welcoming me to your home and for being there for me. I love you! To my husband Ran, thank you for your unwavering love and support. Finally, to my mom and dad, thank you for supporting me from thousands of miles away, for giving me a compass to guide me through the ups and downs, for showing me how to stay optimistic amidst difficult situations, and for always believing in me. Thank you for making my life such a fulfilling and enjoyable journey.

Curriculum Vitæ

Jiamin Zhang

Education

Ph.D. in Chemical Engineering, University of California, Santa Barbara	2021
B.S. in Chemical Engineering, *Magna Cum Laude*, Cornell University	2016

Professional Experience

Graduate Student Researcher, UC Santa Barbara	September 2016 - August 2021
Undergraduate Student Researcher, Cornell University	September 2013 - August 2016
Engineering Co-op Intern, Paladino and Company, MD	Fall 2014 & Summer 2015

Publications

J. Zhang*, G.S. Smith*, P.T. Corona, L.G. Leal, M.E. Helgeson, "Scattering Model for Semiflexible Chains in Flow", *To be submitted.*

J. Zhang, G.S. Smith, L.G. Leal, M.E. Helgeson, "Structural Evidence of Flow-enhanced Scission of Wormlike Micelles", *Preprint available.*

P.T. Corona, **J. Zhang**, B. Berke, K.M. Weigandt, M. Guizar-Sicairos, M. Liebi, L. Gary Leal, M.E. Helgeson, "Flow-induced Structural Transitions of Interacting Non-spherical Particle Dispersions", *Preprint available.*

P. Cheng, **J. Zhang**, L.G. Leal, M.E. Helgeson, "Probing the Influence of Equilibrium Structure on Shear Banding of Concentrated Linear Wormlike Micelles", *In preparation for Rheologica Acta.*

A. Datta, **J. Zhang**, Y. Wang, S. Gulati, P.T. Underhill, M.E. Helgeson, "Modeling Scattering of Dilute Polymers in Shear Flow," *In preparation.*

J. Zhang, A. Jurzyk, M.E. Helgeson, and L.G. Leal, "Modeling Orthogonal Superposition Rheometry to Probe Nonequilibrium Dynamics of Entangled Polymers", *Journal of Rheology*, **65(5)**, 983-998, 2021. *Featured article.* DOI: 10.1122/8.0000272

C.J. Dahlman, N.R. Venkatesan, P.T. Corona, R.M. Kennard, L. Mao, N. Smith, **J. Zhang**, R. Seshadri, M.E. Helgeson, M.L. Chabinyc, "Structural Evolution of Layered Hybrid Lead Iodide Perovskites in Colloidal Dispersions", *ACS Nano*, **14(9)**, 11294-11308, 2020. DOI: 10.1021/acsnano.0c03219

O. Vincent, **J. Zhang**, E. Choi, A. Stroock, "How Solutes Modify the Thermodynamics and Dynamics of Filling and Emptying in Extreme Ink-bottle Pores", *Langmuir*, **35(8)**, 2934-2947, 2019. DOI: 10.1021/acs.langmuir.8b03494

*Authors contributed equally to this work.

Conference Presentations

J. Zhang, P.T. Corona, L.G. Leal, M.E. Helgeson, "Assessing Shear-induced Scission of Wormlike Micelles Using Flow-Small Angle Neutron Scattering", American Physical Society March Meeting, Virtual, March 2021.

J. Zhang, A. Jurzyk, M.E. Helgeson, L.G. Leal, "Probing Nonequilibrium Dynamics of Entangled Polymers Using Orthogonal Superposition Rheometry", International Congress on Rheology, Virtual, December 2020.

J. Zhang, P.T. Corona, L.G. Leal, M.E. Helgeson, "Assessing Shear-Induced Scission of Wormlike Micelles using Flow-SANS", American Conference on Neutron Scattering, Virtual, July 2020.

A. Jurzyk, J. Zhang, M.E. Helgeson, L.G. Leal, "Probing Nonequilibrium Dynamics and Structure of Polymeric Liquids Using Orthogonal Superposition Rheology", Poster presentation at Materials Research Outreach Program, UCSB, January 2020.

J. Zhang, L.G. Leal, M.E. Helgeson, "Scaling of Flow-induced Alignment and the Possibility of Flow-induced Scission in Wormlike Micelles", Society of Rheology Annual Meeting, Raleigh, NC, October 2019.

J. Zhang, L.G. Leal, M.E. Helgeson, "Alignment and Instability in Wormlike Micelles", Southern California Fluids Conference, UCSB, Santa Barbara, CA, April 2019.

J. Zhang, L.G. Leal, M.E. Helgeson, "Probing Non-equilibrium Microstructure of Wormlike Micelles using Rheo-SANS", Poster presentation at American Conference on Neutron Scattering, College Park, MD, June 2018. **This poster presentation was awarded Outstanding Student Poster Prize.**

Honors and Awards

2018 ACNS Outstanding Student Poster Prize

2017 UCSB Chemical Engineering Distinguished Service Award

2016 UCSB Heslin Fellowship

2015 Tau Beta Pi Scholarship

2014 Cornell University Undergraduate Research Grant

Abstract

Integrated Experimental and Modeling Tools for Probing Microstructural Changes of Polymers and Wormlike Micelles under Flow

by

Jiamin Zhang

Flow processing of polymers and wormlike micelles usually involves nonlinear deformations, which can significantly modify both the associated microstructural configuration and dynamics. Determining the connection between processing, structure, and properties remains a grand challenge due to limitations in currently available tools. Thus, the primary focus of this dissertation is to develop combined experimental, theoretical, and computational approaches to gain a deeper understanding of the processing-structure-property relationship of polymers and wormlike micelles.

Wormlike micelles (WLMs) are long, semi-flexible chainlike structures formed by the self-assembly of surfactants and are ubiquitously used in oil and gas industry, as well as in consumer products. The rheology of wormlike micelles is critical to the successful formulation and engineering of these products and processes. Although it is widely accepted that equilibrium micelle scission dynamics greatly influences the rheology of WLMs, there is still considerable theoretical debate regarding whether scission dynamics is affected by flow under nonlinear deformations. Direct structural measurements in flow are needed to directly answer whether and how flow affects scission of WLMs.

In situ small angle neutron scattering (SANS) represents a powerful technique for measuring material microstructures under flow. However, SANS methodology for studying wormlike micelles and polymers is currently limited in terms of available nonequilibrium scattering models and in terms of experimental analysis methods to deconvolute effects

of chain orientation, stretching, inter-chain interactions, and changes in chain length. With respect to scattering models in flow, this dissertation develops a connected-rod model for semiflexible chains in flow and achieves excellent agreement with experimental anisotropic scattering results from wormlike micelles. We also formulate a scattering model for dilute, flexible polymers in shear flow and use results from Brownian dynamics simulations for the polymer conformation in flow. To address the question of how and whether flow affects scission of WLMs, we conducted systematic flow-SANS and rheology experiments on a series of linear wormlike micelles. A combination of SANS modeling, steady-state flow-SANS experiments, and time-resolved flow-SANS experiments enables direct microstructural measurement of wormlike micelles in flow and strongly suggests the presence of flow-enhanced scission.

Additionally, for relating microstructural information to macroscopic dynamic properties of the material, a recently advanced rheometry technique, orthogonal superposition (OSR), is predicted to be very useful. However, relatively little is known about how to interpret the nonlinear viscoelastic results in the context of entangled polymer dynamics. Specifically, there is a need for a deeper theoretical and computational study to provide a fundamental basis for interpreting OSR measurements. We combine numerical calculations and a perturbation analysis using detailed microstructural models to study orthogonal superposition for monodisperse and polydisperse entangled linear polymers. We find that orthogonal superposition gives very useful information about nonlinear material moduli under flow, which can provide better sensitivity for testing constitutive models for nonlinear polymer processing. Results in our work have important implications for the design and interpretation of future OSR experiments.

The tools we develop in this dissertation are important for understanding the rheology, scattering, and microstructures of not only wormlike micelles and polymers, but also other complex fluids that share similar underlying physics.

Contents

List of Figures

List of Tables

Chapter 1

Introduction

1.1 Motivation

1.1.1 The need to understand processing-structure-property relationship of polymers and wormlike micelles

Flow processing of soft materials and complex fluids usually involves nonlinear deformations, which can non-trivially modify both the associated microstructural configuration and dynamics. This is particularly important for entangled polymers and wormlike micelles, where entanglements produce nonlinear relaxation mechanisms that are significantly modified when polymers and micelles stretch and orient in flow, leading to various flow instabilities and complications in material processing. Thus, it is desirable to use combined experimental, theoretical, and computational approaches to develop a deeper understanding of the processing-structure-property relationship of polymers and wormlike micelles.

Wormlike micelles, long, semi-flexible chainlike structures, are formed by the self-assembly of surfactants, which are amphiphilic molecules composed of different chemical moieties that display both solvophilic and solvophobic properties. Wormlike micelles (WLMs) are often likened to “living polymers”, since associations between surfactants are impermanent, leading to dynamic scission and recombination of the micelles due to thermal fluctuations. Because of their rheological properties, combined with their detergency and structure, WLMs are used in the oil and gas industry, and more significantly in consumer products such as shampoo and body wash. In all of these applications, wormlike micelles are subjected to flow during processing and end-use. The rheology of WLMs is critical to the successful formulation and engineering of these products and processes.[1] Such applications benefit from understanding how the microstructures influence the flow properties.

WLMs are often likened to "living polymers", since associations between surfactants are impermanent, leading to dynamic scission and reformation of the micelles due to thermal fluctuations. Although it is widely accepted that equilibrium micelle scission dynamics greatly influences the rheology of WLMs, there is still considerable theoretical debate regarding whether scission dynamics are affected by flow under nonlinear deformations. This is because there are still few if any experiments that have attempted to directly test how flow potentially affects the scission and recombination process and the resulting length distribution of the micelles. Previous experiments relied mostly on rheological measurements, which are sensitive primarily to the long micelle species in flow. Extensional rheology measurements have been used to speculate that micellar breakage can happen as a result of strong flows.[2,3] However, the rheological data typically need to be interpreted in the context of a rheological model. Direct structural measurements in flow are needed to directly answer whether flow affects scission of WLMs in a model-agnostic way.

1.1.2 The need for new experimental, theoretical, and modeling tools

In order to address questions about the processing-structure-property relationship of polymers and wormlike micelles, we need accurate measurements of the material microstructures. While several techniques exist for measuring microstructures on the nanometer scale, small angle neutron scattering (SANS) is particularly advantageous. SANS probes length scales of 1-200 nm, which covers the range of characteristic length scales in WLMs and polymers. Many flow-SANS experiments have probed WLM alignment,[4–6] but no studies have assessed how flow potentially affects the scission and recombination process and the resulting length distribution of the micelles. This is because (i) previous flow-SANS and light scattering[7] experiments were limited by structural complications including entanglement and branching, as well as flow instabilities including shear banding and elastic instability.[6,8] Additionally, (ii) procedures for decoupling changes in micellar length from orientation and inter-chain interactions have not been developed.

More broadly speaking, there is a lack of scattering models for semiflexible chains, which are often used as models for the scattering of wormlike micelles, in flow. This is because the interplay of chain stretching, chain orientation, inter-chain interactions, and chain polydispersity makes it challenging to formulate such a scattering model.

For inferring features of the structures and dynamics of wormlike micelles and polymers at equilibrium, linear rheological measurements have been used extensively. Specifically, the material moduli can be related to the average chain length and be used to estimate different relaxation times. As an extension of the linear viscoelastic measurements to nonlinear flows, orthogonal superposition rheometry (OSR) is recently advanced and is predicted to be very useful for understanding how the chain structures and dynamics change in flow.[9,10] Orthogonal superposition measures the shear-dependent material moduli and can help elucidate the effects of different relaxation mechanisms on the material moduli.[11] However, relatively little is known about how to interpret the nonlinear viscoelastic results in the context of entangled polymer dynamics. Specifically, there are very few theoretical and computational studies that would provide a fundamental basis for interpreting orthogonal superposition measurements. This calls for a deeper theoretical and computational study aimed at understanding how stretch and orientation of polymers influence the interpretation of the orthogonal superposition moduli.

The aim of this dissertation is to develop new experimental, theoretical, and simulation tools for studying microstructures of polymers and wormlike micelles in flow and to use these tools to address specific questions about how flow affects the scission of wormlike micelles and how the stretch and orientation of polymers influence the measured orthogonal superposition moduli. The remainder of this chapter will include a review of the literature and theory pertinent to the study of wormlike micelles and polymers, as well as summarize the objectives and approaches that will be the primary focus of this work.

1.2 Wormlike micelles (WLMs) at equilibrium

1.2.1 Self-assembly of micelles

Surfactants are amphiphilic molecules that have a hydrophilic head group and a hydrophobic hydrocarbon tail (Fig. 1.1). The head group can be charged or neutral. Due to the large entropic penalty from exposure of the hydrocarbon chain to a polar solvent (water), the surfactants will spontaneously aggregate above a concentration referred to as the critical micelle concentration (CMC). The thermodynamically preferred micellar morphology will depend on a balance of different interactions, including those of the head group with itself and the solvent, as well as those of the tail group with itself. This delicate balance of forces is successfully captured by the packing parameter, $p = V/al$, where V is the molecular volume of the surfactant, a is the projected area of the head group, and l is the length of the hydrophobic tail.[12] For $p < 1/3$, surfactants tend to form spherical micelles. When salt is added to a solution of surfactants with charged hydrophilic groups, the electrostatic repulsion of neighboring charged hydrophilic head groups is screened. As a result, the head group area decreases and the packing parameter increases. Wormlike micelles are typically formed when $1/3 < p < 1/2$ (Fig. 1.1).

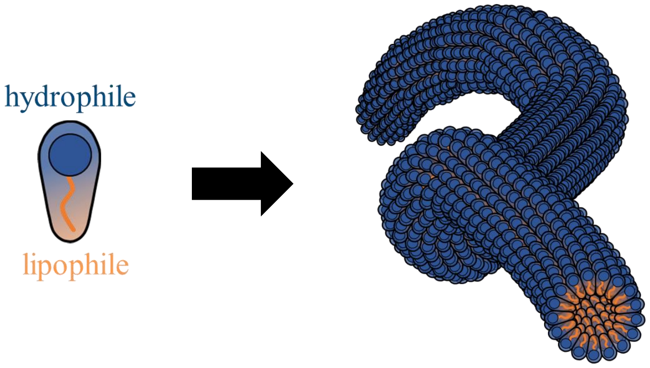

Figure 1.1: Self-assembly of wormlike micelles. The surfactant consists of a hydrophilic headgroup and a hydrophobic tail.

1.2.2 Growth of ionic micelles

WLMs are often likened to “living polymers”, since associations between surfactants are impermanent, leading to dynamic scission and recombination of the micelles due to thermal fluctuations. At equilibrium, the probability of chain scission and recombination is assumed to be equal at any position along the chain, and this results in an exponential length distribution:

$$f\left(L_c\right) \propto \exp\left(-\frac{L_c}{\bar{L}_c}\right). \tag{1.1}$$

A schematic representation of the scission and recombination process and the exponential length distribution are included in Figure 1.2. The average contour length $\bar{L}_c$ is related to the overall volume fraction of the micelles ϕ and the scission energy E_c, as

$$\bar{L}_c = \phi^y \exp\left(\frac{E_c}{2k_BT}\right) \tag{1.2}$$

where the exponent $y = 0.5$ for ideal chains and $y \sim 0.6$ for chains with excluded volume interactions, k_B is the Boltzmann constant, and T is the temperature. For highly charged micelles, the scission energy can depend on ϕ, leading to a stronger dependence of $\bar{L}_c$ on ϕ than that given in Eqn. 1.2.[13,14] This exponential length distribution is derived from a mean-field approach by minimizing the free energy subject to the constraint of constant total volume fraction of micelles. It can also be derived from a population balance.[13,15,16] Specifically, Cates and coworkers assumed that a chain can break with a fixed probability per unit time per unit length anywhere along its length, L_c. It is further assumed that the reverse reaction proceeds at a rate proportional to the product of the concentration of the two reacting subchains and the rate constant involved is independent of the molecular weights of these two subchains. Additionally, the authors assume successive breakage and recombination events for a given chain are uncorrelated. With these assumptions, the equation governing the time development of the number density $f(L)dL$ of chains of length $L \pm \frac{1}{2}dL$ is written as

$$\frac{df(L)}{dt} = -c_1Lf(L) + 2c_1\int_L^\infty f(L')dL' + \frac{c_2}{2}\int_0^L f(L')f(L-L')dL' - c_2f(L)\int_0^\infty f(L')dL'. \tag{1.3}$$

Here, the first term represents the decrease in $f(L)$ by breakage, the second term is the rate of creation of chains of length L by breakage of longer chains, the third term is the rate of creation by recombination of two shorter chains to produce one of length L, and the final term is the decrease in $f(L)$ by reaction of chains of length L with others to form longer chains. The parameters c_1 and c_2 are the rate constants of the breakage and recombination processes respectively. [15] The exponential distribution of equilibrium micelle contour lengths predicted by the Cates' theory is in good agreement with recent measurements on sufficiently long WLMs in dilute and semi-dilute solutions.[17,18]

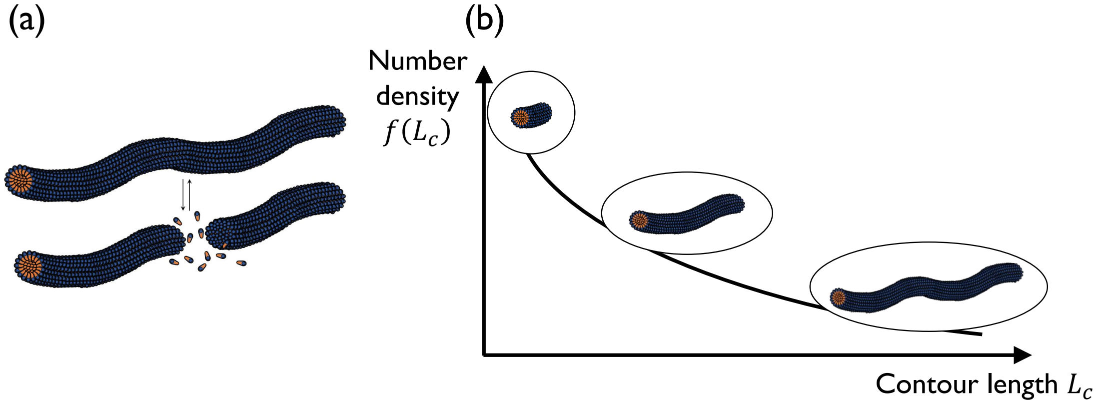

Figure 1.2: (a) Scission and recombination of wormlike micelles and (b) resulting exponential length distribution.

1.2.3 Equilibrium structure of wormlike micelles

WLMs exhibit a hierarchy of length scales: ranging from ∼2 nm for the cross-sectional radius, r_{cs}, to a broad distribution of micellar contour lengths, L_c, with an average length on the order of 100-1000 nm for most systems. Figure 1.3 illustrates the important length scales in a wormlike micelle network. l_p, the persistence length, which is inversely proportional to the micelle flexibility. ξ_M is the mesh size and l_e is the entanglement length.[19]

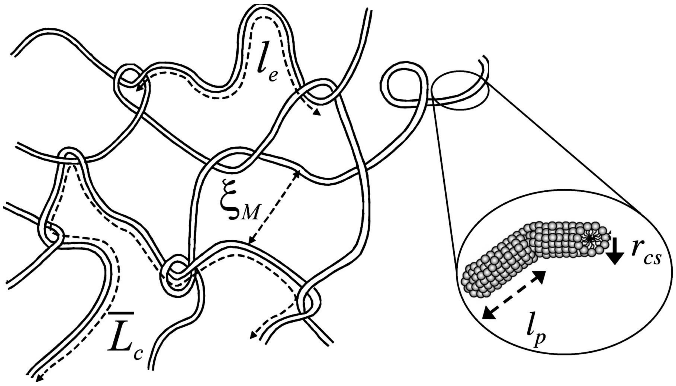

Figure 1.3: Schematic of important length scales of a wormlike micelle network. Reprinted with permission from Liberatore MW, Nettesheim F, Vasquez PA, et al. Microstructure and shear rheologyof entangled wormlike micelles in solution. *Journal of Rheology*. 2009; 53(2): 441–458. Copyright 2009, The Society of Rheology.

1.3 Wormlike micelles in flow

1.3.1 Existing rheological models for WLMs in flow

Although the equilibrium length distribution of wormlike micelles has been well studied, very little is known about whether and how the distribution is modified by flow. There is still debate in the field about whether flow significantly contributes to the scission of wormlike micelles, thereby changing the length distribution. On the one hand, in 1990, Cates extended his original model to nonlinear flows and assumed that scission and recombination are not affected by flow. The nonlinear effects of the flow enter solely through its influence on chain relaxation via reptation.[20] On the other hand, other rheological theories adopted *ad hoc* approaches for modeling the influence of flow on scission and recombination. For example, Vasquez and co-workers developed the VCM model for semi-dilute, shear thinning and shear banding wormlike micelles, in which scission rate of micelles was predicted increase with increasing applied strain, but the recombination rate of chains was assumed to be constant and independent of flow.[21]

By contrast, Graham and coworkers developed a reactive rod model for dilute, shear thickening wormlike micelles which predicts flow-enhanced recombination: flow aligns the micelle, which in turn increases the probability of recombination. Enhanced alignment and recombination create a positive feedback, which causes an increase in the average length of WLMs.[22] So, currently from the theoretical perspective, there is a lack of agreement about how (or whether) flow affects scission.

1.3.2 Key question: how does flow affect the scission of wormlike micelles?

In our view, to build an accurate rheological model for wormlike micelles, the key question we need to address is if and how flow affects the scission of wormlike micelles. Here I will summarize previous experimental and simulations studies that suggested flow-enhanced scission, the limitations in these studies, and our approach of using more direct structural measurements.

Experiments that suggest micellar scission

Previous experiments relied mostly on rheological measurements, which are sensitive primarily to the long micelle species in flow. Extensional rheology experiments and complex flow experiments have suggested micellar breakage can happen as a result of strong flows. Rothstein and Mohammadigoushki recently wrote a comprehensive review about complex flows of wormlike micelles.[3] Here, I will highlight a few studies that directly suggested flow-enhanced scission.

In the work of Rothstein and co-workers,[2,23] a filament stretching rheometer (FiSER) was used to impose a uniaxial extensional flow on a series of WLM solutions. At low extension rates, the fluid filament does not rupture, but instead fails under elasto-capillary thinning. However, above a critical extension rate, the filament abruptly ruptures near its axial mid-plane. The failure of these wormlike micelle filaments occurs before any significant necking has appeared. The authors suggested that the observed filament failure and the dramatic downturn in the extensional viscosity measured through opposed-jet devices[24] are related and both likely stem from the scission of wormlike micelles resulting in a dramatic breakdown of the micelle network *en masse*.[23] In a follow-up study, Bhardwaj et al. studied the effect of pre-shear on extensional deformation of WLMs.[25] When no pre-shear is performed, the value of the elastic tensile stress at filament rupture is independent of the imposed extension rate. However, both the maximum elastic tensile stress and the extensional viscosity decrease dramatically with increasing pre-shear rate and duration. The authors hypothesized that the reduction in the strain hardening suggests that the pre-shear might reduce the size of the WLMs or perhaps change the interconnectivity of the micelle network prior to stretch. This is in stark contrast to the experiments on polymers in which no discernible difference in the steady-state value of the extensional viscosity is observed with and without pre-shear.[26]

Researchers also examined the flow of WLMs past a falling sphere and observed instability in sphere sedimentation velocity or fluid instability in the wake of the sphere (termed wake instability). Chen and Rothstein[27] showed that for conditions that give rise to wake instability, the filament of the WLM undergoes a sudden rupture in the FiSER experiments. The authors asserted that the wake instability is linked to the flow-induced micellar chain scission. Furthermore, Mohammadigoushiki and Muller[28] were able to successfully distinguish steady from unsteady sphere sedimentation experiments by using the maximum local extension rate in the wake of the sphere to generate an extensional Weissenberg number Wi_E and plotting the phase diagram using Wi_E and the Reynolds number Re. The authors suggest that the wake instability in the wormlike micelles is linked to the scission of the wormlike micelles in the wake of the falling sphere, where a strong extensional flow is present.

Although previous extensional flow and complex flow measurements of wormlike micelles have been used to speculate that micellar breakage can happen as a result of strong flows, the experiments typically need to be interpreted in the context of a rheological model. Additionally, no direct microstructural measurements have been intended to directly probe changes in micelle length in flow so far. Therefore, we propose using flow-small angle neutron scattering as a direct structural measurement to directly answer whether flow affects scission of WLMs in a model-agnostic way.

Simulations that suggest micellar scission

Previous simulation studies of wormlike micelles in flow have used molecular dynamics simulations and mesoscopic simulations to investigate the effect of deformation on the micelle length in both shear flow and extensional flow. Here I will summarize the key findings in the most relevant papers.

Kröger and coworkers[29,30] performed nonequilibrium molecular dynamics simulations with a FENE-C potential to study properties of wormlike micelles under equilibrium and shear flow. Results of the simulations on the equilibrium properties (chain length distribution and average length) support the relevance of the microscopic FENE-C model in predicting behavior similar to real micellar systems. Its equilibrium properties are comparable to those predicted by the mean field model from Cates.[13] The average micellar length decreases at high shear rates and the simulation predicts shear thinning results from the decrease of average micellar lengths. One interesting prediction from the simulation that has not been confirmed by experiments is that the length distribution for wormlike micelles is no longer mono-exponential under flow. Briels and coworkers performed coarse-grained molecular dynamics simulations of semidilute wormlike micelles in shear flow. With increasing shear rate, beyond a certain critical shear rate, the contour length decreases and the breaking rate per unit contour length decreases. The critical shear rate decreases with increasing scission and/or activation energy.[31]

Sambasivam and coworkers did the first study using molecular dynamics simulations in the presence of an explicit solvent and salt to study the flow-induced configuration dynamics and scission of rodlike micelles in shear flow.[32] The simulation results show that micelle scission happens through a mechanism in which shear-induced stretching causes the surfactant head groups and adsorbed counterions to be farther apart relative to their spacing at equilibrium, resulting in reduced electrostatic screening and an increase in the overall micelle energy. The overall energy increases linearly with micelle length. Micelle scission occurs when the overall energy exceeds a threshold value, independent of the shear rate. The flow-induced micelle scission results in shear thinning. In a follow-up study by the same group, MD simulations of rodlike and U-shaped micelle in uniaxial elongational flow are performed.[33] Above the critical strain rate, approximately equal to the inverse of the longest micelle relaxation time, hydrodynamic forces overcome the conformational entropy of the micelle and a configurational transition from a folded to a stretched state occurs. As the accumulated strain exceeds a critical value of $\mathcal{O}(100)$, the micelle ruptures through a midplane thinning mechanism facilitated by the advection of counterions toward the micelle end-caps. The molecular picture of micelle deformation that has emerged from this study parallels observations of the thinning and scission of micellar fluid bridges in filament stretching experiments. In a more recent study, Mandal and Larson used coarse-grained MD simulations to determine the effect of uniaxial strain on the stress, scission stress, and scission energy of solutions of wormlike micelles. The breaking stress from the simulations depends on the rate of deformation and roughly agrees with the experimental value of Rothstein[23] from extensional rheology measurements after extrapolation to the much lower experimental rates.

The observation of flow-enhanced scission in studies by multiple research groups using different simulation techniques strongly suggest the possibility of flow-enhanced scission. However, these results are yet to be validated by microstructural experimental measurements. Additionally, different simulation studies seem to suggest different flow-dependence of scission and the underlying mechanism of flow-enhanced scission. Specifically, some studies[29,30] suggest average length decreases with increasing shear rate, while others[32] suggest micelle scission occurs when the overall micellar energy exceeds a threshold value, independent of the shear rate. Furthermore, most of the existing simulation studies of wormlike micelles that include the effect of flow focus on either extensional flow or rodlike micelle and weakly-entangles micelles in shear flow. To our knowledge, no detailed MD simulation for long, entangled micelle in shear flow has been performed to systematically investigate the effect of entanglement on flow-enhanced scission. The remaining knowledge gaps in the simulation studies and the lack of direct comparison with microstructural measurements further motivate our work on using flow-small angle neutron scattering (flow-SANS) to investigate whether and how flow affects the scission and recombination of wormlike micelles.

1.4 Rheology of entangled polymers

In nondilute polymer solutions and melts, the polymer coils interpenetrate each other enough that the molecular motions of one chain are greatly slowed by the interferences of other chains. These interfering effects are attributed to intermolecular entanglements.[34] The modern history of constitutive modeling for polymers begins with the work of Doi and Edwards,[35] who formalized the 'reptation' concept first introduced by de Gennes.[36] Doi and Edwards postulated that the motion of an entangled polymer molecule resembles the motion of a polymer in a tube. This virtual tube is formed by the entangled polymer chains in the surrounding, as suggested by the sketch in Fig. 1.4(a). The theory gives a characteristic timescale for a chain to escape its initial tube and thereby relax its configuration, which is defined as the disentanglement relaxation time τ_d.

Over the course of several decades, other researchers build upon this landmark model, while relaxing some of its more severe approximations and improving the model's applicability in strong flow conditions. In particular, in 2003, Graham, Likhtman, Milner, and McLeish developed the GLaMM model for describing the rheological behavior of entangled monodisperse linear polymer chains under fast deformation.[37] The GLaMM model accounts for an accumulation of stress via affine deformation and relaxation of stress by reptation, chain retraction, and convective constraint release (CCR). As described earlier, reptation describes the curvilinear motion of a polymer chain in a tube formed by entanglements with surrounding chains. When the deformation rate is larger than the inverse of the Rouse time (τ_R), the chain can become stretched, and as a result the length of the chain and the occupied tube exceed their equilibrium configuration. When the strain stops, the chain retracts along the deformed tube until it regains its equilibrium contour (Fig.1.4(b)). Convective constraint release (CCR) is the release of entanglement constraints due to chain retraction from affine deformation in nonlinear flows (Fig. 1.4(c)). The effect of CCR diminishes for shear rates larger than the inverse of the Rouse time.

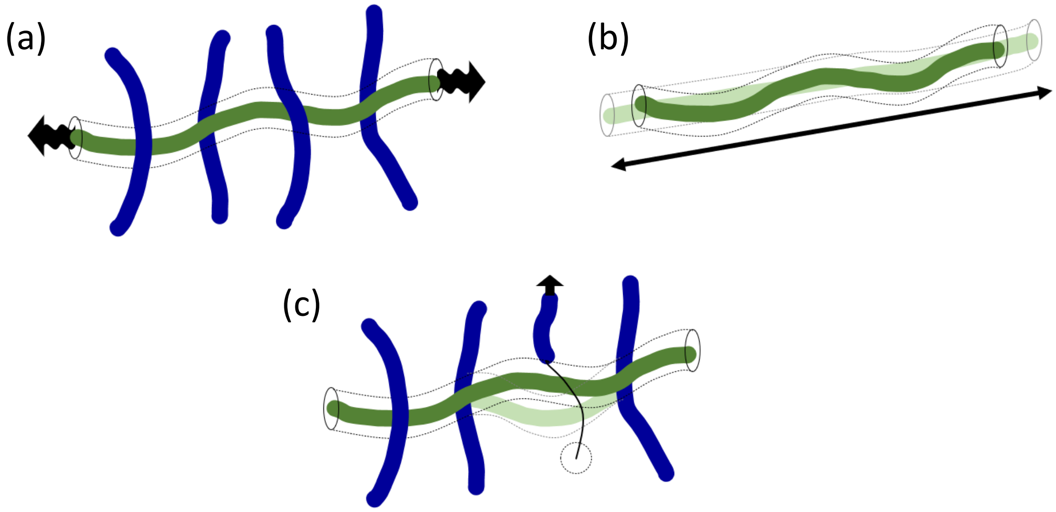

Figure 1.4: Relaxation mechanisms in entangled polymers (a) reptation, (b) retraction, and (c) convective constraint release.

1.5 Orthogonal superposition rheometry

For studying complex fluids, small amplitude oscillatory measurements have been widely used as mechanical spectroscopy. More recently, there has been an increasing amount of interest in superposition flows for probing flow-induced changes in the microstructure of complex fluids. In superposition rheometry, an oscillatory motion can be imposed either parallel ($\dot{\gamma}_{||}$, parallel superposition, PSR) or perpendicular ($\dot{\gamma}_{\perp}$, orthogonal superposition, OSR) to the direction of motion of a steady shear flow (Fig. 1.5). Both experiments and model calculations[38, 39] demonstrated that orthogonal and parallel moduli are not equivalent, due to the tensorial nature of the rheological response. In parallel superposition measurements, the main and the superimposed flow fields are coupled because they are applied in the same direction, which complicates the interpretation of the results. In contrast, orthogonal superposition has a much weaker coupling of the two flow fields, and thus the corresponding moduli can be more directly related to the microstructural configuration under flow. OSR provides measurement of the frequency- and shear-rate-dependent nonlinear viscoelastic superposition moduli (storage and loss moduli, $G'_\perp$ and $G''_\perp$), which are analogous to their linear viscoelastic (LVE) counterparts that characterize equilibrium dynamics, although as we will discuss in Chapter 7, the interpretations of the OSR moduli are different from those for the LVE moduli.

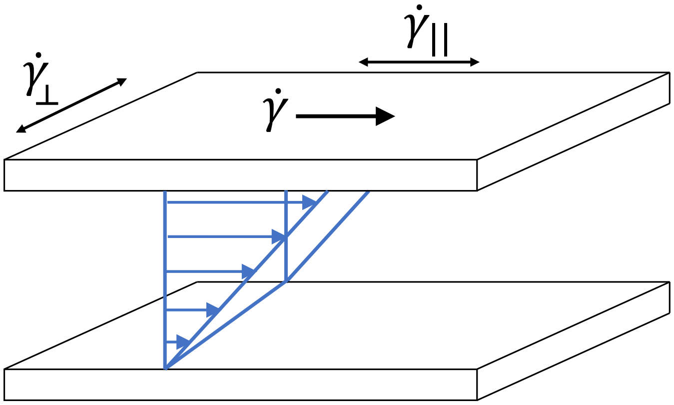

Figure 1.5: Schematic of orthogonal and parallel superposition rheometry.

1.6 Objectives

The objectives of this thesis are two-fold. The first objective is to develop new experimental, theoretical, and simulation tools for studying microstructures of polymers and wormlike micelles in flow. Although small angle neutron scattering can measure structures at length scales that are typically of interest for wormlike micelles and polymers, previous experimental studies have mostly relied on parameterization and averaging of the 2D scattering to interpret the experimental result. For semi-flexible and flexible chains in flow, the interplay among chain stretching, chain orientation, and inter-chain interactions makes it challenging to interpret the experimental result. Thus, it is desirable to develop scattering models for semiflexible chains and flexible polymers in flow to help the design and interpretation of flow-SANS experiments. Furthermore, although orthogonal superposition is a promising technique for probing the frequency- and shear-rate-dependent nonlinear viscoelastic superposition moduli, relatively little is known about how to interpret the nonlinear viscoelastic results in the context of entangled polymer dynamics. Specifically, there are very few theoretical and computational studies that would provide a fundamental basis for interpreting orthogonal superposition measurements. This provides strong motivation for a deeper theoretical and computational study to investigate what is fundamentally being measured in the OSR experiments.

The second objective is to understand processing-structure-property relationships of polymers and wormlike micelles. How flow affects scission of wormlike micelles has been a long-debated question in the field and previous theories have mostly used *ad hoc* approaches for including the effects of scission. Previous experiments haven't been able to address this question directly either because the measurements are not sensitive enough to the microstructures, or the fluid exhibits instabilities (e.g., shear banding). Furthermore, for entangled polymers, no previous studies have clearly addressed how the nonlinear relaxation mechanisms affect orthogonal superposition moduli. In summary, we aim to answer these two questions "how does flow affect scission in wormlike micelles" and "how do stretch and orientation of polymers influence the interpretation of orthogonal superposition moduli" in this work.

1.7 Approach

In order to achieve the identified goals of this work, we need to develop experimental, theoretical, and computational tools. In Chapter 4, we use a connected-rod model to describe the scattering of semiflexible chains in flow and include a segmental orientation distribution that is consistent with the overall stretching and orientation of the chain.

In Chapter 6, we demonstrate the ability to make forward prediction of scattering from polymer conformations in flow and make inverse calculations to extract distributions of polymer deformation from scattering in flow. In Chapter 7, we combine a perturbation analysis and numerical calculations to predict orthogonal superposition moduli for both monodisperse and polydisperse polymers.

The scattering model developed in Chapter 4 will be used, along with steady and transient flow-SANS measurements of wormlike micelles, to identify signatures of flow-enhanced micellar scission in Chapter 5. To enable a clearer interpretation of experimental data, we used a model wormlike micelle system in the concentration regimes that only include linear micelles, not branched ones. Furthermore, we verified the wormlike micelle solutions don't have flow instabilities for the shear rates investigated. In Chapter 7, modeling orthogonal superposition moduli of entangled polymers enables identification of key parameters that determine the shifts of the OSR moduli and identification of qualitative features in OSR moduli that correlate with the degree of polydispersity. The model predictions will aid the design and interpretation of future OSR experiments.

The combination of these experimental, theoretical, and computational approaches will develop a rich understanding of the processing-structure-property relationship of wormlike micelles and polymers. The evidence of flow-enhanced scission for wormlike micelles resolves the long-standing debate in the field and is critical for developing more accurate models for wormlike micelles. The prediction of orthogonal superposition moduli for entangled polymers demonstrates that orthogonal superposition rheometry provides better sensitivity for testing rheological models than conventional rheological techniques. The tools we developed in this dissertation are important for understanding the rheology, scattering, and microstructures of not only WLMs and polymers, but also other complex fluids that share similar underlying physics.

Bibliography

[1] Ezrahi S, Tuval E, Aserin A. Properties, main applications and perspectives of worm micelles. *Advances in colloid and interface science.* 2006; 128: 77–102.

[2] Bhardwaj A, Miller E, Rothstein JP. Filament stretching and capillary breakup extensional rheometry measurements of viscoelastic wormlike micelle solutions. *Journal of Rheology.* 2007; 51(4): 693–719.

[3] Rothstein JP, Mohammadigoushki H. Complex flows of viscoelastic wormlike micelle solutions. *Journal of Non-Newtonian Fluid Mechanics.* 2020: 104382.

[4] Calabrese MA, Wagner NJ. New insights from rheo-small-angle neutron scattering. In *Wormlike Micelles* 193–235 2017.

[5] Helgeson ME, Reichert MD, Hu YT, Wagner NJ. Relating shear banding, structure, and phase behavior in wormlike micellar solutions. *Soft Matter.* 2009; 5(20): 3858–3869.

[6] Helgeson ME, Vasquez PA, Kaler EW, Wagner NJ. Rheology and spatially resolved structure of cetyltrimethylammonium bromide wormlike micelles through the shear banding transition. *Journal of Rheology.* 2009; 53(3): 727–756.

[7] Chen CM, Warr GG. Light scattering from wormlike micelles in an elongational field. *Langmuir.* 1997; 13(6): 1374–1376.

[8] Weston JS, Seeman DP, Blair DL, Salipante PF, Hudson SD, Weigandt KM. Simultaneous slit rheometry and in situ neutron scattering. *Rheologica Acta.* 2018; 57(3): 241–250.

[9] Vermant J, Moldenaers P, Mewis J, Ellis M, Garritano R. Orthogonal superposition measurements using a rheometer equipped with a force rebalanced transducer. *Review of Scientific Instruments.* 1997; 68(11): 4090–4096.

[10] Tao R, Forster AM. End effect correction for orthogonal small strain oscillatory shear in a rotational shear rheometer. *Rheologica Acta.* 2020; 59(2): 95–108.

[11] Jacob AR, Poulos AS, Semenov AN, Vermant J, Petekidis G. Flow dynamics of concentrated starlike micelles: A superposition rheometry investigation into relaxation mechanisms. *Journal of Rheology.* 2019; 63(4): 641–653.

[12] Israelachvili JN. *Intermolecular and surface forces.* Academic press 2015.

[13] Cates M, Candau S. Statics and dynamics of worm-like surfactant micelles. *Journal of Physics: Condensed Matter.* 1990; 2(33): 6869.

[14] Safran S, Pincus P, Cates M, MacKintosh F. Growth of charged micelles. *Journal de Physique.* 1990; 51(6): 503–510.

[15] Cates M. Reptation of living polymers: dynamics of entangled polymers in the presence of reversible chain-scission reactions. *Macromolecules.* 1987; 20(9): 2289–2296.

[16] Marques CM, Turner MS, Cates ME. Relaxation mechanisms in worm-like micelles. *Journal of non-crystalline solids.* 1994; 172: 1168–1172.

[17] Helgeson ME, Hodgdon TK, Kaler EW, Wagner NJ. A systematic study of equilibrium structure, thermodynamics, and rheology of aqueous ctab/nano3 wormlike micelles. *Journal of colloid and interface science.* 2010; 349(1): 1–12.

[18] Chen WR, Butler PD, Magid LJ. Incorporating intermicellar interactions in the fitting of sans data from cationic wormlike micelles. *Langmuir.* 2006; 22(15): 6539–6548.

[19] Liberatore MW, Nettesheim F, Vasquez PA, et al. Microstructure and shear rheology of entangled wormlike micelles in solution. *Journal of Rheology.* 2009; 53(2): 441–458.

[20] Cates M. Nonlinear viscoelasticity of wormlike micelles (and other reversibly breakable polymers). *Journal of Physical Chemistry.* 1990; 94(1): 371–375.

[21] Vasquez PA, McKinley GH, Cook LP. A network scission model for wormlike micellar solutions: I. model formulation and viscometric flow predictions. *Journal of non-newtonian fluid mechanics.* 2007; 144(2-3): 122–139.

[22] Dutta S, Graham MD. Mechanistic constitutive model for wormlike micelle solutions with flow-induced structure formation. *Journal of Non-Newtonian Fluid Mechanics.* 2018; 251: 97–106.

[23] Rothstein JP. Transient extensional rheology of wormlike micelle solutions. *Journal of Rheology.* 2003; 47(5): 1227–1247.

[24] Prud'homme RK, Warr GG. Elongational flow of solutions of rodlike micelles. *Langmuir.* 1994; 10(10): 3419–3426.

[25] Bhardwaj A, Richter D, Chellamuthu M, Rothstein JP. The effect of pre-shear on the extensional rheology of wormlike micelle solutions. *Rheologica acta.* 2007; 46(6): 861–875.

[26] Anna SL, McKinley GH. Effect of a controlled pre-deformation history on extensional viscosity of dilute polymer solutions. *Rheologica acta.* 2008; 47(8): 841–859.

[27] Chen S, Rothstein JP. Flow of a wormlike micelle solution past a falling sphere. *Journal of Non-Newtonian Fluid Mechanics.* 2004; 116(2-3): 205–234.

[28] Mohammadigoushki H, Muller SJ. Sedimentation of a sphere in wormlike micellar fluids. *Journal of Rheology.* 2016; 60(4): 587–601.

[29] Kröger M, Makhloufi R. Wormlike micelles under shear flow: A microscopic model studied by nonequilibrium-molecular-dynamics computer simulations. *Physical Review E.* 1996; 53(3): 2531.

[30] Carl W, Makhloufi R, Kröger M. On the shape and rheology of linear micelles in dilute solutions. *Journal de Physique II.* 1997; 7(6): 931–946.

[31] Padding JT, Boek ES, Briels WJ. Dynamics and rheology of wormlike micelles emerging from particulate computer simulations. *The Journal of chemical physics.* 2008; 129(7): 074903.

[32] Sambasivam A, Sangwai AV, Sureshkumar R. Dynamics and scission of rodlike cationic surfactant micelles in shear flow. *Physical review letters.* 2015; 114(15): 158302.

[33] Dhakal S, Sureshkumar R. Uniaxial extension of surfactant micelles: counterion mediated chain stiffening and a mechanism of rupture by flow-induced energy redistribution. *ACS Macro Letters.* 2016; 5(1): 108–111.

[34] Larson RG. *The structure and rheology of complex fluids*; Vol. 150. Oxford university press New York 1999.

[35] Doi M, Edwards SF. *The theory of polymer dynamics*; Vol. 73 of *International series of monographs on physics.* Oxford: Clarendon Pressreprinted. ed. 1989.

[36] Gennes PGd. *Scaling concepts in polymer physics.* Ithaca, NY: Cornell Univ. Press 1979.

[37] Graham RS, Likhtman AE, McLeish TCB, Milner ST. Microscopic theory of linear, entangled polymer chains under rapid deformation including chain stretch and convective constraint release. *Journal of Rheology.* 2003; 47(5): 1171–1200.

[38] Kim S, Mewis J, Clasen C, Vermant J. Superposition rheometry of a wormlike micellar fluid. *Rheologica Acta.* 2013; 52(8-9): 727–740.

[39] Vermant J, Walker L, Moldenaers P, Mewis J. Orthogonal versus parallel superposition measurements. *Journal of non-newtonian fluid mechanics.* 1998; 79(2-3): 173–189.

Chapter 2

Materials and Methods

This chapter presents a complete description of all materials and experimental measurements used in this work. Unless otherwise noted, materials were prepared and experiments were carried out and analyzed according to the procedures outlined here.

2.1 Materials

2.1.1 Preparation of wormlike micelle solutions

The model wormlike micelle forming system studied in this work is that of cetyltrimethylammonium bromide (CTAB, Sigma Aldrich) in aqueous solution with sodium nitrate ($NaNO_3$, Sigma Aldrich). The molecular structures of CTAB and $NaNO_3$ are given in Figure 2.1. All materials were used as supplied without further purification. For neutron scattering measurements, it was necessary to prepare samples using deuterium oxide (D_2O, 99.9%, Cambridge Isotope Laboratories) to reduce incoherent scattering. These samples were prepared at various concentrations and will be specified in the subsequent chapters. Dry powders of CTAB and $NaNO_3$ were added to D_2O in the appropriate amounts. After agitation for complete powder dispersion, the solutions were placed in a temperature-controlled oven held at 47 °C for at least 1 day to achieve sample equilibration before measurements.

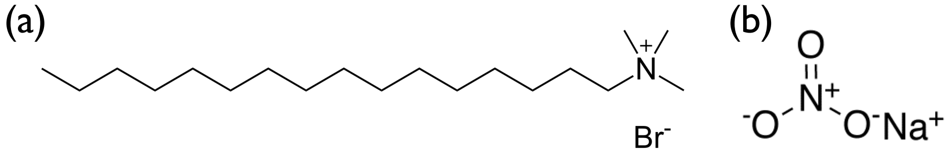

Figure 2.1: Molecular structures of (a) cetyltrimethylammonium bromide and (b) sodium nitrate.

2.2 Rheological characterization

2.2.1 Experimental

Rheological characterization was performed on a TA Instruments AR-G2 stress-controlled rheometer with a Taylor-Couette geometry with a rotating inner cylinder of $R_1 = 13.98$ mm and a stationary outer cylinder of $R_2 = 15.21$ mm. This geometry was chosen to closely resemble the gap size and the radius of curvature in the geometry used in flow-SANS measurements. The fluid temperature was set with a Peltier-controlled outer cylinder. A solvent trap was used to prevent evaporation of D_2O during the measurements. The sample was loaded and conditioned at rest for 700 s at the temperature corresponding to the experiment. A pre-shear of $1s^{-1}$ was applied for 60 s and the sample was allowed to rest for 100 s to erase any loading history and to let the temperature equilibrate. The storage (G') and loss (G'') moduli were measured by performing a frequency sweep at 5% strain (in the linear viscoelastic regime: LVE) from 200 rad/s to 0.1 rad/s and then another from 0.1 rad/s to 200 rad/s. No hysteresis in the LVE measurements was observed for any sample. Steady-shear tests were run with logarithmic spacing for shear rates, $\dot{\gamma}$, ranging from 0.01 to 1500 s^{-1} . For each measurement during the steady-state test, the steady state sensing was turned on, with a 1% tolerance within 3 consecutive points, 60 s maximum equilibration time, and 15 s sample periods, to ensure steady state has been achieved before results were recorded.

2.2.2 Theory

The linear viscoelasticity of entangled micelles at low and intermediate frequencies is well described by a Maxwell model (Fig. 2.2). The plateau modulus (G_0) and longest relaxation time (τ) of a WLM solution are obtained by fitting linear viscoelastic moduli (G' and G'') to a single-mode Maxwell model:

$$G'(\omega) \; = \; \frac{G_0 \; (\tau\,\omega)^2}{1 \, + \, (\tau\,\omega)^2}, \tag{2.1}$$

$$G''(\omega) \; = \; \frac{G_0 \; (\tau\,\omega)}{1 \, + \, (\tau\,\omega)^2} \, + \, \eta_\infty \omega, \tag{2.2}$$

where ω is the applied frequency and η_∞ is the high-frequency viscosity.

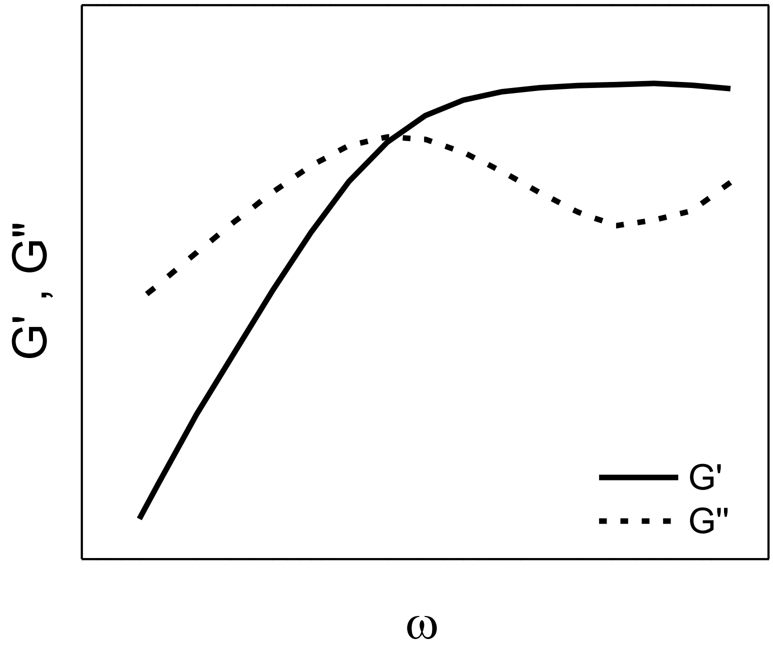

Figure 2.2: Storage (G') and loss (G'') moduli of entangled wormlike micelles at low and intermediate frequencies (ω).

The average number of entanglements per chain is estimated by using $N_e = G_0/G''_{min}$, where G_0 is the plateau value of G' and G''_{min} is the minimum of G''.[1] Although Larson and co-workers recently proposed a mesoscopic simulation method to estimate the structural parameters of semi-dilute WLMs, their method requires LVE measurements in the high frequency regime that were inaccessible in this work.[2] Alternatively, the length of the entanglement strands can be estimated using rubber elasticity theory, by assuming that the micelles form an entanglement network, similar to one made up of cross-linked polymer chains.[3] According to this theory, the mesh size of the entangled network, ξ_m, can be estimated from the plateau modulus (G_0) as

$$\xi_m = \left(\frac{k_B T}{G_0}\right)^{1/3}, \tag{2.3}$$

where k_B is the Boltzmann constant and T is the temperature.[4] The entanglement length,

l_e, is then given in terms of ξ_m by[5]

$$l_e = \frac{\xi_m^{5/3}}{l_p^{2/3}}, \tag{2.4}$$

where l_p is the persistence length. The number density of entanglement strands, ν, is given by

$$\nu = G_0/k_B T. \tag{2.5}$$

2.3 Particle tracking velocimetry

Velocimetry measurements were carried out using particle tracking velocimetry (PTV) on an Anton-Paar Physica MCR300 rheometer using a Taylor-Couette geometry. The outer stationary quartz cup has a fixed radius $R_2 = 17.5$ mm. We used an inner moving anodized aluminum cylinder with a radius $R_1 = 17$ mm, which corresponds to a gap size of 0.5 mm. The temperature of the Couette cell is controlled with a circulating water bath. Sample preparation for PTV measurements consisted of seeding the fluid with approximately 300 ppm of neutrally buoyant hollow silica spheres (8-12 μm diameter, TSI Incorporated). In all cases, addition of tracer particles at such low concentrations produced no significant changes in the measured sample rheology. An incident sheet laser on the inner cylinder was introduced from the side at a height of 6 mm from the bottom of the 15.7 mm tall inner cylinder, and the reflection from the tracer particles was collected through a sapphire window at the bottom of the geometry and imaged using a CCD camera. Both shear stress and PTV measurements were made simultaneously after quickly ramping the applied shear rate of the rheometer from rest to the desired rate within 0.1 s. Measurements were made for $\sim$160 s at each shear rate to ensure the achievement of steady state. The consecutive images taken with the camera were analyzed using a standard particle-tracking algorithm[6] to obtain spatially resolved fluid velocity $v_\theta(r)$ as a function of the position r within the gap, measured from the inner moving cylinder. The steady-velocity profiles were obtained by averaging the PTV data over ∼30 different pairs of consecutive images after the shear stress achieved steady state.

2.4 Flow visualization

To investigate the possibility of elastic instability in wormlike micelles in the Taylor-Couette geometry, we modified the Anton-Paar Physica MCR300 setup, which was originally used for PTV measurements, to allow for visualization of the secondary flow. Specifically, a lamp was placed next to the rheometer to illuminate the side of the Taylor-Couette cell. The Taylor-Couette cell consisted of an outer stationary quartz cup with a radius $R_2 = 17.5$ mm and an inner moving anodized aluminum cylinder with a radius $R_1 = 17$ mm. The temperature of the Couette cell is controlled with a circulating water bath. The fluid was seeded with mica flakes (Iriodin 100 Silver Pearl from EMD Performance Materials, size 10-60 μm, density 2.8-3.0 g/cm^3). Because of the anisotropy in the shape of the mica flakes, if secondary flow (such as roll cell) develops, the fluid will show repeating bright and dark streaks. To delay the onset of rod climbing, a metal cap was placed on top of the shear cell with the bottom surface submerging in the fluid.

2.5 Small angle neuton scattering

Since the microstructures of materials studied in this work possess characteristic length scales much smaller than the wavelength of visible light, neutrons provide a more robust radiation source for their structural characterization. A typical neutron scattering experiment is illustrated in Fig. 2.3 An incident neutron beam (given by the vector $\mathbf{k_0}$)

interacts with the scatterers, resulting in scattering at an angle α (determined by the scattering vector $\mathbf{k}$). The wave vector, $\mathbf{q}$, is defined by $\mathbf{q} = \mathbf{k} - \mathbf{k_0}$, and has magnitude given by:

$$q = \frac{4\pi}{\lambda_0} sin\left(\frac{\alpha}{2}\right). \tag{2.6}$$

Thus, for neutrons with a typical wavelength of 6 Å, the resulting length scales probed by small angle neutron scattering will be $\mathcal{O}(1 - 200nm)$, which spans the range of structures studied in this work, from the micellar radii to the contour length of wormlike micelles and polymers. Thus, small angle neutron scattering (SANS) presents a powerful method to study the microstructures of wormlike micelles and polymers.

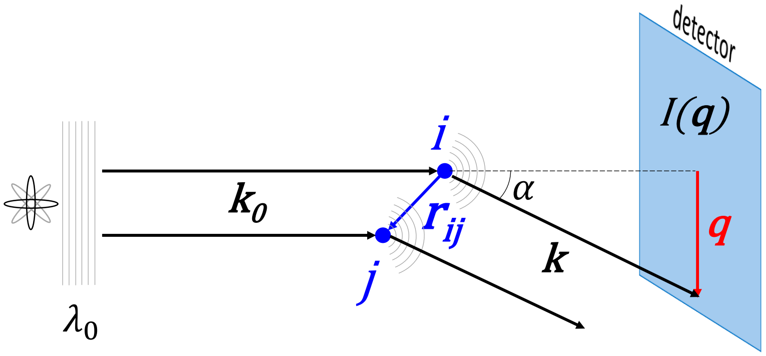

Figure 2.3: Illustration of a typical small angle neutron scattering experiment.

2.5.1 Experimental

Steady state flow-SANS

SANS measurements were performed using the NGB 30m SANS instrument at the National Institute of Standards and Technology Center for Neutron Research (Gaithersburg, MD). Anisotropic scattering was characterized using flow-SANS for simple shear flow in both the flow-gradient $(v - \nabla v)$ plane and the flow-vorticity $(v - \omega)$ planes. Measurements in the flow-gradient plane were made using the 1-2 shear cell sample environment[7] and measurements in the flow-vorticity plane employed a Couette cell controlled by an Anton Parr rheometer. A wavelength of $\lambda_0 = 6$ Å with a wavelength spread of $\Delta\lambda_0/\lambda_0 = 0.14$ was used. Scattering from the sample was collected in the q range $0.005 - 0.2$ Å^{-1}. The temperature was maintained constant at set temperature through the entire experiment with a water bath for the shear cell. The 2D scattering intensities were corrected for empty cell, plexiglass standard, and detector efficiency. Scattering patterns were reduced using standard protocols with Igor Pro software.[8]

Time-resolved flow-SANS

Time-resolved flow-small angle neutron scattering is used to capture structures of wormlike micelles during the startup and cessation of flow. The method requires the synchronization of the scattering and startup of the flow geometry (1-2 plane shear cell or the rheometer). The time-resolved experiments bin data into $n_b = t_{tot}/\Delta t = 150$ bins of Δt duration for a cycle time of t_{tot}. Here the cycle time t_{tot} is 15 s, with 5 s for start up of flow and 10 s for flow cessation. The scattering intensity is collected over a prescribed number of repeated transient experiments n_c and summed to achieve sufficient total scattering intensity. Here we use $n_c \approx 330$ in the rheometer and $n_c \approx 600$ in the shear cell. A prerequisite for choosing a material to be investigated with time-resolved flow-SANS is that it behaves reproducibly for each subsequent transient event so that a sufficient number of cycles can be summed to collect statically valid scattering patterns in each time bin. Here we validate that the sample fully recovers to equilibrium during the relaxation period as evidenced by the isotropic intensity that no longer changes with time.

2.5.2 SANS modeling

The magnitude of the scattering is given by the total coherent scattering cross-section, which for a material comprised of N_p scattering objects in a structureless medium is given by[9]

$$\frac{d\Sigma}{d\Omega} = \frac{1}{V}\sum_{i=1}^{N_p}\langle|f_i(\mathbf{q})|\rangle + \frac{1}{V}\left\langle\sum_{i=1}^{N_p}\sum_{j=1,i\neq j}^{N_p} f_i(\mathbf{q})f_j(\mathbf{q})e^{-i\mathbf{q}\cdot(\mathbf{r}_i-\mathbf{r}_j)}\right\rangle, \tag{2.7}$$

where $\mathbf{r}_i$ and $\mathbf{r}_j$ are the positions of objects i and j, respectively, and $f_i(\mathbf{q})$ is the scattering amplitude given by

$$f_i(\mathbf{q}) = \int_V \left[\rho_i(\mathbf{r}) - \rho_s\right] e^{-i\mathbf{q}\cdot\mathbf{r}} \tag{2.8}$$

where $\rho_i(\mathbf{r})$ and ρ_s are the scattering length densities of the scattering object and the surrounding medium, respectively. Typically, for scattering objects that are polydisperse in structure and orientation, a reasonable approximation for the scattering cross-section is to assume that the scattering amplitude for any scatterer is approximately equal to that of particles with average size and shape.[10] Thus, the scattering cross-section reduces to

$$\frac{d\Sigma}{d\Omega} = n_p\overline{\langle f_i\left(\mathbf{q}\right)\rangle}\left(1 + \overline{\left\langle\sum_{i=1}^{N_p}\sum_{j=1,i\neq j}^{N_p} f_i(\mathbf{q})f_j(\mathbf{q})e^{-i\mathbf{q}\cdot(\mathbf{r}_i-\mathbf{r}_j)}\right\rangle}\right), \tag{2.9}$$

where n_p is the number density of scattering objects, and the overbar represents the average over all scattering objects. Typically, the bracketed term defines the form factor, $P(\mathbf{q})$, and the term in parentheses defines the structure factor, $S(\mathbf{q})$. Using this approximation, and assuming that the coherent scattered intensity measured during SANS experiments is equal to the scattering cross-section, we obtain the following expression for the total scattering intensity:[11]

$$I\left(\mathbf{q}\right) = n_p P\left(\mathbf{q}\right) S\left(\mathbf{q}\right) + I_b \tag{2.10}$$

where I_b is the incoherenet scattered intensity. If the scattering intensity is isotropic (e.g., at equilibrium), the intensity only depends on the magnitude of $\mathbf{q}$. For anisotropic scattering objects, such as wormlike micelles and polymers considered throughout this work, the form and structure factors, and thus the scattered intensity, will depend not only on q, but also on the orientation angle of $\mathbf{q}$ due to the orientational contribution to the interparticle interactions.

In general, the form factor $P(\mathbf{q})$ is related to the distribution of mass within a scattering object and can be defined as the direct Fourier transform of the pair correlation function, $\psi(\mathbf{r}_{ij})$:[11]

$$P(\mathbf{q}) \;=\; \int \left(\psi\left(\mathbf{r}_{ij}\right)\right)^2 \exp\left(-i\mathbf{q}\cdot\mathbf{r}_{ij}\right) d\mathbf{r}_{ij}, \tag{2.11}$$

where the integral is taken over the volume of the object. The pair correlation function $\psi(\mathbf{r}_{ij})$ gives the probability density of finding a point of mass i within the object from a reference point j, normalized such that integration over the entire space yields the object volume V_p.

The structure factor arises from the configuration of an ensemble of scattering objects within a medium, and is thus related to interactions between individual scattering objects. Similarly to the form factor, the structure factor can be mathematically described as the direct Fourier transformation of the pair distribution function $g(r_{12})$ by:

$$S(q) \;=\; 1 + \int \left[g\left(r_{12} - 1\right)\right] \exp\left(-iq\cdot r_{12}\right) d^3 r_{12} \tag{2.12}$$

The pair distribution function is related to the statistical probability of finding the center of a scattering object separated from the center of a reference object by a distance r_{12}. Therefore, $g(r_{12})$ can be related to the potential of intereaction between objects from statistical mechanics.[12] This is typically achieved through the Ornstein-Zernicke equation:[13]

$$g\left(r_{12}\right) \;=\; c\left(r_{12}\right)+n_p\int c\left(r_{13}\right)\left[g\left(r_{23}\right)-1\right]dr_3 \tag{2.13}$$

where n_p is the number density of scatterers and the function $c(r)$ is the direct correlation function, which requires using an appropriate closure approximation where $c(r)$ is typically related to the potential of mean force between interacting particles. Formulating the pair distribution function according to Eqn. 2.13 allows one to relate the structure factor to the Fourier transform of $c(r)$ by using the convolution theorem:[12]

$$S(q) \;=\; \frac{\hat{C}(q)}{1-n_p\hat{C}(q)}, \tag{2.14}$$

where $\hat{C}(q)$ is the direct Fourier transform of $c(r)$.

Subsequent chapters will discuss in more depth the scattering models for wormlike micelles and polymers at equilibrium and in flow.

Bibliography

[1] Granek R, Cates M. Stress relaxation in living polymers: Results from a poisson renewal model. *The Journal of chemical physics.* 1992; 96(6): 4758–4767.

[2] Zou W, Larson RG. A mesoscopic simulation method for predicting the rheology of semi-dilute wormlike micellar solutions. *Journal of Rheology.* 2014; 58(3): 681–721.

[3] Helgeson ME, Hodgdon TK, Kaler EW, Wagner NJ. A systematic study of equilibrium structure, thermodynamics, and rheology of aqueous ctab/nano3 wormlike micelles. *Journal of colloid and interface science.* 2010; 349(1): 1–12.

[4] Ferry JD. *Viscoelastic properties of polymers.* John Wiley & Sons 1980.

[5] Doi M, Edwards SF, Edwards SF. *The theory of polymer dynamics*; Vol. 73. oxford university press 1988.

[6] Hu YT, Lips A. Kinetics and mechanism of shear banding in an entangled micellar solution. *Journal of Rheology.* 2005; 49(5): 1001–1027.

[7] Gurnon AK, Godfrin PD, Wagner NJ, Eberle AP, Butler P, Porcar L. Measuring material microstructure under flow using 1-2 plane flow-small angle neutron scattering. *JoVE (Journal of Visualized Experiments).* 2014(84): e51068.

[8] Kline SR. Reduction and analysis of sans and usans data using igor pro. *Journal of applied crystallography.* 2006; 39(6): 895–900.

[9] Guinier A, Fournet G, Yudowitch KL. Small-angle scattering of x-rays. 1955.

[10] Hayter JB, Penfold J. An analytic structure factor for macroion solutions. *Molecular Physics.* 1981; 42(1): 109–118.

[11] Hammouda B. Probing nanoscale structures-the sans toolbox. national institute of standards and technology. *Center for Neutron Research, Gaithersburg, MD, USA.* 2016.

[12] McQuarrie D. *Statistical mechanics* . 2000.

[13] Ornstein L, Zernike F. The linear dimension of density variations. *Physikalische Zeitschrift.* 1918; 19: 134–137.

Chapter 3

Theory: Equilibrium Modeling of the Scattering of Polymers and Wormlike Micelles

This chapter will focus on an overview of the equilibrium theories for describing the scattering of polymers and wormlike micelles that will lay a foundation for Chapters 4-6, which discuss our new development and application of nonequilibrium scattering models for polymers and wormlike micelles in flow. The discussion will begin with a description of previous scattering models for both dilute, flexible polymers and dilute and semi-dilute wormlike micelles. Finally, we discuss in detail a new scattering model for entangled, concentrated wormlike micelles. This model was originally developed by Peng Cheng, a former graduate student in our groups. I improved the model and the fit to the data.

Sections 3.2.1 to 3.2.4 are adapted with permission from "Cheng, P. (2017). Rheology, kinematics, and structure of shear banding wormlike micelles (Order No. 10599970). Available from Dissertations & Theses @ University of California; ProQuest Dissertations & Theses A&I. (1938226239)."

3.1 Previous models

3.1.1 Equilibrium modeling of dilute, flexible polymers

In general, the scattering intensity for monodisperse polymers is described by

$$I(q) = \phi\,(\Delta\rho)^2\,V_p P(q) S(q) + I_b, \tag{3.1}$$

where ϕ is the volume fraction of the polymers, $\Delta\rho$ is the difference in scattering length density between the polymers and the solvent, V_p is the volume of a chain, and I_b is the incoherent background intensity. $P(q)$ is the form factor, which describes the contribution from intra-chain scattering. $S(q)$ is the structure factor, which measures the contribution from inter-chain scattering (i.e., how individual polymers are positioned in space relative to each other). If the polymer solution is sufficiently dilute, the effects of the structure factor can be neglected ($S(q) \approx 1$). So, for this section, we will only focus on the form factor.

Polymer coils in theta solvents or in the melt state follow Gaussian chain statistics whereby the inter-monomer distance r_{jk} is given by the Gaussian distribution function,

$$\psi\left(r_{jk}\right) = \left(\frac{3}{2\pi\left\langle r_{jk}^2\right\rangle}\right)^{3/2} \exp\left[-\frac{3r_{jk}^2}{2\left\langle r_{jk}^2\right\rangle}\right]. \tag{3.2}$$

Here $\left\langle r_{jk}^2\right\rangle$ is the variance given in terms of the statistical segment length a as:

$$\left\langle r_{jk}^2\right\rangle = a^2\left|j-k\right|. \tag{3.3}$$

Figure 3.1 illustrates the vector $\mathbf{r}_{jk}$ in a polymer chain.

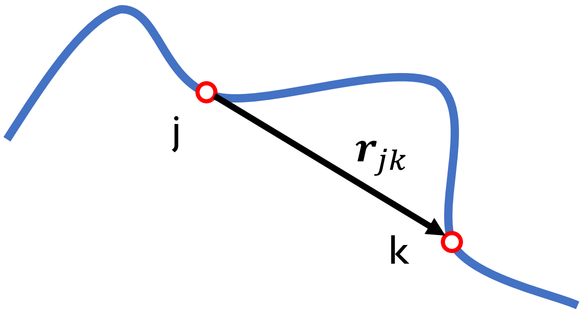

Figure 3.1: Schematic of a polymer chain. $\mathbf{r}_{jk}$ represents the vector between monomer j and monomer k.

For a chain with n statistical segments, the single-chain form factor is given by

$$\begin{aligned} P(q) &= \frac{1}{n^2}\sum_{j,k}^{n}\left\langle -i\mathbf{q}\cdot\mathbf{r}_{jk}\right\rangle \\ &= \frac{1}{n^2}\sum_{j,k}^{n}\int d\mathbf{r}_{jk}\psi\left(r_{jk}\right)\exp\left[-i\mathbf{q}\cdot\mathbf{r}_{jk}\right] \end{aligned} \tag{3.4}$$

For a Gaussian distribution, the integral in the equation above can be evaluated analytically by completing the square in the integral:

$$\begin{aligned} \int d\mathbf{r}_{jk}\psi\left(r_{jk}\right)\exp\left[-i\mathbf{q}\cdot\mathbf{r}_{jk}\right] &= \left(\frac{3}{2\pi\left\langle r_{jk}^2\right\rangle}\right)^{3/2}\int \exp\left[-\frac{3\mathbf{r}_{jk}^2}{2\left\langle r_{jk}^2\right\rangle}-i\mathbf{q}\cdot\mathbf{r}_{jk}\right]d\mathbf{r}_{jk} \\ = \left(\frac{3}{2\pi\left\langle r_{jk}^2\right\rangle}\right)^{3/2}&\int \exp\left[-\frac{3}{2\left\langle r_{jk}^2\right\rangle}\left(\mathbf{r}_{jk}+i\frac{\left\langle r_{jk}^2\right\rangle\mathbf{q}}{3}\right)^2\right]\exp\left[-\frac{q^2\left\langle r_{jk}^2\right\rangle}{6}\right]d\mathbf{r}_{jk} \end{aligned} \tag{3.5}$$

The final exponential in the expression (3.5) above does not depend on $\mathbf{r}_{jk}$ and can be taken outside the integral sign. We also use $\boldsymbol{\rho} = \mathbf{r}_{jk} + i\left\langle r_{jk}^2\right\rangle\mathbf{q}/3$ as the new variable.

Thus, we obtain:

$$
\begin{aligned}
\int d\mathbf{r}_{jk}\psi\left(r_{jk}\right)\exp\left[-i\mathbf{q}\cdot\mathbf{r}_{jk}\right] &= \exp\left[-\frac{q^2\left\langle r_{jk}^2\right\rangle}{6}\right]\underbrace{\left[\left(\frac{3}{2\pi\left\langle r_{jk}^2\right\rangle}\right)^{3/2}\int\exp\left[-\frac{3\boldsymbol{\rho}^2}{2\left\langle r_{jk}^2\right\rangle}\right]d\boldsymbol{\rho}\right]}_{=1} \\
&= \exp\left[-\frac{q^2\left\langle r_{jk}^2\right\rangle}{6}\right]
\end{aligned}
\tag{3.6}
$$

Upon substituting the expression for the integral into Eqn. 3.4, we obtain:

$$
P(q) = \frac{1}{n^2}\sum_{j,k}^{n}\exp\left[-\frac{q^2\left\langle r_{jk}^2\right\rangle}{6}\right] = \frac{1}{n^2}\sum_{j,k}^{n}\exp\left[-\frac{q^2\left|j-k\right|}{6}\right]
\tag{3.7}
$$

Using the general identity $\sum_{j,k}^{n} F\left(|j-k|\right) = n + 2\sum_{m-1}^{n}\left(n-m\right)F(m)$ and assuming the number of chain segments is large ($n \gg 1$), we obtain:

$$
P(q) = \frac{1}{n^2}\left[n + 2\sum_{m=1}^{n}\left(n-m\right)\exp\left(-\frac{q^2a^2m}{6}\right)\right]
\tag{3.8}
$$

Finally, upon transforming the sum into an integral and neglecting the $1/n$ term for large n, we obtain the Debye function for scattering of Gaussian chains:[1]

$$
P(q) = \frac{2}{q^4R_g^4}\left[\exp\left(-q^2R_g^2\right) + q^2R_g^2 - 1\right],
\tag{3.9}
$$

where the radius of gyration is given by $R_g = \sqrt{a^2n/6}$.

In scattering experiments of polymers, the low-q circularly averaged scattering intensity is often used to extract the radius of gyration. The theoretical basis for this analysis can be obtained by performing a small q expansion of the Debye function for $qR_g \ll 1$:

$$
\frac{2}{q^4R_g^4}\left[\exp\left(-q^2R_g^2\right) - 1 + q^2R_g^2\right] \approx 1 - \frac{q^2R_g}{3} + \mathcal{O}(2).
\tag{3.10}
$$

Thus, in a plot of $\log I(q)$ as a function of q^2, the initial slope is $-R_g^2/3$. This analysis is called the Guinier analysis and is only valid in the low-q limit ($qR_g < \sqrt{3}$).

3.1.2 Scattering models for dilute and semi-dilute wormlike micelles

Wormlike micelles (WLMs) exhibit a broad distribution of micellar contour lengths, L_c, ranging from the cross-sectional radius (r_{cs}) to length scales that may considerably exceed the entanglement length (l_e). The contour length distribution of WLMs is typically assumed to follow the theory of Cates and co-workers, which predicts that the equilibrium probability distribution of contour lengths will adopt an exponential form.[2–6] Specifically, for a solution containing micelles with an overall volume fraction ϕ_{total}, the probability density, $f(L_c)$, and resulting volume fraction, $\phi(L_c)$, of micelles having contour length L_c is given by

$$f(L_c) = \begin{cases} L_c < 2r_{cs} : 0 \\ L_c \geq 2r_{cs} : \frac{\exp\left(-L_c/\bar{L}_c\right)}{\int_{2r_{cs}}^{\infty} \exp\left(-L_c/\bar{L}_c\right)}, \end{cases} \tag{3.11}$$

and

$$\phi(L_c) = \begin{cases} L_c < 2r_{cs} : 0 \\ L_c \geq 2r_{cs} : \phi_{total} \cdot \frac{L_c \exp\left(-L_c/\bar{L}_c\right)}{\int_{2r_{cs}}^{\infty} L_c \exp\left(-L_c/\bar{L}_c\right)}, \end{cases} \tag{3.12}$$

where $\bar{L}_c$ is the average contour length of the entire micelle population. $\phi(L_c)$ exhibits a maximum at the average length $\bar{L}_c$. Here, we have modified Cates' original theory by assuming that all wormlike micelles must be longer than their cross-sectional diameter, $2r_{cs}$. This assumption is necessary to describe the length distribution of micelles when $L_c \sim r_{cs}$, which always occurs for a small number of micelles even when the average micelle length is relatively long compared to r_{cs}.

The equilibrium distribution of contour lengths in dilute and semi-dilute wormlike micelle solutions has been well characterized using SANS measurements. In general, the scattering from WLMs is convoluted by a number of factors including both intra-chain and inter-chain correlations, as well as a broad contour length polydispersity. In the dilute and semi-dilute regimes, micelles are well-separated from each other and possess relatively few entanglements.[4–6] Therefore, in this case, the SANS measurement is able to probe the full hierarchy of length scales of the micelles, ranging from the longest contour length, $L_{c,max}$, to the cross-sectional radius, r_{cs}.

For wormlike micelles at relatively low concentrations, the scattering data shows similar dependence on the scattering vector q as that of classical polymers and has different q-dependence in different q ranges. At low enough q ($q \left\langle R_g^2 \right\rangle \ll 1$, where $\left\langle R_g^2 \right\rangle$ is the square average radius of gyration), $I \sim 1 - q^2 \left\langle R_g^2 \right\rangle /3$). The scattering curve levels off at this low-q range (the Guinier region) due to the finite size of the micelles relative to the length probed. Beyond the Guinier region, the scattering crosses over to a power law behavior $q^{-5/3}$ due to the excluded-volume statistics of the micelles. At higher q, the scattering probes the local cylindrical structure and it crosses over to q^{-1}. However, this power law is often masked by the polydispersity in micellar length and the cross-section Guinier region that originates from the finite diameter of the micelles. Beyond this region, the scattering curve drops significantly and at the highest q it follows the Porod law q^{-4} which occurs for objects with sharp interfaces.[6] The scaling in different q regions is shown schematically in Fig. 3.2 below.

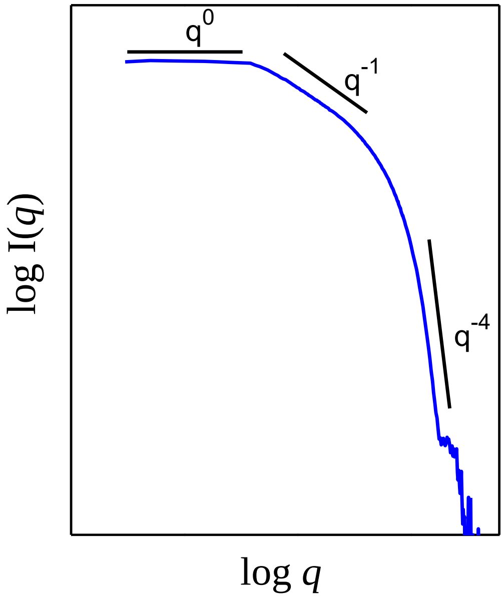

Figure 3.2: Schematic of different regions of q-scaling for scattering intensity of wormlike micelles.

Compared to modeling the scattering of dilute, monodisperse polymers as discussed in the last section, modeling the equilibrium scattering of wormlike micelles poses more challenges. This is because the analysis of the form factor is complicated by many structural features of WLMs, such as chain semi-flexiblity and polydispersity in the length. This section outlines several of the models typically used for wormlike micelles that were developed by Pedersen, Schurtenberger, and coworkers.[6]

For sufficiently dilute chains with polydisperse length and polydisperse radius and an isotropic orientation distribution, the expression of the scattering intensity for monodisperse chains (Eqn. 3.1) is modified to account for polydispersity:

$$I(q) \,=\, \phi\,(\Delta\rho)^2\,\overline{V}_p\overline{P(q)S(q)} + I_b \tag{3.13}$$

where ϕ is the volume fraction of the micelles, $\Delta\rho$ is the difference in scattering length density between the micelles and the solvent, $\overline{V}_p = \pi \bar{r}_{cs}^2 \bar{L}_c$ is the average volume of a chain, and I_b is the incoherent background intensity. $\bar{L}_c$ is the number-average contour length and $\bar{r}_{cs}$ is the average radius of the micelle. If the micelles are sufficiently dilute, such that the average intermolecular distance (correlation length between neighboring chains) is larger than the intramolecular distance, this leads to the decoupling approximation commonly used for wormlike micelles, i.e., the effect of polydispersity in the form factor $P(q)$ and the structure factor $S(q)$ can be separated.[4,5]

The form factor

In general, the form factor for a chain-like object arises from both the shape of the cross-section as well as the possible conformations along the contour of the object. For wormlike micelles, since the contour length is much greater than the cross-sectional dimension, the polydisperse chain form factor can be decoupled into two contributions:[7,8]

$$\overline{P(q)} = \overline{P_L(q) P_{cs}(q)}, \tag{3.14}$$

where $\overline{P_L(q)}$ and $\overline{P_{cs}(q)}$ are the polydisperse form factors for the chain length and cross-section, respectively. For wormlike micelles, a circular cross section of radius r_c with a Gaussian distribution for the polydispersity is typically assumed, such that

$$P_{cs}(q) = \left(\pi r_{cs}^2\right)^2 \left(\frac{2 J_1\left(q r_{cs}\right)}{q r_{cs}}\right)^2. \tag{3.15}$$

and

$$f\left(r_{cs}\right) = \frac{1}{\sqrt{2\pi\sigma^2}} \exp\left[-\frac{\left(\bar{r}_{cs} - r_{cs}\right)^2}{2\sigma^2}\right], \tag{3.16}$$

where $f\left(r_{cs}\right)$ is the length distribution of the micellar radius, $\bar{r}_{cs}$ is the average micellar radius, and σ is the standard deviation.

As discussed previously, the reversible scission of wormlike micelles produces an equilibrium distribution of chain lengths. The chain length at equilibrium has a polydispersity given by an exponential function, according to the Cates model.[2] In the Pedersen-Schurtenberger model, the polydisperse form factor for the chain length is calculated as a weighted average of the monodisperse form factor over the length distribution:

$$\bar{P}_L(q) = \frac{\int_{2r_{cs}}^{\infty} f(L_c) P_L(q, L_c) dL_c}{\int_{2r_{cs}}^{\infty} f(L_c) dL_c}, \tag{3.17}$$

where $f\left(L_c, \bar{L}_c\right) = \exp\left(-L_c/\bar{L}_c\right)$ is the exponential distribution of chain length and $\bar{L}_c$ is the average micellar length.

The Pedersen-Schurtenberger model used an asymptotic matching for the form factor of the chain length.[9,10] Namely, the form factor for a wormlike micelle chain is approximated by that of a Gaussian chain at low q which crosses over to that of a rod at higher q:

$$P_L\left(q, L_c\right) = P_{chain}(q) \cdot \exp\left[-\left(\frac{qb}{5.53}\right)^{5.33}\right] + P_{rod}(q)\left[1 - \exp\left[-\left(\frac{qb}{5.53}\right)^{5.33}\right]\right]. \tag{3.18}$$

$P_{chain}(q)$ is the form factor of flexible chains, $P_{rod}(q)$ is the Burchard-Kajiwara rod-like scattering function, and b is the Kuhn length, which is twice the persistence length, l_p.

$$P_{rod}(q) = \frac{1}{Lbq^2} + \frac{\pi}{L_c q} \tag{3.19}$$

$$\begin{aligned} P_{chain}(q) = {} & P_{Debye}\left(q, L_c, b\right) \\ & + \frac{b}{L_c}\left[\frac{4}{15} + \frac{7}{15q^2 R_g^2\left(L_c, b\right)} - \left[\frac{11}{15} + \frac{7}{15q^2 R_g^2\left(L_c, b\right)}\right] \exp\left[-q^2 R_g^2\left(L_c, b\right)\right]\right] \end{aligned} \tag{3.20}$$

P_{Debye} is the Debye function[1] for the form factor of polymer coils with Gaussian chain statistics that we derived in Section 3.1.1:

$$P_{Debye}\left(q, L_c, b\right) = \frac{2}{\left(q^2 R_g^2\left(L_c, b\right)\right)^2}\left[\exp\left(-q^2 R_g^2\left(L_c, b\right)\right) + q^2 R_g^2\left(L_c, b\right) - 1\right] \tag{3.21}$$

Pedersen and Schurtenberger used the radius of gyration for a wormlike chain (Eqn. 3.22) [9,11] to account for semiflexiblity and included additional terms in Eqn. 3.20 to describe excluded volume interactions, both of which are not included in the original Debye function.

$$R_g = \left[\frac{L_c b}{6}\left[1 - \frac{3b}{2L_c} + \frac{3b^2}{2L_c^2} - \frac{3b^3}{4L_c^3}\left(1 - \exp\left(-\frac{2L_c}{b}\right)\right)\right]\right]^{1/2} \tag{3.22}$$

In Eqn.3.18, the matching term $\exp\left[-\left(\frac{qb}{5.53}\right)^{5.33}\right]$ is approximately equal to 1 for $q < 1/b$, decreases for $1/b < q < 7/b$, and is approximately 0 for $q > 7/b$. So, in the low-q region ($q < 1/b$), the overall form factor is dominated by the scattering of the chain, P_{chain}; in the high-q region ($q > 7/b$), the overall form factor is dominated by the scattering of the rod (persistence length segment), P_{rod}.

The structure factor

In general, the structure factor arises from the configuration of an ensemble of scattering objects within a medium, and is thus related to interactions between individual scattering objects. For modeling the structure factor of wormlike micelles, Pedersen and Schurtenberger used the random phase approximation (RPA) with PRISM-type interactions,[10] which gives

$$S(q) = \frac{1}{1 + \beta P_L\left(q, L\right)} \tag{3.23}$$

where $P_L\left(q, L\right)$ is the chain form factor discussed in the previous section and $\beta = \left[1 - S(0)\right]/S(0)$, where $S(0)$ is the forward contribution to the structure factor, which can be related to the osmotic compressibility of the fluid. For the ionic micelles studied in this work, the appropriate model for $S(0)$ has been empirically derived by fitting of structure factor data obtained from Monte Carlo simulations of wormlike micelles interacting through screened Coulombic interactions. The forward contribution to the structure factor is found to follow:

$$S(0) = \left[1 + \frac{1}{8}\left(9X - 2 + \frac{2\ln(1+X)}{X}\right)\exp\left[0.8\left(\frac{1}{X} + \left(1 - \frac{1}{X^2}\right)\ln(1+X)\right)\right]\right]^{-1} \tag{3.24}$$

where $X = 42.1\phi_{eff}$ and the effective volume fraction is $\phi_{eff} = \left(\frac{r_{cs}+\kappa^{-1}}{r_{cs}}\right)\left(\frac{R_{g,c}}{R_{g,u}}\right)^3$.[6,12] In this expression, κ^{-1} is the Debye length, r_{cs} is the radius of the micelle, ϕ is the volume fraction of the micelle approximated by the volume fraction of the surfactant, and $R_{g,c}$ and $R_{g,u}$ are the theoretical radius of gyration of completely charged and uncharged chain, respectively.

3.2 New development: two-species scattering model for entangled wormlike micelles

This model was originally developed by Peng Cheng, a former graduate student in our groups. I improved the model and the fit to the data. Sections 3.2.1 to 3.2.4 are largely based on text in Peng Cheng's thesis. These are included here for completeness. Sections 3.2.5 and 3.2.6 are my new contributions.

3.2.1 Motivate the need for a new scattering model

At higher surfactant concentrations, wormlike micelles become highly entangled; i.e., many of the longer micelles with lengths longer than $\bar{L}_c$ will have a large number of entanglements. It becomes much more difficult to determine the full contour length distribution because neither rheology nor SANS itself allows the full contour length distribution to be determined. Rheological measurements are dominated by the long, entangled portions of the length distribution, whereas the SANS measurement for a concentrated and entangled system cannot discern length scales larger than the entanglement length. This is because for sufficiently concentrated micelles, the micellar chains will be strongly overlapping, leading to a loss of both intra-chain and inter-chain correlations at length scales longer than the entanglement length l_e. This leads to a strong suppression of the scattering intensity for $q < 2\pi/l_e$, as illustrated in Fig. 3.3. However, the rheological and SANS measurements are complementary, one being sensitive to the long length scales and the other to the short length scales of the contour length distribution. Therefore, we seek an analysis for the length distribution of highly entangled micelles that incorporates both of these measurements.

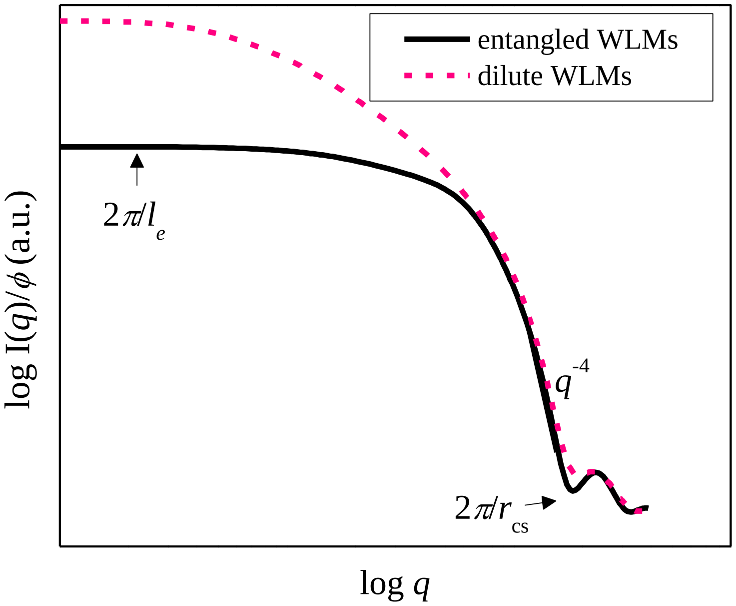

Figure 3.3: Representative schematic of circularly averaged SANS intensity of dilute micelles with contour length distribution given by Eqn. 3.12 (dash line), and concentrated micelles with entanglement length l_e.(Figure reproduced with permission.[13])

Due to the strongly suppressed scattering, it is unlikely that the precise shape of the distributions of micellar contour and sub-chain lengths are distinguishable under these conditions. Therefore, the overall goal in analyzing the SANS data of concentrated WLMs is merely to quantify the relative concentrations of unentangled and entangled micelles (eventually to enable a quantitative comparison of experimental data to predictions from existing rheological models for WLMs, such as the VCM model[14]). For this, we must adopt an interpretation of the length distribution that is relevant to what can be determined from the SANS data of concentrated WLMs and develop a new scattering model.

We will assume that Eqns. 3.11 and 3.12 are valid at all WLM concentrations, i.e., the presence and dynamics of entanglements do not significantly modify the reversible scission process. However, the highly entangled WLMs consist of two distinct populations (see color coding in Fig. 3.4). The first is a population of short, unentangled micelles with $l \leq l_e$ (Fig. 3.4, red lines) whose length distribution will follow Eqns. 3.11 and 3.12. The second is the population of strands between entanglement points that make up the long, entangled micelles. These entanglement strands will have an average length equal to l_e. As already noted, in a concentrated system, SANS cannot distinguish length scales longer than the length of entanglement strands.

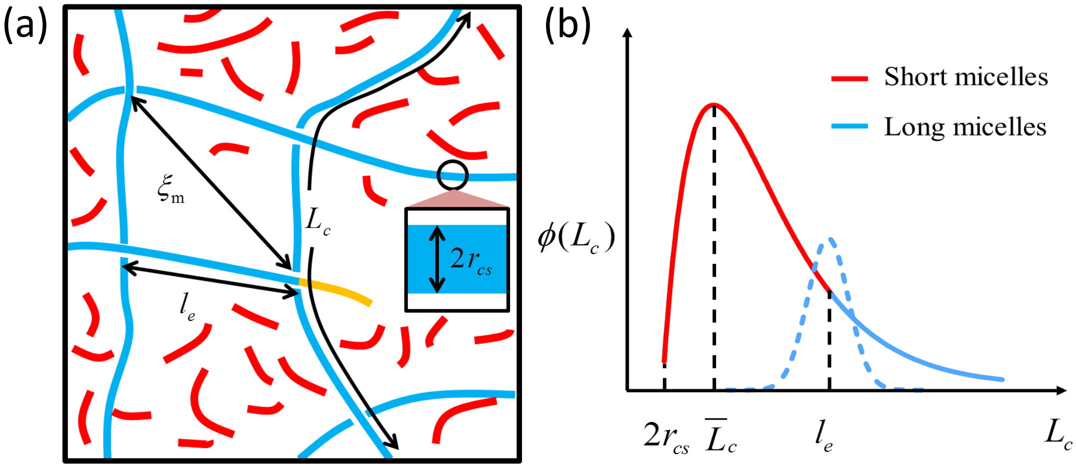

Figure 3.4: Equilibrium structure of highly entangled WLMs. (a) Schematic of highly entangled WLMs composed of (red) unentangled micelles, (blue) entangled micelle strands, and (orange) dangling ends of long, entangled micelles; (b) equilibrium contour length distribution of short, unentangled (solid red line) and long, entangled micelles (solid blue line) given by Eqn. 3.12, the dashed blue line shows the length distribution of entanglement strands belonging to long, entangled micelles given by Eqn. 3.28;. ξ_m, l_e, l_p, ϕ, r_{cs}, and L_c are the mesh size, entanglement length, persistence length, volume fraction, cross-sectional radius, and contour length of WLMs, respectively. (Figure reproduced with permission.[13])

3.2.2 Two populations: unentangled and entangled

Our objective in this section is to develop the theoretical framework that will allow the relative concentrations of unentangled and entangled micelles to be determined from the SANS scattering intensity, $I(q)$. One critical factor for this purpose is the probability distribution function, $f(l)$, that a portion of a micelle of some unit length (e.g., a "monomer") belongs to a micelle of length l in the two populations. One can use Eqns. 3.11 and 3.12 to calculate $f(l)$ for both populations of micelle strands. but in order to do so one must assume a functional form for the length distributions. For the unentangled micelles, this is just the exponential distribution from Eqn. 3.11. The entanglement strands have an average length equal to l_e. To our knowledge, no experimental or theoretical studies exist that would predict a particular distribution of entanglement lengths even for ordinary polymers, let alone wormlike micelles. However, since the entanglement length for ordinary polymers is independent of the overall polymer molecular weight, it is reasonable to assume that, for a large enough number of entanglement strands, the entanglement lengths will be normally distributed , i.e., a Gaussian distribution with a modal value equal to the average entanglement length (l_e). We therefore assume that the length distribution of entanglement strands follows a Gaussian length distribution (dashed blue line in Fig. 3.4 (b)). We note that since SANS can't really distinguish entanglement strands and dangling ends, dangling ends can just be included as entanglement strands. In this study, we are not calculating the relaxation of the chains so the different relaxation modes for dangling ends and entanglement segments don't matter too much.

For the unentangled micelles, $f(l)$ then follows directly from Eqn. 3.11:

$$f_u\left(l\right) = \begin{cases} l < 2r_{cs} : 0 \\ 2r_{cs} \leq l < l_e : \frac{\exp\left(-l/\bar{L}_c\right)}{\int_{2r_{cs}}^{\infty} \exp\left(-l/\bar{L}_c\right)}, \end{cases} \tag{3.25}$$

where $\bar{L}_c$ is the average contour length of the entire micelle population corresponding to the length distribution described in Eqn.3.11. The probability $f(l)$ for the micelle strands between entanglements (coming from micelles with length $L_c > l_e$) is modeled by:

$$f_e\left(l\right) = \begin{cases} l < 2r_{cs} : 0 \\ l \geq 2r_{cs} : \frac{1}{\sigma_e\sqrt{2\pi}} e^{-\frac{(l-l_e)^2}{2\sigma_e^2}}. \end{cases} \tag{3.26}$$

The expressions 3.25 and 3.26 will be used, as explained shortly, for the analysis of SANS data.

Given the functions $f(l)$, the resulting volume fraction, $\phi(l)$, for unentangled micelles and entanglement strands can be obtained, in a similiar manner as Eqn. 3.12. Therefore, the volume fraction of the above two micelle populations can be written as

$$\phi_u(l) = \begin{cases} l < 2r_{cs} : 0 \\ 2r_{cs} \le l < l_e : \phi_{u,tot} \cdot \frac{l \exp\left(-l/\bar{L}_c\right)}{\int_{2r_{cs}}^{\infty} l \exp\left(-l/\bar{L}_c\right)}, \end{cases} \tag{3.27}$$

$$\phi_e(l) = \begin{cases} l < 2r_{cs} : 0 \\ l \ge 2r_{cs} : \frac{\phi_{e,tot}}{\sigma_e\sqrt{2\pi}} e^{-\frac{(l-l_e)^2}{2\sigma_e^2}}. \end{cases} \tag{3.28}$$

The total volume fraction of micellar segments, ϕ_{total}, is therefore

$$\phi_{total} = \phi_{u,tot} + \phi_{e,tot}, \tag{3.29}$$

where $\phi_{u,tot}$, $\phi_{e,tot}$ correspond to the overall volume fraction of surfactant molecules belonging to the unentangled micelles (with contour length $L_c < l_e$) and entanglement strands (coming from micelles with length $L_c > l_e$), respectively.

3.2.3 Materials

A series of 0.3 M hexadecyltrimethylammonium bromide (CTAB, Sigma Aldrich) solutions were prepared in deuterium oxide (D_2O, 99.9%, Cambridge Isotope Laboratories) with varying concentrations of sodium nitrate ($NaNO_3$, Sigma Aldrich) ranging from 0.2 M to 0.4 M. All materials were used as supplied without further purification. Dry powders of CTAB and $NaNO_3$ were added to D_2O in the appropriate amounts. After agitation for complete powder dispersion, the solutions were placed in a temperature-controlled oven held at 40 °C for at least 3 days to achieve sample equilibration before measurements. All measurements on the samples were performed at 30 °C. The experiments were conducted by Peng Cheng.[13]

3.2.4 Small angle neutron scattering experiment

Equilibrium micelle morphology and length distributions were characterized by static SANS measurements at the NIST Center for Neutron Research (NCNR) on the NG7 30m SANS instrument. Static SANS patterns were collected at rest in standard titanium scattering cells with 1 mm path length, and placed in the 10CB temperature-controlled sample environment held at 30 °C. The wavelengths of the neutron beam are 6 Å at sample-detector distances of 1 m and 4 m and 8.09 Å at sample-detector distance of 15 m. Reduction and normlization of the SANS data are done in the NCNR Igor software[15] using standard methods.[16] These experiments were conducted by Peng Cheng.

3.2.5 Scattering theory

For the analysis of the SANS data, we need to make an assumption about the shape of the micelle strands. In this work, we will utilize the fact that the micelles are sufficiently entangled and the mean length of an entanglement strand is short enough to be comparable to the persistence length, $l_e \sim l_p$. Thus, the scattering from all strands can be considered to be equivalent to that from rigid rods without any significant loss of accuracy. If the micelles are also sufficiently dilute such that the average inter-chain distance is large compared to the micelle diameter, we can use the decoupling approximation commonly used for wormlike micelles,[4,5] i.e.,

$$I(q) \,=\, \phi\,(\Delta\rho)^2\,\overline{V}_p\overline{P(q)S(q)} + I_b \tag{3.30}$$

which is Eqn. 3.13 that was introduced in Section 3.1.2 when discussing the Pedersen-Schurtenberger model. The polydisperse form factor $\overline{P\,(q)}$ is computed as a weighted average of the form factor for rigid rods of length l, the length of a sub-chain strand, which is integrated over the length probability distribution given by Eqns. 3.25 and 3.26, in a similar manner as in previous work.[4,5]

For $l_e \sim l_p$, we assume that all intra-chain correlations are lost at length scales larger than l_e. Therefore, ignoring any intra-chain contributions to the structure factor, the average structure factor can be modeled by the inter-chain correlations alone. In other words, we model the average structure factor as though the micellar solution were a suspension of concentrated interacting rods. We coarse-grained the system of micelles to having just two characteristic "average" lengths: $\bar{L}_c$ (average contour length of the entire micelle population, which is used here to approximate the length of unentangled micelles that have an exponential length distribution) and l_e (average length of entanglement segments). We calculated an average structure factor for each population using its average length. For the ionic micelles considered here, we calculate $\overline{S\left(q\right)}$ using the Hayter-Penfold structure factor model for screened Coulombic repulsions calculated via the average structure factor approximation under the mean spherical approximation (MSA) closure to account for the strong electrostatic interactions between micelles.[17,18]

3.2.6 Fitting of experimental results

It is now clear that SANS measurements on highly entangled WLMs (i.e., where $l_e \sim l_p$) will be dominated by structural information on length scales at or below the entanglement length. For structural analysis at larger length scales corresponding to the full contour length of entangled micelles ($L_c > l_e$), it has become customary to use linear viscoelastic measurements. This is because the linear viscoelasticity (LVE) of sufficiently entangled WLMs at low and intermediate frequencies is dominated by the contribution from the long micelles, and is similar to the behavior of a Maxwell fluid. By contrast, the relaxation time of the unentangled micelles (and the dangling ends) is very short, such that their contribution to the linear rheology is important only in the high-frequency regime. Therefore, the length scale and dynamics of the entanglement strands can be estimated from the LVE measurement using rubber elasticity theory[5] (for more information, see Chapter 2 Section 2.2.2). In the limit $l_e \sim l_p$, each entanglement strand is assumed to be a rod-like cylinder whose volume is given by $V_e = \pi r_{cs}^2 l_e$, where r_{cs} is the cross-sectional radius of the micelle and can be estimated from the SANS data. The volume fraction of the entanglement strands, $\phi_{e,tot}$, is therefore given by

$$\phi_{e,tot} = \nu V_e = \frac{\pi r_{cs}^2 l_e G_0}{k_B T}, \tag{3.31}$$

where ν is the number density of entanglement strands. $\phi_{e,tot}$ defined in this way is the same quantity defined in Eqn. 3.28. The quantities l_e and $\phi_{e,tot}$ therefore provide a critical link to the measures of the micelle length distributon accessible by LVE and SANS measurements.

Frequently, this analysis is further used to extract a nominal length of the micelles, as has been done previously for relatively dilute micelles with a small number of entanglements.[5] However, it is important to stress that any micelle length obtained in this way will be strongly weighted toward the portion of the micelle contour length distribution that is highly entangled, because the low-frequency linear viscoelasticity of WLMs will be most sensitive to this portion of the length distribution. It is also important to note that the average contour length of entangled micelles predicted in this manner will be significantly larger than the average contour length of all micelles. For this reason, we choose to use LVE measurements solely to estimate l_e and $\phi_{e,tot}$, rather than any other information about the micelle contour lengths.

From the preceding discussion, we have established that SANS and LVE measurements on highly entangled WLMs probe very different aspects of the length distribution. The former captures the micellar solution as being comprised of distinct populations of unentangled micelles, dangling ends, and entanglement strands. The latter captures the elasticity of the solution contributed exclusively by the part of the micelle population that is entangled. We therefore use a combination of these two analyses to fully characterize the length distribution of highly entangled WLMs.

The procedure for doing so is as follows. First, LVE measurements can be used to determine l_e and $\phi_{e,tot}$. This requires independent knowledge of the persistence length, l_p, which has been measured for a range of surfactant systems by flow-birefringence[19] and neutron spin echo measurements.[20] SANS measurements are then fit to Eqn. 3.30 by using the model described for unentangled micelles and entanglement strands comprised of electrostatically-interacting, rigid rods with volume fraction probability distributions given by Eqns. 3.27, 3.28, and 3.29. The SANS modeling fitting then yields best-fit values for the volume fraction of unentangled micelles $\phi_{u,tot}$, the average contour length of all micelles $\bar{L}_c$, the cross-sectional radius r_{cs}, and the standard deviation of the entanglement length σ_e.

Circularly averaged intensities, $I(q)$, of the static SANS patterns are plotted for 0.3 M CTAB with 0.2, 0.3, and 0.4 M $NaNO_3$ in D_2O in Fig. 3.5. Different regimes can be seen in the one-dimensional SANS intensity profiles, which are consistent with the schematic in Fig. 3.3 for highly entangled WLMs. The scattering intensities almost plateau in the low-q regime ($< 0.005\,\text{Å}^{-1}$), followed by a mild decrease with increasing q (Fig. 3.5). As discussed previously, for such highly entangled WLMs, the contribution to the SANS intensity due to intra-chain correlations is strongly suppressed, such that a plateau in the intensity occurs at $q \sim 2\pi/l_e$ (Fig. 3.5). In this low-q regime, the intensity increases with increasing $NaNO_3$, which indicates both enhanced electrostatic screening and growth of the micelles, given that the volume fraction of the surfactant is held constant. A sharp decrease in the intensity, $I(q) \sim q^{-4}$, occurs in the high-q regime ($q > 0.06\,\text{Å}^{-1}$), which corresponds to the sharp interface between surfactant molecules and the solvent (Fig. 3.5).[6] The high-q scattering is insensitive to $NaNO_3$ concentration, which indicates that the cross-section of the micelles remains unchanged.

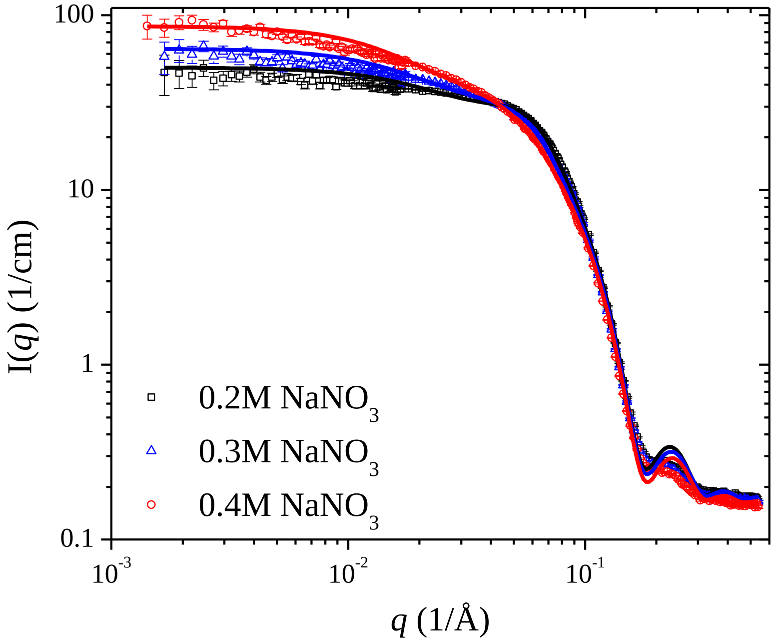

Figure 3.5: Static SANS spectra for 0.3 M CTAB in D_2O at 30 °C with various $NaNO_3$ concentrations. Lines are fits to a rod-like cylinder model with length distribution given by Eqn. 3.27 and Eqn. 3.28.

The fits of the SANS model to the experimental data are shown in Fig. 3.5 and the fitting parameters are summarized in Table 3.1. The model fits well with the SANS data across the entire q-range investigated. The volume fraction of the unentangled micelles decreases and that of the entangled micelles increases (both in absolute and relative terms) with increasing $NaNO_3$ concentration, which is consistent with the salt-induced elongation and growth of WLMs. The total volume fraction of micelles, ϕ_{total}, is approximately constant for WLM samples with 0.2, 0.3, and 0.4 M $NaNO_3$, and thus consistent with the fact that the surfactant concentration is held fixed. Furthermore, the fitted average contour length for all the micelles increases with increasing $NaNO_3$, which agrees with our expectation that on average the micelles become longer with increasing salt concentration due to the increase in the micellization enthalpy as well as the micellar scission energy.[5] We re-emphasize that the objective of the above analysis was to quantify the relative volume fractions of unentangled and entangled micelles, rather than the overall contour length distribution which is not distinguishable by the SANS data of the concentrated WLMs. The good fitting quality and the correct trends for the dependence of the structural parameters on the salt concentration indicates that the model with entanglement strands and unentangled micelles is suitable for providing estimates of the relative concentrations of unentangled and entangled micelle populations. This is critical to enable direct, quantitative comparisons with two-species rheological models for wormlike micelles, such as the VCM model.[14]

Table 3.1: Structural parameters estimated from the fit of the SANS data to a rod-like cylinder model

	0.2M $NaNO_3$	0.3M $NaNO_3$	0.4M $NaNO_3$
Cross-sectional radius (r_{cs})	2.21±0.001 nm	2.18±0.001 nm	2.16±0.001 nm
Volume fraction of unentangled micelles ($\phi_{u,tot}$)	0.0828±0.0007	0.0745±0.0006	0.0647±0.0005
Average contour length of all micelles ($\bar{L}_c$)	10.2±0.1 nm	12.1±0.1 nm	14.5±0.2 nm
Volume fraction of entanglement strands ($\phi_{e,tot}$)	0.0196±0.0004*	0.0228±0.0006*	0.0279±0.0010*
Average length of entanglement strands (l_e)	23.1±0.5nm*	27.8±0.8 nm*	33.4±1.2 nm*
Standard deviation of l_e (σ_e)	4.8±0.04nm	6.5±0.04 nm	3.3±0.07 nm
Average charge per micelle (Z)	58.8±0.9 e**	78.1±1.4 e**	74.4±0.3 e**
Total volume fraction ($\phi_{tot} = \phi_{u,tot} + \phi_{e,tot}$)	0.1020±0.0008	0.0973±0.0009	0.0926±0.0011

*Estimated from the rubber elasticity theory **$e = 1.6x10^{-19}C$ (Coulomb) **± indicates uncertainty associated with a 95% confidence interval of the fitting

3.3 Conclusions

In this chapter, we discussed widely used models for the equilibrium scattering of polymers and wormlike micelles, namely, the Debye function and the Pedersen-Schurtenberger model, respectively. For the case of highly entangled wormlike micelles, previous models were not sufficient to explain the suppression of the intensity at low-q. We developed a scattering model for entangled micelles by modeling the entanglement segments and the unentangled micelles separately. The equilibrium scattering models discussed in this chapter lay a foundation for the subsequent chapters which discuss the development and application of nonequilibrium scattering models for polymers and wormlike micelles in flow.

Bibliography

[1] Debye P. Molecular-weight determination by light scattering. *The Journal of Physical Chemistry.* 1947; 51(1): 18–32.

[2] Cates M. Reptation of living polymers: dynamics of entangled polymers in the presence of reversible chain-scission reactions. *Macromolecules.* 1987; 20(9): 2289–2296.

[3] Cates M, Candau S. Statics and dynamics of worm-like surfactant micelles. *Journal of Physics: Condensed Matter.* 1990; 2(33): 6869.

[4] Chen WR, Butler PD, Magid LJ. Incorporating intermicellar interactions in the fitting of sans data from cationic wormlike micelles. *Langmuir.* 2006; 22(15): 6539–6548.

[5] Helgeson ME, Hodgdon TK, Kaler EW, Wagner NJ. A systematic study of equilibrium structure, thermodynamics, and rheology of aqueous ctab/nano3 wormlike micelles. *Journal of colloid and interface science.* 2010; 349(1): 1–12.

[6] Pedersen JS, Cannavacciuolo L, Schurtenberger P. Scattering from wormlike micelles. *Giant Micelles.* 2007: 179–222.

[7] Kratky O, Porod G. Diffuse small-angle scattering of x-rays in colloid systems. *Journal of colloid science.* 1949; 4(1): 35–70.

[8] Pedersen J, Schurtenberger P. Cross-section structure of cylindrical and polymer-like micelles from small-angle scattering data. i. test of analysis methods. *Journal of applied crystallography.* 1996; 29(6): 646–661.

[9] Pedersen JS, Schurtenberger P. Scattering functions of semiflexible polymers with and without excluded volume effects. *Macromolecules.* 1996; 29(23): 7602–7612.

[10] Pedersen JS, Schurtenberger P. Scattering functions of semidilute solutions of polymers in a good solvent. *Journal of Polymer Science Part B: Polymer Physics.* 2004; 42(17): 3081–3094.

[11] Benoit H, Doty P. Light scattering from non-gaussian chains. *The Journal of Physical Chemistry.* 1953; 57(9): 958–963.

[12] Cannavacciuolo L, Pedersen JS, Schurtenberger P. Monte carlo simulation study of concentration effects and scattering functions for polyelectrolyte wormlike micelles. *Langmuir.* 2002; 18(7): 2922–2932.

[13] Cheng P. *Rheology, kinematics, and structure of shear banding wormlike micelles.* PhD thesisUniversity of California, Santa Barbara 2017.

[14] Vasquez PA, McKinley GH, Cook LP. A network scission model for wormlike micellar solutions: I. model formulation and viscometric flow predictions. *Journal of non-newtonian fluid mechanics.* 2007; 144(2-3): 122–139.

[15] Kline SR. Reduction and analysis of sans and usans data using igor pro. *Journal of applied crystallography.* 2006; 39(6): 895–900.

[16] Glinka C, Barker J, Hammouda B, Krueger S, Moyer J, Orts W. The 30 m small-angle neutron scattering instruments at the national institute of standards and technology. *Journal of applied crystallography.* 1998; 31(3): 430–445.

[17] Hansen JP, Hayter JB. A rescaled msa structure factor for dilute charged colloidal dispersions. *Molecular Physics.* 1982; 46(3): 651–656.

[18] Hayter JB, Penfold J. An analytic structure factor for macroion solutions. *Molecular Physics.* 1981; 42(1): 109–118.

[19] Shikata T, Dahman SJ, Pearson DS. Rheo-optical behavior of wormlike micelles. *Langmuir.* 1994; 10(10): 3470–3476.

[20] Nettesheim F, Wagner NJ. Fast dynamics of wormlike micellar solutions. *Langmuir.* 2007; 23(10): 5267–5269.

Chapter 4

Nonequilibrium modeling of the scattering of semiflexible chains

4.1 Introduction

Understanding changes in microstructural dynamics under nonlinear deformations is critical for designing flow processing of semiflexible chains. Semiflexible chains, such as wormlike micelles, bottlebrush polymers, DNA, and certain types of polyelectrolytes, are an important class of soft materials. In addition to rheology, flow-small angle neutron scattering (flow-SANS) is useful for studying how the material deforms in flow. While scattering models have been developed to understand the scattering from chain-like objects at equilibrium, they don't lend themselves to fitting scattering from semiflexible polymers in flow. Lacking a detailed flow-SANS model of semiflexible chains, researchers have used parameterizations of 2D scattering to compare experiments and simulation. Specifically, by calculating the sector average of the scattering intensity, researchers compared intensity in the directions parallel to and perpendicular to flow. Additionally, Picken and coworkers[1] and Walker and coworkers[2] introduced a scalar quantification of the degree of anisotropy in the scattering, the alignment factor, which has been used extensively when analyzing flow-SANS data. However, neither of these methods can adequately describe the anisotropic scattering (specifically, the shape, magnitude, and dependence on the scattering wave vector). Therefore, developing 2D models for scattering in flow is critically important for understanding the microstructural changes encoded in the anisotropic scattering patterns.

Instead of scattering in flow, models have been developed to describe the scattering of semiflexible chains at equilibrium, such as the wormlike chain model by Kratky and Porod[3] and the model by Pedersen and Schurtenberger.[4–6] For scattering in flow, models exist for rod-like particles and flexible chains. Specifically, Hayter and Penfold developed a model to describe orientation of rodlike particles in shear flow.[7] The GLaMM model includes an expression for the single chain form factor for entangled, flexible polymers in flow.[8] Other authors modified the Debye function to describe scattering of flexible chains in flow[9–11] and stretched semiflexible chains.[12] However, the gap between the rod-like limit and the flexible chain limit hasn't been bridged by previous models.

Several challenges need to be overcome in order to develop a scattering model for semiflexible chains in flow. Specifically, (i) we need to develop a form factor for the semiflexible chain that accounts for both the contribution from individual segments and the conformation of the entire chain. (ii) We also need an orientation distribution function of the segments that is consistent with the overall stretch and orientation of the chain. This work addresses (i) by extending the flow-SANS prediction of single rods by Hayter and Penfold to model the form factor of connected-cylinders, where each cylinder represents the Kuhn length on the chain. This work addresses (ii) by incorporating an orientation distribution for the segments that is self-consistent with the overall stretch and orientation of the chain. Additionally, we include a structure factor to describe the interactions between chains in flow. The scattering model we develop here will help inform material microstructural deformation obtained from flow-SANS experiments of semiflexible chains.

4.2 Theory

4.2.1 Previous theory

Form factor of a single rod in flow

For a single cylinder in flow, the scattering intensity has been predicted by Hayter and Penfold.[7] In the original formulation of the model, the scattering plane is the flow-vorticity $(v-\omega)$ plane. We modified the expressions in the model to predict scattering in the flow-gradient $(v-\nabla v)$ plane. Figure 1 (a) is a representation of the coordinate system used. A cylinder with length L_{cyl} and radius r_{cyl} is oriented at an angle θ from the vorticity direction (z-axis) and its projection in the flow-gradient plane forms an angle ϕ from the flow direction (x-axis). The scattering wavevector q is in the flow-gradient plane and makes an angle ψ with the x-axis. The normalized form factor amplitude is calculated as

$$\begin{aligned} F(\boldsymbol{q}) = F\left(q,\zeta\right) &= \frac{1}{V_p}\int_{V_p} \exp\left(-i\boldsymbol{q}\cdot\boldsymbol{r}\right) d^3\boldsymbol{r} \\ &= \frac{2J_1\left(qr_{cyl}\sin\zeta\right)}{qr_{cyl}\sin\zeta}\frac{\sin\left(q\frac{L_{cyl}}{2}\cos\zeta\right)}{q\frac{L_{cyl}}{2}\cos\zeta} \end{aligned} \tag{4.1}$$

where ζ is the angle between the scattering wavevector q and the cylinder axis and $V_p = \pi r_{cyl}^2 L_{cyl}$ is the volume of the cylinder. The scattering intensity for rods with an orientation distribution $p(\theta,\phi)$ is

$$I\left(q,\psi\right) = \Phi\left(\Delta\rho\right)^2 V_p \int_0^{2\pi} d\phi \int_0^{2\pi} p\left(\theta,\phi\right) F^2\left(q,\zeta\right)\sin\theta d\theta \tag{4.2}$$

where Φ is the volume fraction of the cylinders and $\Delta\rho$ is the difference in scattering length density between the cylinders and the solvent.

In the Hayter-Penfold model, the orientational probability distribution function (OPDF)[7] is

$$p\left(\theta, \phi\right) = \frac{\left(1 - \cos 2\phi_0\right)\left(1 + \sin^2\theta \cos 2\phi_0\right)^{3/2}}{4\pi\left[1 - \sin^2\theta \cos 2\phi \cos 2\left(\phi - \phi_0\right)\right]^2} \tag{4.3}$$

where the average orientation angle ϕ_0 depends on the flow strength.

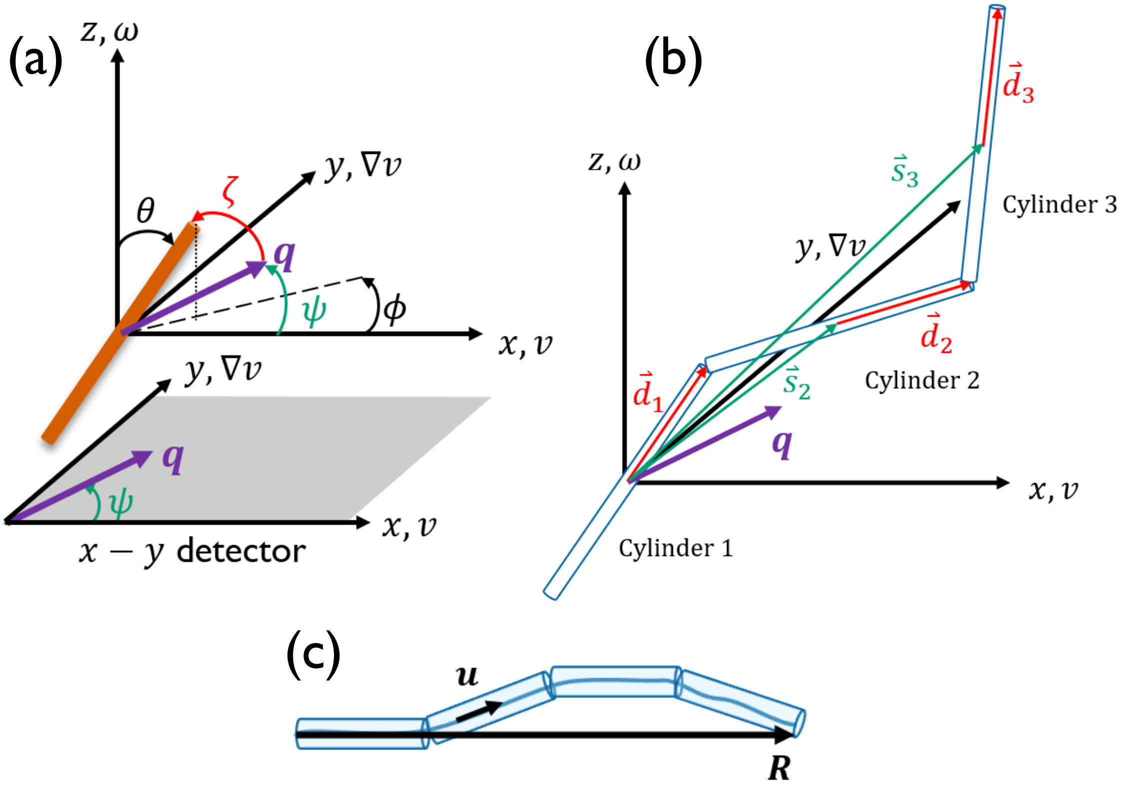

Figure 4.1: Schematic of the connected rod model (a) definition of coordinate system for a single rod. The scattering wave vector $\mathbf{q}$ is in the flow-gradient $(v - \nabla v)$ plane. (b) geometric representation of connections between rods and definitions of vectors used in the model (c) orientation vectors for the rods and end-to-end vector for the chain as used in the orientation distribution function.

4.2.2 New theory

Form factor of connected rods to represent semiflexible chain

We extend ideas from the Hayter-Penfold model to describe scattering for semi-flexible chains in flow for the first time. We use identical cylinders of length L_{cyl} and radius r_{cyl}). The cylinders are placed end-to-end and can freely rotate. Cylinder i is oriented at an angle θ_i from the vorticity direction (z-axis) and its projection in the flow-gradient plane forms an angle ϕ_i from the flow direction (x-axis). For multiple cylinders, the scattering amplitude is:

$$F(\boldsymbol{q}, \boldsymbol{s_1}, ..., \boldsymbol{s_n}) = F_1\left(\boldsymbol{q}, \boldsymbol{s_1}\right) + F_2\left(\boldsymbol{q}, \boldsymbol{s_2}\right) + F_3\left(\boldsymbol{q}, \boldsymbol{s_3}\right) ... \tag{4.4}$$

where $\boldsymbol{s_i}$ is the vector from the origin to the center of cylinder i (See Fig. 4.1(b)). For the first cylinder, $\boldsymbol{s_1} = 0$ at the origin and the form factor amplitude for the cylinder #1 is the same as Eqn. 4.1:

$$\begin{aligned} F_1(\boldsymbol{q}) &= \frac{1}{V_p} \int_{V_{p,1}} \exp\left(-i\boldsymbol{q} \cdot \boldsymbol{r}\right) d^3\boldsymbol{r} \\ &= \frac{2J_1\left(qr_{cyl} \sin\zeta_1\right)}{qr_{cyl} \sin\zeta_1} \frac{\sin\left(q\frac{L_{cyl}}{2} \cos\zeta_1\right)}{q\frac{L_{cyl}}{2} \cos\zeta_1} \end{aligned} \tag{4.5}$$

Here $\boldsymbol{r}$ is the vector from the center of the cylinder #1 (also at the origin) to different positions inside the cylinder. For the second cylinder, $\boldsymbol{r}$ is the vector from the center of the cylinder to different positions inside the cylinder, but now, the center of the cylinder is placed at the end of vector $\boldsymbol{s_2}$ away from the origin. So, we can change coordinates from $\boldsymbol{r'}$ to $\boldsymbol{r}$ using the relation $\boldsymbol{r'} = \boldsymbol{r} + \boldsymbol{s_2}$. In general, for the ith cylinder, $\boldsymbol{r'} = \boldsymbol{r} + \boldsymbol{s_i}$

and the form factor amplitude is:

$$\begin{aligned} F_i(\boldsymbol{q}, \boldsymbol{s_i}) &= \frac{1}{V_p} \int_{V_{p,i}} \exp\left(-i\boldsymbol{q} \cdot \boldsymbol{r'}\right) d^3\boldsymbol{r'} \\ &= \frac{1}{V_p} \int_{V_{p,i}} \exp\left(-i\boldsymbol{q} \cdot (\boldsymbol{r} + \boldsymbol{s_i})\right) d^3\boldsymbol{r} \\ &= \exp\left(-i\boldsymbol{q} \cdot \boldsymbol{s_i}\right) \frac{2J_1\left(qr_{cyl}\sin\zeta_i\right)}{qr_{cyl}\sin\zeta_i} \frac{\sin\left(q\frac{L_{cyl}}{2}\cos\zeta_i\right)}{q\frac{L_{cyl}}{2}\cos\zeta_i} \end{aligned} \tag{4.6}$$

So far, we haven't discussed how to express the angle between each cylinder and the scattering vector, ζ_i, in terms of ψ, θ_i, and ϕ_i. We define a vector $\boldsymbol{d_i}$ from the center of cylinder i along its axis to the end of cylinder i. In spherical coordinates, the vector is written as

$$\boldsymbol{d_i} = \frac{L_{cyl}}{2} \begin{pmatrix} \cos\phi_i \sin\theta_i \\ \sin\phi_i \sin\theta_i \\ \cos\theta_i \end{pmatrix}. \tag{4.7}$$

The scattering vector, which is in the flow-gradient plane (x-y plane), is written in terms of its magnitude q and angle ψ as:

$$\boldsymbol{q} = q \begin{pmatrix} \cos\psi \\ \sin\psi \\ 0 \end{pmatrix}. \tag{4.8}$$

So, we have

$$\boldsymbol{q} \cdot \boldsymbol{d_i} = \cos\zeta_i = \cos\psi\cos\phi_i\sin\theta_i + \sin\psi\sin\phi_i\sin\theta_i. \tag{4.9}$$

Furthermore, for $i > 1$, we have

$$\boldsymbol{s_i} = \boldsymbol{d_i} + \boldsymbol{d_{i-1}} + \boldsymbol{s_{i-1}}, \tag{4.10}$$

which finally enables the computation of $\boldsymbol{q} \cdot \boldsymbol{s_i}$ for the form factor amplitude of cylinder i.

For a chain with n cylinders, the form factor amplitude $F\left(q, \theta_1, \phi_1 ... \theta_n, \phi_n\right)$ is calculated following Eqns. 4.4-4.10. To calculate the orientationally averaged form factor, we need to average over the orientation distribution for each cylinder as follows:

$$\begin{aligned} P(\boldsymbol{q}) = \frac{1}{n^2} \int_0^{2\pi} ... \int_0^{2\pi} d\phi_1 ... d\phi_n \int_0^{\pi} ... \int_0^{\pi} p\left(\theta_1, \phi_1\right) ... \\ p\left(\theta_n, \phi_n\right) \left|F\left(q, \theta_1 ... \theta_n, \phi_1 ... \phi_n\right)\right|^2 \sin\theta_1 ... \sin\theta_n d\theta_1 ... d\theta_n \end{aligned} \tag{4.11}$$

Here the form factor is normalized over the volume of the chain. We divide by n^2 to ensure the form factor goes to 1 at low-q, as required for the normalized form factor. We initially used the orientation distribution (Eqn. 4.3) proposed by Hayter-Penfold for a single cylinder as the orientation distribution for each rod in the connected-rod model. However, using the Hayter-Penfold orientation distribution for the connected-rod model has several limitations. First, it is not self-consistent with the overall stretching and orientation of the entire chain. Specifically, in simple shear flow, the chain rotates and tumbles as it is being oriented and stretched in flow. Even at large shear rates accessible experimentally, not all segments in the chain are aligned in the flow direction; instead, only the average orientation of the end-to-end vector of the chain is in the flow direction. Second, in the Hayter-Penfold orientation distribution, the average orientation angle is still larger than 0 even for very sharply peaked orientation distribution, which contradicts observation from scattering experiments of wormlike micelles that show the average orientation angle is close to zero even for scattering patterns with relatively low anisotropy, which is indicative of a broad orientation distribution.

Improved segmental orientation distribution

Previous work by Pandey and Underhill[13] on Brownian dynamics simulation of DNA gives a suitable approach for deriving an orientation distribution for segments in a semiflexible chain that is self-consistent with the overall stretch and orientation of the chain. We briefly describe the approach here. We consider a chain whose extension vector (end-to-end vector) is denoted as $\boldsymbol{R}$ and whose maximum extension is $R_0 = nL_{cyl}$, where n is the number of cylinders which also represents the number of Kuhn steps and L_{cyl} is the length of each cylinder which also represents the Kuhn length. The chain with extension $\boldsymbol{R}$ represents an average over all the configurations for which an end-to-end vector is $\boldsymbol{R}$. Therefore, the extension is related to the average of a rod $\boldsymbol{R} = nL_{cyl} \langle \boldsymbol{u} \rangle$, where the unit vector $\boldsymbol{u}$ represents the orientation of an individual rod in the chain and $\langle \boldsymbol{u} \rangle$ represents the average orientation of all rods in the chain. To simplify the notation, we use $\boldsymbol{\lambda} \equiv \langle \boldsymbol{u} \rangle$, so that $\frac{\boldsymbol{R}}{R_0} = \boldsymbol{\lambda}$. $\boldsymbol{\lambda}$ represents *both* the fractional extension (i.e., stretch) of the chain and the average of the rod orientation. Thus, the stretch of the chain determines the average of the rod orientation vector. However, the stretch of the chain does not determine the orientation distribution. Pandey and Underhill followed a similar approach as Lee and Larson[14] and postulated that the orientation distribution is the one in which the rod is subject to an external "force" $\boldsymbol{f}$ and the force is determined such that the average over the distribution is the correct known average. Therefore, the probability distribution of rod angles is $p(\boldsymbol{u}) \propto \exp\left[\boldsymbol{f}(\boldsymbol{\lambda}) \cdot \boldsymbol{u}/k_B T\right]$. This choice is only self-consistent if we calculate the average orientation vector and obtain $\boldsymbol{\lambda}$. Because of the form of the distribution, we can calculate the average analytically. This self-consistency requires that we choose the force as $\boldsymbol{f}(\boldsymbol{n}) = \frac{\mathcal{L}^{-1} \boldsymbol{\lambda} k_B T}{\lambda}$, where the nonboldface λ denotes the magnitude of the vector and $\mathcal{L}^{-1}$ is the inverse Langevin function $\left[\mathcal{L}(x) = \coth x - \frac{1}{x}\right]$. The inverse Langevin function is approximated as

$$\frac{f}{k_BT} = \mathcal{L}^{-1}(\lambda) \approx \frac{3\lambda - \lambda^3}{1 - \lambda^2}. \tag{4.12}$$

Furthermore, we assume that the average orientation of the chain is in the flow-flow gradient plane (the out-of-plane angle $\theta_0 = \pi/2$). We thus obtain the orientation distribution:

$$p(\boldsymbol{u}) \propto \exp\left[\frac{3\lambda - \lambda^3}{1 - \lambda^2} \cos\left(\phi - \phi_0\right) \sin\theta\right], \tag{4.13}$$

where θ is the angle formed between a cylinder and the vorticity direction (z-axis), ϕ is the angle formed between the projection of a cylinder in the flow-gradient plane and the flow direction (x-axis), and ϕ_0 is the average orientation angle in the flow-gradient plane of all cylinders on the chain.

Upon normalization to unity (when integrating over all angles), we obtain:

$$p(\boldsymbol{u}) = \frac{\exp\left[\frac{3\lambda-\lambda^3}{1-\lambda^2}\cos\left(\phi - \phi_0\right)\sin\theta\right]}{4\pi\frac{1-\lambda^2}{3\lambda-\lambda^3}\sinh\left(\frac{3\lambda-\lambda^3}{1-\lambda^2}\right)}. \tag{4.14}$$

Using Eqn. 4.14 in the expression for the form factor (Eqn. 4.11), we obtain the following for the orientationally averaged form factor:

$$\begin{split} P(\boldsymbol{q}) = \frac{1}{n^2}\int_0^{2\pi} ... \int_0^{2\pi} d\phi_1 ... d\phi_n \int_0^{\pi} ... \int_0^{\pi} p\left(\theta_1, \phi_1, \phi_0, \lambda\right) ... p\left(\theta_n, \phi_n, \phi_0, \lambda\right) \\ \left|F\left(q, \theta_1 ... \theta_n, \phi_1 ... \phi_n\right)\right|^2 \sin\theta_1 ... \sin\theta_n d\theta_1 ... d\theta_n \end{split} \tag{4.15}$$

Structure Factor

For systems with interchain interactions, a structure factor is needed to fully describe the scattering intensity. At equilibrium, for semiflexible chains, typically the structure factor is expressed using a random phase approximation (RPA) with PRISM-type interactions,[4, 5] which gives

$$S(q) = \frac{1}{1+\beta P\left(q\right)} \tag{4.16}$$

where $P\left(q\right)$ (with only the magnitude of $\boldsymbol{q}$) is the form factor of the chain at equilibrium and $\beta = \left[1 - S(0)\right]/S(0)$, where $S(0)$ is the forward contribution to the structure factor (i.e., it is the $q = 0$ value of the structure factor). We generalize the expression for the structure factor to account for changes in interchain interactions due to chain stretching and orientation in flow. At equilibrium, the structure factor is a result of excluded volume interactions and electrostatic repulsions between charged chains. To date, no anisotropic structure factor model has been developed for semiflexible chains with internal structures, or more generally for polymeric fluids in flow. A good approximation for the structure factor in flow is to replace the equilibrium chain form factor in the expression for the equilibrium structure factor (Eqn.4.16 from the RPA model) with the orientationally averaged form factor of the connected-rod model (Eqn.4.15):

$$S(\boldsymbol{q}) = \frac{1}{1+\beta P(\boldsymbol{q})}. \tag{4.17}$$

We note that Eqn. 4.17 is identical to Eqn. 4.16 except for the vectorial dependence on the scattering wave vector q. A similar approach has been used previously to model the structure factor of rodlike particles in flow and was shown to work quite well.[15] The overall scattering intensity for a monodisperse system is:

$$I(\boldsymbol{q}) = \Phi\left(\Delta\rho\right)^2 n\pi r_{cyl}^2 L_{cyl} P(\boldsymbol{q}) S(\boldsymbol{q}) + bkgd \tag{4.18}$$

where Φ is the volume fraction of the chains, $\Delta\rho$ is the difference in scattering length density between the chain and the solvent, and $bkgd$ is the background intensity (in an experiment).

Include polydispersity of the number of cylinders for equilibrium predictions

For systems with polydispersity, the form factor needs to be averaged over the length distribution function. One important consideration is that the fractional extension λ depends on the length of chain, thus, at a given shear rate, chains with different length will have different values for λ. Here, we will only show the functional form of the polydisperse model at equilibrium and will leave the discussion of the polydisperse model under flow for future work. As an example, for chains with an exponential length distribution, the form factor is:

$$\overline{P(q)} = \frac{\int_0^\infty \exp\left(-L/L_c\right) P(q,L) dL}{\int_0^\infty \exp\left(L/L_c\right) dL} \tag{4.19}$$

where L_c is the average contour length of the chains. In our connected-rod model, since the chains are made up of discrete segments with the same length, we use a discretized version of Eqn.4.19 as follows:

$$\overline{P(q)} = \frac{\sum_{i=1}^{n} \exp\left(-n_i/\overline{n}\right) P\left(q, n_i\right)}{\sum_{i=1}^{n} \exp\left(-n_i/\overline{n}\right)}, \tag{4.20}$$

where n_i is the number of cylinders in chain i and $\overline{n}$ is the average number of cylinders in the chains. The average chain length is then $\overline{n}\, L_{cyl}$. Using the length-averaged form factor in Eqn. 4.16 for the structure factor, we obtain:

$$\overline{S(q)} = \frac{1}{1 + \beta \overline{P\left(q\right)}}. \tag{4.21}$$

Finally, the equilibrium intensity for a polydisperse system is:

$$I(q) = \Phi \left(\Delta\rho\right)^2 \pi r_{cyl}^2 L_{cyl} \overline{P(q) S(q)} + bkgd. \tag{4.22}$$

Eqn. 4.22 does not have the factor of n in the prefactor because the dependence of the form facor on the number of segments is included in the length-averaged form factor $\overline{P(q)}$.

4.3 Methods

4.3.1 Numerical calculations and fitting

We wrote codes in Fortran to enable the model calculations. To compare with experiments, the experimental values for q_x and q_y are used to make the 2D predictions of scattering. To evaluate the multidimensional integral in Eqn. 4.15,we used the integration method developed by Lepage,[16] which is an iterative and adaptive Monte Carlo scheme. For fitting the model to the equilibrium circular average intensity from experiments, we used the Levenberg-Marquardt algorithm for the nonlinear least squares curve fitting.[17,18] The algorithm combines two numerical minimization algorithms: the gradient descent method and the Gauss-Newton method. In the gradient descent method, the sum of the squared errors is reduced by updating the parameters in the steepest-decent direction. In the Gauss-Newton method, the sum of the squared errors is reduced by assuming the least squares function is locally quadratic in the parameters, and finding the minimum of this quadratic. Note: The Fortran code is available to the reader upon request.

4.3.2 Flow-SANS experiment of wormlike micelles

Solutions containing 60 mM cetyltrimethylammonium bromide (CTAB, Sigma Aldrich) were prepared in deuterium oxide (D_2O, 99.9%, Cambridge Isotope Laboratories) with 1:3 molar ratio of CTAB to sodium nitrate ($NaNO_3$, Sigma Aldrich). All materials were used as supplied without further purification. For neutron scattering measurements, it was necessary to prepare samples using deuterium oxide to reduce incoherent scattering.

Dry powders of CTAB and $NaNO_3$ were added to D_2O in the appropriate amounts. After agitation for complete powder dispersion, the solutions were placed in a temperature-controlled oven held at 47 °C for at least 1 day to achieve sample equilibration before measurements.

SANS measurements were performed using the NGB 30m SANS instrument at the National Institute of Standards and Technology Center for Neutron Research (Gaithersburg, MD). Anisotropic scattering was characterized using flow-SANS for simple shear flow in the flow-gradient ($v - \nabla v$) plane using the 1-2 shear cell sample environment.[19] A wavelength of $\lambda_0 = 6$ Åwith a wavelength spread of $\Delta\lambda_0/\lambda_0 = 0.14$ was used. The scattering vector q is defined as $q = 4\pi \sin(\alpha/2)/\lambda_0$ where α is the angle at which the neutron is scattered and λ_0 is the neutron wavelength. Scattering from the sample was collected in the q range $0.005 - 0.2$ Å^{-1} to span the entire range of length scales from the radius up to the contour length of the micelles. The temperature was maintained constant at 25 °C through the entire experiment with a water bath for the shear cell. The 2D scattering intensities were corrected for empty cell, plexiglass standard, and detector efficiency. Scattering patterns were reduced using standard protocols with Igor Pro software.[20]

4.4 Results

4.4.1 Equilibrium fitting

To validate the model, we will compare model predictions with flow-small angle neutron scattering (flow-SANS) experiments of wormlike micelles. We chose wormlike micelles, instead of monodisperse polymers, as a model system because they are known to be semiflexible and have significant contribution from the cross section. Furthermore, the typical length scale (1 nm-hundreds of nm) for wormlike micelles enable measurement from the radius up to the contour length in flow-SANS experiments. Wormlike micelles also show significant anisotropy in flow due to segmental orientations, in contrast to weak anisotropy in most flexible and semiflexible polymers, which allows better testing of the orientation distribution in the scattering model.

Wormlike micelles are polydisperse with an exponential length distribution at equilibrium. First, we used the polydisperse version of the model to fit circular average of scattering intensity at equilibrium in order to extract average chain length (Fig. 4.2(a)). As an initial guess, we used the Kuhn length of the wormlike micelles determined from previous work on the same system as an estimate for the cylinder length. Specifically, Helgeson et al.[21] determined the persistence length l_p to be 25 nm for the 60 mM CTAB/180 mM $NaNO_3$ sample using flow-birefringence measurements. We used 10 chains with an increasing number of cylinders ($n_i = 1$ to 12). The number density distributions for the chains with different length follow an exponential distribution. For wormlike chains, the Kuhn length is twice the persistence length, $b = 2 * l_p = 50$ nm. Previously, the Pedersen-Schurtenberger model was used to fit the equilibrium intensity and the average length was found to be 325 nm whereas the average length estimated from linear viscoelastic rheology is 264 nm.[21] Fig. 4.2(b) compares the continuous exponential distribution with the discretized exponential distribution used in the polydisperse fitting. In an exponential distribution with an average chain length close to $4 * b$, chains with more than 12 Kuhn segments have a very small volume fraction, thus their contributions are negligible. We performed multiple fittings and verified that increasing the maximum number of segments beyond 12 did not change the fitting results significantly.

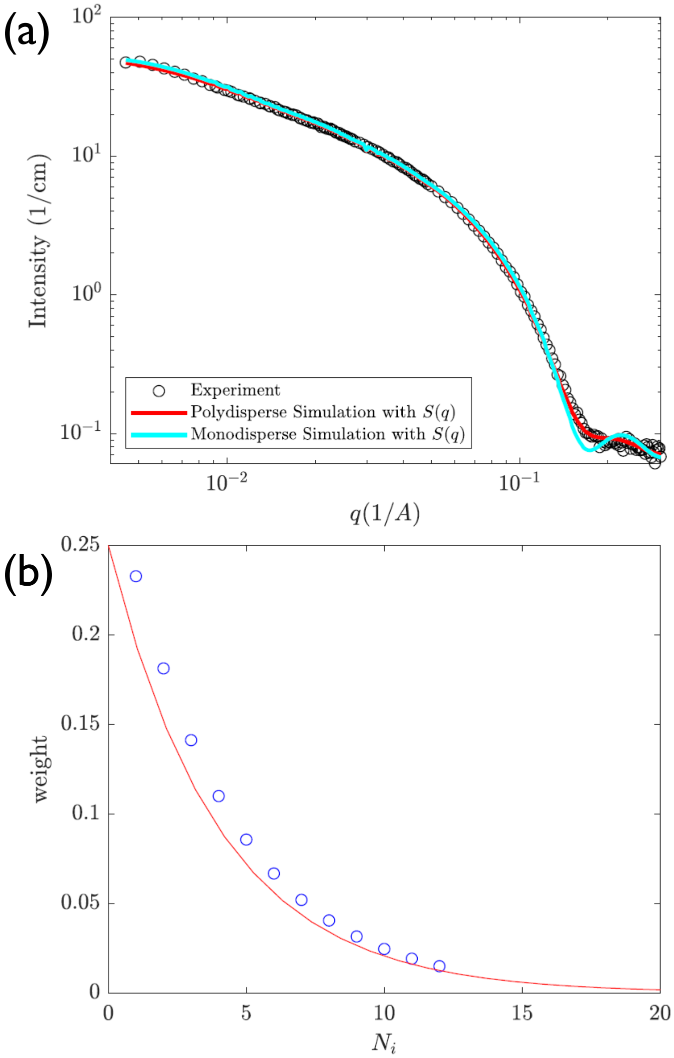

Figure 4.2: Equilibrium Fitting (a) Comparison of equilibrium scattering intensity from wormlike micelle experiment, polydisperse connected-rod model fitting, and monodisperse connected-rod calculation (b) Discretization of exponential distribution. The red curve is the continuous exponential distribution and the points are values corresponding to the discretized exponential distribution.

In Fig. 4.2(a), the black symbols represent the experimental results and the red curve represents the polydisperse model fit of the experiment. The model does an excellent job fitting the experimental result. The fitting results are reported in Table 4.1. The cyan curve in Fig. 4.2(a) represents the monodisperse calculation using $\overline{n}$ from the polydisperse fit as the number of cylinders. The monodisperse calculation also gives very good agreement with the experimental result. Although it is well known wormlike micelles have an exponential length distribution at equilibrium, whether the length distribution and average length of wormlike micelles change in flow is still highly debated. Thus, when comparing flow-SANS experiments of wormlike micelles with the model predictions in the next section, we will only use the monodisperse version of the model.

Table 4.1: Parameters for model fitting of equilibrium intensity

$\overline{n}$	r_{cyl} (nm)	L_{cyl} (nm)	β	$Bkgd$ $(1/cm)$
4	2.3	43.1	3.11	0.065

Since the Pedersen-Schurtenberger model has been well-established for describing semiflexible chains at equilibrium, to further validate our model, it is worth examining the characteristic scaling of the scattering intensity with the scattering wavevector q as we change the flexibility of the chain and comparing with the Pedersen-Schurtenberger model. Keeping the total chain length at 172.5 nm, we systematically varied the cylinder length. In Fig. 4.3(a), the blue curve represents $n = 1$, $L_{cyl} = 172.5\,\text{nm}$, the red curve represents $n = 4$, $L_{cyl} = 43.1\,\text{nm}$, and the black curve represents $n = 10$,$L_{cyl} = 17.2\,\text{nm}$. The flexibility of the chain increases as the ratio of chain length to segment length (L_{chain}/L_{cyl}) decreases. For $n = 1$, we get the rigid-rod limit, with a slope of -1 at low-q, for $n >= 10$, we obtain the flexible chain limit with excluded volume interactions, with a slope of -5/3. For intermediate values of n, we are in the semiflexible limit. Thus, the connected-rod model can span the full range of flexibility for the chain. In Fig. 4.3(b), the connected-rod model prediction is compared with the Pedersen-Schurtenberger model for $L_{cyl} = 43.1\,\text{nm}$ and $L_{chain} = 172.5\,\text{nm}$. The Pedersen-Schurtenberger model explicitly includes excluded volume interactions. In the connected-rod model, excluded volume interactions are naturally built in because the cylinders are placed end-to-end and we explicitly account for the location of adjacent segments relative to each other. Thus, it is very unlikely for segments to exactly overlap on top of each other.

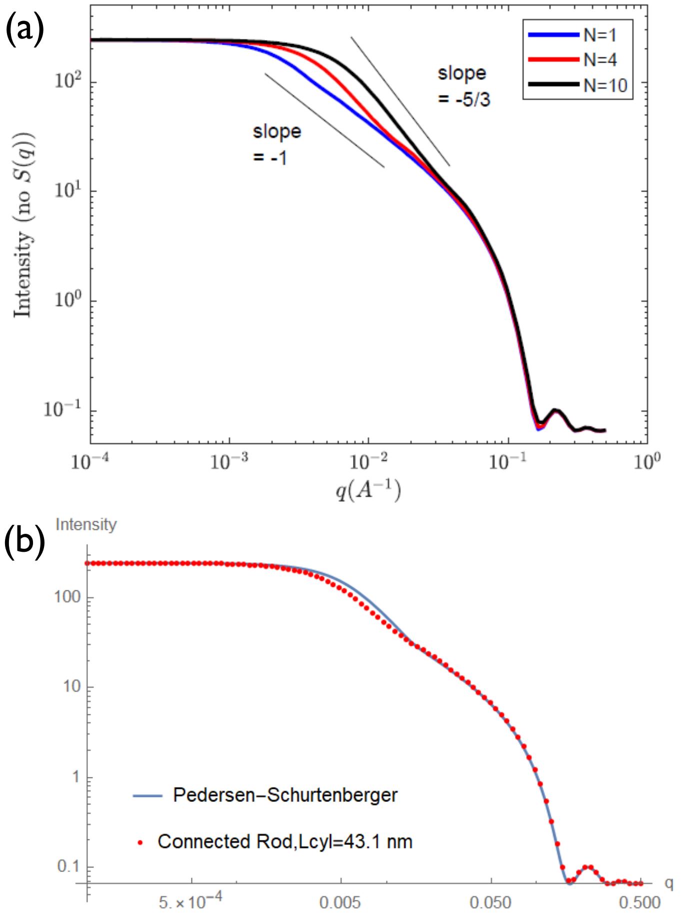

Figure 4.3: Check for characteristic scaling in connected rod model (a) Scattering intensity (without structure factor) for fixed chain length and varying number of segments (b) Compare connected rod model with Pedersen-Schurtenberger model for the same parameters.

4.4.2 Model predictions in flow

Flow-Small Angle Neutron Scattering (flow-SANS) was used to probe the microstructures of wormlike micelles (60 mM CTAB/180 mM $NaNO_3$ sample) in flow. 2D scattering patterns in the mid-q configuration of the flow-flow gradient plane are shown in the top panel of Fig. 4.4. At equilibrium, the 2D scattering is isotropic because the micelles are randomly oriented. As shear rate increases, the scattering pattern shows increasing anisotropy. Also, in the flow-flow gradient plane, the average orientation of WLMs changes with shear rate. This is expected because in shear flow, the micelles tumble in the flow-flow gradient plane. At a very low shear rate, the average orientation angle with respect to the flow direction is 45°. As shear rate increases, the average orientation shifts towards the flow direction. At high enough shear rate, the average orientation of the micelles is in the flow direction. The circular region of very low intensity (blue circle) at the center of the scattering patterns comes from the beam stop of the scattering instrument.

In order to compare the predictions of the connected-rod model with experiments, we need to determine the average orientation angle ϕ_0 and the fractional extension λ in the orientation probability distribution function (Eqn. 4.14). We first calculate the annular average of the scattering intensity from experiments at $q = 0.025\text{Å}^{-1}$, which is the q value corresponding to the persistence length of the micelles. Following conventional analysis of the 2D anisotropic scattering data,[1,2] we fit the Maier-Saupe distribution to the annularly averaged intensity $I_c\left(q,\phi\right)$ to obtain the average orientation angle, which is used in the connected-rod calculation to match experimental data. Then, we numerically integrated the annular-averaged intensity to compute the alignment factor according to:

$$A_f = -\frac{\int_0^{2\pi} I_c\left(q,\phi\right)\cos\left[2\left(\phi-\phi_0\right)\right]d\phi}{\int_0^{2\pi} I_c\left(q,\phi\right)d\phi} \tag{4.23}$$

The alignment factor quantifies the degree of segmental alignment of the micelles induced by flow. We systematically vary the fractional extension λ in the simulation and compare the resulting alignment factor with that in the experiment. We then choose the values of the fractional extension λ that give the best match of experimental A_f and the simulation.

Results using these λ values are shown in the bottom panel of Fig. 4.4. The rest of the model parameters are fixed from the equilibrium fitting. Once the average orientation and degree of anisotropy are fitted, the connected-rod model does a very good job capturing the shape of the anisotropy and the gradual change in the anisotropy with increasing shear (increasing fractional extension). Here, the experimental data and predicted scattering are shown with the same color bar. The model describes the dumbbell shape of the anisotropy at mid-q and high-q really well.

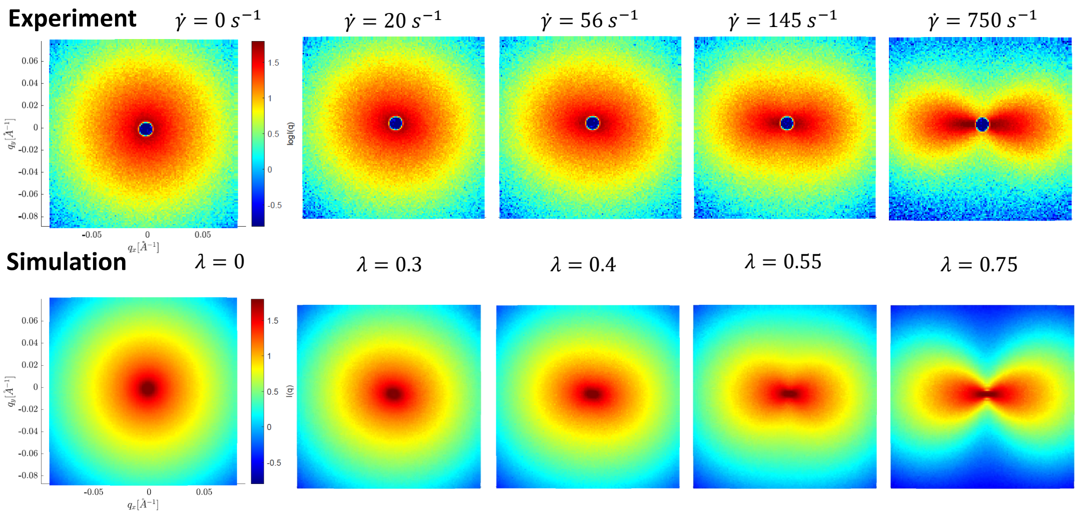

Figure 4.4: Comparison of 2D scattering intensity in the mid-q range from wormlike micelle experiments and the connected-rod model prediction using the Underhill OPDF. The values for the effective stretch, λ, are chosen to give the best match of the alignment factor calculated from experimental results and the simulation. All of the scattering patterns are plotted with the same color scale.

Fig. 4.5 presents a comparison of experimental scattering patterns and connected-rod model predictions for the low-q configuration using the same ϕ_0 and λ as in Fig. 4.4. Again, we achieve very good agreement between the experiment and simulation. In the low-q region, the scattering intensity is more sensitive to the polydispersity and potential net breakage of the micelles in flow. Since we are using the monodisperse calculation with fixed chain length, any quantitative differences between the experiment and simulation at low-q can be a result of polydispersity or chain breakage.

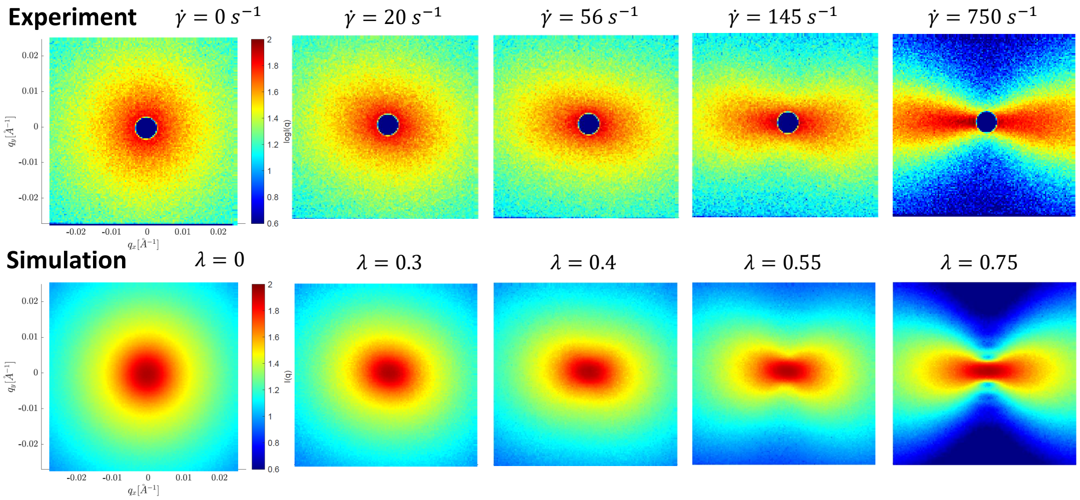

Figure 4.5: Comparison of 2D scattering intensity in the low-q range from wormlike micelle experiments and the connected-rod model prediction using the Underhill OPDF. The values for the effective stretch, λ, are chosen to give the best match of the alignment factor calculated from experimental results and the simulation. All of the scattering patterns are plotted with the same color scale.

To better visualize whether the model can capture the shape of the scattering anisotropy, we make a comparison of the annular average of the experimental scattering pattern and the at $q = 0.025$ Å^{-1} in Fig. 4.6. The scattering intensity is normalized by the average value of the intensity. For all 4 shear rates, the simulation exactly matches the shape of the annular average for the same alignment factor. This further validates the scattering model.

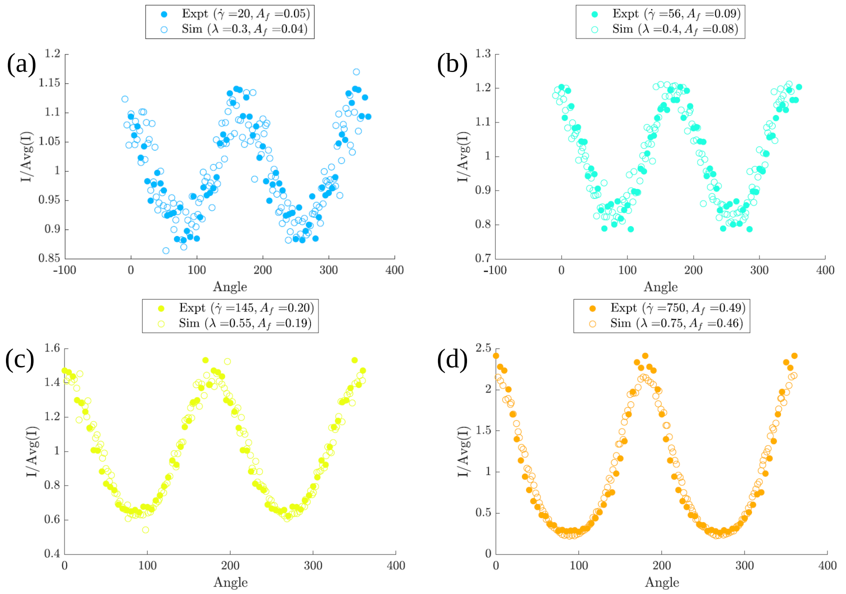

Figure 4.6: Comparison of annular average of intensity from experiment and connected-rod model prediction using the Underhill OPDF with the same degree of anisotropy (a)$A_f = 0.05$ (b)$A_f = 0.09$ (c)$A_f = 0.20$ (d)$A_f = 0.45$.

One remaining question we should answer is whether the values for the fractional extension we obtain from matching the degree of anisotropy between simulation and experiments are physically reasonable. Thus, we plot the fractional extension as a function of experimental shear rate in Fig. 4.7. To better compare with literature predictions of the chain stretching, here, we use the dimensionless shear rate, Wi, defined as $Wi = \tau\dot{\gamma}$, where $\tau = 0.2s$ is the relaxation time obtained from linear viscoelastic measurement of the wormlike micelles. The Wi-dependence is qualitatively similar to previous experiments of stretching DNA and FENE chain predictions.

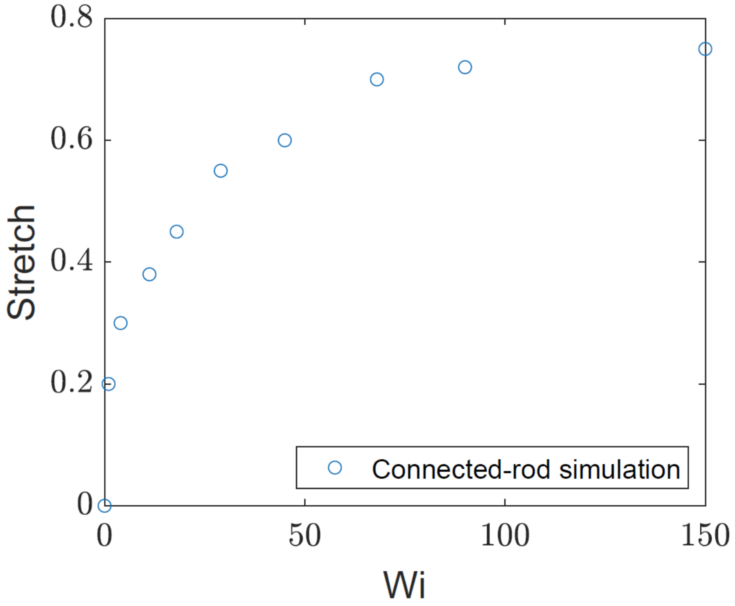

Figure 4.7: Plot effective stretch λ as a function of shear rate obtained from matching degree of anisotropy in connected-rod model prediction with experiment.

In addition to matching the alignment factor between simulation and experiment at $q = 0.025\text{Å}^{-1}$, which corresponds to the inverse of the persistence length, we are interested in verifying whether the model can capture the correct q-dependence of the scattering anisotropy. Thus, we make a comparison at different q values for the simulation and experiment (Fig. 4.8) corresponding to the shear rate and effective stretch in Fig. 4.6(d) above. For all q values investigated, the normalized intensity (i.e., annular averaged intensity divided by average intensity) shows excellent agreement between simulation and experiments. Furthermore, the computed alignment factor at each q value also shows good agreement between simulation and experiment. Thus, the connected-rod model with the Underhill OPDF is able to capture the q-dependent anisotropy in scattering experiments of semiflexible chains in flow.

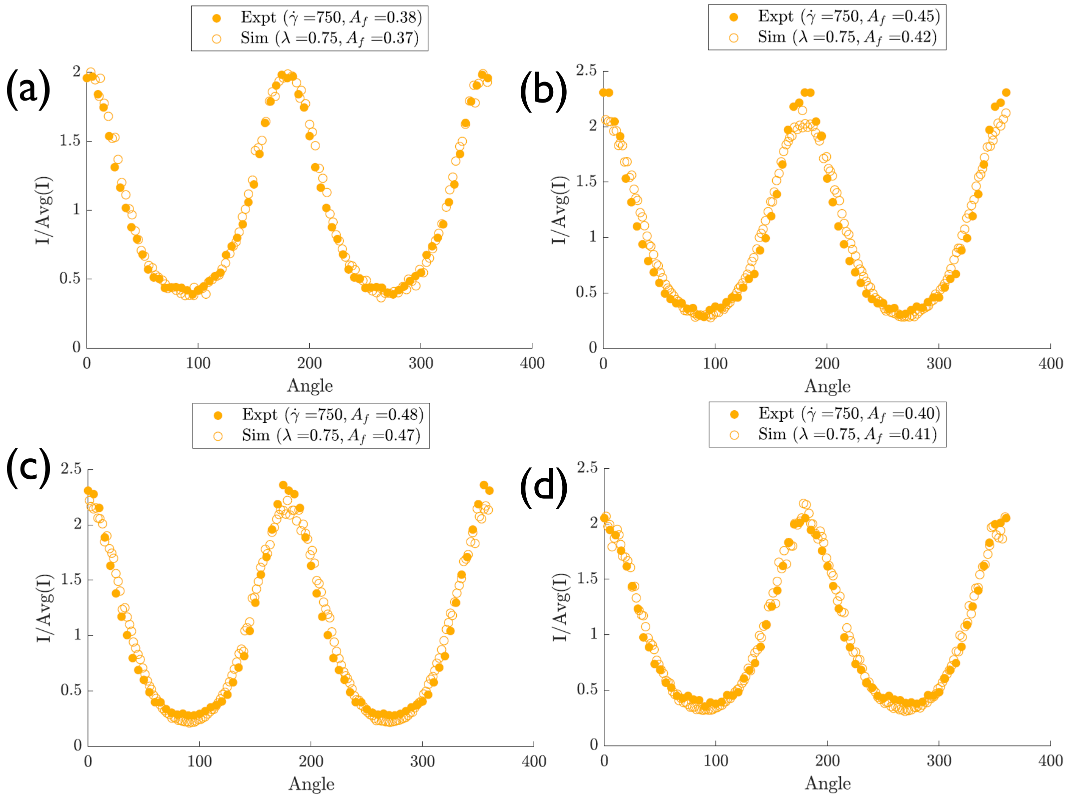

Figure 4.8: Compare q-dependent annular average in experiment ($\dot{\gamma} = 750s^{-1}$) and model prediction ($\lambda = 0.75$) for (a) $q = 0.006$Å^{-1} (b) $q = 0.01$Å^{-1} (c) $q = 0.05$Å^{-1} (d) $q = 0.1$Å^{-1}.

4.5 Discussion

Given the results just presented, we will now provide perspectives on how this work could provide insights for how material microstructures change in flow.

In the theory section, we talked about the limitations associated with using the orientation distribution developed by Hayter-Penfold in the connected-rod model. Here, we will make a comparison of the connected-rod model predictions using the Hayter-Penfold OPDF and Underhill OPDF and demonstrate the sensitivity of the anisotropic scattering to the orientation distribution.

We predict the scattering using Eqn. 4.18 with the Hayter-Penfold OPDF given in

Eqn. 4.3. In the Hayter-Penfold OPDF, the only adjustable parameter is the average orientation angle ϕ_0. In the original Hayter-Penfold paper, the orientation angle is related to the applied shear rate and the rotational diffusivity of the rod. Since we are most interested in determining whether this OPDF can capture the qualitative features in the scattering anisotropy, regardless of whether it predicts the correct shear-rate dependence, to simplify the comparison, we directly varied the average orientation angle ϕ_0 instead of changing the shear rate. Shown in the top panel of Fig. 4.9 are the scattering patterns from the wormlike micelle experiment. The scattering patterns in the bottom panel are from the connected-rod model prediction with the Hayter-Penfold OPDF. All of the other model parameters are the same as those used in the calculations with the Underhill OPDF (Fig. 4.4). To determine what ϕ_0 to use in the simulation, we matched the degree of anisotropy between the experiment and the simulation by calculating the annular average of the intensity and obtaining the alignment factor, as discussed previously. It is important to note here, since the Hayter-Penfold OPDF only has one adjustable parameter, ϕ_0 determines both the average orientation angle and the sharpness of the OPDF. In all cases shown here, for the same degree of anisotropy, the orientation angle in the simulation is larger than that in the experiment. Additionally, the dumbbell shape in the simulation is more elongated in the simulation than in the experiment. In order words, even if the difference in the direction of the tilt of the anisotropy can be accounted for, the shape of the anisotropy in the experiment is not fully captured by the Hayter-Penfold OPDF. This effect is more directly seen in a comparison of the annular average of the simulation and experiments corresponding to the same parameters in the 2D scattering, as shown in Fig. 4.10. For the same degree of anisotropy, there is a significant offset in the average orientation angle in the simulation compared to the experiment. The simulation also has a sharper peak for the intensity than in the experiment. This indicates the Hayter-Penfold OPDF, which only uses one parameter to describe both the average orientation angle and the shape of the OPDF, cannot satisfactorily describe the orientation distribution of segments in semiflexible chains.

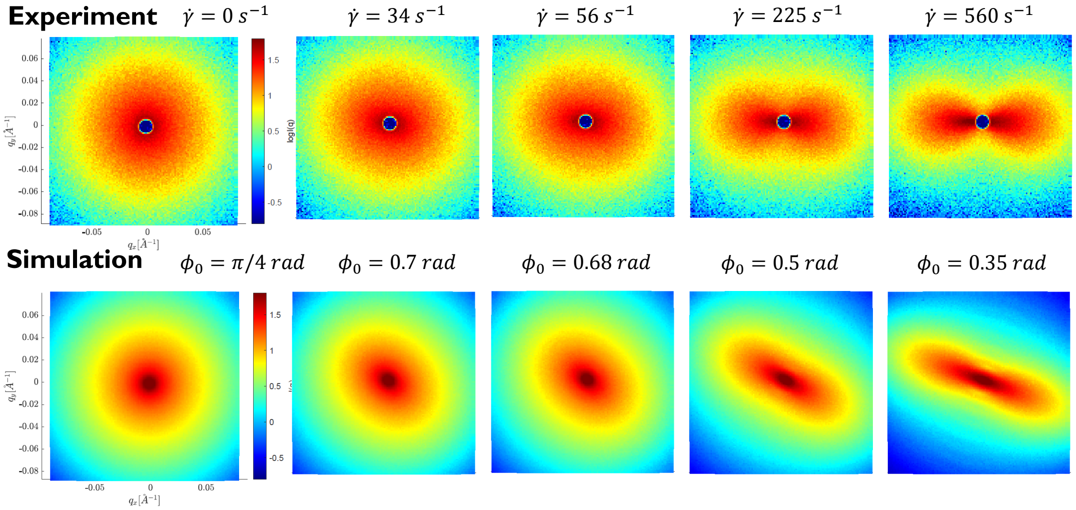

Figure 4.9: Comparison of 2D scattering intensity in the mid-q range from wormlike micelle experiments and the connected-rod model prediction using the Hayter-Penfold OPDF. The values for the average orientation angle, ϕ_0, are chosen to give the best match of the alignment factor calculated from experimental results and the simulation. All of the scattering patterns are plotted with the same color scale.

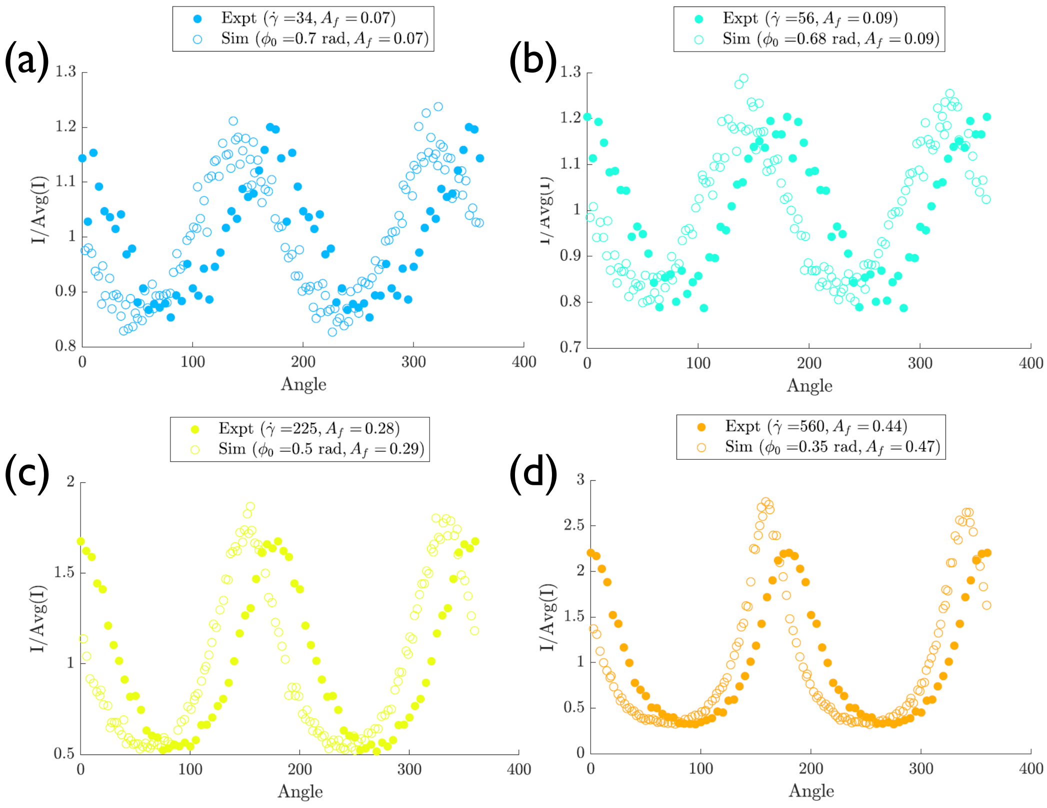

Figure 4.10: Comparison of annular average of intensity from experiment and simulation using Hayter-Penfold OPDF with the same degree of anisotropy (a) $A_f = 0.07$ (b) $A_f = 0.09$ (c) $A_f = 0.27$ (d) $A_f = 0.44$.

Furthermore, our approach illustrates the importance of including internal structures (i.e., connected segments) and contribution from cross sections (i.e., finite radius) when describing semiflexible chains with thick cores (e.g., wormlike micelles, bottle-brush polymers). If a modified Debye function is used to predict the scattering of polymer chains in flow, the scattering function only works in the low-q region and cannot fully describe the segmental contribution to the scattering.

Finally, when comparing with wormlike micelle experiments, we did not include polydispersity and breakage in the current scattering model in flow. This is because including polydispersity would require assuming a length-dependence of the fractional extension for each chain and we wouldn't be able to easily adjust the fractional extension to match the degree of anisotropy between the experiment and simulation. Furthermore, there is not clear consensus in the field about if and how the length distribution of wormlike micelles change in flow.

The near quantitative agreement between the monodisperse version of the connected-rod model with Underhill OPDF and wormlike micelle experiments suggests that the scattering of WLMs in flow can be described as semiflexible chains with stretching, orientation, and interchain interactions. More sensitive measurements are needed to probe whether the length distribution and average length of wormlike micelles change in flow. Examples of these measurements, such as transient-SANS measurements, steady flow-SANS measurements on WLMs of different concentrations at different temperatures will be analyzed in the framework of the current model in an upcoming publication. In this regard, the development of the scattering model is a key step to decoupling the contributions of chain stretch, orientation, and interactions to the scattering intensity from possible changes in chain length distribution in flow.

4.6 Conclusions

In this work, we develop a scattering model for semiflexible chains in flow. The model uses connected rods with a segmental orientation distribution that is self-consistent with the overall stretch of the chain and includes an RPA-type structure factor in flow. By using a discrete, polydisperse version of the model, we show that the model can be used to fit experimental data of wormlike micelles (and semiflexible polymers) and obtain chain length and Kuhn length that are consistent with previous literature results. By using a monodisperse version of the model in flow, we show that the flow-SANS results of wormlike micelles can be quantitatively predicted by the connected-rod model using parameters determined from the equilibrium fit and with the fractional extension and average orientation angle determined from flow-SANS experiments.

Furthermore, we illustrate the importance of including an orientation distribution (Underhill OPDF) that is self-consistent with the overall stretch and orientation of the chain. Specifically, by comparing the Underhill OPDF with the Hayter-Penfold OPDF, we show that the former has an excellent agreement with q-dependent anisotropy observed in experiments while the Hayter-Penfold OPDF cannot accurately capture either the average angle or the shape of the anisotropy. In the next chapter, the model developed in this chapter will be compared with more sensitive flow-SANS experiments of wormlike micelles to identify the signatures of chain scission. Although the focus of the experimental comparison in this work is on wormlike micelles, the flow-scattering model can be used to describe other types of semiflexible chains, in particular, systems with significant segmental orientation and contribution from finite cross sections that cannot be described by currently existing models. We expect the model will prove useful for extracting information about material deformation in flow, beyond simple analysis of alignment factor and sector average that are more frequently used in flow-SANS studies so far.

Bibliography

[1] Picken SJ, Aerts J, Visser R, Northolt MG. Structure and rheology of aramid solutions: X-ray scattering measurements. *Macromolecules.* 1990; 23(16): 3849–3854.

[2] Walker LM, Wagner NJ. Sans analysis of the molecular order in poly (γ-benzyl l-glutamate)/deuterated dimethylformamide (pblg/d-dmf) under shear and during relaxation. *Macromolecules.* 1996; 29(6): 2298–2301.

[3] Kratky O, Porod G. Diffuse small-angle scattering of x-rays in colloid systems. *Journal of colloid science.* 1949; 4(1): 35–70.

[4] Pedersen JS, Schurtenberger P. Scattering functions of semiflexible polymers with and without excluded volume effects. *Macromolecules.* 1996; 29(23): 7602–7612.

[5] Pedersen JS, Schurtenberger P. Scattering functions of semidilute solutions of polymers in a good solvent. *Journal of Polymer Science Part B: Polymer Physics.* 2004; 42(17): 3081–3094.

[6] Pedersen JS, Cannavacciuolo L, Schurtenberger P. Scattering from wormlike micelles. *Giant Micelles.* 2007: 179–222.

[7] Hayter JB, Penfold J. Use of viscous shear alignment to study anisotropic micellar structure by small-angle neutron scattering. *The Journal of Physical Chemistry.* 1984; 88(20): 4589–4593.

[8] Graham RS, Likhtman AE, McLeish TC, Milner ST. Microscopic theory of linear, entangled polymer chains under rapid deformation including chain stretch and convective constraint release. *Journal of Rheology.* 2003; 47(5): 1171–1200.

[9] Benoit H, Duplessix B, Ober R, et al. Scattered intensity by a polymer chain in a sample with external constraints. *Macromolecules.* 1975; 8(4): 451–453.

[10] Ullman R. Small angle neutron scattering from polymer networks. *The Journal of Chemical Physics.* 1979; 71(1): 436–449.

[11] Korolkovas A, Prévost S, Kawecki M, et al. The viscoelastic signature underpinning polymer deformation under shear flow. *Soft matter.* 2019; 15(3): 371–380.

[12] Hsu HP, Paul W, Binder K. Scattering function of semiflexible polymer chains under good solvent conditions. *The Journal of chemical physics.* 2012; 137(17): 174902.

[13] Pandey H, Underhill PT. Coarse-grained model of conformation-dependent electrophoretic mobility and its influence on dna dynamics. *Physical Review E.* 2015; 92(5): 052301.

[14] Liao WC, Watari N, Wang S, Hu X, Larson RG, Lee LJ. Conformation dependence of dna electrophoretic mobility in a converging channel. *Electrophoresis.* 2010; 31(16): 2813–2821.

[15] Corona PT. *Probing nanostructure and rheology of complex fluids in complex flow histories using small angle scattering.* PhD thesisUC Santa Barbara 2020.

[16] Lepage GP. A new algorithm for adaptive multidimensional integration. *Journal of Computational Physics.* 1978; 27(2): 192–203.

[17] Levenberg K. A method for the solution of certain non-linear problems in least squares. *Quarterly of applied mathematics.* 1944; 2(2): 164–168.

[18] Marquardt DW. An algorithm for least-squares estimation of nonlinear parameters. *Journal of the society for Industrial and Applied Mathematics.* 1963; 11(2): 431–441.

[19] Gurnon AK, Godfrin PD, Wagner NJ, Eberle AP, Butler P, Porcar L. Measuring material microstructure under flow using 1-2 plane flow-small angle neutron scattering. *JoVE (Journal of Visualized Experiments).* 2014(84): e51068.

[20] Kline SR. Reduction and analysis of sans and usans data using igor pro. *Journal of applied crystallography.* 2006; 39(6): 895–900.

[21] Helgeson ME, Hodgdon TK, Kaler EW, Wagner NJ. A systematic study of equilibrium structure, thermodynamics, and rheology of aqueous ctab/nano3 wormlike micelles. *Journal of colloid and interface science.* 2010; 349(1): 1–12.

Chapter 5

Experimental investigation of flow-enhanced scission of wormlike micelles

5.1 Introduction

Understanding structure-property relationships in surfactant-based fluids is critical for modeling the fluid to achieve the desired flow properties and to avoid flow instabilities. Wormlike micelles (WLMs) are long, semi-flexible chainlike surfactant aggregates that show polymer-like viscoelastic properties. Because of their rheological properties, combined with their detergency and structure, WLMs are used in the oil and gas industry, and more noticeably in consumer products such as shampoo and body wash. In all of these applications, wormlike micelles are subjected to flow during processing and end-use. The rheology of WLMs is critical to the successful formulation and engineering of these products and processes.[1] Such applications benefit from understanding how the microstructures influence the flow properties.

WLMs are often likened to “living polymers”, since associations between surfactants are impermanent, leading to dynamic scission and recombination of the micelles due to thermal fluctuations. At equilibrium, the probability of chain scission and recombination is assumed to be equal at any position along the chain, and this results in an exponential length distribution. Mean field theories and population balances by Cates and coworkers have predicted an exponential equilibrium length distribution,[2,3] which is in good agreement with structural measurements of sufficiently long WLMs in dilute and semi-dilute solutions.[4,5] Although the equilibrium length distribution of wormlike micelles has been well studied, very little is known about how the distribution is modified by flow. There is still debate in the field about whether flow significantly contributes to the scission of wormlike micelles, thereby changing the length distribution. On the one hand, extensions of the Cates model to nonlinear flows have assumed that scission and recombination are not affected by flow.[6] The nonlinear effects of the flow enter solely through its influence on chain relaxation via reptation.[6] On the other hand, other rheological theories adopted ad hoc approaches for modeling the influence of flow on scission and recombination. For example, Vasquez and co-workers developed the VCM model for semi-dilute, shear thinning and shear banding wormlike micelles, in which flow-enhanced scission of micelles was predicted to result from increased tension in the chains with increasing applied strain, but the recombination rate of chains was assumed to be constant and independent of flow.[7] In contrast, Graham and coworkers developed a reactive rod model for dilute, shear thickening wormlike micelles which predicts flow-enhanced recombination: flow aligns the micelle, which in turn increases the probability of recombination. Enhanced alignment and recombination create a positive feedback, which causes an increase in the average length of WLMs.[8] So, currently from the theoretical perspective, there is a lack of agreement about how (or whether) flow affects scission, and the resulting length distribution.

Despite the predictions discussed above, there is currently no direct microstructural evidence from experiments for how flow affects the scission and recombination process in WLMs. Previous experiments relied mostly on rheological measurements, which are sensitive primarily to the long micelle species, not the entire length distribution. Extensional rheology experiments have suggested that micellar breakage can happen as a result of strong flows.[9] Rothstein and co-workers[10,11] measured the extensional rheology of wormlike micelles using a filament stretching rheometer and observed the filament abruptly ruptures near its axial mid-plane above a critical extension rate. The failure of the wormlike micelle filaments occurs before any significant necking has appeared. The authors suggested that the observed filament failure likely stems from the scission of wormlike micelles resulting in a dramatic breakdown of the micelle network en masse.[10] Bhardwaj et al. [12] studied the effect of pre-shear on extensional deformation of WLMs and found the value of the elastic tensile stress at filament rupture and the extensional viscosity decrease dramatically with increasing pre-shear rate and duration, which the authors attribute to possible reduction in the size of WLMs due to pre-shear. Furthermore, researchers[13,14] suggest the wake instability found in WLMs past a falling sphere is related to the scission of wormlike micelles in the wake of the falling sphere, where a strong extensional flow is present. Although previous extensional and complex flow measurements of wormlike micelles have suggested flow-induced scission, these measurements can't directly probe the microstructures of the wormlike micelles in flow and researchers typically need to interpret observations at the macroscopic level (e.g., filament fracture and wake instability) and hypothesize that the effects are caused by micellar scission. Therefore, direct structural measurements in flow are needed confirm the presence of flow-induced scission of wormlike micelles and to do so in a model-agnostic way.

Small angle neutron scattering (SANS) is a very useful technique for measuring microstructures of WLMs because it probes length scales from 1-200 nm, which covers the range of characteristic length scales in WLM solutions. WLMs exhibit a hierarchy of length scales: ranging from a few nm for the cross-sectional radius, r_{cs}, to a broad distribution of micellar contour lengths, L_C, with an average length ranging from 100 nm to 1 μm, depending on the type of WLM and solution conditions.[15] The WLM persistence length, l_p, is a measure of the chain stiffness and is typically 20 nm, at which length scale the wormlike micelles can be considered locally rigid.[1] For wormlike micelles at relatively low concentrations, the scattering data shows similar dependence on the scattering vector q as that of classical polymers. At low enough q ($q \left\langle R_g^2 \right\rangle \ll 1$, where $\left\langle R_g^2 \right\rangle$ is the square average radius of gyration), $I \sim 1 - q^2 \left\langle R_g^2 \right\rangle /3$). The scattering curve levels off in this low-q range (the Guinier region) due to the finite size of the micelles relative to the length probed. Beyond the Guinier region, the scattering crosses over to a power law behavior $q^{-5/3}$ due to the excluded-volume statistics of the micelles. At higher q, the scattering probes the local cylindrical structure and it crosses over to q^{-1}. However, this power law is often masked by the polydispersity in micellar length and the cross-section Guinier region that originates from the finite diameter of the micelles. Beyond this region, the scattering curve drops significantly and at the highest q it follows the Porod law q^{-4} which occurs for objects with sharp interfaces.[16]

Static SANS scattering of wormlike micelles has been studied extensively both experimentally [4,17] and theoretically.[18] In particular, Pedersen and Schurtenberger extended models originally developed for polymers and used Monte Carlo simulations to develop WLM scattering models ,[19,20] which have been shown to give very good agreement with experimental data at equilibrium.[4,16] Specifically, the theory captures the q-dependence across all the characteristic length scales in WLMs, from the cross-sectional radius, to the persistence length, to the radius of gyration of the chain. Furthermore, the theory takes into account excluded volume and concentration effects. However, no theories have been developed for scattering of WLMs in flow due to the combined effect of the micelle length polydispersity, changes in length distribution, orientation, and interchain interactions on the projected flow-induced anisotropic scattering in the detector plane.

Many flow-SANS experiments have probed WLM alignment,[21–23] but no studies have probed how flow potentially affects the scission and recombination process and the resulting length distribution of the micelles. This is because (i) previous flow-SANS and light scattering[24] experiments were limited by structural complications including entanglement and branching, as well as flow instabilities including shear banding and elastic instability.[23,25] Additionally, (ii) procedures for decoupling changes in micellar length from changes in orientation and structure factor effects have not been developed. The present study addresses (i) by conducting SANS experiments on a carefully designed series of linear, weakly entangled WLMs, which provides access to stable flows up to relatively large shear rates, and addresses (ii) by developing new approaches for analyzing both the steady-state and time-resolved flow-SANS patterns to deconvolute the contributions to scattering from changes in micelle orientation and stretching, from effects due to changes in micelle length in flow. Knowledge of how flow affects the average micellar length will offer key insights for developing new models for wormlike micelles.

5.2 Methods

5.2.1 Selection of model wormlike micelle system and wormlike micelle preparation

We chose to use cetyltrimethylammonium bromide (CTAB) as the surfactant and sodium nitrate (NaNO3) as the salt for forming wormlike micelles because (1) in the presence of CTAB, NO_3^- was found to be the most effective at producing elongated micelles compared to other simple inorganic salts[26] and (2) the equilibrium length distribution and linear rheology of WLMs made from CTAB and $NaNO_3$ has been extensively studied, which provides a good basis for studying effects of flow on micellar length distribution.[4] For this, we chose a concentration range that produced linear, weakly entangled WLMs that do not exhibit shear banding.

Solutions containing 60 mM, 80 mM, and 100 mM cetyltrimethylammonium bromide (CTAB, Sigma Aldrich) were prepared in deuterium oxide (D_2O, 99.9%, Cambridge Isotope Laboratories) with 1:3 molar ratio of CTAB to sodium nitrate ($NaNO_3$, Sigma Aldrich). All materials were used as supplied without further purification. For neutron scattering measurements, it was necessary to prepare samples using deuterium oxide to reduce incoherent scattering. Dry powders of CTAB and $NaNO_3$ were added to D_2O in the appropriate amounts. After agitation for complete powder dispersion, the solutions were placed in a temperature-controlled oven held at 47 °C for at least 1 day to achieve sample equilibration before measurements.

5.2.2 Rheological characterization

Rheological characterization was performed on a TA Instruments AR-G2 stress-controlled rheometer with a Taylor-Couette geometry with a rotating inner cylinder of R_1 = 13.98 mm and a stationary outer cylinder of R_2 = 15.21 mm. This geometry was chosen to closely resemble the curvature and the gap size of the geometry used in flow-SANS measurements. The fluid temperature was set with a Peltier-controlled outer cylinder. A solvent trap was used to prevent evaporation of D_2O during the measurements. The sample was loaded and conditioned at rest for 700 s at the temperature corresponding to the experiment. A pre-shear of $1s^{-1}$ was applied for 60 s and the sample was allowed to rest for 100 s to erase any loading history and to let the temperature equilibrate. The storage (G') and loss (G'') moduli were measured by performing a frequency sweep at

5% strain (in the linear viscoelastic regime: LVE) from 200 rad/s to 0.1 rad/s and then another from 0.1 rad/s to 200 rad/s. No hysteresis in the LVE measurements was observed for any sample. Steady-shear tests were run with logarithmic spacing for shear rates, $\dot{\gamma}$, ranging from 0.01 to 1500 s^{-1} . For each measurement during the steady-state test, the steady state sensing was turned on, with a 1% tolerance within 3 consecutive points, 60 s maximum equilibration time, and 15 s sample periods, to ensure steady state has been achieved before results were recorded.

5.2.3 Particle tracking velocimetry

Velocimetry measurements were carried out using particle tracking velocimetry (PTV) on an Anton-Paar Physica MCR300 rheometer using a Taylor-Couette geometry. The outer stationary quartz cup has a fixed radius $R_2 = 17.5$ mm. We used an inner moving anodized aluminum cylinder with a radius $R_1 = 17$ mm, which corresponds to a gap size of 0.5 mm. The temperature of the Couette cell is controlled with a circulating water bath. Sample preparation for PTV measurements consisted of seeding the fluid with approximately 300 ppm of neutrally buoyant hollow silica spheres (8-12 μm diameter, TSI Incorporated). In all cases, addition of tracer particles at such low concentrations produced no significant changes in the measured sample rheology. An incident sheet laser on the inner cylinder was introduced from the side at a height of 6 mm from the bottom of the 15.7 mm tall inner cylinder, and the reflection from the tracer particles was collected through a sapphire window at the bottom of the geometry and imaged using a CCD camera. Both shear stress and PTV measurements were made simultaneously after quickly ramping the applied shear rate of the rheometer from rest to the desired rate within 0.1 s. Measurements were made for $\sim$160 s at each shear rate to ensure the achievement of steady state. The consecutive images taken with the camera were analyzed using a standard particle-tracking algorithm[27] to obtain spatially resolved fluid velocity $v_\theta(r)$ as a function of the position r within the gap, measured from the inner moving cylinder. The steady-velocity profiles were obtained by averaging the PTV data over ∼30 different pairs of consecutive images after the shear stress achieved steady state.

5.2.4 Small angle neutron scattering

Steady state flow-SANS

SANS measurements were performed using the NGB 30m SANS instrument at the National Institute of Standards and Technology Center for Neutron Research (Gaithersburg, MD). Anisotropic scattering was characterized using flow-SANS for simple shear flow in both the flow-gradient $(v - \nabla v)$ plane and the flow-vorticity $(v - \omega)$ planes. Measurements in the flow-gradient plane were made using the 1-2 shear cell sample environment[28] and measurements in the flow-vorticity plane employed a Couette cell controlled by an Anton Parr rheometer. A wavelength of $\lambda_0 = 6$ Å with a wavelength spread of $\Delta\lambda_0/\lambda_0 = 0.14$ was used. The scattering vector q is defined as $q = 4\pi \sin\left(\alpha/2\right)/\lambda_0$ where α is the angle at which the neutron is scattered and λ_0 is the neutron wavelength. Scattering from the sample was collected in the q range $0.005 - 0.2$ Å^{-1}. The temperature was maintained constant at set temperature through the entire experiment with a water bath for the shear cell. The 2D scattering intensities were corrected for empty cell, plexiglass standard, and detector efficiency. Scattering patterns were reduced using standard protocols with Igor Pro software.[29]

Time-resolved flow-SANS

Time-resolved flow-small angle neutron scattering is used to capture structures of wormlike micelles during the start up and cessation of flow. The method requires the synchronization of the scattering and start up of the flow geometry (1-2 plane shear cell or the rheometer). The time-resolved experiments bin data into $n_b = t_{tot}/\Delta t = 150$ bins of Δt duration for a cycle time of t_{tot}. Here the cycle time t_{tot} is 15 s, with 5 s after the start up of flow and 10 s after flow cessation. The next cycle starts immediately after the end of the first cycle. The scattering intensity is collected over a prescribed number of repeated transient experiments n_c and summed to achieve sufficient total scattering intensity. Here we use $n_c \approx 330$ in the rheometer and $n_c \approx 600$ in the shear cell. A prerequisite for choosing a material to be investigated with time-resolved flow-SANS is that it behaves reproducibly for each subsequent transient event so that a sufficient number of cycles can be summed to collect statically valid scattering patterns in each time bin. Here we validate that the sample fully recovers to equilibrium during the relaxation period as evidenced by the magnitude of the isotropic intensity that no longer changes with time.

5.3 Results

The results section will be divided into four sections. In the first section, we report linear viscoelastic and steady shear flow rheological characterization of the wormlike micelle solutions. We fit the linear viscoelastic measurements to single-mode Maxwell model to extract parameters describing the equilibrium properties of the solution. In the second section, we report 2D flow-SANS measurements in two projection planes and discuss methods of parameterization to extract useful information about changes in average intensity and the degree of anisotropy in flow. In the third section, we compare the steady state flow-SANS experimental results with predictions of the connected-rod model that we introduced in Chapter 4 to investigate the possibility of flow-enhanced scission. In the final section, we analyze time-resolved flow-SANS measurements to quantify the timescales associated with different relaxation mechanisms.

5.3.1 Rheological Characterization

The linear viscoelasticity of the solution containing 60 mM CTAB/180 mM $NaNO_3$, 80 mM CTAB/240 mM $NaNO_3$, and 100 mM CTAB/300 mM $NaNO_3$ prepared in D_2O at 25 °C, are shown in Fig. 5.1(a). Strain sweeps demonstrated that the results are in the linear viscoelastic regime. The storage modulus G' is shown in filled symbols and the loss modulus G'' is shown in open symbols. The storage modulus scales as ω^2 and the loss modulus scales as ω in the low frequency region. With increasing concentration, the moduli curves shift upwards and to the left. Two time scales can be defined from the data: the longest relaxation time, τ, is defined by the frequency at the crossover $\omega_r = 1/\tau$ of G' and G''; the breakage time, τ_{br}, is defined from the higher frequency $\omega_{min} = 1/\tau_{br}$, where ω_{min} is the frequency at which a local minimum in G'' is observed.[30] The results are well described by a single-mode Maxwell model:

$$G'(\omega) = \frac{G_0\,(\tau\,\omega)^2}{1 + (\tau\,\omega)^2}, \tag{5.1}$$

$$G''(\omega) = \frac{G_0\,(\tau\,\omega)}{1 + (\tau\,\omega)^2} + \eta_\infty \omega. \tag{5.2}$$

Here, G_0 is the plateau modulus, τ is the longest relaxation time (as defined above), and η_∞ is the high-frequency viscosity. The average number of entanglements per chain is estimated by using $N_e = G_0/G''_{min}$, where G_0 is the plateau value of G' and G''_{min} is the minimum of G''.[31] The estimated numbers of entanglements per chain are 3, 5, and 8 for the three samples respectively. Previous experiments showed that wormlike micelles made from surfactant and salt in our concentration range remain linear, not branched.[4] Results from the Maxwell fitting are included in Table 5.1. Since all three WLM solutions exhibit single-mode Maxwell behavior, the solutions are in the fast-breaking limit as the values of τ are much greater than those for τ_{br}. Therefore, the reptation time τ_{rep} can be calculated from Cates' theory by $\tau_{rep} = (\tau^2/\tau_{br})$, and are listed in Table 5.1.

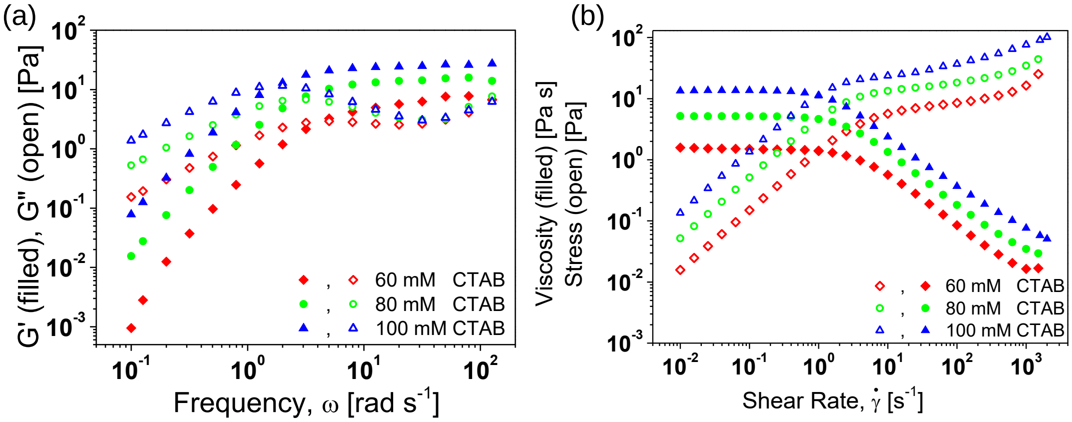

Figure 5.1: Linear and nonlinear rheology of 60 mM CTAB, 80 mM CTAB, and 100 mM CTAB wormlike micelles in D_2O at 25 °C.

Table 5.1: Parameters from single-mode Maxwell fits of the linear viscoelastic data of WLMs.

CTAB	NANO$_3$	T	G_0	G''_{min}	τ	τ_{br}	τ_{rep}	N_e	η_∞
(mM)	(mM)	(°C)	(Pa)	(Pa)	(s)	(s)	(s)		(Pa s)
60	180	25	6.6	2.5	0.19	0.040	0.90	2.6	0.049
80	240	25	14.4	3.1	0.34	0.037	3.31	4.6	0.056
100	300	25	25.1	3.0	0.52	0.031	8.51	8.3	0.047

Steady-state shear stress versus shear rate curves for the WLM solution are shown in Fig. 5.1(b). The shear stress σ (shown in open symbols) initially increases nearly linearly with shear rate $\dot{\gamma}$, then the slope of the stress-shear rate curve decreases; at even higher shear rates, the shear stress again starts to increase rapidly with shear rate. The viscosity (shown in filled symbols) is defined as the ratio of the shear stress and the shear rate: $\eta = \sigma/\dot{\gamma}$. At low shear rates, the viscosity is constant, and the fluid behaves as a

Newtonian fluid; at higher shear rates (corresponding to $Wi > 1$), the viscosity decreases and this is called the shear-thinning region. In complex fluids such as suspensions of non-spherical particles and polymer solutions, shear thinning is usually associated with flow-induced alignment of particles (or polymer chains) which decreases the particle's disturbance to the flow, and thus the viscosity decreases. For wormlike micelles, which undergo dynamic scission and recombination, the shear thinning could also be caused by flow-induced scission.

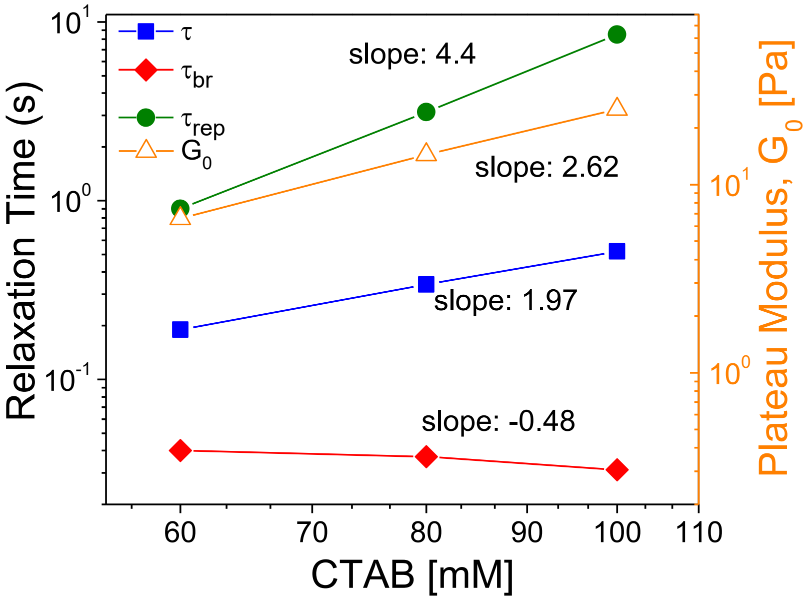

Figure 5.2: Relaxation times identified from linear viscoelastic measurement as a function of CTAB concentration.

To compare how the different relaxation times scale with concentration in the experiments and in theory predictions, we plot the longest relaxation time τ, the breakage time τ_{br}, and the reptation time τ_{rep} as a function of CTAB concentration in Fig. 5.2. In deriving the scaling relationships for the relaxation times, Cates and Candau assumed that the spontaneous unimolecular scission rate is independent of concentration (which is a valid assumption for ionic surfactant micelles at high enough salt concentration).[2,3]

Since $\tau_{br} = \frac{1}{c_{br}\bar{L}}$, where c_{br} is the breakage rate, and $\bar{L} = \phi^{1/2} \exp\left(E_{sciss}/2k_BT\right)$, τ_{br} scales as $\phi^{-1/2}$. The reptation time is estimated using a semi-empirical relation $\tau_{rep} \sim \bar{L}^3\phi^2$ found for the case of unbreakable polymers in the mean-field regime, again assuming the spontaneous unimolecular scission rate is independent of concentration. After substituting in the ϕ dependence for $\bar{L}$, we obtain $\tau_{rep} \sim \phi^{7/2}$. Finally, in the fast-breaking limit, $\tau = \left(\tau_{rep}\tau_{br}\right)^{1/2}$, thus Cates-Candau theory predicts $\tau \sim \phi^{3/2}$. Cates and Candau generalized their original theory to include free volume interactions between micelle segments, resulting in $\bar{L} = \phi^{y} \exp\left(E_{sciss}/2k_BT\right)$. For ideal chains, $y = 1/2$, whereas $y = 0.6$ taking into account excluded volume interactions. Using 0.6 as the scaling exponent for ϕ-dependence of the average length, we obtain $\tau \sim \phi^{1.6}$. The data shows similar scaling exponents for the relaxation times as those predicted in the theory, although the scaling exponents for τ_{rep} and τ are both slightly larger than the theoretical predictions. This is because electrostatic interactions between chain segments were not included in the original Cates and Candau model. Although with a salt to surfactant ratio of 3:1 in our experiments, the electrostatic interactions are largely screened by the added salt, the electrostatic interactions can still play a non-negligible role in the dependence of average micelle length on ϕ. Electrostatic interactions are accounted for in the model by Mackintosh et al.[32,33] for the case of ionic wormlike micelles, which predicts a larger exponent for the average chain length dependence on ϕ. Furthermore, in the semi-dilute regime studied here, the Cates theory[3] predicts that the plateau modulus scales as $\phi^{9/4}$ and our experiment shows $G_0 \sim \phi^{2.62}$ (Fig. 5.2).

Compared to samples at higher concentration with shear-banding that were studied previously, the WLMs in this work have larger slopes for the stress vs shear rate in the shear-thinning region and the stress plateau usually observed in shear-banding WLMs is absent, which suggests our samples don't exhibit shear-banding. To further confirm the absence of shear-banding, we performed particle tracking velocimetry (PTV) on the sample with the highest concentration investigated in this study: 100 mM CTAB/300 mM $NaNO_3$ at 25 °C (Fig. 5.3), across the nonlinear regime of fluid rheology. Nearly linear velocity profiles are observed in all cases, demonstrating that the sample mildly shear thins, but does not shear band. Since 100 mM CTAB at 25 °C is more viscoelastic than the 60 mM sample and 80 mM sample (higher relaxation time, higher plateau modulus, and smaller slope of stress vs shear rate in shear thinning region) and it doesn't show shear banding, we can be sure that the other samples don't show shear banding either.

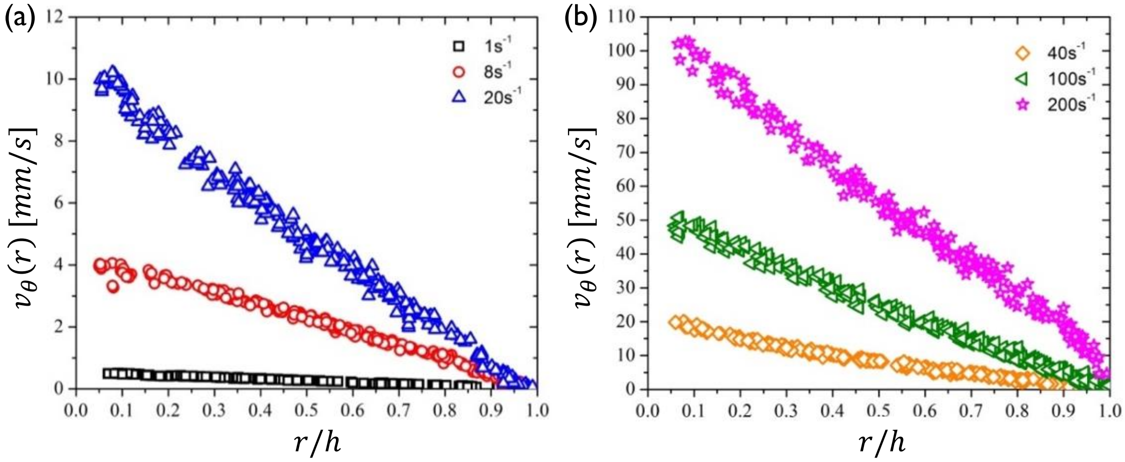

Figure 5.3: Steady-state velocity profiles measured by PTV for 100 mM CTAB/300 mM $NaNO_3$ in H_2O at 25 °C at the shear rates indicated. r/h is the nondimensionalized position, where $r/h = 0$ is the inner (rotating) wall and $r/h = 1$ is the outer (stationary) wall.

5.3.2 Parameterization of 2D scattering in flow

Flow-small angle neutron scattering (flow-SANS) was used to probe the microstructures of wormlike micelles in flow. 2D scattering intensity profiles were measured for the 60 mM CTAB/180 mM $NaNO_3$ sample with increasing shear rate (Fig. 5.4(a)). The dimensionless shear rates, Wi, in Fig. 5.4(a) are marked in Fig. 5.4(b) on the viscosity vs. Wi curve. As shear rate increases, the scattering pattern shows increasing anisotropy. The shear rate at which anisotropy is first apparent corresponds to the point where the viscosity of the solution begins to decrease (green dotted line in Fig. 5.4 (a) and (b)). Also, in the flow-flow gradient plane, the average orientation of WLMs changes with shear rate. This is expected because in shear flow, the micelles tumble in the flow-flow gradient plane. At a very low shear rate, the average orientation angle with respect to the flow direction is 45°. As shear rate increases, the alignment shifts towards the flow direction. At high enough shear rate, the average orientation of the micelles is in the flow direction.

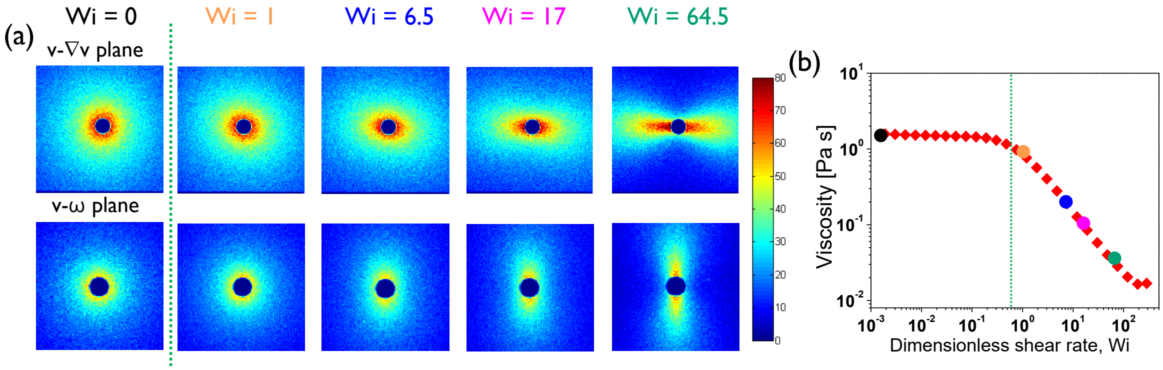

Figure 5.4: (a) Representative 2D SANS patterns for 60 mM CTAB/180 mM $NaNO_3$ in the flow-gradient ($v-\nabla v$) and flow-vorticity ($v-\omega$) planes at various dimensionless shear rate, Wi. All patterns provide the respective intensity value on a linear scale indicated by the color bar to the right of the patterns. The patterns are reported in q_x,q_y coordinates. (b) The viscosity of 60 mM CTAB WLM solution as a function of dimensionless shear rate, Wi. The large color dots correspond to the Wi values included in (a). The green dotted line in (a) represents the onset of anisotropy in scattering patterns, which corresponds to the onset of shear thinning in (b).

Even without developing a full 2D scattering model for wormlike micelles, we can extract useful information from the circular average and the annular average of the 2D scattering patterns. In both the flow-flow gradient ($v-\nabla v$) plane and flow-vorticity ($v-\omega$) plane, the low-q circularly averaged intensity decreases as shear rate increases, whereas in the intermediate-q and high-q region, the intensity appears to remain constant (Fig. 5.5(a)). In the subsequent analyses, only results in the flow-flow gradient plane ($v-\nabla v$) are shown, although similar results were obtained in the flow-vorticity ($v-\omega$)

plane. To better visualize the changes in the scattering anisotropy, we calculated the annular average of the intensity at $q = 0.005$ Å^{-1} (Fig. 5.5(b)). With increasing Wi, the annularly averaged intensity changes from nearly constant at all angles to more peaked. The minimum in the intensity corresponds to the direction of average alignment, which is $\phi = 90°$ (in the flow direction) for the highest Wi.

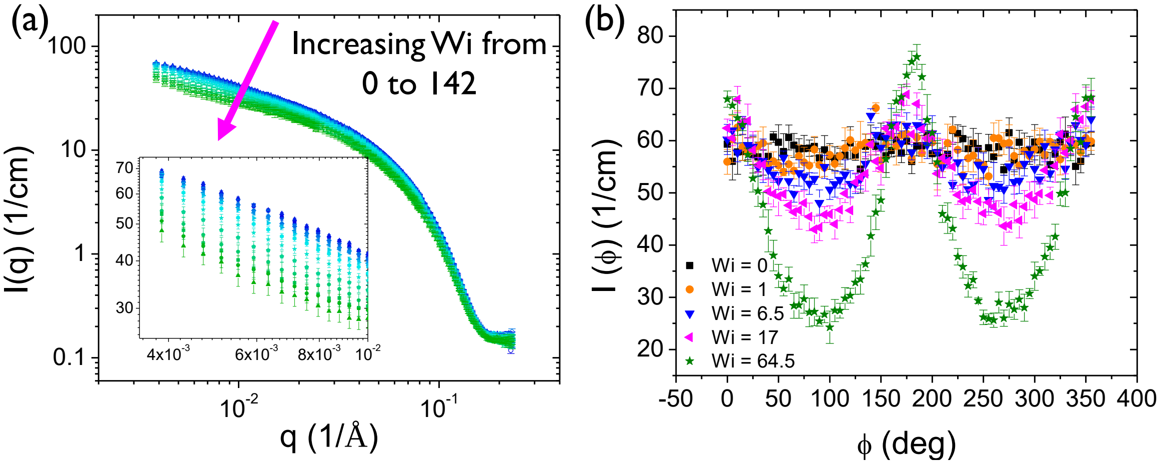

Figure 5.5: 1D parameterization of 2D scattering for 60 mM CTAB in the $v - \nabla v$ plane (a)circularly averaged intensity as a function of wave vector q. From top (dark blue) to bottom (dark green) are Wi from 0 to 142. (b) Annularly averaged intensity as a function of angle for various Wi at $q = 0.005$ Å^{-1}.

The scattering intensity for wormlike micelles is described by

$$I(q) = \phi \, (\Delta\rho)^2 \, \overline{V}_p \overline{P(q)S(q)} + I_b \tag{5.3}$$

where ϕ is the volume fraction of the micelles, $\Delta\rho$ is the difference in scattering length density between the micelles and the solvent, $\overline{V}_p = \pi \bar{r}_{cs}^2 \bar{L}_c$ is the average volume of a chain, and I_b is the incoherent background intensity. $\bar{L}_c$ is the number-average contour length and $\bar{r}_{cs}$ is the average radius of the micelle. $P(q)$ is the form factor, which describes the contribution from intra-chain scattering. $S(q)$ is the structure factor, which measures the contribution from inter-chain scattering (i.e., how individual micelles are positioned in space relative to each other). Since the average volume of the micelle is proportional to the average micellar length, the scattering intensity is also proportional to the micellar length. Thus, the monotonic decrease of the circularly averaged intensity with increasing Wi that we observed in Fig. 5.5 is consistent with the net shortening of the micelles. However, to determine the existance of flow-enhanced scission, we also need to know how the form factor and structure factor change in flow, i.e., how chain stretch, orientation, and interactions in flow affect the scattering intensity. Ultimately, distinguishing these different contributions to the scattering intensity requires comparing the experimental result to model simulations, such as the connected-rod model described in Chapter 4, which we will discuss in Section 5.3.3. First, we will perform additional analyses of the circular average and annular average results of the scattering intensity (Fig. 5.5) to quantify the change in intensity and the degree of anisotropy.

To obtain a more quantitative measure of the change in intensity at different q values, we averaged the intensity at three adjacent q-values for each shear rate, normalized the intensity in flow by the intensity at the corresponding q-values at no shear, then subtracted the ratio from 1. The quantity $1 - I_{flow}/I_{eqm}$ vs. Wi are shown for different q-values in Fig. 5.6 (a). $(1 - I_{flow}/I_{eqm}) = 0$ corresponds to no change in the intensity and larger values of $1 - I_{flow}/I_{eqm}$ correspond to larger changes in intensity. The data clearly indicate that the intensity changes most strongly with shear rate at the lowest q-values. Since $L \sim 2\pi/q$, the length scale corresponding to this q value is 105 nm, which is on the same order of magnitude as the average micelle length estimated experimentally for the 60 mM CTAB/180 mM $NaNO_3$ sample.[4] At higher q, the change in intensity becomes less and the trend is monotonic with q.

Using conventional analysis of the 2D anisotropic scattering data,[34,35] we fitted the Maier-Saupe distribution to the annularly averaged intensity $I_c(q, \phi)$ to obtain the average orientation angle ϕ_0. Then, we numerically integrated the annular-averaged intensity to compute the alignment factor according to:

$$A_f = -\frac{\int_0^{2\pi} I_c\left(q,\phi\right)\cos\left[2\left(\phi-\phi_0\right)\right]d\phi}{\int_0^{2\pi} I_c\left(q,\phi\right)d\phi} \tag{5.4}$$

The alignment factor quantifies the degree of segmental alignment of the micelles induced by flow. At all q values analyzed, the alignment factor increases monotonically with Wi. Interestingly, the alignment factor changes non-monotonically with q: from the lowest q value probed (0.006 Å^{-1}) to the q value corresponding to the persistence length of the micelle (q = 0.025 Å$^{-1}\sim 2\pi/l_p$), the alignment factor at a given Wi increases with q; but for $q >$ 0.025 Å^{-1}, the alignment factor decreases with increasing q. This is consistent with the fact that the micelles are considered rigid at the length scale of the persistence length and out of the different length scales present in the wormlike micelle, the persistence length segments are oriented the most in flow.

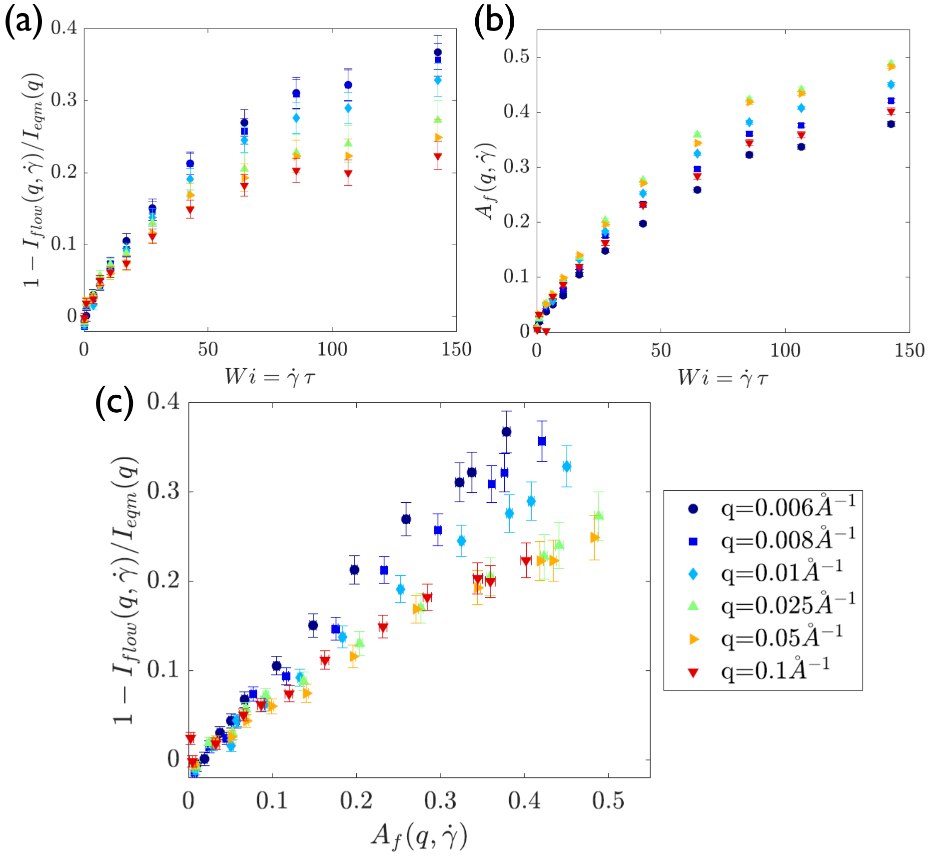

Figure 5.6: Parameterization of 2D SANS pattern for 60 mM CTAB in the $v - \nabla v$ plane (a) change in intensity as a function of Wi (b) degree of anisotropy (alignment factor) as a function of Wi (c) change in intensity vs alignment factor for different q values indicated in the legend to the right of the three plots.

Both parameterization methods described so far contain direct dependence on Wi. Physical interpretation of this data would therefore require a rheological model that would provide predictions for how the structure of the micelles depends on Wi. To circumvent this dependence and facilitate comparison between simulation and experiments which often have different (or sometimes unclear) definitions of the deformation rate and relaxation time, we introduce a new method of parameterization for the 2D scattering pattern. In Figure 5.6(c), we plot changes in intensity as a function of the degree of anisotropy, i.e., $1 - I_{flow}/I_{eqm}$ vs. A_f. In this representation, we can match the degree of anisotropy between experiments and simulations and compare the changes in intensity directly. In other words, this new representation removes the need to know the particular physics that causes alignment and enables more directly probing the potential changes in the micellar length. At the lowest q probed experimentally, the quantity $1 - I_{flow}/I_{eqm}$ scales linearly with the alignment factor and the slope is ~ 1 . Going from $q = 0.006$ Å^{-1} to $q = 0.01$ Å^{-1}, the relationship is still approximately linear but the slope decreases. At q larger than or equal to 0.025 Å^{-1}, which is the q value corresponding to the persistence length of the micelles, the relationship between $1 - I_{flow}/I_{eqm}$ and the alignment factor no longer shows any q dependence and the scaling becomes nonlinear. As we will see later when comparing the experimental results with the simulation results, the q-independence at $q \geq 0.025$Å^{-1} is an important feature. In this q range, we are probing length scales shorter than the persistence length of the micelles and the wormlike micelles are locally rigid. The change in the magnitude of the intensity is primarily caused by the alignment of the persistence length segments in flow, instead of effects of chain stretch and scission. Thus, the curves of $1 - I_{flow}/I_{eqm}$ as a function of the alignment factor don't show any q-dependence in this q range.

Before proceeding with comparing model predictions and experimental results, we first want to confirm if the q-dependent trends in the change in intensity versus alignment factor are general for the other surfactant concentrations we investigated. Thus, we performed a similar set of analyses for the 2D scattering data in the flow-flow gradient plane ($v - \nabla v$) for the 100 mM sample. Shown in Figure 5.7 are changes in the intensity plotted on the y-axis and alignment factor plotted on the x-axis for q-values ranging from 0.006Å^{-1} to 0.1Å^{-1}. We observe similar trends as those for the 60 mM sample. Namely, for q values larger than and equal to the q value (0.025Å^{-1}) corresponding to the persistence length, all of the data collapse onto one line. For $q < 0.025$Å^{-1}, the slope of changes in intensity vs. alignment factor increases as q decreases. As is shown in Appendix A, wormlike micelles are prone to elastic instabilities at high shear rates due to the curved streamline in concentric cylinder geometries. The onset of secondary flow, as is observed by flow visualization, corresponds to similar shear rates as those observed for the onset of the decrease of the alignment factor, which is at 65 s^{-1} for 100 mM CTAB and 1200 s^{-1} for 60 mM CTAB. As is discussed in Appendix A. although the decrease in the alignment factor with increasing shear rate can also be caused by flow-enhanced scission, the possible contribution of secondary flows makes the interpretation of the SANS data more challenging. Thus, for all of the analyses in this chapter, we only focus on the shear rate range prior to the alignment factor peak. Since the 60 mM CTAB sample allows probing of a larger shear rate range for homogeneous flow and the effect of entanglement and interchain interactions have less effect on the scattering intensity for this more dilute sample, for the subsequent comparison with connected-rod simulations at steady state, we will focus on the 60 mM sample.

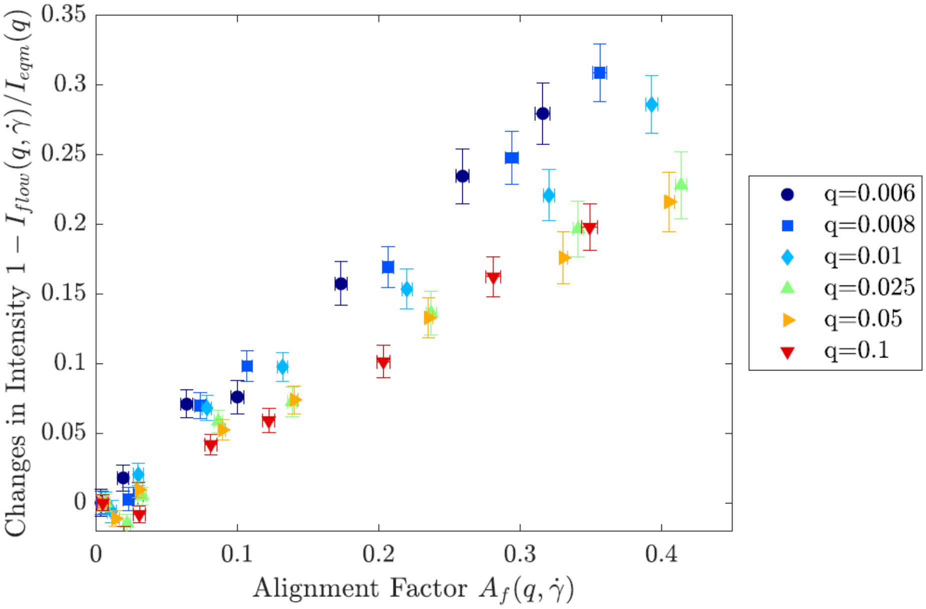

Figure 5.7: Change in intensity vs alignment factor for 100 mM CTAB wormlike micelle in the $v - \nabla v$ plane.

5.3.3 Predictions of the connected-rod model

In chapter 4, we introduced the connected-rod model for predicting scattering of semiflexible chains. We fit the polydisperse version of the model at equilibrium to the circularly averaged intensity of the equilibrium SANS experiment to obtain the average number of cylinders per chain $\bar{n}$, the cylinder radius r_{cyl}, the cylinder length L_{cyl}, β, the parameter that characterizes the strength of the inter-chain interactions in the structure factor, and the background intensity. Details of the fitting procedure are described in Section 4.3.1 in Chapter 4 and the fitting results are summarized in Table 5.2 below. We then use these parameters in the monodisperse model in flow to make flow-SANS predictions. We vary the value for the effective stretch from 0 to 0.8 in the predictions. A polydisperse version of the model was not used for the predictions in flow because doing so would require using a length-dependent effective stretch for the micelles of different lengths at a given shear rates, which requires additional model assumptions and may suffer from issues with robustness (i.e., too many degrees of freedom leading to unrealistic optima in the fitting routine). The initial, qualitative comparisons with 2D scattering and annular average (as shown in Chapter 4) demonstrate that the scattering model is able to capture the shape of the anisotropy in the scattering experiments. Here we use the new parameterization method we introduced in Sec. 5.3.2 to make a more quantitative comparison between experiments and the connected-rod model predictions. In Figure 5.8(a), we plot the changes in intensity on the y-axis and alignment factor on the x-axis for q values from 0.006Å^{-1} to 0.12Å^{-1} for both the experimental data (in filled symbols) and the simulation results (as curves). The model is able to capture both the magnitude of the change in intensity at a given degree of anisotropy and the q-dependent trends in the experimental results, namely, the q-dependent slope at low-q and the collapse of the data at mid to high-q. To better visualize the agreement between model and simulation, in Fig. 5.8(b) and (c) we plot the changes in intensity vs. alignment factor for low-q and mid to high-q, respectively, after vertically shifting the data for different q values. For most of the q values, nearly quantitative agreement is obtained between the model predictions and experiments. Some deviations between model predictions and experiments occur for $0.0158 \leq q \leq 0.025$Å^{-1}, which is potentially caused by the absence of polydispersity in the model prediction in flow. As is seen in Fig.4.2 in the previous chapter, the equilibrium polydisperse predictions show excellent agreement with experimental circular average while the monodisperse prediction has small deviations in the mid-q range.

Table 5.2: Parameters used in connected-rod model predictions.

$\overline{n}$	r_{cyl} (nm)	L_{cyl} (nm)	β	$Bkgd$ ($1/cm$)
4	2.3	43.1	3.11	0.065

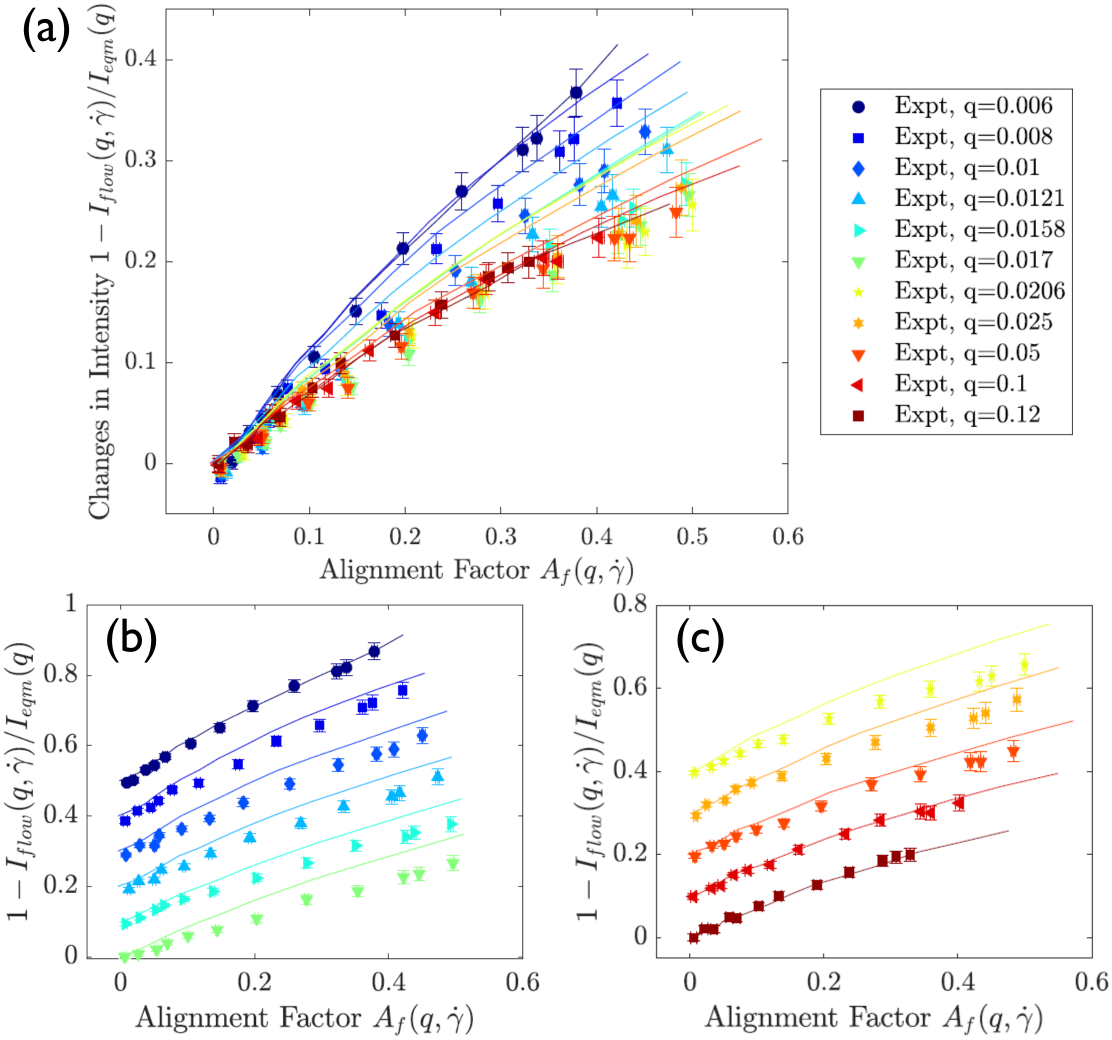

Figure 5.8: Compare connected-rod simulations and experiments for 60 mM CTAB in the $v - \nabla v$ plane for (a) $q = 0.006 - 0.012$Å^{-1} (b) $q = 0.006 - 0.017$Å^{-1} shifted vertically (c) $q = 0.0206 - 0.12$Å^{-1} shifted vertically. The experimental results are plotted as various filled symbols (as listed in the legend). For the same q value, the simulation results are plotted as curves with the same color as the experimental results.

At a given degree of anisotropy, the changes in the magnitude of the intensity compared to equilibrium intensity are potentially affected by orientation, chain stretching, interchain interactions (structure factor), and changes in chain length. The connected-rod model includes the first three effects, but not changes in chain length. To separate the effects of structure factor from the other contributions to the changes in intensity, we plot changes in intensity versus alignment factor for $0.006 < q < 0.12\text{Å}^{-1}$ for different β values in Figure 5.9, where β describes the strength of the interaction. Results for different β values are plotted in different colors, at the same β, the data for different q values are plotted in the symbols as described by the legend in Fig. 5.8. With increasing β, although the maximum of changes in intensity and alignment factor decreases due to the suppression of scattering intensity with stronger interchain-interactions, the spread of the data (i.e., for a given degree of anisotropy, the difference between the maximum in the change in intensity and the minimum in the change in intensity) remains unchanged. In the flow-SANS predictions using the connected-rod model, we assumed β is constant in flow and used the value for β from equilibrium fitting. Recent work on rod-like particles with electrostatic interactions in shear flow demonstrated that β stays constant for low and intermediate shear rates.[36] Thus, the decrease of the low-q intensity with increasing shear rate in the wormlike micelle experiments is unlikely to be due to changes in the structure factor.

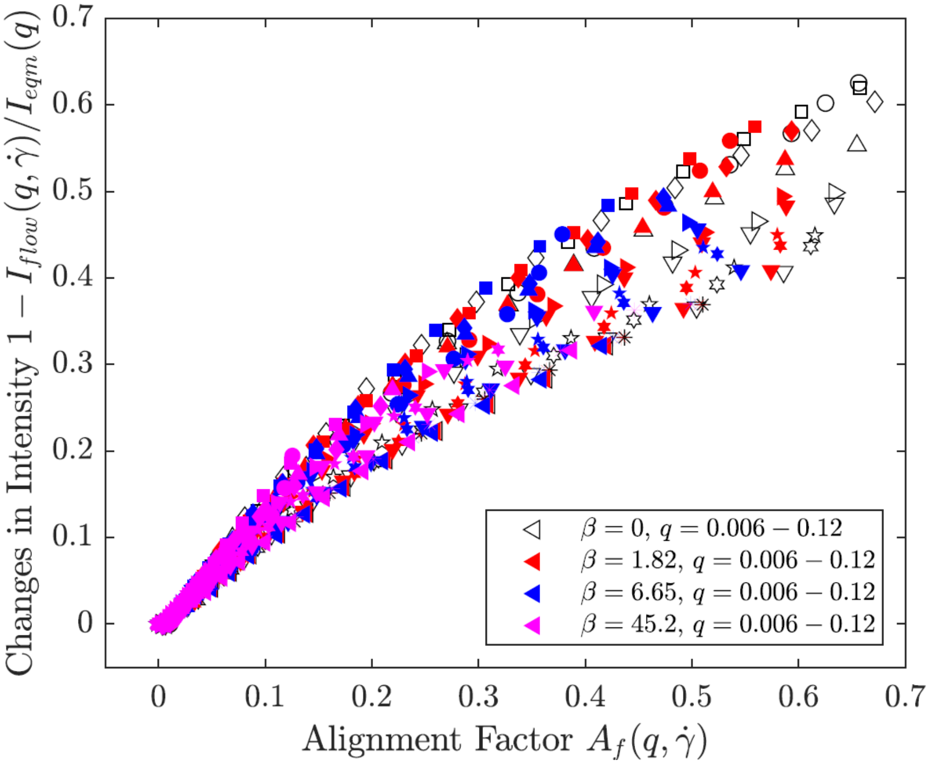

Figure 5.9: Effect of interaction strength on the magnitude of intensity and the alignment factor ($\beta = 0 - 45.2$). The symbols correspond to the same q values as those listed in the legend in Fig. 5.8.

Although the comparison in Fig. 5.8 enables more quantitative comparison between experiments and model predictions, this representation of the experimental data alone is not enough to probe the presence of flow-enhanced scission. This is because as micelles get shorter in flow, at a given shear rate, the relaxation time for the micelle becomes shorter. Thus, the local dimensionless shear rate for the micelle becomes smaller, making it more difficult the align the micelles in flow. In other words, when micelles become shorter, the relationship between the intensity ratio and the alignment factor will change. Thus, we decided to more directly probe the kinetics of microstructural changes of wormlike micelles in flow and be more conclusive about the presence or absence of flow-enhanced scission by using time-resolved flow-SANS measurements.

5.3.4 Time-resolved flow-SANS

We conducted time-resolved flow-SANS experiments both in the $v - \nabla v$ plane using the shear cell and in the $v - \omega$ plane using the rheometer. For these studies, the 100 mM CTAB sample was used because the larger concentration and longer micelles give better signal to noise ratio and enables better statistics in the time-resolved SANS measurements. The sample temperature was kept at 25 °C. For each shear rate measured ($5\,s^{-1}$, $15\,s^{-1}$, $40\,s^{-1}$ and $65\,s^{-1}$), the cycle consisted of 5 seconds of flow start-up and 10 seconds of flow cessation. In order to achieve enough statistics, the cycle was repeated ∼330 times in the rheometer and ∼600 times in the shear cell. The scattering intensity is binned into 150 bins for the 15 s cycle. For the 2D scattering intensity in each bin, we calculated the alignment factor, A_f and the ratio of intensity $1 - I_{flow}\left(q, \dot{\gamma}\right)/I_{eqm}\left(q\right)$ using the methods described in Sec. 5.3.2. As an example, we plot the alignment factor and the ratio of intensity as a function of time for $\dot{\gamma} = 15s^{-1}$ and $q = 0.008$Å^{-1} in Fig. 5.10 (a). Upon the start up of flow, both A_f and $1 - I_{flow}\left(q, \dot{\gamma}\right)/I_{eqm}\left(q\right)$ increase with time, which indicate the scattering becomes more anisotropic and the magnitude of the circularly averaged intensity decreases. Both quantities exhibit an overshoot, which is occurring in a similar manner as an overshoot in the stress that is typical of entangled wormlike micelles and polymers. Between time = 2 s to 5 s, the microstructural changes reach a steady state, thus both A_f and $1 - I_{flow}\left(q, \dot{\gamma}\right)/I_{eqm}\left(q\right)$ reach a plateau. Upon flow cessation, both A_f and $1 - I_{flow}\left(q, \dot{\gamma}\right)/I_{eqm}\left(q\right)$ decrease with time, which indicate the scattering intensity becomes less anisotropic and the circularly averaged intensity increases. After ∼2 s, both quantities approach 0, the equilibrium value. To compare the timescale of relaxation for A_f and $1 - I_{flow}\left(q, \dot{\gamma}\right)/I_{eqm}\left(q\right)$, we fitted an exponential function $f(t) = a * \exp\left(t/\tau_{tr}\right)$ to the data during flow-cessation. τ_{tr} is the relaxation time. Shown in Fig.5.10(b) and (c) are comparisons of the fit with experimental data. In order to better visualize the quality of the fit, we plotted both A_f and $1 - I_{flow}\left(q,\dot{\gamma}\right)/I_{eqm}\left(q\right)$ on a log scale and time on a linear scale. A straight line on this semi-log plot is indicative of an exponential dependence on time. Since the error bars are also plotted on a log-scale, they appear to be quite large at longer times as both A_f and $1 - I_{flow}\left(q,\dot{\gamma}\right)/I_{eqm}\left(q\right)$ tend towards zero. However, the magnitude of the error at these longer times is comparable to the error at shorter times.

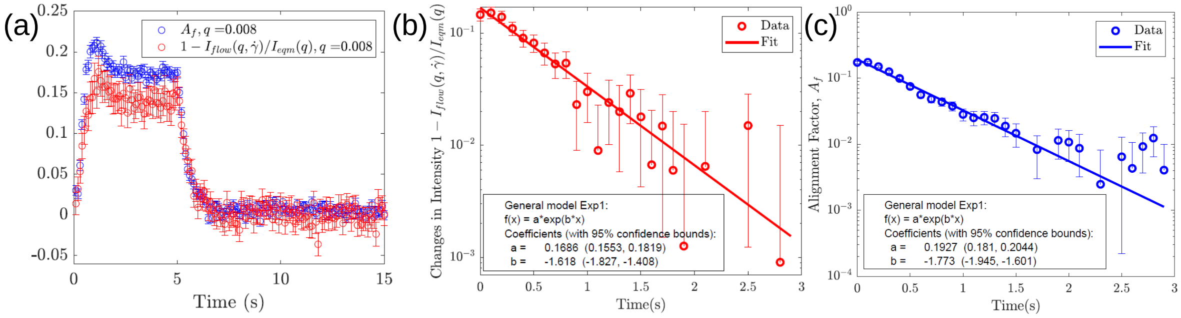

Figure 5.10: (a)Transient-SANS at $\dot{\gamma} = 15\,s^{-1}, q = 0.008$ Å^{-1} for 5 s startup and 10 s flow cessation (b) exponential fitting of changes in intensity after flow cessation (time 5 s - 8 s) (c) exponential fitting of alignment factor after flow cessation (time 5 s - 8 s).

For the 100 mM CTAB sample, we conducted time-resolved flow-SANS measurements at $\dot{\gamma} = 5\,s^{-1}, 15\,s^{-1}, 40\,s^{-1}, \text{and}\, 65\,s^{-1}$. The longest relaxation time identified from linear viscoelastic measurement is 0.52 s. At $\dot{\gamma} = 5\,s^{-1}$, the Weissenberg number is only 2.2. Thus, the scattering pattern only differs slightly from the isotropic scattering pattern at equilibrium. As a result, both A_f and $1 - I_{flow}\left(q,\dot{\gamma}\right)/I_{eqm}\left(q\right)$ are close to zero (with a maximum in 0.04 for both A_f and $1 - I_{flow}\left(q,\dot{\gamma}\right)/I_{eqm}\left(q\right)$). The fitting is very noisy and the resulting relaxation time has a very large error bar. Thus, we exclude the relaxation time obtained at $5\,s^{-1}$ in subsequent analysis.

In Fig. 5.11, we compare the relaxation time τ_{tr} from the exponential fitting of both A_f and $1 - I_{flow}\left(q,\dot{\gamma}\right)/I_{eqm}\left(q\right)$ at (a) $q = 0.008$Å^{-1}, $q = 0.01$Å^{-1}, and $q = 0.025$Å^{-1} for all three shear rates investigated ($\dot{\gamma} = 15\,s^{-1}, 40\,s^{-1}, 65\,s^{-1}$). The $15 s^{-1}$ data come from experiments in the flow-gradient ($v - \nabla v$) plane and the $40\,s^{-1}$ and $65\,s^{-1}$ data are form experiments in the flow-vorticity ($v - \omega$) plane. Results for $15\,s^{-1}$ are similar in the $v - \nabla v$ plane and in the $v - \omega$. Since the results in the $v - \nabla v$ have better signal to noise ratio, we used this measurement for $15s^{-1}$. The relaxation times are also listed in Table. 5.3. The relaxation times determined from time-resolved SANS are plotted as a function of the dimensionless shear rate, Weissenberg number, on the bottom x-axis. The Weissenberg number is defined as the product of the longest relaxation time τ from the linear viscoelastic measurement and the applied shear rate: $Wi = \tau\dot{\gamma}$. On the top x-axis, we indicate the corresponding breakage-Weissenberg number, i.e., the product of the breakage time and the applied shear rate, $Wi_{br} = \tau_{br}\dot{\gamma}$. For a more direct comparison between the relaxation time from the linear viscoelastic (LVE) measurement and the time-resolved SANS experiment, we plot the longest relaxation time from LVE as a black dashed line in Fig. 5.11(a), (b), and (c).

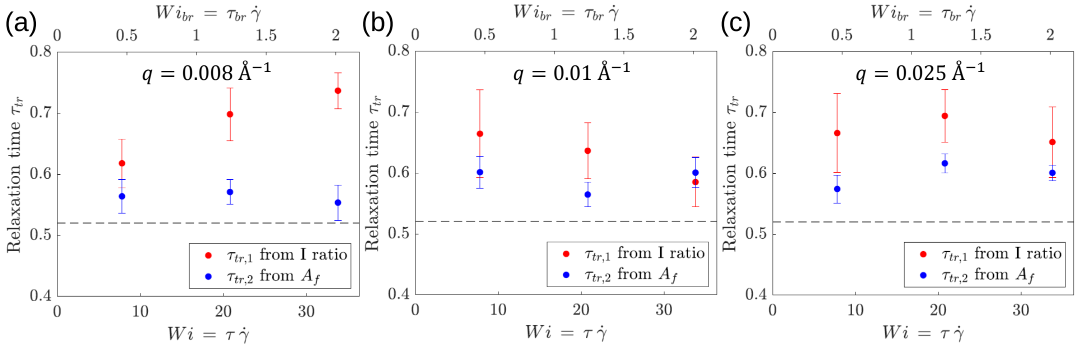

Figure 5.11: Relaxation time for intensity ratio and alignment factor after flow cessation as a function of shear rate for (a) $q = 0.008$ Å^{-1}, (b) $q = 0.01$ Å^{-1}, (c) $q = 0.025$ Å^{-1}. The bottom x-axis uses the shear rate scaled by the longest relaxation time ($Wi = \tau\dot{\gamma}$). The top x-axis uses the shear rate scaled by the breakage time ($Wi_{br} = \tau_{br}\dot{\gamma}$). The horizontal dotted line in each figure denotes the longest relaxation time ($\tau = 0.52\,s$) estimated from the linear viscoelastic measurement.

Table 5.3: Relaxation times from exponential fit of flow cessation in time-resolved SANS experiment

q (Å^{-1})	Shear rate $\dot{\gamma}$ (s^{-1})	$\tau_{tr,1}$ for $1 - I_{flow}(q,\dot{\gamma})/I_{eqm}(q)$	$\tau_{tr,2}$ for A_f
0.008	15	**0.62(±0.04)**	**0.56(±0.03)**
	40	**0.70(±0.04)**	**0.57(±0.02)**
	65	**0.74(±0.03)**	**0.55(±0.03)**
0.01	15	0.66(±0.07)	0.60(±0.03)
	40	0.64(±0.05)	0.56(±0.02)
	65	0.59(±0.04)	0.60(±0.03)
0.025	15	0.67(±0.06)	0.57(±0.02)
	40	0.69(±0.04)	0.62(±0.02)
	65	0.65(±0.06)	0.60(±0.01)

An important feature in the relaxation times is the larger relaxation time of the intensity ratio, $\tau_{tr,1}$, compared to the relaxation time of the alignment factor,$\tau_{tr,2}$, at the lowest q value investigated ($q = 0.008$Å^{-1}). The relaxation time of the alignment factor is associated with the relaxation of the orientation of the micelles upon flow cessation, thus, the relaxation time of the alignment factor,$\tau_{tr,2}$, is similar in magnitude to the longest relaxation time, τ, from LVE.

The scattering intensity of wormlike micelles in flow can be affected by several factors, namely, chain orientation, chain stretch, changes in inter-chain interactions (structure factor), and chain scission. When a chain relaxes its orientation, both the scattering anisotropy and the magnitude of intensity relax towards the equilibrium values. Thus, if relaxation of orientation were the only relaxation mechanism, we would expect the relaxation time for the intensity ratio and the alignment factor to be the same. The larger relaxation time for the intensity ratio suggests that additional relaxation mechanisms affect the magnitude of the intensity, but not the anisotropy. Assuming the Random Phase Approximation (RPA) is a good model for the anisotropic structure factor (as was used in Chapter 4 and in the model predictions in this chapter), then the structure factor should evolve over an identical time scale as the alignment because the anisotropic form factor appears in the expression for the structure factor. Therefore, changes in intermicellar interactions during flow cessation do not explain the observed longer time scale for the magnitude of the intensity and its dependence on shear rate. Furthermore, micelle stretching only has a small contribution to the changes in the scattering intensity. This is because at low shear rates, the micelles are not significantly stretched; whereas at higher shear rates, when micelles stretch, they can be subjected to flow-enhanced scission and relax the stress locally.[37]

Given the proceeding discussion, we hypothesize that the longer relaxation time for the magnitude of the intensity and its dependence on shear rate are due to recombination of micelles during the flow cessation. Namely, the micelles likely relax their orientation before the equilibrium length is re-established. Therefore, the recombination process continues even after the orientation has relaxed to equilibrium. This additional relaxation mechanism results in the slower relaxation for the intensity ratio. Furthermore, we observe the difference between the relaxation time for the intensity ratio and A_f increases with increasing shear rate at the lowest-q value investigated. In other words, although the relaxation time for A_f stays relatively constant across shear rates at $q = 0.008$Å^{-1}, the relaxation time for $1 - I_{flow}(q, \dot{\gamma})/I_{eqm}(q)$ continues to increase with increasing shear rate. This suggests that micellar recombination during flow cessation has a bigger contribution at larger shear rates.

5.4 Discussion

Here we will examine the results presented in the last section more closely and discuss what the results suggest for flow-enhanced scission of wormlike micelles. In previous temperature-jump studies,[38] a perturbation of temperature (a jump up in temperature) is added to a wormlike micelle solution at equilibrium, which results in a decrease in the equilibrium average length. Light scattering measurements were used to monitor the relaxation of the new average length as a function of time. It was found that the relaxation time equals $\tau_{br}/2$. We observe that the relaxation time of the intensity ratio is much longer than $\tau_{br}/2$. Therefore, if this result were indicative of relaxation of flow-induced scission, recombination of micelles after flow cessation would need to take much longer than micellar breakage at equilibrium. However, this could easily be the case due to the changes in orientation and stretch of the micelles that is present in flow but absent upon a temperature jump.

We estimated that the breakage time (as estimated from LVE) is τ_{br} is 0.031 s for 100 mM CTAB at 25 °C. For $\dot{\gamma} > 1/\tau_{br} \approx 35s^{-1}$, the applied shear will induce the breakdown of micelles at a faster rate than the thermodynamic micelle breakage. Thus, with increasing shear rate beyond $35\, s^{-1}$, we expect the average micelle length when the flow reaches steady state to decrease with increasing shear rate. The remaining question is how can we relate the observation of the trends in the relaxation times during flow cessation to microstructural changes of the micelles in flow.

In entangled polymer systems, the free ends of any chain are often approximated as stress-free (neither aligned nor stretched), in which case it would not be possible for an imposed flow to affect the kinetics of end recombination. For dilute, unentangled rodlike micelles, one cannot neglect flow-induced alignment effects at chain ends.[8,39,40] In fact, for dilute, rodlike micelles, flow-induced alignment produces shear thickening and flow-induced structures.[41,42] For the 100 mM CTAB sample investigated here, the average number of entanglements is 8 per chain and the wormlike micelle solution is in the semi-dilute regime, thus we can approximate the micellar chain ends as stress-free. Therefore, we can assume the rate constant for the end recombination is always at its equilibrium value and is independent of the length for either species involved in the recombination. This is the approach that was taken in the recently published Living Rolie Poly (LRP) model by Peterson and Leal.[37] After flow cessation, since the effect of flow is absent, we also expect the breakage rate to be at its equilibrium value. So why would the relaxation time for the intensity ratio $(1 - I_{flow}/I_{eqm})$ increase with increasing shear rate? The answer lies in the changes in the microstructures during the steady flow (i.e., at the end of flow start-up, before flow cessation). Although the rate of recombination does not depend on the flow rate, if the micelles are much shorter before the start of flow cessation than the equilibrium micelle length, *more* recombination events are needed before the micelle length distribution can relax back to its equilibrium value. The shorter the micelles are, the longer it will take for the intensity to relax back to equilibrium. Thus, the increase of the relaxation time of the intensity ratio suggests the micelles are getting shorter with increasing shear rates in flow.

If the increase in the relaxation time of the intensity ratio with increasing shear rate for $q = 0.008$Å^{-1} is indeed due to flow-enhanced scission in flow prior to flow cessation, we need to understand why the shear rate-dependence is only observed at $q = 0.008$Å^{-1} but not at higher q-values. We again utilize predictions from the connected-rod model. For the simplest case, if we have monodisperse chains at equilibrium, as the chain length decreases, equivalently, as the number of Kuhn length (cylinders) decreases, the scattering intensity decreases the most at low-q, while at q values closer to the inverse of the Kuhn length and persistence length ($q = 0.0125$Å^{-1} and $q = 0.025$Å^{-1}, respectively), the intensity stays relatively constant. This effect is shown in Figure 5.12, in which we plot circularly average intensity as a function of q for chains with 4 cylinders, 3 cylinders, and 2 cylinders. Similarly, in a polydisperse system, as the average length decreases, we also expect to see the most decrease in the intensity at low-q. In summary, the larger relaxation time for the intensity ratio than the alignment factor and the increase of the relaxation time for the intensity ratio with increasing shear rate observed in flow-cessation experiments are consistent with a net-shortening of wormlike micelles in flow.

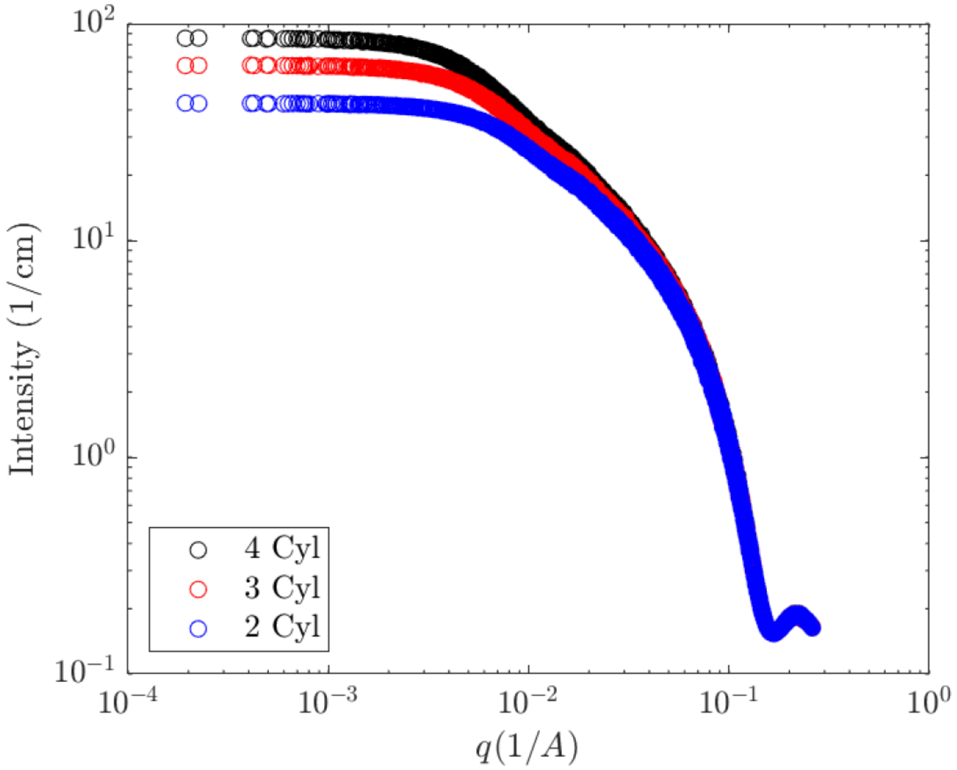

Figure 5.12: Investigate the q-dependence of scattering intensity upon micelle scission by comparing equilibrium intensity for different numbers of cylinders using the connected-rod model.

5.5 Conclusions

In this work, we conducted steady state and time-resolved flow-small angle neutron scattering experiments on linear, weakly entangled wormlike micelles in homogeneous shear flow to identify potential signatures of flow-enhanced micellar scission. The monotonic decrease of circular average intensity with increasing shear rate is consistent with the net shortening of wormlike micelles. To distinguish effects of chain scission from effects of chain stretch, orientation, and interchain interactions in flow, we compared the experimental results with the connected-rod model that we recently developed. To facilitate the comparison between simulation and experiments, we developed a novel approach of parameterizing circular averaged intensity and the degree of anisotropy to fingerprint how changes in orientation and structure contribute to changes in the scattering intensity. This new parameterization method will also be useful for analyzing anisotropic scattering of other types of deformable materials, such as polymers and polyelectrolytes, in flow.

Detailed analysis of time-resolved measurements enables identification of different relaxation time scales for the changes in the magnitude of the intensity and the relaxation of the scattering anisotropy during flow cessation. Differences in the magnitude and shear-rate dependence of the relaxation times of the magnitude of the intensity and the degree of anisotropy suggest flow-enhanced scission of wormlike micelles. Specifically, for both shear rate = $40s^{-1}$ and $65s^{-1}$, the relaxation time of the intensity ratio is larger than the relaxation time of the alignment factor. Furthermore, the relaxation time of the intensity ratio at low-q increases with increasing shear rate. Both observations suggest flow-enhanced scission of wormlike micelles during steady flow prior to the start of flow-cessation.

To our knowledge, this is the first time such detailed analysis of flow-SANS experiments has been performed to obtain information about changes in micelle length in flow. The evidence for flow-enhanced micellar scission will help inform the development of more accurate rheological models for wormlike micelles and the experimental, modeling, and analysis methods will find broad applications in other types of deformable materials in flow.

Bibliography

[1] Ezrahi S, Tuval E, Aserin A. Properties, main applications and perspectives of worm micelles. *Advances in colloid and interface science.* 2006; 128: 77–102.

[2] Cates M. Reptation of living polymers: dynamics of entangled polymers in the presence of reversible chain-scission reactions. *Macromolecules.* 1987; 20(9): 2289–2296.

[3] Cates M, Candau S. Statics and dynamics of worm-like surfactant micelles. *Journal of Physics: Condensed Matter.* 1990; 2(33): 6869.

[4] Helgeson ME, Hodgdon TK, Kaler EW, Wagner NJ. A systematic study of equilibrium structure, thermodynamics, and rheology of aqueous ctab/nano3 wormlike micelles. *Journal of colloid and interface science.* 2010; 349(1): 1–12.

[5] Chen WR, Butler PD, Magid LJ. Incorporating intermicellar interactions in the fitting of sans data from cationic wormlike micelles. *Langmuir.* 2006; 22(15): 6539–6548.

[6] Cates M. Nonlinear viscoelasticity of wormlike micelles (and other reversibly breakable polymers). *Journal of Physical Chemistry.* 1990; 94(1): 371–375.

[7] Vasquez PA, McKinley GH, Cook LP. A network scission model for wormlike micellar solutions: I. model formulation and viscometric flow predictions. *Journal of non-newtonian fluid mechanics.* 2007; 144(2-3): 122–139.

[8] Dutta S, Graham MD. Mechanistic constitutive model for wormlike micelle solutions with flow-induced structure formation. *Journal of Non-Newtonian Fluid Mechanics.* 2018; 251: 97–106.

[9] Rothstein JP, Mohammadigoushki H. Complex flows of viscoelastic wormlike micelle solutions. *Journal of Non-Newtonian Fluid Mechanics.* 2020: 104382.

[10] Rothstein JP. Transient extensional rheology of wormlike micelle solutions. *Journal of Rheology.* 2003; 47(5): 1227–1247.

[11] Bhardwaj A, Miller E, Rothstein JP. Filament stretching and capillary breakup extensional rheometry measurements of viscoelastic wormlike micelle solutions. *Journal of Rheology.* 2007; 51(4): 693–719.

[12] Bhardwaj A, Richter D, Chellamuthu M, Rothstein JP. The effect of pre-shear on the extensional rheology of wormlike micelle solutions. *Rheologica acta.* 2007; 46(6): 861–875.

[13] Chen S, Rothstein JP. Flow of a wormlike micelle solution past a falling sphere. *Journal of Non-Newtonian Fluid Mechanics.* 2004; 116(2-3): 205–234.

[14] Mohammadigoushki H, Muller SJ. Sedimentation of a sphere in wormlike micellar fluids. *Journal of Rheology.* 2016; 60(4): 587–601.

[15] Liberatore MW, Nettesheim F, Vasquez PA, et al. Microstructure and shear rheology of entangled wormlike micelles in solution. *Journal of Rheology.* 2009; 53(2): 441–458.

[16] Pedersen JS, Cannavacciuolo L, Schurtenberger P. Scattering from wormlike micelles. In *Giant Micelles* 179–222 CRC Press 2007.

[17] Walker LM. Scattering from polymer-like micelles. *Current opinion in colloid & interface science.* 2009; 14(6): 451–454.

[18] Hayter JB, Penfold J. Use of viscous shear alignment to study anisotropic micellar structure by small-angle neutron scattering. *The Journal of Physical Chemistry.* 1984; 88(20): 4589–4593.

[19] Pedersen JS, Schurtenberger P. Scattering functions of semiflexible polymers with and without excluded volume effects. *Macromolecules.* 1996; 29(23): 7602–7612.

[20] Pedersen JS, Schurtenberger P. Scattering functions of semidilute solutions of polymers in a good solvent. *Journal of Polymer Science Part B: Polymer Physics.* 2004; 42(17): 3081–3094.

[21] Calabrese MA, Wagner NJ. New insights from rheo-small-angle neutron scattering. In *Wormlike Micelles* 193–235 2017.

[22] Helgeson ME, Reichert MD, Hu YT, Wagner NJ. Relating shear banding, structure, and phase behavior in wormlike micellar solutions. *Soft Matter.* 2009; 5(20): 3858–3869.

[23] Helgeson ME, Vasquez PA, Kaler EW, Wagner NJ. Rheology and spatially resolved structure of cetyltrimethylammonium bromide wormlike micelles through the shear banding transition. *Journal of Rheology.* 2009; 53(3): 727–756.

[24] Chen CM, Warr GG. Light scattering from wormlike micelles in an elongational field. *Langmuir.* 1997; 13(6): 1374–1376.

[25] Weston JS, Seeman DP, Blair DL, Salipante PF, Hudson SD, Weigandt KM. Simultaneous slit rheometry and in situ neutron scattering. *Rheologica Acta.* 2018; 57(3): 241–250.

[26] Jiang N, Li P, Wang Y, Wang J, Yan H, Thomas RK. Aggregation behavior of hexadecyltrimethylammonium surfactants with various counterions in aqueous solution. *Journal of colloid and interface science.* 2005; 286(2): 755–760.

[27] Hu YT, Lips A. Kinetics and mechanism of shear banding in an entangled micellar solution. *Journal of Rheology.* 2005; 49(5): 1001–1027.

[28] Gurnon AK, Godfrin PD, Wagner NJ, Eberle AP, Butler P, Porcar L. Measuring material microstructure under flow using 1-2 plane flow-small angle neutron scattering. *JoVE (Journal of Visualized Experiments).* 2014(84): e51068.

[29] Kline SR. Reduction and analysis of sans and usans data using igor pro. *Journal of applied crystallography.* 2006; 39(6): 895–900.

[30] Schubert BA, Kaler EW, Wagner NJ. The microstructure and rheology of mixed cationic/anionic wormlike micelles. *Langmuir.* 2003; 19(10): 4079–4089.

[31] Granek R, Cates M. Stress relaxation in living polymers: Results from a poisson renewal model. *The Journal of chemical physics.* 1992; 96(6): 4758–4767.

[32] MacKintosh F, Safran S, Pincus P. Self-assembly of linear aggregates: the effect of electrostatics on growth. *EPL (Europhysics Letters).* 1990; 12(8): 697.

[33] MacKintosh F, Safran S, Pincus P. Equilibrium size distribution of charged'living'polymers. *Journal of Physics: Condensed Matter.* 1990; 2(S): SA359.

[34] Picken SJ, Aerts J, Visser R, Northolt MG. Structure and rheology of aramid solutions: X-ray scattering measurements. *Macromolecules.* 1990; 23(16): 3849–3854.

[35] Walker LM, Wagner NJ. Sans analysis of the molecular order in poly (γ-benzyl l-glutamate)/deuterated dimethylformamide (pblg/d-dmf) under shear and during relaxation. *Macromolecules.* 1996; 29(6): 2298–2301.

[36] Corona PT. *Probing nanostructure and rheology of complex fluids in complex flow histories using small angle scattering.* PhD thesisUC Santa Barbara 2020.

[37] Peterson JD, Gary Leal L. Predictions for flow-induced scission in well-entangled living polymers: The "living rolie-poly" model. *Journal of Rheology.* 2021; 65(5): 959-982.

[38] Candau S, Merikhi F, Waton G, Lemaréchal P. Temperature-jump study of elongated micelles of cetyltrimethylammonium bromide. *Journal de Physique.* 1990; 51(10): 977–989.

[39] Turner MS, Cates ME. Brownian motion of rod-like micelles under flow. *Journal of the Chemical Society, Faraday Transactions.* 1991; 87(13): 2073–2078.

[40] Hommel RJ, Graham MD. Constitutive modeling of dilute wormlike micelle solutions: Shear-induced structure and transient dynamics. *Journal of Non-Newtonian Fluid Mechanics.* 2021: 104606.

[41] Dehmoune J, Decruppe JP, Greffier O, Xu H. Rheometric and rheo-optical investigation on the effect of the aliphatic chain length of the surfactant on the shear thickening of dilute worm-like micellar solutions. *Rheologica acta.* 2007; 46(8): 1121–1129.

[42] Liu Ch, Pine D. Shear-induced gelation and fracture in micellar solutions. *Physical review letters.* 1996; 77(10): 2121.

Chapter 6

Modeling scattering of dilute, flexible polymers in flow

This chapter summarizes the work to-date of a new project I helped with in the last year of my PhD. The current work is in collaboration with first-year graduate student Anukta Datta in our group and the Brownian Dynamics simulation is done by Professor Patrick Underhill's group at RPI. I derived the theoretical predictions in section 6.2 and developed the codes for predicting the scattering. Anukta ran the scattering simulations and analyzed the simulation results. Future work on this project in our group will be carried out by Anukta.

6.1 Goal and approach

This work aims to provide new, molecular-scale understanding for how polymer topology influences molecular deformation and scission at extreme rates in dilute solutions, which is a problem with important implications for processes and technologies spanning lubrication, drag reduction, enhanced oil recovery and inkjet printing. To do so, we will utilize a new experimental technique, capillary rheoSANS,[1] which enables neutron scattering measurements at shear rates exceeding 10^6 s^{-1}. We will integrate the experiments with molecular simulation approaches to quantify and provide mechanistic insight into the internal distribution of dynamics in polymer chains.

As a first step, we aim to develop scattering theories and forward and inverse calculation methods, i.e., to calculate scattering from known molecular configuration distribution and estimate a distribution of molecular configurations from a scattering pattern. This will be the focus of the current chapter.

6.2 Theory

6.2.1 Dumbbells in shear flow

First, we model the scattering of dilute linear polymer chains as two infinitesimal beads of constant scattering length connected by an elastic spring with the same scattering length density as the solvent (Fig. 6.1). This situation is the scattering equivalent of the elastic bead-spring dumbbell model used to model polymer stretch and implicitly assumes that the distribution of scattering density in the polymer is proportional to the end-to-end vector probability distribution function from an elastic dumbbell model. We consider this assumption to be approximately valid in the Guinier regime ($qR_g \sim 1$, where q is the scattering wave vector and R_g is the radius of gyration of the entire chain), where scattering contributions from finer-scale chain conformations are negligible. This approach was first proposed by Patrick Corona in our research group and we extended the theoretical approach in our work.

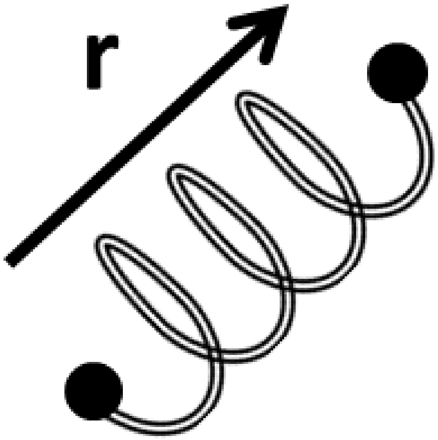

Figure 6.1: Pictorial representation of the combined micromechanical and scattering model for dilute polymer chains in flow. The black beads at the end of the spring are point sources of scattering density and hydrodynamic drag, which are enlarged in this picture to finite size, and are subject to thermal fluctuations. The spring connecting the two beads (outlined with a black line) has a scattering length density matching the surrounding solvent and a Hookean spring constant. The vector describing the separation of the chain ends ($\mathbf{r}$) completely describes the chain's conformation in this model.

The scattering from polymer chains is related to correlations between segments of the chain. In general, the coherent scattering is calculated as

$$I(\mathbf{q}) = \frac{I_0}{n^2} \sum_{j,k}^{n} \int \exp\left(-i\mathbf{q} \cdot \mathbf{r}_{jk}\right) \psi_{jk}\left(r_{jk}\right) d\mathbf{r}_{jk} \tag{6.1}$$

where I_0 is a constant prefactor related to the scattering density contrast in the system, n is the number of scattering points considered, $\mathbf{r}_{jk}$ is the vector describing the separation between the j^{th} and k^{th} scattering point, and $\psi_{jk}(\mathbf{r}_{jk})$ is the conformation distribution function describing the probability of finding scatterers j and k a separation distance of $\mathbf{r}$ apart.[2] This expression does not consider correlations between two polymer chains, for which one would also need to incorporate an inter-chain structure factor. Since the system considered in this work is dilute polymers, in which the chains are far apart from each other, we do not need to include the structure factor. We can factor out the "self" contributions to the scattering to get

$$I(\mathbf{q}) = \frac{I_0}{n^2}\left(n + \sum_{j,k\neq j}^{n}\int \exp\left(-i\mathbf{q}\cdot\mathbf{r}_{jk}\right)\psi_{jk}\left(\mathbf{r}_{jk}\right)d\mathbf{r}_{jk}\right). \tag{6.2}$$

First, we will consider the situation in Figure 6.1 where $n = 2$ and the conformation distribution between the two points is described by a Hookean dumbbell model. Simplifying the expression for $n = 2$ yields

$$I(\mathbf{q}) = \frac{I_0}{2}\left(1 + \int \exp\left(-i\mathbf{q}\cdot\mathbf{r}\right)\psi(\mathbf{r})d\mathbf{r}\right) \tag{6.3}$$

where $\mathbf{r}$ is the vector describing the separation between the beads, and $\psi(\mathbf{r}) = \psi_{12}\left(\mathbf{r}_{12}\right) = \psi_{21}\left(\mathbf{r}_{21}\right)$ is the conformation distribution function of the probability (PDF) that the chain ends are located at a separation distance $\mathbf{r}$. Furthermore, $\psi(\mathbf{r})$ is normalized such that $\int \psi(\mathbf{r})d\mathbf{r} = 1$. Again, this expression is only valid in the low-$\mathbf{q}$ regime such that scattering due to intra-chain correlations do not contribute to the scattering intensity. The determination of conformation distribution functions for dilute polymer solutions has been explored extensively, as discussed in Chapter 3. Here, we will consider the situation where analytical progress can be made for polymer solutions in flow.

For the situation of two thermal beads connected with a Hookean spring in a homogeneous flow field (see Fig. 6.1), the conformation distribution function can be solved analytically for arbitrary flow histories as

$$\psi\left(\mathbf{r},t\right) = \frac{\left(H/2\pi k_B T\right)^{3/2}}{\sqrt{\det\alpha}}\exp\left[-\left(H/2k_B T\right)\left(\boldsymbol{\alpha}^{-1}:\mathbf{rr}\right)\right], \tag{6.4}$$

$$\boldsymbol{\alpha} = \boldsymbol{\delta} - \frac{1}{\tau_H}\int_{-\infty}^{t} e^{-(t-t')/\tau_H}\left(\boldsymbol{\delta} - \mathbf{B}\left(t',t\right)\right)dt', \tag{6.5}$$

where H is the Hookean spring constant, τ_H is the Hookean spring's relaxation time, $\boldsymbol{\delta}$ is the identity tensor, and $\mathbf{B}$ is the Finger strain tensor.[3]

For a Hookean dumbbell, we have the following relationship between the radius of gyration and the spring constant:

$$R_{g,eqm}^2 = \frac{3k_BT}{4H}. \tag{6.6}$$

Thus, we can rewrite Eqn. 6.4 as:

$$\psi\left(\mathbf{r},t\right) = \frac{\left(3/8\pi R_{g,eqm}^2\right)^{3/2}}{\sqrt{\det\alpha}}\exp\left[-\frac{3}{8R_{g,eqm}^2}\boldsymbol{\alpha}^{-1}:\mathbf{rr}\right]. \tag{6.7}$$

For steady simple shear flow, the conformation distribution function reduces to

$$\psi\left(x,y,z\right) = \frac{\left(3/8\pi R_{g,eqm}^2\right)^{3/2}}{\sqrt{1+Wi^2}}\exp\left[\frac{3\left(x^2-2Wixy+\left(1+2Wi^2\right)y^2+\left(1+Wi^2\right)z^2\right)}{8R_{g,eqm}^2\left(1+Wi^2\right)}\right] \tag{6.8}$$

where x, y, z are the coordinates of $\mathbf{r}$ in the flow, flow-gradient, and vorticity directions respectively and $Wi = \tau_H\dot{\gamma}$ is the Weissenberg number where $\dot{\gamma}$ is the shear rate. Using this conformation distribution function in Eqn. 6.3 for the scattering intensity yields

$$I(\mathbf{q}) = \frac{I_0}{2}\left(1+\exp\left[\frac{-2R_{g,eqm}^2\left(q_x^2\left(1+2Wi^2\right)+2Wiq_xq_y+q_y^2+q_z^2\right)}{3}\right]\right), \tag{6.9}$$

where q_x, q_y, q_z are the scattering vectors in the flow, flow-gradient, and vorticity directions, respectively. This is the Guinier-Dumbbell model under steady simple shear flow.

As we will discuss in the results section, to connect between simulations and experiments, a more useful formulation of the model is to write the scattering intensity in terms of components of the gyration tensor, which are readily available from Brownian dynamics simulations, rather than the Weissenberg number. To do so, we first evaluate the components of the gyration tensor by taking the second moment of the configuration distribution function ψ. For example, for the xx-component of the gyration tensor, we have

$$S_{xx} = \langle R_g R_g \rangle_{xx} = \frac{1}{4}\int_{-\infty}^{\infty}\int_{-\infty}^{\infty}\int_{-\infty}^{\infty} xx\psi dxdydz = \frac{1}{3}R_{g,eqm}^2 \alpha_{xx}, \tag{6.10}$$

where α_{xx} is the xx-component of the $\boldsymbol{\alpha}$ that appears in Eqn. 6.7. After doing similar calculations for the other non-zero components of the gyration tensor, we find that all of the gyration tensor components are related to the respective components of the $\boldsymbol{\alpha}$ tensor. So, we can solve for the components of $\boldsymbol{\alpha}$ in terms of the gyration tensor components. In general, we obtain:

$$\boldsymbol{\alpha} = \frac{3}{R_{g,eqm}^2}\boldsymbol{S} \tag{6.11}$$

where $\boldsymbol{S}$ represents the gyration tensor.

Using Eqn. 6.11 in Eqn. 6.7 for $\boldsymbol{\alpha}$, we obtain the configuration distribution function written in terms of components of the gyration tensor:

$$\psi = \frac{(1/8\pi)^{3/2}}{\sqrt{S_{xx}S_{yy}S_{zz} - S_{xy}^2 S_{zz}}} \exp\left[-\frac{S_{yy}x^2 - 2S_{xy}xy + S_{xx}y^2 + \frac{1}{S_{zz}}\left(S_{xx}S_{yy} - S_{xy}^2\right)z^2}{8\left(S_{xx}S_{yy} - S_{xy}^2\right)}\right]. \tag{6.12}$$

Finally, using Eqn. 6.12 in Eqn. 6.3 for the scattering intensity yields

$$I\left(q_x.q_y, q_z\right) = \frac{I_0}{2}\left(1 + \exp\left[-2\left(S_{xx}q_x^2 + 2S_{xy}q_xq_y + S_{yy}q_y^2 + S_{zz}q_z^2\right)\right]\right). \tag{6.13}$$

For the Hookean dumbbell model, $S_{yy} = S_{zz} = \frac{R_{g,eqm}^2}{3}$. If the spring is non-Hookean, such as a FENE-spring, the yy and zz-components of the gyration tensor do not necessarily equal their equilibrium value. To maintain the generality of our approach, we will use S_{yy} and S_{zz} in Eqn. 6.13 in the calculations in the results section.

To check for consistency between our approach at equilibrium and previous theoretical results for dilute polymer chains at equilibrium, we set $Wi = 0$ in Eqn. 6.13 to yield:

$$I(q) = \frac{I_0}{2}\left(1+\exp\left[\frac{-2R_{g,eqm}^2\left(q_x^2+q_y^2+q_z^2\right)}{3}\right]\right) = \frac{I_0}{2}\left(1+\exp\left[\frac{-2R_{g,eqm}^2 q^2}{3}\right]\right). \tag{6.14}$$

We can Taylor expand this expression for $qR_{g,eqm} \ll 1$ to obtain $I(q) \approx I_0\left(1-\frac{R_g^2 q^2}{3}+...\right)$. We recognize the first two terms in the expansion are the same as the Taylor expansion of $e^{-R_{g,eqm}^2 q^2/3}$, thus we obtain:

$$I(q) \approx I_0 e^{-\frac{R_{g,eqm}^2 q^2}{3}}, \tag{6.15}$$

which is the same as the low-q expansion of the Debye function for dilute polymers that we discussed in Chapter 3. Eqn. 6.15 is also called the Guinier approximation, which is a general property of equilibrium scattering for $qR_{g,eqm} < \sqrt{3}$ for a scattering object of any shape. The Guinier analysis is used to extract the equilibrium radius of gyration from circularly averaged scattering intensity. Specifically, when we plot $\log I$ as a function of q^2, the slope is $-R_{g,eqm}^2/3$.

The dumbbell model with the Hookean spring law allows us to get analytical results of the scattering intensity in terms of the components of the gyration tensor, which enables fast scattering predictions. However, the Hookean dumbbell model ignores finite extensibility of the chain, hydrodynamic interactions (HI), and excluded volume (EV), which are present in a physical system. Once finite extensibility, HI, and EV are included, it becomes difficult, if not impossible, to derive analytical expressions for the scattering intensity because the conformation distribution starts to deviate from the Gaussian form.

Thus, we rely on the more general form of the intensity for the dumbbell model (Eqn. 6.3) and use Brownian dynamics simulations to obtain a discretized conformation distribution function numerically.

6.2.2 Multiple-bead-spring chains in shear flow

The dumbbell model discussed in the previous section is only expected to be valid in the low-q regime where intra-chain structures are negligible. If we want to resolve higher-q structures, we need to use multiple-bead-spring chains to represent the polymer. Shown in Fig. 6.2 is a representative schematic of a multiple-bead-spring chain. In this case, 5 beads are used.

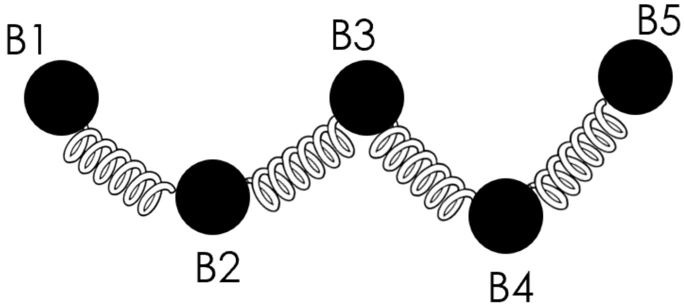

Figure 6.2: Schematic of the multiple-bead-spring chain.

If hydrodynamic interactions and excluded volume are excluded and the Hookean springs are used, the multiple-bead-spring model is the Rouse chain model. Previous work has attempted to predict the scattering of the Rouse chain in flow using normal mode analysis. The resulting analytical solution contains complicated sums over the different modes and typically need to be evaluated numerically.[4,5] Furthermore, to better represent experimental conditions, one needs to include HI, EV, and finite extensibility, which again makes the analytical solution impossible. Thus, we start from the more general expression of the scattering intensity for $n > 2$, Eqn. 6.2, which is included again for convenience below:

$$\begin{aligned} I(\mathbf{q}) &= \frac{1}{n^2}\sum_{j,k}^{n}\int \exp\left(-i\mathbf{q}\cdot\mathbf{r}_{jk}\right)\psi_{jk}\left(\mathbf{r}_{jk}\right)d\mathbf{r}_{jk} \\ &= \frac{1}{n^2}\left(n+\sum_{j,k\neq j}^{n}\int \exp\left(-i\mathbf{q}\cdot\mathbf{r}_{jk}\right)\psi_{jk}\left(\mathbf{r}_{jk}\right)d\mathbf{r}_{jk}\right) \end{aligned} \tag{6.16}$$

For the case of a chain with five beads, as is shown in Fig. 6.2 and discussed in more detail in the Results section, because of symmetry in the chain, there are 6 unique bead-bead pairs: 1-2, 2-3, 1-3, 1-4, 1-5, and 2-4. Within pairs equivalent to 1-2, there are four possibilities: B1-B2, B2-B1, B4-B5, B5-B4. In other words, the 1-2 pairs involve one bead at one end of the chain and the bead directly adjacent to that bead. Similarly, for the other pairs, there are multiple equivalent duplicates. The knowledge of these equivalent duplicates simplifies the calculation, as shown below:

$$\begin{aligned} I(\mathbf{q}) = \frac{1}{25}\Big(5 &+ 4\int \exp\left(-i\mathbf{q}\cdot\mathbf{r}_{12}\right)\psi_{12}\left(\mathbf{r}_{12}\right)d\mathbf{r}_{12} + 4\int \exp\left(-i\mathbf{q}\cdot\mathbf{r}_{23}\right)\psi_{23}\left(\mathbf{r}_{23}\right)d\mathbf{r}_{23} \\ &+ 4\int \exp\left(-i\mathbf{q}\cdot\mathbf{r}_{13}\right)\psi_{13}\left(\mathbf{r}_{13}\right)d\mathbf{r}_{13} + 4\int \exp\left(-i\mathbf{q}\cdot\mathbf{r}_{14}\right)\psi_{14}\left(\mathbf{r}_{14}\right)d\mathbf{r}_{14} \\ &+ 2\int \exp\left(-i\mathbf{q}\cdot\mathbf{r}_{15}\right)\psi_{15}\left(\mathbf{r}_{15}\right)d\mathbf{r}_{15} + 2\int \exp\left(-i\mathbf{q}\cdot\mathbf{r}_{24}\right)\psi_{24}\left(\mathbf{r}_{24}\right)d\mathbf{r}_{24}\Big). \end{aligned} \tag{6.17}$$

The ψ_{jk} in Eqn. 6.16 and Eqn. 6.17 above represents the distribution function of the vector connecting bead j and bead k and are obtained from Brownian dynamics simulation. As we will discuss in the Results section below, the combination of Eqn. 6.16 and Brownian dynamics results with finite extensibility allows realistic prediction of scattering of dilute polymers up to higher-q values and ultimately enables direct comparison with experiments.

6.3 Results

For the scattering predictions in this section, we use either the gyration tensor components or the discretized conformation distribution function as the input in the calculations. Both the gyration tensor components and the discretized PDF are obtained in Brownian Dynamics simulations made by our collaborators at RPI. Since this is the beginning of this new collaborative project, I will only briefly summarize the work to-date. Future work will be carried out by Anukta Datta in her PhD work. To simplify the discussion, I will only show results for Hookean dumbbell without HI and 5-bead FENE chain without HI.

6.3.1 Dumbbells at equilibrium

We first used Eqn. 6.13 and components of the gyration tensor at $Wi = 0$ to calculate scattering of Hookean dumbbell at equilibrium. For all of the subsequent calculations, we are predicting the scattering in the flow-gradient plane. Thus, we set the scattering vector in the vorticity direction (q_z) to be zero. We also set I_0 to be 1, since we are not directly comparing with experiments yet. The 2D scattering pattern is shown in Fig. 6.3(a). q_x and q_y are the scattering wave vectors in the flow direction and gradient direction, respectively. The equilibrium value for the radius of gyration from the BD simulation is 4.96 nm. This is obtained from $R_{g,eqm} = \sqrt{S_{xx} + S_{yy} + S_{zz}}$, where S_{xx}, S_{yy}, and S_{zz} are the diagonal components of the gyration tensor.

As expected, the scattering intensity is isotropic for the dumbbell model at equilibrium. To validate the scattering calculation, we conduct a Guinier analysis on the circularly averaged equilibrium intensity by plotting $\log I$ as a function of q^2, where $q^2 = q_x^2 + q_y^2$ (Fig. 6.3(b)). We do a linear fit of the $\log I$ result in the region corresponding to $qR_g < \sqrt{3}$, which is the Guinier region. The slope equals $-R_{g,qm}^2/3 = 821.52\text{Å}^2$ so the equilibrium radius of gyration determined from the Guinier analysis is 4.96 nm, which is comparable to the radius of gyration from the Brownian dynamics simulation (4.98 nm).

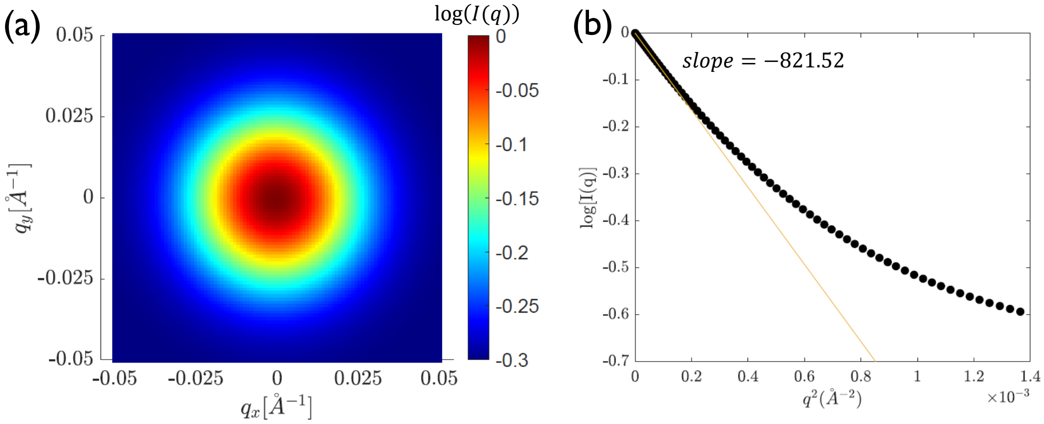

Figure 6.3: Scattering predictions for the dumbbell model at equilibrium. (a) 2D prediction using components of the gyration tensor (b) Guinier analysis for extracting the radius of gyration.

6.3.2 Dumbbells in flow

We also made comparisons between scattering predictions using the gyration tensor components in Eqn. 6.13 and the discretized conformation distribution function in Eqn. 6.3. In Fig. 6.4(a) and (b), we show the scattering patterns for the gyration tensor calculation with $Wi = 0.1$ and $Wi = 3$, respectively. For $Wi = 0.1$, the scattering pattern is only weakly anisotropic, whereas for $Wi = 3$, the scattering pattern has significant anisotropy, which suggests the dumbbells are significantly aligned in flow. In Fig. 6.4(c) and (d), we plot the scattering patterns from the discretized PDF calculation for $Wi = 0.1$ and $Wi = 3$, respectively. The predictions using the gyration tensor and the discretized PDF are qualitatively the same for both Weissenberg numbers. The computational time for the discretized PDF calculation is >1000 times longer than that for the gyration tensor calculation because the former requires looping through discretized PDF which has 200 bins in the x, y, and z directions for our current BD simulation results and is very computationally expensive. For the dumbbell model, the analytical scattering results using the gyration tensor components is advantageous and can be used for doing inverse calculations, as we will discuss below.

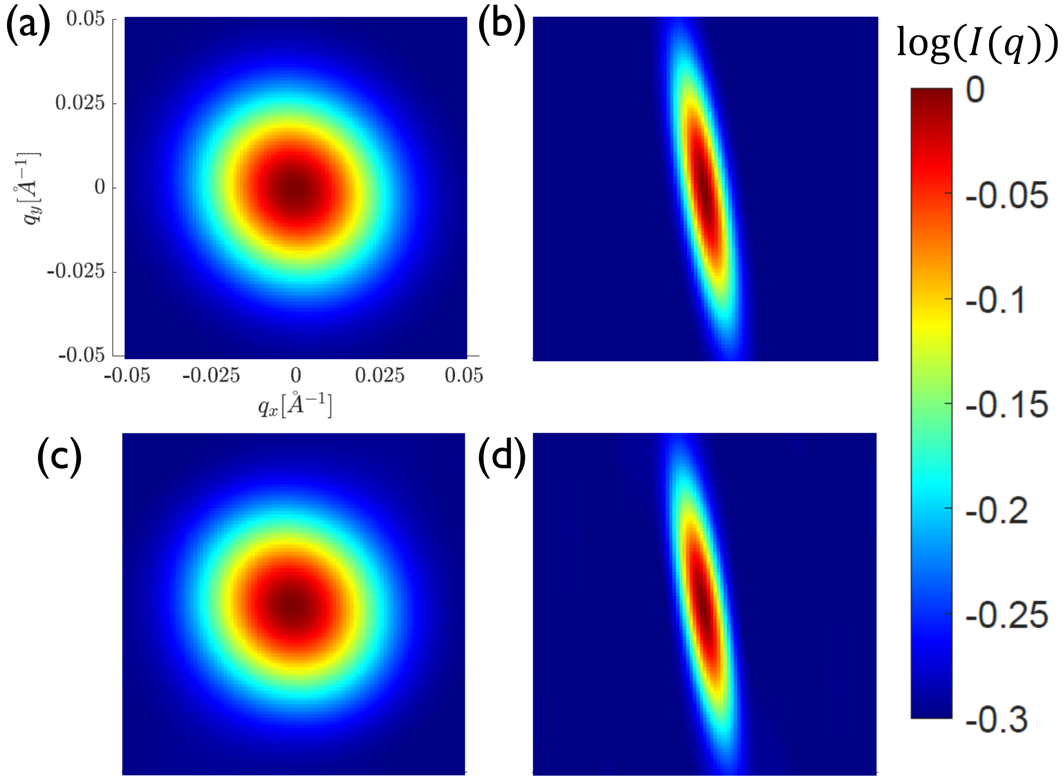

Figure 6.4: Scattering predictions for the dumbbell model using gyration tensor components for (a) $Wi = 0.1$ and (b) $Wi = 3$. Scattering predictions for the dumbbell model using discretized probability distribution function for (c) $Wi = 0.1$ and (d) $Wi = 3$. q_x is the scattering wave vector in the flow direction and q_y is the scattering wave vector in the gradient direction. The x and y axes in (b)-(d) are the same as those in (a). All four figures have the same color scale.

6.3.3 Inverse calculations for dumbbells

One main long-term objective of this project is to develop an integrated experimental and simulation method to extract distributions of polymer deformation from rheoSANS experiments. The analysis of experimental results for polymers will be conducted in future studies. We want to first develop the inverse calculation method based on simulation results. Namely, using the 2D scattering patterns in Fig. 6.4, we want to do nonlinear fitting of the scattering results to extract the components of the gyration tensor and to compare with our input parameters. To do so, we again utilize Eqn. 6.13 and use the nlinfit function in Matlab to obtain fitted values for the parameters S_{xx}, S_{yy}, and S_{xy}. We fitted both the gyration tensor scattering results and the discretized PDF scattering results. The fitted values are compared with the gyration tensor results from the BD simulation in Table 6.1. For the fitting of the gyration tensor calculation, we get exactly the same value as the components of the gyration tensor used as input for the scattering prediction. For the fitting of the discretized PDF calculation, the agreement between the input gyration tensor components and the fitted values is also quite good, with $< 3\%$ difference.

Table 6.1: Compare input parameters for scattering prediction and results from inverse fitting for scattering simulation using gyration tensor components and scattering simulation using discretized probability distribution function for $Wi = 3$. Units for the gyration tensor components are Å^2.

	BD Simulation	Fitting of ψ Calc	Fitting of R_g Calc	% Difference
S_{xx}	16098	16484	16098	2.40%
S_{yy}	840	829	840	1.31%
S_{xy}	2539	2544	2539	0.20%

6.3.4 Scattering from multiple-bead chains

As was discussed in the theory section, although the Hookean dumbbell offers the advantage of obtaining analytical results for the scattering intensity, only including two beads is not enough to resolve the intra-chain structures and the Hookean spring does not account for the finite extensibility of the polymer chains. Thus, our collaborators run

BD simulations for multiple-bead-spring FENE chains. In the example shown below, the chains have 5 beads. We use Eqn. 6.17 and a discretized PDF for each unique bead-bead pair for the scattering prediction at $Wi = 0.1, 1, 10$ (Fig. 6.5). With increasing Wi, the scattering anisotropy increases which indicates the chains are more aligned in flow.

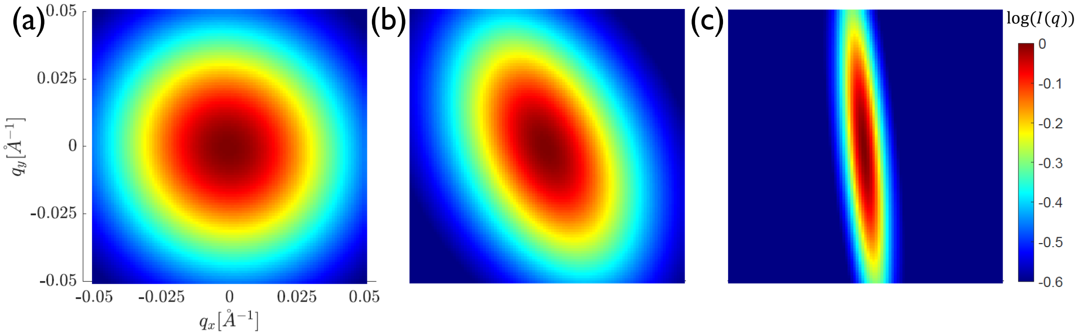

Figure 6.5: Scattering prediction for 5-bead FENE chain (with HI) using discretized probability distribution function for (a) $Wi = 0.1$, (b) $Wi = 1$, and (c) $Wi = 10$.

6.4 Future work

Since this is the beginning of a 3-year project for our research group, there are many directions that are yet to be explored. Based on our current results, I will now make some recommendations for future work on this project both in the short term and long term.

We have demonstrated the validity of our forward and inverse calculation method for the dumbbell model. It will be important to also develop an inverse calculation method for the multiple-bead-spring model to enable extraction of more internal structures of the chains. To do so, we first need to develop analytical or parameterized expressions of the scattering of multi-bead chains. Several possible avenues are likely to be fruitful. A mathematically rigorous method is to use the spherical harmonic decomposition developed by Yangyang Wang and coworkers to extract components of the gyration tensor.[6,7] Alternatively, the low-q expansion of Rouse chains has been worked out and can be used as a fitting function.[8] Finally, one can attempt to derive approximate expressions of the scattering after including finite extensibility, hydrodynamic interactions, and excluded volume effects.

So far, the inverse method has only been tested on noise-free simulation results. When using the inverse method on experimental scattering patterns, one immediate challenge is the noise in experimental data. Previously in our group, a maximum a posteriori scattering inference (MAPSI) method has been developed for extracting the orientation distribution function of rodlike particles in flow, which accounts for the experimental uncertainty associated with the scattering intensity.[9] We can look into extending the MAPSI method to extract conformation distribution function of polymers. Alternatively, the singular value decomposition (SVD) method has been used to extract orientation distribution from scattering[10] and we can check its usefulness for extracting the conformation distribution of polymers.

Finally, the end goal of this project is to study the influence of polymer topology on the molecular deformation and scission at extreme rates. To first establish the forward and inverse calculation methods, we focused on the linear polymers. Future work should extend the current model to other polymer architectures, such as branched and star polymers. Equilibrium models for such architectures already exist.[11] For predictions in flow, we propose either using Brownian Dynamics simulations of different polymer architectures to obtain the discretized conformation distribution and use it directly in scattering calculations as shown in this chapter or looking into methods to derive analytical expressions for the scattering intensity based on the gyration tensor components of chains with different architectures.

Bibliography

[1] Murphy RP, Riedel ZW, Nakatani MA, et al. Capillary rheosans: measuring the rheology and nanostructure of complex fluids at high shear rates. *Soft Matter.* 2020; 16(27): 6285–6293.

[2] Hammouda B. Sans from homogeneous polymer mixtures: A unified overview. *Polymer Characteristics.* 1993: 87–133.

[3] Bird RB, Curtiss CF, Armstrong RC, Hassager O. *Dynamics of polymeric liquids, volume 2: Kinetic theory.* Wiley 1987.

[4] Peterlin A, Reinhold C. Light scattering by linear macromolecules oriented in laminar flow. iii. perfectly flexible necklace model with no hydrodynamic interaction. *The Journal of Chemical Physics.* 1964; 40(4): 1029–1032.

[5] Pierleoni C, Ryckaert JP. Excluded volume effects on the structure of a linear polymer under shear flow. *The Journal of Chemical Physics.* 2000; 113(13): 5545–5558.

[6] Huang GR, Wang Y, Do C, et al. Determining gyration tensor of orienting macromolecules through their scattering signature. *The journal of physical chemistry letters.* 2019; 10(14): 3978–3984.

[7] Wang Z, Lam CN, Chen WR, et al. Fingerprinting molecular relaxation in deformed polymers. *Physical Review X.* 2017; 7(3): 031003.

[8] Roitman D, Schrag J. Elastic light scattering from rouse chains in flowing solutions. In *AIP Conference Proceedings*; Vol. 137: 77–82American Institute of Physics 1986.

[9] Corona PT, Silmore KS, Adkins R, et al. Bayesian estimations of orientation distribution functions from small-angle scattering enable direct prediction of mechanical stress in anisotropic materials. *Physical Review Materials.* 2021; 5(6): 065601.

[10] Bender P, Zákutná D, Disch S, Marcano L, Alba Venero D, Honecker D. Using the singular value decomposition to extract 2d correlation functions from scattering patterns. *Acta Crystallographica Section A: Foundations and Advances.* 2019; 75(5): 766–771.

[11] Higgins JS, Benoit HC. Polymers and neutron scattering. 1994.

Chapter 7

Modeling orthogonal superposition rheometry to probe nonequilibrium dynamics of entangled polymers

This chapter is reproduced from:

Jiamin Zhang, Andres Jurzyk, Matthew E. Helgeson, and L. Gary Leal, “Modeling Orthogonal Superposition Rheometry to Probe Nonequilibrium Dynamics of Entangled Polymers”, *Journal of Rheology*, **65(5)**, 983-998, 2021. *Featured article.* DOI: 10.1122/8.0000272,

with the permission of AIP publishing.

7.1 Introduction

Flow processing of soft materials and complex fluids usually involves nonlinear deformations, which can non-trivially modify both the associated microstructural configuration and dynamics. This is particularly important for entangled polymeric fluids, where entanglements produce nonlinear relaxation mechanisms that are significantly modified when polymers stretch and orient in flow, leading to various flow instabilities and complications in polymer processing. Various recent flow protocols have been proposed to highlight the nonlinear contributions to the relaxation: one is Large Amplitude Oscillatory Shear (LAOS),[1] and another is superposition rheology, which was originally proposed by Tanner and Simmons.[2,3] Although in LAOS the frequency dependence offers the possibility to probe different time scales, the method relies on subjecting the sample to a very complex kinematic history.[4] Alternatively, superposition rheology still enables frequency dependent measurements while retaining simpler kinematics. As a result, superposition of a small-strain oscillatory motion onto a steady or transient shear flow can provide a clearer insight into the effects of flow on the mechanisms underlying the nonlinear response of rheologically complex fluids.[5] The oscillatory motion can be imposed either parallel ($\dot{\gamma}_{\|}$, parallel superposition, PSR) or perpendicular ($\dot{\gamma}_{\perp}$, orthogonal superposition, OSR) to the direction of motion for the steady shear flow. Of these, orthogonal superposition offers the advantage that the two flow fields are not coupled and, as we show in this work, the corresponding moduli can be more directly related to the microstructural configuration under flow. OSR provides measurement of the frequency- and shear-rate-dependent nonlinear viscoelastic superposition moduli (storage and loss moduli, $G'_{\perp}$ and $G''_{\perp}$), which are analogous to their linear viscoelastic (LVE) counterparts that characterize equilibrium dynamics. So, in principle, OSR is a very promising experimental method for studying the coupling of microstructural dynamics and nonlinear rheological response in polymeric liquids.

In practice, however, it has been difficult to achieve OSR measurements experimentally due to instrumental challenges and measurement sensitivity. The earlier devices for OSR by Simmons,[3] Mewis and Schoukens,[6] and Zeegers et al.[7] have a complex and delicate mechanical design and only cover a rather narrow viscosity range. Vermant et al.[8]

described an orthogonal superposition technique based on a simple modification of the force rebalance transducer in a commercial rheometer and introduced the design of a double wall Couette cell with open bottom for the inner cylinder to avoid pumping flow. These new instrument developments finally enabled implementation of sensitive orthogonal superposition on commercial rheometers. A recent experimental and simulation study thoroughly investigated the calibration procedures and corrections needed for non-idealized flow field in the OSR setup on commercial rheometers.[9] Orthogonal superposition rheometry (OSR) has been used to study structural changes during flow in complex fluids, including polymeric fluids,[10,11] starlike and wormlike micelles,[5,12] and both in Brownian dynamics simulations[13] and experiments for colloidal suspensions.[4,14–17]

Because OSR has only recently become experimentally available on commercial rheometers, relatively little is known about how to interpret the nonlinear viscoelastic results in the context of entangled polymer dynamics. Specifically, there are very few theoretical and computational studies that would provide a fundamental basis for interpreting orthogonal superposition measurements. To date, most of the experimental studies have interpreted the data by analogy to interpretation of linear viscoelastic measurements. However, though proposed analogies between linear viscoelasticity and orthogonal viscoelasticity have been used (e.g. using empirical rules to estimate chain length[18–20]), these analogies have not been theoretically verified. This provides strong motivation for a deeper theoretical and computational study to investigate what is fundamentally being measured in the OSR experiments.

To better understand superposition experiments, the resulting moduli should be described by suitable rheological constitutive models. Lacking a generally valid nonlinear rheological constitutive equation, previous studies have used various phenomenological models. Yamamoto proposed a strain rate-dependent relaxation spectrum, which demonstrates that the parallel moduli reflect the coupling between shear and superimposed flow, while orthogonal superposition moduli do not.[21] Wong and Isayev predicted the orthogonal moduli with the Leonov model;[22] Kwon and Leonov later corrected the predictions.[11] The corrected predictions agree qualitatively well with early experimental work by Simmons on polymer solutions.[10] Kim et al. used the Giesekus model to predict parallel and orthogonal superposition moduli and compared with experiments on wormlike micelles.[5]

For studying entangled polymers in superposition flows, only two molecularly based models have been used. The first involved a prediction of parallel superposition moduli by Unidad and Ianniruberto[23] using the differential constitutive equation accounting for convective constraint release (CCR) proposed by Marrucci and Ianniruberto: the double-convection-reptation model with chain stretch (DCR-CS model).[24] However, interpretation of parallel superposition results is complicated by the coupling of the steady shear flow and oscillatory flow. The second study by Mead[25] uses the monodisperse and polydisperse MLD models to predict PSR and OSR moduli.[26–28] A potential weakness of the MLD model is that the stretch and orientation dynamics are treated using separate dynamical equations, which can lead to problems even in monodisperse rheology predictions.[29] As pointed out by Boudara et al.,[30] the decoupling approximation is even more problematic for polydisperse blends because couplings between constraint release and chain retraction must be readmitted in an *ad hoc* fashion and do not arise naturally from the model. Furthermore, both the studies by Mead as well as by Unidad and Ianniruberto neglected chain stretch. So far, no studies have systematically studied the effect of polydispersity on OSR moduli using models that treat stretch and orientation in the same equation and probed a sufficiently wide range of shear rates and frequencies so that significant shifts in the moduli can be observed with increasing shear rate.

The current investigation addresses these limitations of previous studies by using molecularly based models that treat orientation and stretch in the same equation for predicting OSR moduli. Specifically, we use the Rolie-Poly model[31] for monodisperse polymers and the Rolie-Double-Poly model[30] for polydisperse polymers. These models account for the detailed nonlinear relaxation processes of entangled polymers including reptation, chain retraction, and convective constraint release. Furthermore, by combining a perturbation analysis and numerical calculations, we can obtain OSR moduli across a wide range of frequencies and shear rates and systematically vary the degree of chain polydispersity. After the detailed modeling study, we will discuss our results in a broader context to help design and interpret future OSR experiments. We find the relationships governing OSR moduli for the Rolie-Poly model also work for a broader class of constitutive models. We suggest an analogy to Laun's rule[32] to relate OSR moduli to the first normal stress difference. Additionally, we derive expressions to extract model parameters from experiments without the need for detailed model fitting. By making an analogy to the linear relaxation spectrum, we show the utility of OSR experiments to obtain material structural information that would be difficult to obtain from conventional rheological measurements. In this way, studying orthogonal superposition computationally not only provides important comparison to future experiments, but also provides better sensitivity for testing models for nonlinear polymer processing.

7.2 Theory

7.2.1 Storage and loss moduli in linear viscoelastic measurement

Storage and loss moduli have been used ubiquitously to describe viscoelastic materials, such as entangled polymers. The storage modulus G' is proportional to the energy storage and therefore reflects the elasticity in the system. The loss modulus G'' is proportional to the dissipation or loss of energy, reflecting the viscous nature of the system.[33] The most common approach to obtain information about the deformation-induced structural rearrangement within a complex fluid is to measure the two moduli using small amplitude oscillatory shear (SAOS). In this regime, the material response is independent of the strain amplitude, and this is known as the linear viscoelastic behavior.[34]

The storage and loss moduli at equilibrium can be used to estimate the average contour length of entangled polymers and wormlike micelles, as demonstrated in previous works.[18] Specifically, based on the polymer network theory, the number of entanglements of a chain is given by the ratio of the plateau modulus G_N^0 and the minimum of the loss modulus G''_{min}. The entanglement length, l_e, is evaluated in the context of a particular chain model (e.g. a flexible chain or a semiflexible chain).[19,20] Thus, one can estimate the average chain length, L_c, as follows:

$$L_c = l_e \frac{G_N^0}{G''_{\text{min}}} \tag{7.1}$$

7.2.2 Rolie-Poly model for monodisperse polymers

Before discussing the model for polydisperse polymers, we first take a moment to review the classic Rolie-Poly model of Likhtman and Graham,[31] which has its origin in the full GLaMM model. The GLaMM model was originally proposed by Graham and co-workers[35] as a full chain molecular theory for entangled monodisperse linear polymer chains under fast deformation. The GLaMM model accounts for an accumulation of stress via affine deformation and relaxation of stress by reptation, chain retraction, and convective constraint release (CCR). Reptation was included in the original tube model introduced by Doi and Edwards[19] and describes the curvilinear motion of a polymer chain in a tube formed by entanglements with surrounding chains. When the deformation becomes much faster than the inverse of the Rouse time, the chain can become stretched, and as a result the length of the chain and the occupied tube exceed their equilibrium configuration. When the strain stops, the chain retracts along the deformed tube until it regains its equilibrium contour. Convective constraint release (CCR) is the release of entanglement constraints due to chain retraction from affine deformation in nonlinear flows. The effect of CCR diminishes for shear rates larger than the inverse of the Rouse time.

Although the GLaMM model is successful in predicting the rheology of fast flows, it is computationally prohibitive for nonviscometric flow calculations and for OSR calculations that span several orders of magnitude of frequency and shear rate. Hence, as a simplified version of the GLaMM model, Likhtman and Graham derived a one-mode approximation of the GLaMM model to produce a differential constitutive model for entangled monodisperse polymer chains: the Rolie-Poly model (for Rouse linear entangled polymers).[31] The time evolution of the contribution to the stress tensor due to the polymer, $\boldsymbol{\sigma}$, is calculated via the conformation tensor for an entanglement segment, $\boldsymbol{A}$ as

$$\boldsymbol{\sigma} = G_N^0 \cdot \mathbf{A}. \tag{7.2}$$

and

$$\begin{aligned}\frac{\mathrm{d}\mathbf{A}}{\mathrm{d}t} &= \underbrace{\boldsymbol{\kappa} \cdot \mathbf{A} + \mathbf{A} \cdot \boldsymbol{\kappa}^{\mathrm{T}}}_{\text{convection}} - \underbrace{\frac{1}{\tau_{\mathrm{d}}} (\mathbf{A} - \mathbf{I})}_{\text{reptation}} - \underbrace{\frac{2\left(1 - \lambda^{-1}\right)}{\tau_{\mathrm{R}}} \mathbf{A}}_{\text{retraction}} \\ &\quad - \underbrace{\beta_{\mathrm{CCR}} \frac{2\left(1 - \lambda^{-1}\right)}{\tau_{\mathrm{R}}} \lambda^{2\rho} (\mathbf{A} - \mathbf{I})}_{\text{convective constraint release}}.\end{aligned} \tag{7.3}$$

Here, G_{N}^0 is the plateau modulus, κ is the velocity gradient tensor, and the stretch ratio of the polymer chains, i.e. the ratio of the current to equilibrium-with-no-flow chain contour lengths, is defined as

$$\lambda = \sqrt{\frac{\mathrm{tr}\mathbf{A}}{3}}. \tag{7.4}$$

The reptation term (with τ_d) is a single time relaxation towards equilibrium. It's also possible to include the effect of contour length fluctuation (CLF) with the reptation term by modifying the reptation time.[30,36] However, as shown by Boudara et al.,[30] the inclusion or absence of CLF only affects the quantitative agreement of the model with experiment without affecting the qualitative trends. To keep the physical picture simple, we will not include CLF in our calculations. The CCR term is also a relaxation towards equilibrium, but with the rate dependent on the amount of stretch λ and the Rouse time τ_R. Retraction is relaxation to zero stress, also with the rate dependent on λ and τ_R. β_{CCR} specifies the CCR contribution and is analogous to c_ν in the full GLaMM model. c_ν determines the number of retraction events necessary to result in one tube hop of a tube diameter with a value of $c_\nu \leq 1$.[35] To fit the GLaMM model to experiments, the authors used $c_\nu = 0.1$, which approximately corresponds to $\beta_{CCR} = 1$. ρ is an additional fitting parameter. $\beta_{\mathrm{CCR}} = 1$, $\rho = -0.5$ are the optimal values to fit the Rolie-Poly model prediction to the full GLaMM theory, thus these are generally used in the Rolie-Poly model and also in this work.

The Rolie-Poly model incorporates changes in the conformation due to orientation and stretch in the same equation. Thus, the model avoids anomalous shear thickening behavior at shear rates corresponding to chain stretch predicted by models that decouple stretching and orientation.[29] Furthermore, since Rolie-Poly model is a single mode approximation of the full GLaMM model, it has sound microstructural basis while still making the calculation of OSR moduli computationally feasible.

7.2.3 Rolie-Double-Poly (RDP) model for polydisperse polymers

To develop a constitutive model for polydisperse entangled polymer, Boudara and co-workers used ideas from both the Rolie-Poly model[31] and the double reptation approximation[37] to formulate the RDP model.[30] The "RDP model" is used to refer the "Rolie-Double-Poly" model, where "Double" signifies both "double reptation" and "double poly" as in "POLYdisperse POLYmers. The RDP model can be formally derived as a greatly simplified approximation of the detailed molecular theory for bidisperse polymer melts of Read and co-workers.[38]

In the RDP model, the total polymer contribution to the stress is the sum of the contributions coming from each species i, weighted by their volume fraction, ϕ_i

$$\boldsymbol{\sigma} = G_N^0 \sum_{\mathrm{i}=1}^{\mathrm{N}} \phi_{\mathrm{i}} \mathbf{A}_{\mathrm{i}}, \tag{7.5}$$

with

$$\lambda_{\mathrm{i}} = \sqrt{\frac{\mathrm{tr}\mathbf{A}_{\mathrm{i}}}{3}}. \tag{7.6}$$

The conformation tensor $\mathbf{A}_i$ accounts for the stresses that come from the interaction of the species i with itself and the other $n-1$ species:

$$\mathbf{A}_{\mathrm{i}} = \sum_{\mathrm{j}=1}^{\mathrm{N}} \phi_{\mathrm{j}} \mathbf{A}_{\mathrm{ij}}, \tag{7.7}$$

where $\mathbf{A}_{ij}$ is the stress conformation tensor on the i-chains coming from their entanglements with the j-chains.

$$\begin{aligned}\frac{\mathrm{d}\mathbf{A}_{\mathrm{ij}}}{\mathrm{d}t} &= \underbrace{\boldsymbol{\kappa}\cdot\mathbf{A}_{\mathrm{ij}}+\mathbf{A}_{\mathrm{ij}}\cdot\boldsymbol{\kappa}^{\mathrm{T}}}_{\text{convection}} - \frac{1}{2}\left(\underbrace{\frac{1}{\tau_{\mathrm{d,i}}}\left(\mathbf{A}_{\mathrm{ij}}-\mathbf{I}\right)}_{\text{reptation}} + \underbrace{\frac{\beta_{\mathrm{th}}}{\tau_{\mathrm{d,j}}}\left(\mathbf{A}_{\mathrm{ij}}-\mathbf{I}\right)}_{\text{constraint release}}\right) \\ &- \underbrace{\frac{2\left(1-\lambda_{\mathrm{i}}^{-1}\right)}{\tau_{\mathrm{R,i}}}\mathbf{A}_{\mathrm{ij}}}_{\text{retraction}} - \underbrace{\beta_{\mathrm{CCR}}\frac{2\left(1-\lambda_{\mathrm{j}}^{-1}\right)}{\tau_{\mathrm{R,j}}}\lambda_{\mathrm{i}}^{2\rho}\left(\mathbf{A}_{\mathrm{ij}}-\mathbf{I}\right)}_{\text{convective constraint release}}\end{aligned} \tag{7.8}$$

In the original Rolie-Poly model, τ_{d} specifies the terminal stress relaxation time of the polymer. However, in the RDP model, the effects of reptation are explicitly separated out from thermal constraint release (CR) given by the parameter β_{th}. Due to the interaction of different chains, reptation of a smaller chain causes the constraint release of a longer chain. Thus, CR needs to appear in a separate term. To ensure that the RDP model converges to the Rolie-Poly model in the monodisperse limit, the reptation term and the CR term are divided by two. This choice is physically sound because the reptation term in the Rolie-Poly model is the effective reptation term that actually includes both reptation and CR.

7.3 Methods

7.3.1 Numerical approach

Monodisperse calculation

To evaluate the orthogonal superposition moduli, it is necessary to calculate the transient stress response under a combination of axial steady shear flow and orthogonal oscillation. The velocity gradient tensor is

$$\boldsymbol{\kappa} = \begin{bmatrix} 0 & \dot{\gamma} & 0 \\ 0 & 0 & 0 \\ 0 & \dot{\gamma}_{\perp}(t) & 0 \end{bmatrix} \tag{7.9}$$

where $\dot{\gamma}$ is the steady state shear rate and $\dot{\gamma}_{\perp}(t) = \gamma_{0,\perp}\,\omega\cos\omega t$ is the oscillatory superposition term. In this work, we kept $\gamma_{0,\perp} = 0.05$ to remain in the linear viscoelastic region, as determined in the strain sweep (see Appendix B Fig. B.1). The six chain conformation tensor components of Equation 7.3 need to be calculated numerically by transiently solving the coupled differential equations. First, the equations are nondimensionlized using the Rouse time τ_R and the plateau modulus G_N^0. Specifically, the Deborah number De is defined as the dimensionless frequency ($De = \omega \cdot \tau_R = \tilde{\omega}$), the Weissenberg number is the dimensionless shear rate ($Wi = \dot{\gamma} \cdot \tau_R$), the dimensionless time is $t' = t/\tau_R$, and non-dimensionalized stress tensor is $\tilde{\boldsymbol{\sigma}} = \boldsymbol{\sigma}/G_N^0$. Furthermore, the ratio of the reptation time and the Rouse time is $\tau_d/\tau_R = \theta = 3Z$, where Z is the number of entanglement points per chain. In this work for the monodisperse calculations, we take $Z = 20$ for a well entangled polymer system.

The six transient equations for the conformation tensor components of Equation 7.3 were solved using the MATLAB built-in solvers "ode45" and "ode15s". "ode15s" is applied for the low frequency range to take advantage of the significant acceleration of the computation using adaptive mesh refinement. However, for the high frequency range, the adaptive mesh refinement caused large fluctuations in the moduli for adjacent frequency values. Consequently, for the high frequency range the very robust solver "ode45" is applied, which allows a user-defined time discretization. For this work, a logarithmic time spacing enables a sufficient sampling of the oscillations, across the entire frequency range simulated ($De = 10^{-4}$ to 100).

The shear stress in the orthogonal direction ($_\perp$) is used for the determination of $G'_\perp$ and $G''_\perp$ using

$$\frac{G'_\perp}{G_N^0} = \frac{\tilde{\sigma}_{0,\perp}}{\gamma_{0,\perp}\sqrt{1+(\tan\delta)^2}}, \tag{7.10}$$

$$\frac{G''_\perp}{G_N^0} = \frac{\tilde{\sigma}_{0,\perp}\tan\delta}{\gamma_{0,\perp}\sqrt{1+(\tan\delta)^2}} + \eta_s\tilde{\omega}, \tag{7.11}$$

where $\tilde{\sigma}_{0,\perp}$ and $\gamma_{0,\perp}$ are the amplitudes of the dimensionless shear stress and the applied strain, whereas δ defines their phase shift. Furthermore, the term $\eta_\mathrm{s}\tilde{\omega}$ denotes the solvent contribution, which is purely viscous and therefore only appears in $G''_\perp$, with the scaled solvent viscosity $\eta_s = 0.001$ in this work.

To determine the values of δ and $\tilde{\sigma}_{0,\perp}$ from the simulation, we first need to identify the start of the steady state in the main shear flow. The shear stress $\tilde{\sigma}_{xy}$ is plotted as a function of time (Fig.7.1 (a)). Within the plateau, the stress continues oscillating with a very small amplitude due to the superposed oscillation. We specify the plateau criterion as the smaller value of 10^{-3} and $10^{-2}\tilde{\omega}$ to account for the dependence of the amplitude of the stress oscillation on the frequency. The start of the plateau is defined as the first point in the transient shear stress with a moving standard deviation that is smaller than the specified plateau criterion. Once the time for the start of the plateau for $\tilde{\sigma}_\mathrm{xy}$ is specified, the same time is used to identify the start of steady state for the stress in the orthogonal direction ($\tilde{\sigma}_\mathrm{yz}$), which is plotted in Fig.7.1 (b) along with the applied strain rate ($\dot{\gamma}_\perp$). The grey section of the figure illustrates the transient start-up before the harmonic oscillation. After neglecting the start-up phase, $\tilde{\sigma}_\mathrm{yz}$ and $\dot{\gamma}_\perp$ are fitted by sine functions. Since the strain rate is a cosine function, it needs to be shifted by $\pi/2$ for the fitting of a sine function. Equations 7.12 and 7.13 define the two functions, including their fitting parameters c_1, and c_2.

$$\tilde{\sigma}_{\mathrm{yz}} = \tilde{\sigma}_{0,\perp} \cdot \sin(\tilde{\omega} \cdot t' + c_1). \tag{7.12}$$

$$\dot{\gamma}_{\perp} = \gamma_{0,\perp}\tilde{\omega} \cdot \sin(\tilde{\omega} \cdot t' + \mathrm{c}_2 + \frac{\pi}{2}). \tag{7.13}$$

In the equations, $\tilde{\sigma}_{0,\perp}$ and $\gamma_{0,\perp}$ specify the amplitudes of the orthogonal stress and the applied strain in the orthogonal direction, respectively. Furthermore, the difference of the resulting coefficients defines the phase shift between the two wave functions: $\delta = \mathrm{c}_1 - \mathrm{c}_2$. With the phase shift and the amplitude values, the OSR moduli $G'_{\perp}$ and $G''_{\perp}$ are calculated for each combination of shear flow strength Wi and superposed oscillation frequency De according to Equations 7.10 and 7.11.

Finally, before using the numerical method above to make predictions of $G'_{\perp}$ and $G''_{\perp}$, we verified that $\gamma_{0,\perp} = 0.05$ is small enough to be in the linear viscoelastic region by conducting a strain sweep at a fixed oscillation frequency (see Appendix B Fig. B.1 (a)). Furthermore, we validated the numerical method by comparing steady state predictions with predictions reported with the original Rolie-Poly model formulation[31] and comparing orthogonal superposition predictions using a Giesekus model with analytical results from the work by Kim and co-workers[5] (see Appendix B Fig. B.2).

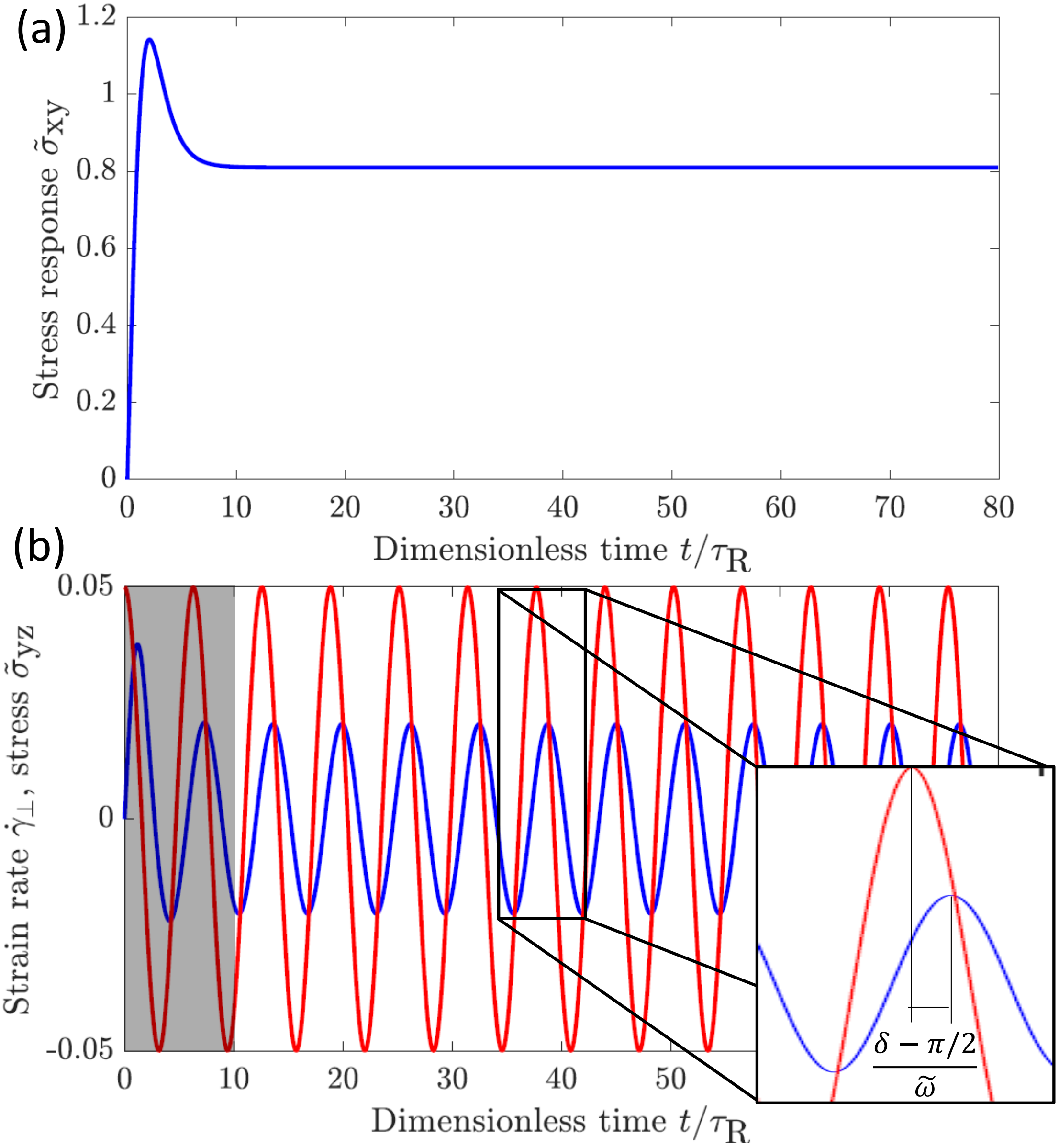

Figure 7.1: Schematic showing the steps for calculating superposition moduli numerically (for $Wi = 1$ and $\tilde{\omega} = 1$) (a) Identification of steady state from shear stress response as a function of time (b) Applied strain rate and yz−component of stress response as a function of time, inset shows the phase shift.

Polydisperse calculation

The $G'_{\perp}$ and $G''_{\perp}$ calculations for polydisperse polymers follow the same workflow as the monodisperse calculation. The only difference is that several different conformation tensors $\mathbf{A}_{ij}$ need to be calculated before the summation, given by Equations 7.5 and 7.7, is computed. For the nondimensionalization, the Rouse time (τ_R) of the weight-average chain length ($\bar{Z} = 20$) is used to define the dimensionless shear rate Wi, the dimensionless frequency $\tilde{\omega}$, and the dimensionless time t'. Furthermore, the continuous length distribution must be discretized into different species, each with its own chain length and volume fraction. However, the computational expense significantly increases with the number of species by a factor of N^2. For this study, a maximum $N = 32$ is used. To systematically study the effect of polydispersity on the OSR moduli, we assumed a log-normal distribution for the volume fraction distribution with varying degrees of polydispersity while keeping the weight-average molecular weight (M_w) the same. The log-normal distribution is frequently seen in polymers used for rheological studies.[39] The continuous distribution is defined as:

$$\phi(Z) = \frac{1}{Zs\sqrt{2\pi}} \exp\left[-\frac{(\ln(Z) - \mu)^2}{2s^2}\right], \tag{7.14}$$

with $s^2 = \ln(I_p)$ and $\mu = \ln(\bar{Z}/\sqrt{I_p})$. $\phi(Z)\delta Z$ gives the volume fraction of chains with entanglement number falling in the range $Z \pm \delta Z/2$ for asymptotically small δZ. We also define $\bar{Z} = \int \phi Z \mathrm{d}Z$ as the mean number of entanglements per chain and $I_p = M_w/M_n = \bar{Z} \int \phi(Z)/Z \mathrm{d}Z$ as the polydispersity index. We then partition the continuous distribution into N sections, where the $i = 1, 2, 3, ...N$ section is bracketed by chains with entanglement numbers $\hat{Z}_{i-1}$ and $\hat{Z}_i$. In the approach used in this work and first developed by Peterson,[40,41] the partitions are drawn at lines of equal volume fraction. In our view, this is the simplest discretization scheme that guarantees convergence to the correct cumulative distribution when $N \to \infty$. Written in terms of the cumulative distribution function $\Phi_0(Z)$, the distribution scheme is formally given by:

$$\Phi_0(Z) \;=\; \int_0^Z \phi(Z')\mathrm{d}Z' \;=\; \frac{1}{2}\left[1+\mathrm{erf}\left[\frac{\ln(Z)-\mu)}{s\sqrt{2}}\right]\right], \tag{7.15}$$

$$\Phi_0(\hat{Z}_i) \;=\; i/N. \tag{7.16}$$

For the log-normal distribution, $\Phi_0(Z)$ can be inverted to obtain the set of $\hat{Z}_i$:

$$\hat{Z}_i \;=\; \exp\left[\mu + s\sqrt{2}\mathrm{erf}^{-1}\left[2\frac{i}{N}-1\right]\right]. \tag{7.17}$$

Now defining Z_i as the weight average molecular weight of chains in the range between $\hat{Z}_{i-1}$ and $\hat{Z}_i$, we approximate the continuous distribution by a discrete distribution of N components with entanglement numbers $Z_1, Z_2, Z_3, ..., Z_N$ and equal volume fractions $\phi_1 = \phi_2 = \phi_3 = ... = 1/N$. This strategy ensures that the mean entanglement number $\bar{Z} = \sum_i \phi_i Z_i$ is not changed by discretization. The end result for the discretization scheme is:

$$\begin{aligned} Z_i \;=\; \frac{1}{2}N\exp\left[\mu+\frac{1}{2}s^2\right]\Bigg[&\mathrm{erf}\left(\mathrm{erf}^{-1}\left(\frac{2i}{N}-1\right)-\frac{s}{\sqrt{2}}\right) \\ &-\mathrm{erf}\left(\mathrm{erf}^{-1}\left(\frac{2(i-1)}{N}-1\right)-\frac{s}{\sqrt{2}}\right)\Bigg]. \end{aligned} \tag{7.18}$$

7.3.2 Perturbation analysis

For orthogonal superposition, the oscillatory flow is assumed to be in the linear viscoelastic regime. Thus, the strain amplitude $\gamma_{0,\perp} \ll 1$ and $\gamma_{0,\perp}\tilde{\omega} \ll Wi$. Wi is the shear rate of the mean flow nondimensionalized by the Rouse time τ_R. In this case, we can use a perturbation analysis with a small parameter ϵ being the ratio of the magnitudes of the strain amplitudes of the orthogonal and main flow: $\epsilon = \frac{\gamma_{0,\perp}}{|\dot{\gamma}|}$. We shall assume a regular asymptotic solution structure and retain only the first order perturbation to the steady state solution. The superscript ”(0)” denotes the constant, order-one steady state solution and the superscript ”(1)” denotes the order-ϵ perturbation to the steady state value. With these notations, the stress tensor components and the chain stretch can be expressed as an expansion about the steady state levels: $\sigma_{ij}(t) = \sigma_{ij}^{(0)} + \epsilon\sigma_{ij}^{(1)}(t)$ and $\lambda(t) = \lambda^{(0)} + \epsilon\lambda^{(1)}(t)$. Furthermore, as in the numerical calculation, we nondimensionalize the stress by the plateau modulus G_N^0: $\tilde{\sigma}_{ij} = \sigma_{ij}/G_N^0$, which also equals the conformation tensor components A_{ij} according to Eqn. 7.2. Thus, we have $A_{ij}(t) = A_{ij}^{(0)} + \epsilon A_{ij}^{(1)}(t)$. We will first write the mathematical framework for the perturbation analysis using the monodisperse Rolie-Poly model. A similar procedure is used for the RDP model. For all six equations of the stress components in Equation 7.3, we collect the $\mathcal{O}(1)$ terms $^{(0)}$ and the $\mathcal{O}(\epsilon)$ terms $^{(1)}$. For the purpose of calculating the OSR moduli, we only need to solve the $\mathcal{O}(\epsilon)$ equation for $A_{yz}^{(1)}$:

$$\begin{aligned}\frac{\mathrm{d}A_{yz}^{(1)}}{\mathrm{d}t} &= A_{yy}^{(0)}\gamma_0\tilde{\omega}\cos(\tilde{\omega}t) \\ &- \left(\frac{1}{\theta} + 2\left(1-\frac{1}{\lambda^{(0)}}\right) + \frac{2\left(1-\frac{1}{\lambda^{(0)}}\right)}{\lambda^{(0)}}\right)A_{yz}^{(1)}.\end{aligned} \tag{7.19}$$

We can write this equation completely in terms of $\lambda^{(0)}$ by obtaining the steady state solution for $A_{yy}^{(0)}$:

$$A_{yy}^{(0)} = \frac{\lambda^{(0)} + 2\left(1-\frac{1}{\lambda^{(0)}}\right)\theta}{\lambda^{(0)} + 2\left(1-\frac{1}{\lambda^{(0)}}\right)\theta + 2\left(\lambda^{(0)}-1\right)\theta} \tag{7.20}$$

The equation for $A_{yz}^{(1)}$ can then be rewritten as:

$$\frac{\mathrm{d}A_{yz}^{(1)}}{\mathrm{d}t} + B\,A_{yz}^{(1)} = A_{yy}^{(0)}\gamma_0\tilde{\omega}\cos(\tilde{\omega}t) \tag{7.21}$$

with

$$B \;=\; \frac{1}{\theta} + 2\left(1 - \frac{1}{\lambda^{(0)}}\right) + \frac{2\left(1 - \frac{1}{\lambda^{(0)}}\right)}{\lambda^{(0)}}. \tag{7.22}$$

Equation 7.21 can be solved analytically for the OSR storage and loss moduli:

$$\frac{G'_{\perp}}{G_N^0} \;=\; \frac{A_{yy}^{(0)}\,\tilde{\omega}^2}{B^2 \,+\, \tilde{\omega}^2}, \tag{7.23}$$

$$\frac{G''_{\perp}}{G_N^0} \;=\; \frac{A_{yy}^{(0)}\,B\,\tilde{\omega}}{B^2 \,+\, \tilde{\omega}^2}. \tag{7.24}$$

Here, only the polymeric contribution is included. To include the solvent contribution, we can add $\eta_s\tilde{\omega}$ as in Eqn. 7.11. In Equation 7.23 and 7.24, $A_{yy}^{(0)}\left(\dot{\gamma}\right)$ and $B\left(\dot{\gamma}\right)$ are evaluated numerically from steady state Rolie-Poly equations without superposition. The values are then used in the equations to calculate $G'_{\perp}$ and $G''_{\perp}$ analytically. The perturbation analysis gives a speed-up of more than 100 times while offering the same accuracy compared to the numerical calculation of OSR moduli (see Appendix B Fig. B.3 for a comparison of the two results).

A similar procedure is used for the perturbation analysis using the RDP model for polydisperse polymers. In this case, $A_{ij}^{yy(0)}\left(\dot{\gamma}\right)$ and $B_{ij}\left(\dot{\gamma}\right)$ of each entanglement pair need to be determined from the steady state calculation. The OSR moduli are then sums of contributions from all entanglement pairs:

$$\frac{G'_{\perp}}{G_N^0} \;=\; \sum_{i=1}^{n}\sum_{j=1}^{n}\phi_i\phi_j\frac{A_{ij}^{yy(0)}\,\tilde{\omega}^2}{B_{ij}^2 \,+\, \tilde{\omega}^2}, \tag{7.25}$$

$$\frac{G''_{\perp}}{G_N^0} \;=\; \sum_{i=1}^{n}\sum_{j=1}^{n}\phi_i\phi_j\frac{A_{ij}^{yy(0)}\,B_{ij}\,\tilde{\omega}}{B_{ij}^2 \,+\, \tilde{\omega}^2}. \tag{7.26}$$

At this point, we reflect on the way in which we derived these relationships and their potential generality. Results for the orthogonal moduli in terms of the $yy-$component of the polymer conformation tensor come about from the convection of the normal stress through the upper-convected time derivative to the $yz-$component of the stress, which is the direction of the oscillation. Regardless of the constitutive model that is used, this is the procedure and the mathematical propagation that gives us a relationship similar to Eqn. 7.25 and 7.26. In fact, the linear proportionality between the plateau value of $G'_{\perp}$ and $A_{ij}^{yy(0)}(\dot{\gamma})$ not only holds for Rolie-Poly and RDP models, but also for any model with the upper-convected time derivative of the conformation tensor $\mathbf{A}$ and stress relaxation terms that are linear in the conformation tensor and any linear superposition of these models. The results are valid regardless of how the chain conformation is quantified: i.e., whether the end-to-end vector or the orientation tensor is used. A similar analysis on the DCR-CS model by Marrucci and Ianniruberto[24] (see Appendix B Section B.2.2) and the MLD model by Mead[25] produces the same relationship.

7.4 Results

7.4.1 Monodisperse case

We first present numerical calculations to obtain the orthogonal superposition moduli using the Rolie-Poly model. Figure 7.2 shows the computational results of a frequency De sweep for the oscillatory shear at different shear rates of the steady flow, i.e., Weissenberg numbers, $Wi = \dot{\gamma} \cdot \tau_{\mathrm{R}}$, ranging from 1 to 100. Initial studies of OSR on entangled polymers were limited to relatively low Wi, but recent advances in instrumentation have extended the accessible range to cover the range of Wi we study. These results are for a monodisperse polymer with an entanglement number of $Z = 20$, which is the same as what accompanied the original Rolie-Poly model formulation.[31] Consequently the ratio of the two relaxation timescales $\theta = \tau_{\rm d}/\tau_{\rm R} = 60$. We find two distinctive trends in the moduli behavior with increasing Wi. First of all, a horizontal shift is observed, which can be seen best in the rightwards shifting of the $G'_\perp$ - $G''_\perp$ crossover point. Secondly, $G'_\perp$ decreases monotonically with increasing main flow shear rates Wi. This effect can be seen best by the plateau values of the $G'_\perp$ curves. Comparing $G'_\perp$ and $G''_\perp$ at $Wi = 0.001$ to the linear viscoelastic moduli G' and G'' in the absence of flow (Fig. B.1 (b) in Appendix B) verifies that results at low flow rates approximate the result at equilibrium.

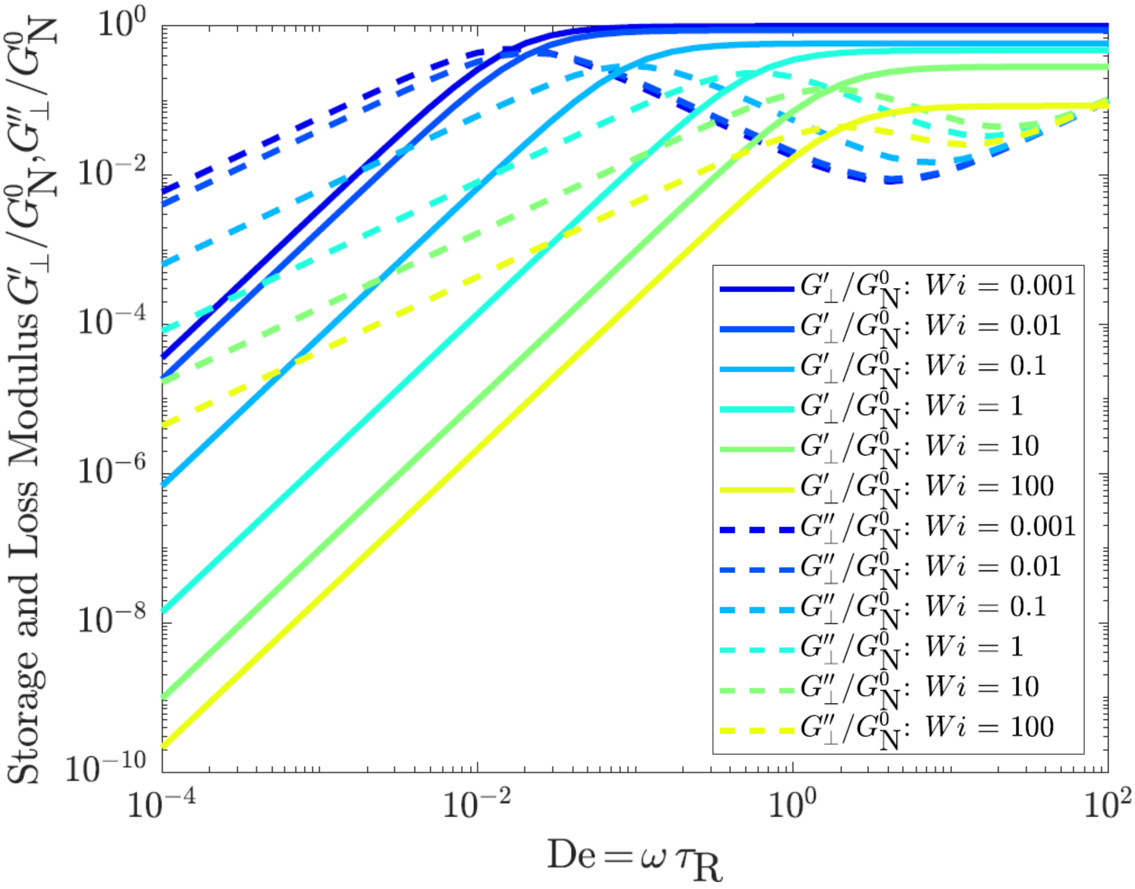

Figure 7.2: Orthogonal superposition moduli for monodisperse polymers at six different shear rates (Wi).

Furthermore, evaluating the contribution of each stress relaxation mechanism (reptation, retraction and CCR) in the $yz-$component of the stress, $\tilde{\sigma}_{yz}$, provides a better understanding of the causes of the shifts in the OSR moduli. Figure 7.3 shows the fractional contribution of relaxed orthogonal stress terms separated by relaxation mechanism, at a frequency of $De = 0.001$. The shape of the plots is independent of the choice of the frequency. As Wi increases, contributions of the stretch-based phenomena (retraction and CCR) increase, with CCR developing a maximum and then decreasing. In contrast, reptation starts at 100 % for very low shear rates and decreases with Wi to a value close to 0 %. This is because the stress relaxed by reptation approaches a constant when the inverse of the disentanglement time τ_d is reached. Consequently, the reptation contribution in the Rolie-Poly model remains constant, while retraction and CCR start dominating relaxation for increasing Wi. In the first part of their increase, the same slope is observed. However, as Wi continues to increase the chains can retract only partially from affine stretch, and convective constraint release is less effective and the relative magnitude of the CCR contribution decreases. At the same frequencies, the retraction term develops a shoulder. Finally, at sufficiently large Wi, retraction dominates the relaxed stress with a value close to 100 %.

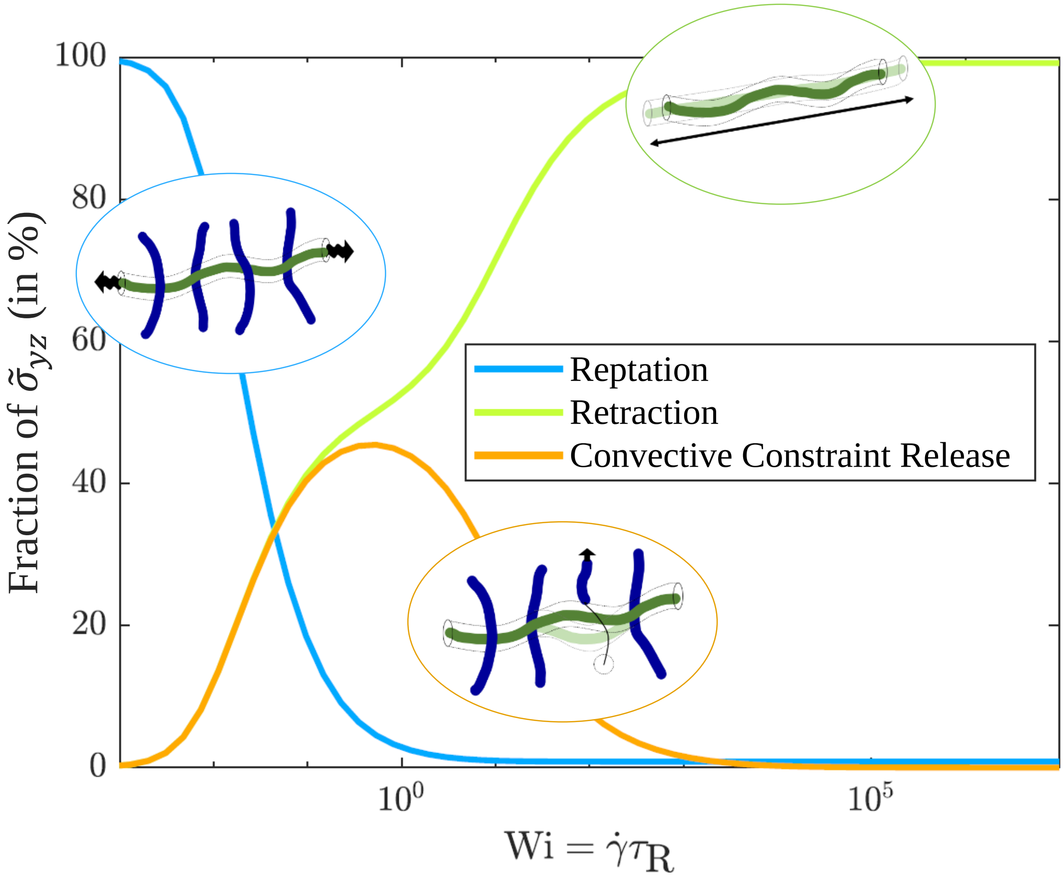

Figure 7.3: Fractional stress contribution of different relaxation mechanisms in $yz-$component of polymer stress.

By examining the numerical results alone, it is difficult to pinpoint what physical phenomena directly cause the horizontal and vertical shifts. If these were purely linear viscoelastic measurements under different temperatures and concentrations, researchers would typically perform a time-temperature superposition or time-concentration superposition and force all of these curves to collapse. Here, we show that we can achieve such a collapse with shift factors. Furthermore, these shift factors can be predicted based on the perturbation analysis results in Eqns. 7.23 and 7.24. By assuming the superposed oscillation is a small perturbation to the main shear flow ($\gamma_{0,\perp} << 1$ and $\gamma_{0,\perp}\, De << Wi$), we obtained analytical expressions for $G'_\perp$ and $G''_\perp$ in Equations 7.23 and 7.24. Using the two parameters $A_{yy}^{(0)}\left(\dot{\gamma}\right)$ and $B\left(\dot{\gamma}\right)$ identified in the analytical expressions, we scaled the numerical results from Figure 7.2 after subtracting out the solvent contribution $(\eta_s\tilde{\omega})$. This procedure completely collapses all the Wi-dependent moduli onto a single set of curves. Specifically, we divided the OSR moduli by $A_{yy}^{(0)}\left(\dot{\gamma}\right)$ and divided the dimensionless frequency by $B\left(\dot{\gamma}\right)$ (Fig. 7.4(a)). The collapse of the curves suggests that the steady shear flow only speeds up the relaxation and decreases the effective oscillatory driving force, without changing the relaxation mechanism.

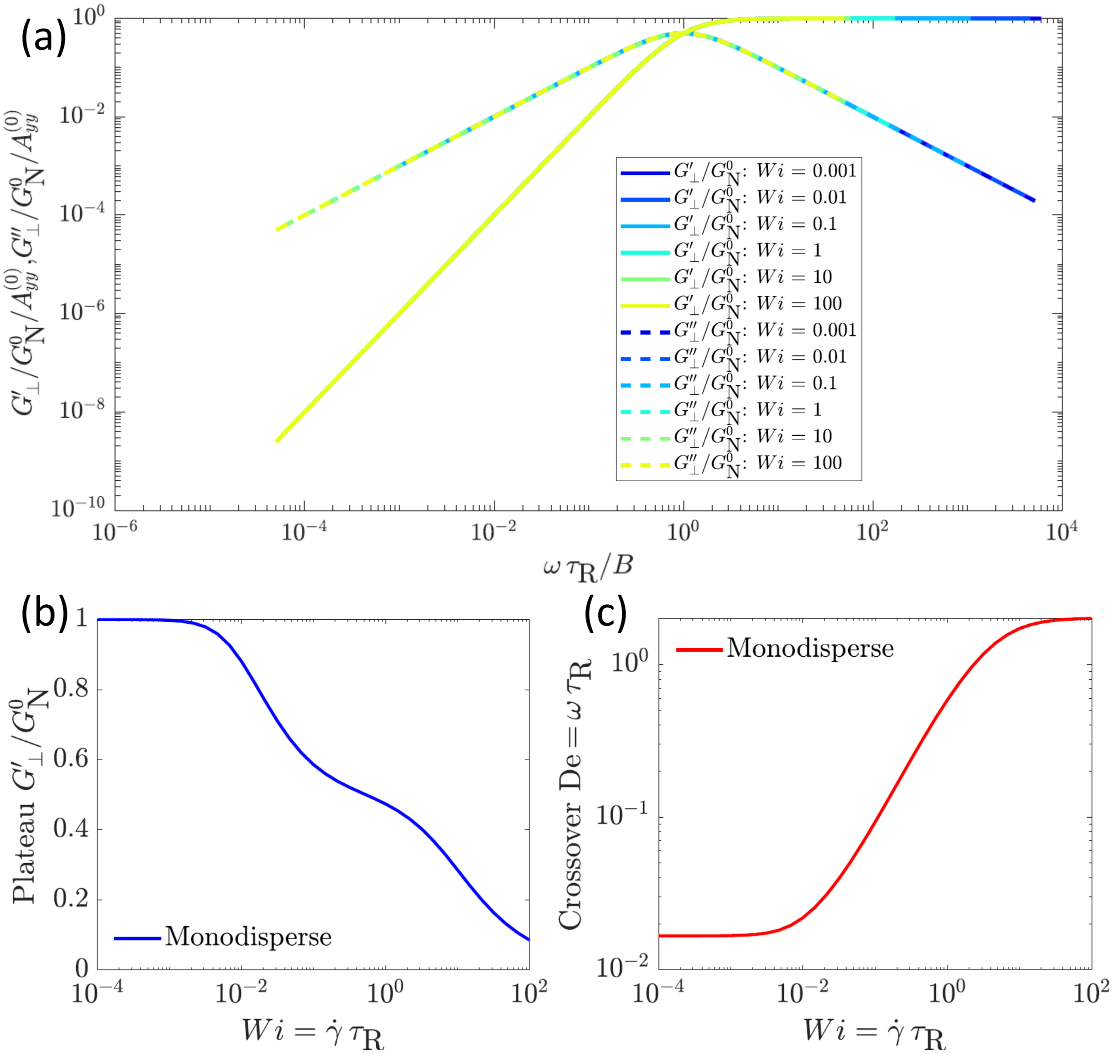

Figure 7.4: (a) Rescaling superposition moduli by $A^{(0)}_{yy}$ and frequency by B collapses superposition moduli at different shear rates onto one set of curves. (b) Changes in plateau modulus ($A^{(0)}_{yy}$) as a function of Wi. (c) Changes in crossover frequency as a function of Wi.

We can further quantify the magnitude of the vertical shift by plotting the plateau value of dimensionless $G'_\perp$ as a function of Wi (Fig. 7.4(b)). In fact, in the plateau, we have: $\lim_{\tilde\omega>>1}\frac{G'_\perp}{G^0_N} = A^{(0)}_{yy}(\dot\gamma)$. With increasing Wi, the $G'_\perp$ monotonically decreases. Around $Wi = 1$, a shoulder shape appears in the plateau (also in $A^{(0)}_{yy}(\dot\gamma)$), similar to the shoulder shape in the retraction contribution in Fig. 7.3. This shoulder again arises due to the competition of retraction and convective constraint release. Since Wi is defined in terms of the Rouse time τ_R, $Wi = 1$ represents the start of significant chain stretch, which results in increased contribution of the stress relaxation by chain retraction. We can also quantify the horizontal shift by plotting the frequency at the crossover of $G'_\perp$ and $G''_\perp$ as a function of Wi (Fig. 7.4(c)). With increasing Wi, the crossover frequency monotonically increases. In linear viscoelastic measurements, the inverse of the crossover frequency gives a characteristic relaxation time of the system: $\tau = 1/\omega_c$. So, Fig. 7.4(c) indicates the effective relaxation time of the polymers is decreasing with increasing Wi. By examining Eqn. 7.23 and 7.24, we find the crossover frequency equals B. To get a better understanding of what $A^{(0)}_{yy}\left(\dot{\gamma}\right)$ and $B\left(\dot{\gamma}\right)$ represent physically, we can return the $G'_\perp$ and $G''_\perp$ results in Eqns. 7.23 and 7.24 to dimensional form:

$$G'_\perp = \frac{\sigma^{(0)}_{yy}\left(\tau_{eff}\omega\right)^2}{1+\left(\tau_{eff}\omega\right)^2} \text{ and } G''_\perp = \frac{\sigma^{(0)}_{yy}\tau_{eff}\omega}{1+\left(\tau_{eff}\omega\right)^2}, \tag{7.27}$$

with

$$\tau_{eff} = \frac{\tau_d}{1+\frac{\tau_d}{\tau_R}\left(2-\frac{2}{\lambda^2}\right)}. \tag{7.28}$$

The effective relaxation time τ_{eff} represents the speedup of the stress relaxation in flow. Its asymptotic value changes from $\tau_{eff} = \tau_d$ at low Wi before the onset of chain stretch to $\tau_{eff} = \tau_R/2$ for very large chain stretch. So, $A^{(0)}_{yy}\left(\dot{\gamma}\right)$ represents the nonlinear shear-dependent chain conformation in the $yy-$direction, which is orthogonal to the main flow direction, and $B\left(\dot{\gamma}\right)$ represents the nonlinear shear-dependent relaxation rate.

As discussed in Section 7.2.1, for conventional linear viscoelastic measurements, the plateau modulus G^0_N is used to estimate the entanglement length while the ratio of the plateau modulus and G''_{min} is used to estimate the number of entanglements. Thus, LVE G' and G'' moduli are used to estimate average chain length, and previous investigators have assumed that the corresponding orthogonal superposition (OSR) moduli can be interpreted in the same way, thus providing a way to explore the effect of a steady shear flow on chain scission for wormlike micelles and other "living" polymers.[5,42] However, we see that the decrease in $G'_{\perp}$ with increasing Wi in Fig. 7.4(b) and the decrease in the ratio of the plateau and G''_{min} in Fig. 7.2 occur without any modification to the properties of the chain; for example, those that might be extracted from a scaling analysis of the linear viscoelasticity (i.e. the number of entanglements is fixed at 20 per chain). The plateau value and the crossover frequency change due to chain stretch and orientation, as illustrated in the contribution of stress relaxation in Fig. 7.3. Therefore, changes in the plateau modulus and relaxation time cannot be interpreted simply as due to changes in the scaling variables (e.g. entanglement length, entanglement density, etc.). This is consistent with a recent Brownian dynamics simulation for star polymers,[43] in which Metri and Briels showed that the shear relaxation modulus from orthogonal superposition is not the same as the stress relaxation modulus from step strain (as is the case for linear viscoelastic experiment at equilibrium), even for weak shear flow in the OSR experiment.

Although the data interpretation from the OSR measurement is complicated even for a monodisperse polymer, the perturbation analysis nevertheless offers physical insights to pinpoint the material properties that cause the change in the OSR moduli. Before moving to the polydisperse calculations, we first demonstrate the generality of the perturbation analysis by applying it to a different model, the DCR-CS (double-convection-reptation model with chain stretch) by Marrucci and Ianniruberto.[24] As shown in Appendix B Section B.2.2, the resulting expressions for the OSR moduli are the same as those from the Rolie-Poly model (Eqns. 7.23 and 7.24). The differences are in the expressions for $A^{(0)}_{yy}\left(\dot{\gamma}\right)$ and $B\left(\dot{\gamma}\right)$. Even though these expressions are different, the similarity in the functional dependence of $G'_{\perp}$ and $G''_{\perp}$ on $A^{(0)}_{yy}\left(\dot{\gamma}\right)$ and $B\left(\dot{\gamma}\right)$ indicates that the dependence of the plateau shift on the $yy-$component of the chain conformation and the horizontal shift on the effective relaxation time are model-independent and represent the physical phenomena that determine the OSR moduli for linear polymers of fixed chain length.

7.4.2 Polydisperse case: log-normal distribution

To systematically study the effect of polydispersity on the OSR moduli, we used a discretized log-normal molecular weight distribution, as discussed in Section 7.3.1. Specifically, we used 32 bins to represent the continuous MW distribution with equal volume fraction in each bin. The polydispersity index was varied from 1.01, which is nearly monodisperse, to 5, which has a long tail. The weight-average molecular weight (weight-average number of entanglements per chain, $\bar{Z}$) is fixed at 20. Figure 7.5(a) plots all of the molecular weight distributions used in this work. First, we compare the numerical calculations at two representative cases of the degree of polydispersity: $PDI = 1.01$ and $PDI = 2$ in Figure 7.5(b) and (c), respectively. For $PDI = 1.01$, the results are nearly identical to the monodisperse results in Fig. 7.2. For $PDI = 2$, the effects of polydispersity are more evident. Specifically, the shoulder in the storage modulus becomes broader at all Wi and the plateau value decreases less. The gradual evolution of the polydisperse moduli reflects the broad relaxation spectrum in the highly polydisperse system (i.e. many relaxation times). As we will show below, the weakened softening of the plateau for the polydisperse case compared to the monodisperse case arises from the nonlinear dependence of $A_{ij}^{yy(0)}$ on the chain length Z_i. The presence of the short chains causes the plateau to decrease less than the monodisperse case.

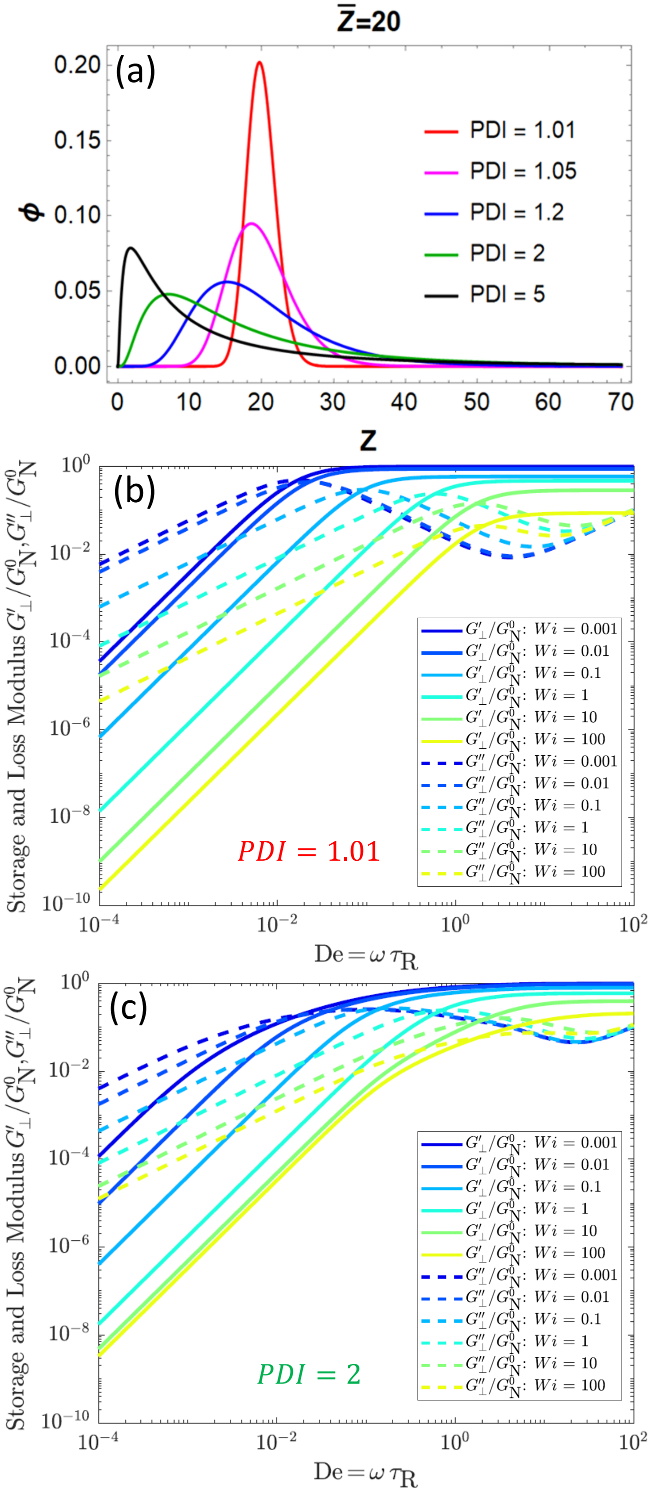

Figure 7.5: Polydisperse calculations: (a) Log-normal molecular weight distributions used in this work. (b) OSR moduli for $PDI = 1.01$ (c) OSR moduli for $PDI = 2$.

To better quantify the horizontal and vertical shifts in the OSR moduli, we can plot the plateau value and the location of the apparent crossover frequency as a function of Wi for different PDI. However, having to account for N^2 number of chain pairs for all combinations of De and Wi significantly increases the computational time for the polydisperse case compared to the monodisperse case. Thus, once again, we turn to a perturbation analysis to obtain analytical expressions for the OSR moduli, which makes prediction of OSR moduli at finely resolved Wi and De possible. The procedure for the perturbation analysis and the main results are described in Section 7.3.2. We verified that the perturbation analysis produced identical results as the full numerical calculations. So, subsequently, we only report results from the perturbation analysis.

Figure 7.6 quantifies changes in the OSR moduli and crossover frequency as a function of Wi for varying degrees of polydispersity: PDI = 1.01, 1.05, 1.2, 2, 5 and for the monodisperse result (shown as the solid black curve). The crossover frequency $G'_\perp$ and $G''_\perp$ increases monotonically with increasing Wi for all cases except for $PDI = 5$ (Fig. 7.6(a)). For $PDI = 5$ and $Wi > 10$, the decrease of the crossover frequency at large Wi is a result of significant stretching of the longest chains in the system. Such extreme stretching is unphysical for finitely extensible chains, and can be removed with the inclusion of a Warner spring[44] (see Appendix B Fig. B.7(a)). Figure B.7 compares the linear spring calculation with the Warner spring calculation. The sub-figures (a)-(d) are organized similarly to those in Figure 7.6 here. Predictions using the Warner spring only start to differ significantly from predictions for the linear spring for $Wi > 10$ and $PDI \geq 2$. On the one hand, across most of the parameter space (spanning different shear rates and PDI) that is accessible experimentally, the predictions for the linear and Warner spring are very similar. On the other hand, the Warner spring adds extra complications associated with an additional parameter λ_{max}, the maximum chain stretch. Thus, we will only discuss results for the linear spring in the main paper. At low dispersity, the moduli value at the crossover decreases monotonically with Wi (Fig. 7.6(b)). However, for $PDI = 2$ and 5, the moduli at the crossover first increase then decrease with Wi. The $G'_{\perp}$ plateau decreases monotonically with increasing Wi for all cases (Fig. 7.6(c)). With increasing PDI, the curves deviate more and more from the monodisperse curve. Additionally, the shoulder shape in the monodisperse result that arises from the competition between retraction and CCR becomes smoothed out with increasing polydispersity. Interestingly, the monodisperse result for the moduli at the crossover has the same shape as the monodisperse plateau value, with the former being half of the magnitude. This effect is better illustrated in Fig. 7.6(d), in which the ratio of the crossover moduli and the plateau moduli is plotted as a function of Wi for the monodisperse case and all polydisperse cases. The monodisperse case is a flat line at 0.5 for all Wi which indicates that for a monodisperse polymer, the moduli value at the crossover is exactly half of the plateau value for all Wi. Examining the perturbation result for the monodisperse case (Eqns. 7.23 and 7.24) illustrates this point more clearly. At the crossover, $G'_{\perp} = G''_{\perp}$ and $B\left(\dot{\gamma}\right) = \tilde{\omega}$. Thus, the moduli value at the crossover equals $A^{(0)}_{yy}\left(\dot{\gamma}\right)/2$. However, the Wi-independent, constant moduli ratio is not preserved in the polydisperse cases. With increasing polydispersity, the ratio decreases and becomes more non-monotonic (Fig. 7.6(d)).

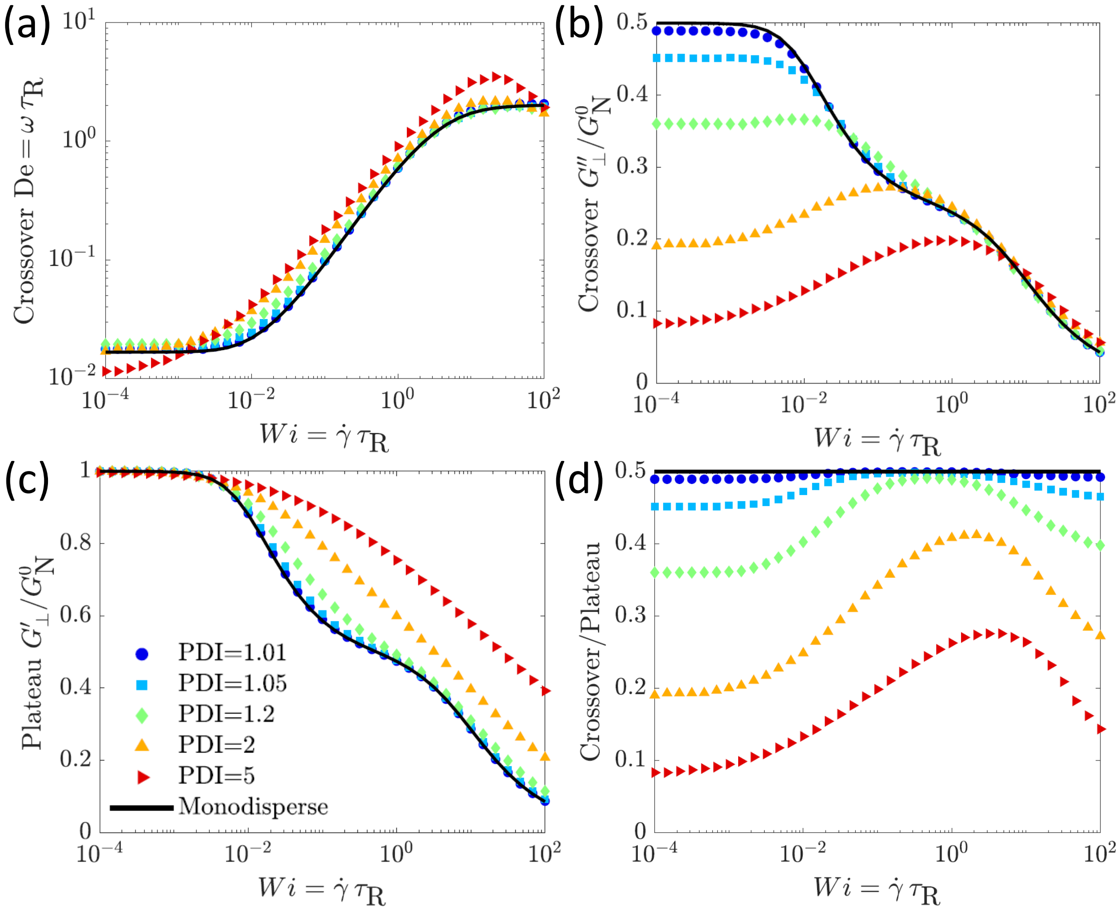

Figure 7.6: Quantify changes in OSR moduli as a function of Wi for varying degree of polydispersity: (a) crossover frequency, (b) moduli at crossover, (c) plateau modulus, (d) ratio of moduli at crossover and plateau.

The reason for all the changes in the polydisperse results compared to the monodisperse result, as illustrated in Fig. 7.6(a)-(d), arises from the fact that the OSR moduli for the polydisperse case are summations of the contributions from all entanglement pairs and the OSR moduli are affected by the interactions between chains of different length (Eqns. 7.25 and 7.26). In particular, instead of being solely determined by the $A_{yy}^{(0)}(\dot{\gamma})$ component of a single chain length as in the monodisperse case, the polydisperse plateau modulus is determined by $\sum_{i=1}^{n}\sum_{j=1}^{n}\phi_i\phi_j\,A_{ij}^{yy(0)}(\dot{\gamma}) = A_{yy}^{(0)}(\dot{\gamma})$, which represents the dimensionless weight-average chain conformation in the $yy-$direction of the entire population of chains.

However, a weight-average of $B_{ij}\left(\dot{\gamma}\right)$ for all entanglement pairs does not yield the overall effective relaxation rate (i.e., the crossover frequency) for the polydisperse case. This is because $B_{ij}\left(\dot{\gamma}\right)$ appears in the denominator of the individual moduli terms that are summed together. Thus, for polydisperse systems, although there is a qualitative correlation of the data with the degree of polydispersity, as shown in Fig. 7.6 especially in (d) for the ratio of the moduli, no simple scaling exists to explain the shifts in the moduli, as in the monodisperse case.

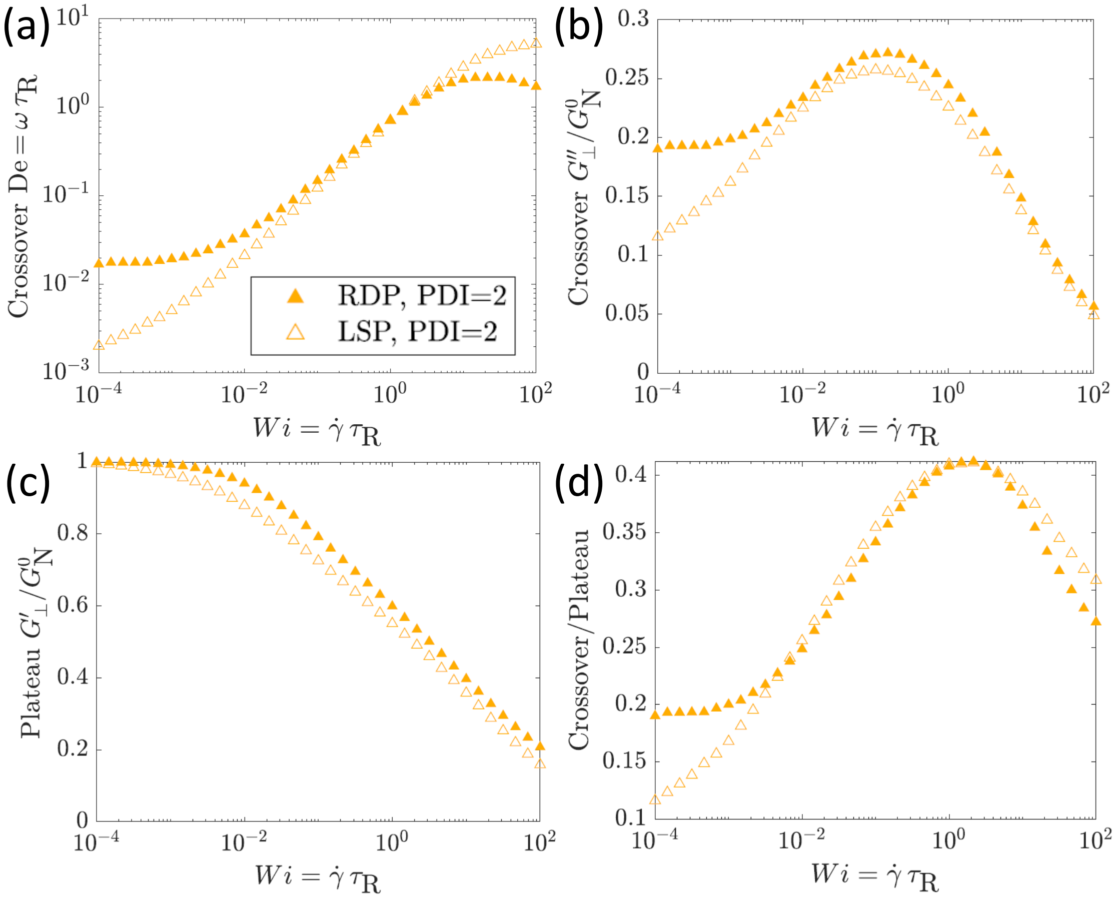

Figure 7.7: Comparison of results for RDP model with a simple linear superposition (LSP) of monodisperse results for $PDI = 2$; (a) crossover frequency, (b) modulus at crossover, (c) plateau modulus, (d) ratio of moduli at crossover and plateau.

One may wonder to what extent the changes in the OSR moduli in the polydisperse case can be understood by simple superposition of results for the discrete chains as opposed to needing the full double reptation physics included in the RDP model. Here, we make a comparison of the RDP results for $PDI = 2$ shown in Fig. 7.6 and the results of the simple superposition of the monodisperse results for each discrete species in the polydisperse calculation. Thus, for the linear superposition case, we have, $\frac{G'_{\perp}}{G_N^0} = \sum_{i=1}^{n} \phi_i \frac{A_i^{yy(0)} \tilde{\omega}^2}{B_i^2 + \tilde{\omega}^2}$ and $\frac{G''_{\perp}}{G_N^0} = \sum_{i=1}^{n} \phi_i \frac{A_i^{yy(0)} B_i \tilde{\omega}}{B_i^2 + \tilde{\omega}^2}$, where $A_i^{yy(0)}(\dot{\gamma})$ and $B_i(\dot{\gamma})$ are calculated from the perturbation analysis for the monodisperse case for chains of length Z_i and the values for Z_i are obtained from the discretization of the log-normal distribution. The sub-figures (a)-(d) in Fig. 7.7 are organized similarly to the sub-figures in Fig. 7.6. Although the two sets of predictions share similar qualitative trends, the simple superposition cannot quantitatively capture the changes in the crossover frequency and crossover moduli at low Wi. Thus, the full double reptation physics is needed to quantitatively describe the OSR moduli. We also note that the amount of discrepancy between the simple superposition results and the RDP results increases with increasing PDI. Nevertheless, since the plateau value at large Wi ($Wi = 100$) is nearly identical for the simple superposition and the RDP model, the simple superposition results can be used to explain the weakened softening of the plateau value for the polydisperse case compared to the monodisperse case, as observed in Fig. 7.5(c) and Fig. 7.6(c). As shown in Appendix B Fig. B.7, the $yy-$component of the conformation tensor $A_i^{yy(0)}$ depends nonlinearly on the chain length Z_i. Thus, for a discretized distribution of the log-normal distribution with a weight-average the same as the chain length in the monodisperse case, the weight-average of $A_i^{yy(0)}$ is not the same as $A_{yy}^{(0)}$ for the monodisperse case.

In conclusion, the presence of chains of different length results in the smoother transition to the plateau. The presence of short chains and the nonlinear dependence of $A_{ij}^{yy(0)}$ on the chain length results in the weakened softening of the plateau compared to the monodisperse case. Although a simple superposition of the monodisperse results can capture the qualitative trends observed in the polydisperse OSR moduli, to obtain quantitative predictions, the double reptation physics is needed.

7.5 Discussion

Given the results just presented, we will now provide perspective on how this work could potentially help aid the design and interpretation of orthogonal superposition experiments.

7.5.1 An analogy to Laun's rule

By using a combination of numerical calculations and perturbation analysis, we showed for both the monodisperse case and the polydisperse case, the plateau of the orthogonal modulus is completely determined by the $yy-$component of the polymer conformation in the steady imposed shear, namely:

$$\lim_{\tilde{\omega}>>1} \frac{G'_{\perp}\left(\dot{\gamma}\right)}{G_N^0} = A_{yy}^{(0)}\left(\dot{\gamma}\right), \tag{7.29}$$

where $A_{yy}^{(0)}\left(\dot{\gamma}\right) = \sum_{i=1}^{n}\sum_{j=1}^{n}\phi_i\phi_j A_{ij}^{yy(0)}\left(\dot{\gamma}\right)$ is the weight-averaged result for the polydisperse case. As we discussed in the theory section 7.3.2, Eqn. 7.29 is generally valid for any model with the upper-convected derivative of the conformation tensor $\boldsymbol{A}$ and relaxation terms that are linear in the conformation tensor or any linear superposition of these models. Given this result and its generality, we can use orthogonal superposition measurements to obtain estimates of $A_{yy}^{(0)}\left(\dot{\gamma}\right)$. Experimentally, this is accomplished by shifting $G'_{\perp}$ and $G''_{\perp}$ at different shear rates to achieve a complete overlap, in the same manner performed routinely for linear viscoelastic measurements for the purpose of time-temperature or time-concentration superposition, one can obtain shift factors

$\alpha\left(\dot{\gamma}\right) = \frac{G'_{\perp}(\omega,\dot{\gamma})}{G'_{\perp}(\omega,\dot{\gamma}=0)} = \frac{G''_{\perp}(\omega,\dot{\gamma})}{G''_{\perp}(\omega,\dot{\gamma}=0)}$. We can use the vertical shift factors to obtain $A^{(0)}_{yy}\left(\dot{\gamma}\right)$:

$$A^{(0)}_{yy}\left(\dot{\gamma}\right) = \alpha\left(\dot{\gamma}\right) A^{(0)}_{yy}\left(\dot{\gamma} = 0\right) = \alpha\left(\dot{\gamma}\right). \tag{7.30}$$

It's worth noting here that in time-temperature superposition, the conventional nomenclature for the vertical shift factor is b. Since we already used B to represent the dimensionless crossover frequency, which is related to the horizontal shift, we are using α to represent the vertical shift factor.

Since a rheological constitutive equation for an incompressible fluid only specifies the stress to within an arbitrary isotropic component, we cannot use $A^{(0)}_{yy}\left(\dot{\gamma}\right)$ to directly determine the normal stress component in the $yy-$direction, σ_{yy}. However, we can attempt to make predictions of the first normal stress difference, N_1. In particular, for the Rolie-Poly model, we can solve for the steady state value of $A^{(0)}_{xx}\left(\dot{\gamma}\right)$ using the $\mathcal{O}(1)$ equation in the perturbation analysis (see section B.2.5 in Appendix B for the detailed derivation). Then, using results for $A^{(0)}_{yy}\left(\dot{\gamma}\right)$ and $B\left(\dot{\gamma}\right)$, we obtain:

$$N_1\left(\dot{\gamma}\right) = G^0_N\left(A^{(0)}_{xx} - A^{(0)}_{yy}\right) = 2G^0_N A^{(0)}_{yy}\left[\frac{Wi}{B}\right]^2. \tag{7.31}$$

If we recall that $Wi = \dot{\gamma}\cdot\tau_R$ and $B\left(\dot{\gamma}\right)$ represents the dimensionless crossover frequency, $B\left(\dot{\gamma}\right) = \tilde{\omega}_{c,\dot{\gamma}} = \omega_{c,\dot{\gamma}}\cdot\tau_R$, we get:

$$N_1\left(\dot{\gamma}\right) = 2G^0_N A^{(0)}_{yy}\left[\frac{\dot{\gamma}}{\omega_{c,\dot{\gamma}}}\right]^2. \tag{7.32}$$

Experimentally, this means we can use the plateau value of $G'_{\perp}\left(\dot{\gamma}\right)$, i.e., $G^0_N A^{(0)}_{yy}\left(\dot{\gamma}\right)$, the applied shear rate, $\dot{\gamma}$, and the shear-rate dependent crossover frequency, $\omega_{c,\dot{\gamma}}$, to completely determine the first normal stress difference $N_1\left(\dot{\gamma}\right)$. In the limit where a single-mode model accurately describes the experimental data, one can use this relation to determine $N_1(\dot{\gamma})$. We can further rearrange Eqn. 7.32 to get:

$$\lim_{\omega \to \infty} \left[\frac{G'_{\perp}(\omega, \dot{\gamma})}{\omega^2_{c,\dot{\gamma}}} \right] = \frac{N_1(\dot{\gamma})}{2\dot{\gamma}^2}. \tag{7.33}$$

Previously, several relations have been proposed to connect the first normal stress difference or the yy-component of the stress to more easily measurable quantities in shear flow. Specifically, Holroyd et al.[45] derived analytical solutions of the Rolie-Poly model and found an expression to relate the recoverable strain to the yy-component of the stress, $\gamma_{rec} = \frac{\sigma^0_{xy}}{\sigma^0_{yy}}$. This theoretical result has been verified in molecular dynamics simulations of entangled polymers.[46] In LAOS measurements, Lee et al. found $N_1(t) = 2G(t)\gamma^2_{rec}(t)$, where $G(t)$ is the recoverable strain-dependent elastic modulus and γ_{rec} is the recoverable strain.[47] Tanner and Williams[48] used the phenomenological K-BKZ model[49,50] to derive a relationship between the OSR moduli and the first normal stress difference: $\lim_{\omega \to 0} \left[\frac{G'_{\perp}(\omega,\dot{\gamma})}{\omega^2} \right] = \frac{N_1(\dot{\gamma})}{2\dot{\gamma}^2}$. This relation only works in the low-frequency limit and is specific to the K-BKZ model. The well-known Laun's rule[32] relates the first normal stress difference to the linear viscoelastic moduli and is predicted to work for any general viscoelastic model: $N_1(\dot{\gamma}) = 2G'(\omega) \left[1 + \left(\frac{G'(\omega)}{G''(\omega)} \right)^2 \right]^{0.7} \bigg|_{\omega = \dot{\gamma}}$. Our result is an alternative set of relations that may prove more useful depending on where the sensitivity of the measurement lies. Previous rules provide relationships that are generally valid at asymptotically small frequencies and shear rates. We can now make a similar comparison at asymptotically large frequencies, which is usually the region with better instrumental sensitivity. Notably, the normal stress component is obtained as a byproduct of measuring the plateau of the orthogonal modulus without having to build extra instrumentation to measure the normal stress.

7.5.2 Determination of constitutive parameters

From the perturbation analysis, we found the horizontal shift of the OSR moduli is determined by the effective relaxation rate $B\left(\dot{\gamma}\right)$. In the context of the Rolie-Poly model (i.e. for monodisperse polymers), since both $A_{yy}^{(0)}\left(\dot{\gamma}\right)$ and $B\left(\dot{\gamma}\right)$ only depend on the ratio of relaxation time θ, the CCR parameter β_{CCR}, and chain stretch due to the steady shear flow $\lambda^{(0)}$, OSR experiments can be used to estimate chain stretch and the CCR parameter β_{CCR}. Specifically, one can first use linear viscoelastic measurements to estimate the Rouse time τ_R and the reptation time τ_d. Then, one can subtract the solvent contribution from the orthogonal superposition measurement (in the values for $G''_\perp$). Next, $G'_\perp$ and $G''_\perp$ at different shear rates are shifted numerically to achieve a complete overlap with associated shift factors $\alpha\left(\dot{\gamma}\right)$ and $B\left(\dot{\gamma}\right)$. Finally, we can use the crossover frequencies to obtain the relaxation rate $B\left(\dot{\gamma}\right)$. For the simplest case of $\beta_{CCR} = 1$ as we assumed in the previous calculations, we can obtain chain stretch $\lambda\left(\dot{\gamma}\right)$ from the crossover frequency:

$$\lambda\left(\dot{\gamma}\right) = \sqrt{\frac{2}{2 - \left(\omega_{c,\dot{\gamma}}\,\tau_R - \omega_{c,eqm}\,\tau_R\right)}}. \tag{7.34}$$

In order to obtain both $\lambda\left(\dot{\gamma}\right)$ and β_{CCR}, we need to use expressions for $A_{yy}^{(0)}\left(\dot{\gamma}\right)$ and $B\left(\dot{\gamma}\right)$ that include β_{CCR}:

$$A_{yy}^{(0)} = \frac{\lambda^{(0)} + 2\beta_{CCR}\left(1 - \frac{1}{\lambda^{(0)}}\right)\theta}{\lambda^{(0)} + 2\beta_{CCR}\left(1 - \frac{1}{\lambda^{(0)}}\right)\theta + 2\left(\lambda^{(0)} - 1\right)\theta} \tag{7.35}$$

$$B = \frac{1}{\theta} + 2\left(1 - \frac{1}{\lambda^{(0)}}\right) + \frac{2\beta_{CCR}\left(1 - \frac{1}{\lambda^{(0)}}\right)}{\lambda^{(0)}}. \tag{7.36}$$

By fitting the shear rate dependent experimental values of $A_{yy}^{(0)}\left(\dot{\gamma}\right)$ and $B\left(\dot{\gamma}\right)$ to Eqns. 7.35 and 7.36, we can obtain $\lambda\left(\dot{\gamma}\right)$ and β_{CCR}. Furthermore, using Eqn. 7.30 and converting $B(\dot{\gamma})$ to dimensional form ($B(\dot{\gamma}) = \omega_{c,\dot{\gamma}}\,\tau_R$), we obtain expressions for $\lambda(\dot{\gamma})$ and β_{CCR} in terms of the vertical shifting factor $\alpha(\dot{\gamma})$ and crossover frequency measured in experiments:

$$\lambda(\dot{\gamma}) = \frac{2}{2 - \omega_{c,\dot{\gamma}}\,\tau_R\,(1 - \alpha(\dot{\gamma}))}, \tag{7.37}$$

and

$$\beta_{CCR} = \frac{\alpha(\dot{\gamma})\,\omega_{c,\dot{\gamma}}\,\tau_R - \frac{\tau_R}{\tau_d}}{\omega_{c,\dot{\gamma}}\,\tau_R\,(1 - \alpha(\dot{\gamma})) - \frac{\omega_{c,\dot{\gamma}}^2\,\tau_R^2\,(1-\alpha(\dot{\gamma}))^2}{2}}. \tag{7.38}$$

Typically, the CCR parameter is assumed to be a constant and independent of shear rate. In the case that model predictions are used to generate the OSR moduli, as in the present analysis, Eqn. 7.38 can be used to test the self-consistency of β_{CCR}. More interestingly, in the case of experimental data where the apparent value(s) of the nonlinear constitutive model parameter(s) is unknown and in the limit where a single mode model accurately describes the experimental data, one can use this shifting procedure in order to extract and fit model parameters of the desired constitutive equation. In order to successfully estimate model parameters from OSR experiments, we therefore give the following recommendations: 1) The shear rates need to span a large enough range to cover both the case of no chain stretch and the case of significant chain stretch ($\dot{\gamma}\tau_R > 1$). 2) The frequency range needs to span from values below the crossover frequency at equilibrium to frequency values corresponding to the plateau of $G'_\perp$ in flow.

7.5.3 Physical interpretation of OSR moduli

We now discuss the implications of our analysis on the more general issue of the physical interpretation of OSR moduli measured in experiments in the absence of a particular constitutive model. In light of Figure 7.6, the plateau modulus for both the monodisperse and polydisperse cases decreases with increasing Wi and the moduli shifts horizontally without any modification to the properties of the chain; e.g., those that might be extracted from a scaling analysis of the linear viscoelasticity. For example, in previous orthogonal superposition experiments on wormlike micelles by Vermant and coworkers[5] and Rothstein and coworkers,[42] the authors assumed by analogy with linear viscoelasticity $\xi_m\left(\dot{\gamma}\right) = \left(\frac{k_BT}{G'_{\perp}\left(\dot{\gamma}\right)|_{\omega\to\infty}}\right)^{1/3}$ to estimate the apparent, shear-rate dependent mesh size, ξ_m, from the plateau modulus of orthogonal superposition moduli, $G'_{\perp}\left(\dot{\gamma}\right)|_{\omega\to\infty}$. Vermant and coworkers linked the systematic decrease of the plateau modulus to shear-induced changes in the mesh size of the micellar network. Rothstein and coworkers went further to suggest the change in the mesh size is related to the breakage of micelles in flow. However, our analysis of OSR for the Rolie-Poly model clearly shows, even in the context of regular polymers, the plateau modulus decreases with increasing shear flow due to stretch-based relaxation mechanisms (CCR and retraction), in the absence of any chain breakage. A comparison between the experiments on WLMs by Rothstein and coworkers and our RDP model calculation with a log-normal distribution of $PDI = 2$ shows a similar change in the plateau modulus ($\sim 20\%$) over the comparable range of Wi, suggesting that changes in entanglement dynamics are important and must be considered in this range. Additionally, the effect of polydispersity adds another complication for any analysis that tries to extract chain length in flow from the plateau of OSR moduli. As such, one cannot simply use empirical relationships for estimating length that are developed for equilibrium linear viscoelastic measurements, such as those described in Section 7.2.1, to interpret OSR results. This knowledge from simulations is very useful for interpreting OSR experiments.

In addition to the applicability of linear viscoelastic scaling analysis, one may wonder about the potential for using OSR moduli to infer or understand polydispersity effects given the present analysis. We identified new parameterization of the OSR moduli to qualitatively relate to the degree of polydispersity. Specifically, the ratio of the moduli at the crossover to the plateau modulus as a function of shear rate becomes increasingly nonmonotonic and deviates from the constant value of 0.5 with increasing degree of polydispersity (Fig. 7.6(d)). Although Fig. 7.6 focuses on the result for the log-normal distribution, the qualitative trend also holds for other continuous, broad distributions, except for a bi-modal distribution with sharp peaks. In particular, for $PDI = 1.01$, the shape of the molecular weight distribution is nearly identical for log-normal and Gaussian; similarly, for $PDI = 2$, the shape of the molecular weight distribution is very similar for the log-normal and exponential. Although in our analysis we primarily focused on the log-normal distribution, by changing the degree of polydispersity, we are also changing the shape of the molecular weight distribution.

Conventionally, viscoelastic measurements of polydisperse systems have been used to extract information about the distribution of relaxation times, i.e., the discrete linear response relaxation spectrum. In Fig.7.7 and Fig. B.9 in Appendix B, we show that the nonlinear decomposition of the orthogonal modulus into its relative contributions $A_{ij}^{yy}(\dot{\gamma})$ is sensitive to the spectrum of the nonlinear relaxation times. In this way, these measurements could be used as a nonlinear analog to linear viscoelastic measurements in terms of obtaining the spectra of nonlinear relaxation rates. The idea of extracting a shear rate-dependent relaxation spectrum from OSR measurement was proposed by Yamamoto.[21] However, this approach has a drawback because one has to assume a functional form of the relaxation spectrum beforehand. For the Rolie-Poly and RDP models, we can analytically derive the results for the superposition moduli that naturally contain a sum of the individual chain pairs in the system (Eqn. 7.25 and 7.26). In this case, the relaxation rate of individual modes is proportional to $A_{ij}^{yy}(\dot{\gamma})$. Thus, if the experimental system can be accurately described by these relationships, then one can fit experimental data to these two equations and just leave $A_{ij}^{yy}(\dot{\gamma})$ and $B_{ij}(\dot{\gamma})$ as adjustable parameters for some number of modes. Then, what one measures is the discrete nonlinear relaxation spectrum and the resulting $A_{ij}^{yy}(\dot{\gamma})$ and $B_{ij}(\dot{\gamma})$ in the nonlinear case are equivalent to G and τ for the multi-mode Maxwell model in the linear viscoelastic limit. The advantage of this approach is that we don't need to presuppose anything about what $A_{ij}^{yy}(\dot{\gamma})$ and $B_{ij}(\dot{\gamma})$ are, as long as a general multi-mode model with the upper-convected time derivative of the conformation tensor and relaxation terms linear in the conformation tensor describes the material of interest. For the specific case of the RDP model, we actually know what $A_{ij}^{yy}(\dot{\gamma})$ and $B_{ij}(\dot{\gamma})$ are, whereas if we presuppose a form for the relaxation spectrum, we wouldn't necessarily know what $A_{ij}^{yy}(\dot{\gamma})$ and $B_{ij}(\dot{\gamma})$ are. In other words, our results reaffirm the approach by Yamamoto that one can define some effective nonlinear relaxation spectrum, but beyond this, it gives proof to the idea that the relaxation spectrum should be related to the underlying constitutive behavior of the fluid. Going a step further, for the case of the Rolie-Poly and the RDP models, we can obtain analytical expressions for the discrete nonlinear relaxation spectrum from the expressions for the OSR moduli (Eqn. 7.25 and 7.26).

To summarize the previous discussions, our study emphasizes the critical importance of comparing OSR experiments with this type of detailed OSR predictions using rheological models to understand the physical meaning of changes in orthogonal superposition moduli as is now routinely done for other types of nonlinear rheological measurement protocols.

7.6 Conclusions

In this work, we combine numerical calculations and a perturbation analysis using detailed microstructural models (Rolie-Poly and Rolie-Double-Poly models) to study orthogonal superposition for monodisperse and polydisperse entangled linear polymers. A perturbation analysis allows identification of key parameters ($A_{yy}^{(0)}(\dot{\gamma})$ and $B(\dot{\gamma})$) that determine the shifts of the OSR moduli. By quantifying the shifts in an OSR experiment and using the expressions for $A_{yy}^{(0)}(\dot{\gamma})$ and $B(\dot{\gamma})$, we can estimate the average chain stretch

$\lambda(\dot{\gamma})$, the CCR parameter β_{CCR}, and the first normal stress difference N_1.

By systematically varying the degrees of polydispersity while keeping the weight-average molecular weight constant in a log-normal distribution of the molecular weight, we find qualitative signatures in the OSR moduli that correlate with the degree of polydispersity. Furthermore, the presence of short chains and the nonlinear dependence of $A_{ij}^{yy(0)}$ on the chain length results in the weakened softening of the plateau compared to the monodisperse case. Although a simple superposition of the monodisperse results can capture the qualitative trends observed in the polydisperse OSR moduli, to obtain quantitative predictions, the double reptation physics is needed. By making an analogy with the discrete relaxation spectrum obtained from LVE moduli, we showed that OSR moduli can be used to extract a nonlinear relaxation spectrum, which reveals a potential significant advantage of OSR measurement over conventional rheological measurements.

We also found that the contributions of different relaxation mechanisms and polydispersity to the shifts of OSR moduli complicate the analysis of estimating changes in chain length in flow. Thus, we cannot simply use conventional scaling analyses developed for LVE measurements to interpret OSR results.

The perturbation analysis and simulation scheme developed in this work are quite general and can be applied for other rheological models and material systems. In fact, we found the result for yy-component of the chain conformation determining the plateau value of the orthogonal moduli to be a general result for any model with the upper-convected time derivative of the conformation tensor and relaxation terms that are linear in the conformation tensor. Our result can be used as an analogy to Laun's rule for relating OSR moduli to the first normal stress difference.

In summary, we found that orthogonal superposition gives very useful information about nonlinear material moduli under flow, which can provide better sensitivity for testing constitutive models for nonlinear polymer processing. Results in our work have important implications for the design and interpretation of future orthogonal superposition experiments.

Bibliography

[1] Hyun K, Wilhelm M, Klein CO, et al. A review of nonlinear oscillatory shear tests: Analysis and application of large amplitude oscillatory shear (laos). *Progress in Polymer Science.* 2011; 36(12): 1697–1753.

[2] Tanner R, Simmons J. Combined simple and sinusoidal shearing in elastic liquids. *Chemical Engineering Science.* 1967; 22(12): 1803–1815.

[3] Simmons JM. A servo-controlled rheometer for measurement of the dynamic modulus of viscoelastic liquids. *Journal of Scientific Instruments.* 1966; 43(12): 887–892.

[4] Colombo G, Kim S, Schweizer T, et al. Superposition rheology and anisotropy in rheological properties of sheared colloidal gels. *Journal of Rheology.* 2017; 61(5): 1035–1048.

[5] Kim S, Mewis J, Clasen C, Vermant J. Superposition rheometry of a wormlike micellar fluid. *Rheologica Acta.* 2013; 52(8-9): 727–740.

[6] Mewis J, Schoukens G. Mechanical spectroscopy of colloidal dispersions. *Faraday Discussions of the Chemical Society.* 1978; 65: 58–64.

[7] Zeegers J, Ende D, Blom C, Altena EG, Beukema GJ, Mellema J. A sensitive dynamic viscometer for measuring the complex shear modulus in a steady shear flow using the method of orthogonal superposition. *Rheologica acta.* 1995; 34(6): 606–621.

[8] Vermant J, Moldenaers P, Mewis J, Ellis M, Garritano R. Orthogonal superposition measurements using a rheometer equipped with a force rebalanced transducer. *Review of Scientific Instruments.* 1997; 68(11): 4090–4096.

[9] Tao R, Forster AM. End effect correction for orthogonal small strain oscillatory shear in a rotational shear rheometer. *Rheologica Acta.* 2020; 59(2): 95–108.

[10] Simmons JM. Dynamic modulus of polyisobutylene solutions in superposed steady shear flow. *Rheologica Acta.* 1968; 7(2): 184–188.

[11] Kwon Y, Leonov AI. Remarks on orthogonal superposition of small amplitude oscillations on steady shear flow. *Rheologica acta.* 1993; 32(1): 108–112.

[12] Jacob AR, Poulos AS, Semenov AN, Vermant J, Petekidis G. Flow dynamics of concentrated starlike micelles: A superposition rheometry investigation into relaxation mechanisms. *Journal of Rheology.* 2019; 63(4): 641–653.

[13] Lee YJ, Jin H, Kim S, Myung JS, Ahn KH. Brownian dynamics simulation on orthogonal superposition rheology: Time–shear rate superposition of colloidal gel. *Journal of Rheology.* 2021; 65(3): 337–354.

[14] Mobuchon C, Carreau PJ, Heuzey MC, Reddy NK, Vermant J. Anisotropy of nonaqueous layered silicate suspensions subjected to shear flow. *Journal of rheology.* 2009; 53(3): 517–538.

[15] Jacob AR, Poulos AS, Kim S, Vermant J, Petekidis G. Convective cage release in model colloidal glasses. *Physical Review Letters.* 2015; 115(21): 218301.

[16] Sung SH, Kim S, Hendricks J, Clasen C, Ahn KH. Orthogonal superposition rheometry of colloidal gels: Time-shear rate superposition. *Soft Matter.* 2018; 14(42): 8651–8659.

[17] Moghimi E, Vermant J, Petekidis G. Orthogonal superposition rheometry of model colloidal glasses with short-ranged attractions. *Journal of Rheology.* 2019; 63(4): 533–546.

[18] Granek R, Cates ME. Stress relaxation in living polymers: Results from a poisson renewal model. *The Journal of chemical physics.* 1992; 96(6): 4758–4767.

[19] Doi M, Edwards SF. *The theory of polymer dynamics*; Vol. 73. Oxford University Press 1988.

[20] De Gennes PG. *Scaling concepts in polymer physics.* Cornell University Press 1979.

[21] Yamamoto M. Rate-dependent relaxation spectra and their determination. *Transactions of the Society of Rheology.* 1971; 15(2): 331–344.

[22] Wong C, Isayev A. Orthogonal superposition of small and large amplitude oscillations upon steady shear flow of polymer fluids. *Rheologica acta.* 1989; 28(2): 176–189.

[23] Unidad HJ, Ianniruberto G. The role of convective constraint release in parallel superposition flows of nearly monodisperse entangled polymer solutions. *Rheologica Acta.* 2014; 53(2): 191–198.

[24] Marrucci G, Ianniruberto G. Flow-induced orientation and stretching of entangled polymers. *Philosophical Transactions of the Royal Society of London. Series A: Mathematical, Physical and Engineering Sciences.* 2003; 361(1805): 677–688.

[25] Mead DW. Small amplitude oscillatory shear flow superposed on parallel or perpendicular (orthogonal) steady shear of polydisperse linear polymers: The mld model. *Journal of Non-Newtonian Fluid Mechanics.* 2013; 195: 99–113.

[26] Mead DW. Development of the “binary interaction” theory for entangled polydisperse linear polymers. *Rheologica acta.* 2007; 46(3): 369–395.

[27] Mishler S, Mead D. Application of the mld “toy” model to extensional flows of broadly polydisperse linear polymers: Part ii. comparison with experimental data. *Journal of Non-Newtonian Fluid Mechanics.* 2013; 197: 80–90.

[28] Mead DW, Larson RG, Doi M. A molecular theory for fast flows of entangled polymers. *Macromolecules.* 1998; 31(22): 7895–7914.

[29] Wapperom P, Keunings R. Impact of decoupling approximation between stretch and orientation in rheometrical and complex flow of entangled linear polymers. *Journal of non-newtonian fluid mechanics.* 2004; 122(1-3): 33–43.

[30] Boudara VAH, Peterson JD, Leal LG, Read DJ. Nonlinear rheology of polydisperse blends of entangled linear polymers: Rolie-double-poly models. *Journal of Rheology.* 2019; 63(1): 71–91.

[31] Likhtman AE, Graham RS. Simple constitutive equation for linear polymer melts derived from molecular theory: Rolie–poly equation. *Journal of Non-Newtonian Fluid Mechanics.* 2003; 114(1): 1–12.

[32] Laun H. Prediction of elastic strains of polymer melts in shear and elongation. *Journal of Rheology.* 1986; 30(3): 459–501.

[33] Eckstein A, Suhm J, Friedrich C, et al. Determination of plateau moduli and entanglement molecular weights of isotactic, syndiotactic, and atactic polypropylenes synthesized with metallocene catalysts. *Macromolecules.* 1998; 31(4): 1335–1340.

[34] Macosko CW. *Rheology: Principles, measurements, and applications.* Advances in interfacial engineering seriesNew York: VCH 1994.

[35] Graham RS, Likhtman AE, McLeish TCB, Milner ST. Microscopic theory of linear, entangled polymer chains under rapid deformation including chain stretch and convective constraint release. *Journal of Rheology.* 2003; 47(5): 1171–1200.

[36] Likhtman AE, McLeish TCB. Quantitative theory for linear dynamics of linear entangled polymers. *Macromolecules.* 2002; 35(16): 6332–6343.

[37] Cloizeaux J. Double reptation vs. simple reptation in polymer melts. *Europhysics Letters (EPL).* 1988; 5(5): 437–442.

[38] Read DJ, Jagannathan K, Sukumaran SK, Auhl D. A full-chain constitutive model for bidisperse blends of linear polymers. *Journal of Rheology.* 2012; 56(4): 823-873.

[39] Nichetti D, Manas-Zloczower I. Viscosity model for polydisperse polymer melts. *Journal of rheology.* 1998; 42(4): 951–969.

[40] Peterson JD. *Shear induced demixing in polymer melts and solutions.* PhD thesisUniversity of California, Santa Barbara 2018.

[41] Peterson JD, Fredrickson GH, Gary Leal L. Shear induced demixing in bidisperse and polydisperse polymer blends: Predictions from a multifluid model. *Journal of Rheology.* 2020; 64(6): 1391–1408.

[42] Khandavalli S, Hendricks J, Clasen C, Rothstein JP. A comparison of linear and branched wormlike micelles using large amplitude oscillatory shear and orthogonal superposition rheology. *Journal of Rheology.* 2016; 60(6): 1331–1346.

[43] Metri V, Briels W. Brownian dynamics investigation of the boltzmann superposition principle for orthogonal superposition rheology. *The Journal of chemical physics.* 2019; 150(1): 014903.

[44] Warner Jr HR. Kinetic theory and rheology of dilute suspensions of finitely extendible dumbbells. *Industrial & Engineering Chemistry Fundamentals.* 1972; 11(3): 379–387.

[45] Holroyd GA, Martin SJ, Graham RS. Analytic solutions of the rolie poly model in time-dependent shear. *Journal of Rheology.* 2017; 61(5): 859–870.

[46] Anwar M, Graham RS. Nonlinear shear of entangled polymers from nonequilibrium molecular dynamics. *Journal of Polymer Science Part B: Polymer Physics.* 2019; 57(24): 1692–1704.

[47] Lee JCW, Weigandt KM, Kelley EG, Rogers SA. Structure-property relationships via recovery rheology in viscoelastic materials. *Physical review letters.* 2019; 122(24): 248003.

[48] Tanner R, Williams G. On the orthogonal superposition of simple shearing and small-strain oscillatory motions. *Rheologica Acta.* 1971; 10(4): 528–538.

[49] Kaye A. Non-newtonian flow in incompressible fluids. *College of Aeronautics Note 134 & 149.* 1962.

[50] Bernstein B, Kearsley E, Zapas L. A study of stress relaxation with finite strain. *Transactions of the Society of Rheology.* 1963; 7(1): 391–410.

Chapter 8

Conclusions and future directions

8.1 Conclusions

The main conclusions of the dissertation will now be summarized. The outcomes from this dissertation can be divided into three categories: (1) the development of new tools for the measurement and analysis of flow-SANS experiments (2) the modeling of orthogonal superposition rheometry (3) new physical insights into the nonlinear flow-induced deformations of wormlike micelles and polymers. Additionally, future directions for studies of wormlike micelles and polymers will be proposed.

8.1.1 Outcomes: Flow-SANS measurement and modeling tools

In this dissertation, several advancements were demonstrated toward analysis and modeling of small angle neutron scattering of wormlike micelles and polymers. In Chapter 3 Section 3, a new equilibrium scattering model for entangled wormlike micelles was discussed. The model successfully captured the plateau of the intensity in the low-q regime, which was attributed to the inability of SANS to probe length scales beyond the mesh size for highly concentrated WLMs and the effect of electrostatic repulsion. The model was used to estimate the relative amount of unentangled and entangled wormlike micelles, which allows direct comparison with two-species rheological models for WLMs.

In Chapter 5, a new parameterization method for 2D anisotropic scattering data was developed, in which the ratio of circular average intensity in flow to that at equilibrium was plotted as a function of the alignment factor. This representation of the measurement enables summarizing all the key features for the q-dependent changes in the anisotropy and in the magnitude of intensity at different shear rates in one plot. Furthermore, by parameterizing out the direct shear rate dependence, the new representation allowed direct comparison with simulation results. The 2D parameterization enabled fingerprinting microstructural signatures in the anisotropic scattering.

In Chapter 4, we extended the Hayter-Penfold model for rodlike micelles to develop a connected-rod model for semiflexible chains in flow. By incorporating a segmental orientation distribution that is consistent with the overall stretching and orientation of the chain, we successfully captured the q-dependence of the anisotropy in the flow-SANS experiments of wormlike micelles. The study also demonstrated the sensitivity of the resulting scattering to the shape of the segmental orientation distribution. The model can be used not only for wormlike micelles, but also for other semiflexible chains, such as bottlebrush polymers, DNA, and electrolytes with semi-flexibility.

In Chapter 6, we formulated a scattering model for dilute, flexible polymers in shear flow and used results from Brownian Dynamics simulations for the polymer conformation in flow. We demonstrated the ability to both make a forward prediction of the scattering from polymer deformation and perform the inverse calculation to extract components of the gyration tensor from anisotropic scattering.

8.1.2 Outcomes: Modeling of orthogonal superposition rheometry

In Chapter 7, we combined numerical calculations and a perturbation analysis using detailed microstructural models (Rolie-Poly and Rolie-Double-Poly models) to study orthogonal superposition (OSR) for monodisperse and polydisperse entangled linear polymers. A perturbation analysis allowed identification of key parameters that determine the shifts of the OSR moduli. By quantifying the shifts in an OSR experiment, we can estimate the average chain stretch $\lambda\left(\dot{\gamma}\right)$, the CCR parameter β_{CCR}, and the first normal stress difference N_1. By systematically varying the degrees of polydispersity while keeping the weight-average molecular weight constant in a log-normal distribution of the molecular weight, we found qualitative signatures in the OSR moduli that correlate with the degree of polydispersity. The perturbation analysis and simulation scheme developed in this work are quite general and can be applied for other rheological models and material systems. In fact, we found the result for yy-component of the chain conformation, which determines the plateau value of the orthogonal moduli, to be a general result for any model with the upper-convected time derivative of the conformation tensor and relaxation terms that are linear in the conformation tensor. Our result can be used as an analogy to Laun's rule for relating OSR moduli to the first normal stress difference. In summary, we found that orthogonal superposition gives very useful information about nonlinear material moduli under flow that can provide better sensitivity for testing constitutive models for nonlinear polymer processing. Results in our work have important implications for the design and interpretation of future orthogonal superposition experiments.

8.1.3 Outcomes: Physical understanding of processing-structure-property relationship of polymeric fluids

Flow-enhanced scission of wormlike micelles

We conducted flow-SANS and rheology experiments on a series of linear wormlike micelles at various surfactant concentrations and temperatures, which were discussed in Chapter 5. From the analysis of time-resolved flow-SANS measurements at different shear rates, we observed the relaxation time for the magnitude of the intensity is always larger than the relaxation time for the alignment factor; this is especially so at the lowest-q value investigated. Furthermore, the relaxation time for the magnitude of the intensity increases with increasing shear rate at the lowest-q. Since the alignment factor quantifies the degree of anisotropy, which is related to the micellar orientation, the relaxation of the alignment factor describes the relaxation of the micelle orientation after flow cessation. If orientation were the only factor that changes the scattering anisotropy and the magnitude of the circularly averaged intensity, we would expect the relaxation time of the magnitude of the intensity to be the same as the relaxation time of the alignment factor. The larger relaxation time for the magnitude of the intensity, especially at the largest shear rate and lowest-q value investigated suggests that additional relaxation mechanism, namely, relaxation of flow-enhanced scission, is responsible for changes in the magnitude of the intensity. Therefore, the time-resolved flow-SANS measurements suggest flow-enhanced scission of the micelles. By comparing with simulations of the connected-rod model with different numbers of cylinders, we further confirmed that when the micelles get shorter (fewer number of Kuhn segments), the magnitude of the intensity is affected the most at the low-q. This is consistent with the increase of the relaxation time of the magnitude of the intensity at the low-q with increasing shear rate and the relatively constant relaxation time with shear rate at higher-q. In summary, a combination of SANS modeling, steady-state flow-SANS experiments, and time-resolved flow-SANS experiments enables direct microstructural measurement of wormlike micelles in flow and suggests the presence of flow-enhanced scission.

Entangled polymers

In Chapter 7, we demonstrated the shifts of the orthogonal superposition moduli were determined by the yy component of the polymer conformation and the effective relaxation rate. By making an analogy with the discrete relaxation spectrum obtained from LVE moduli, we showed that OSR moduli can be used to extract a nonlinear relaxation spectrum, which reveals a potential significant advantage of OSR measurement over conventional rheological measurements. We also found that the contributions of different relaxation mechanisms and polydispersity to the shifts of OSR moduli complicates the analysis of estimating changes in chain length in flow. Thus, we cannot simply use conventional scaling analyses developed for LVE measurements to interpret OSR results.

8.2 Recommendations for future work

8.2.1 Experimental validation of model predictions

At the time of developing the orthogonal superposition modeling, there was limited experimental data for OSR experiments of monodisperse polymers and polydisperse polymers with well characterized degree of polydispersity and relaxation time. Furthermore, previous experimental studies were limited in the range of shear rates and frequencies that could be achieved. With new improvements of the orthogonal superposition instrumentation and especially recent incorporation in a commercial rheometer, probing rheology of entangled polymers at higher shear rates and frequency ranges to access the region with significant chain stretch becomes a possibility. Future studies on OSR experiments of monodisperse and polydisperse entangled polymers will allow validation of our model predictions. Specifically, it is desirable to validate the relationship between the first normal stress difference and OSR moduli that we derived in Chapter 7:

$$\lim_{\omega\to\infty}\left[\frac{G'_{\perp}\left(\omega,\dot{\gamma}\right)}{\omega_{c,\dot{\gamma}}^{2}}\right] = \frac{N_1\left(\dot{\gamma}\right)}{2\dot{\gamma}^2}. \tag{8.1}$$

It will also be interesting to extract the chain stretch from OSR moduli using the relations we derived in Chapter 7.

When developing the connected rod model for semiflexible chains, we compared the model prediction with flow-SANS experiments of wormlike micelles instead of other semiflexible chain systems. This is because currently there is a lack of flow-SANS measurements on semiflexible polymers in flow, which is partially due to the smaller relaxation time and weaker segmental orientation compared to wormlike micelles. Thus, much higher shear rates are needed to observe significant scattering anisotropy and the shear rates required are near the highest shear rates achievable in rheometers and shear-cells ($\sim 2000s^{-1}$). Recently, scientists at NIST developed a capillary rheoSANS device that enables measurements up to shear rates of $10^7 s^{-1}$.[1] It will be useful to use this device to measure scattering of semiflexible chain systems in addition to wormlike micelles to further validate the connected-rod model predictions.

8.2.2 Development of new theoretical and computational tools

For the scattering model of semiflexible chains in flow, so far, we have only included polydispersity in chain length for the equilibrium prediction; the predictions in flow use the monodisperse version of the model. At a given shear rate, we used the effective stretch parameter in the orientation distribution as a fitting parameter to match the degree of anisotropy between simulation and experiments. It would be desirable to include polydispersity in chain length for the predictions in flow to better resemble the microstructures of wormlike micelles and other semiflexible systems with length polydispersity. However, with chain polydispersity included, one can no longer use the effective stretch as a fitting parameter to match the degree of anisotropy between simulation and experiments because for a given shear rate, chains of different lengths have different effective stretch. To our knowledge, current experimental studies on wormlike micelles have not investigated the dependence of chain stretch on chain length. Thus, one may need to rely on molecular dynamics simulations[2,3] or rheological models[4] to obtain effective chain stretch as a function of shear rate and chain length. Once the chain polydispersity is included in the scattering model in flow, the model can be used to fit 2D flow-SANS experimental data to extract the average chain length (or chain length distribution) as a function of shear rate. This will enable more directly probing the effect of flow on the scission of wormlike micelles.

From the modeling of orthogonal superposition rheometry for entangled polymers, we demonstrated the plateau of the orthogonal storage moduli decreases with increasing shear, without any chain breakage. A comparison with previous experiments on wormlike micelles in the literature yields a similar percentage of reduction in the plateau value after matching the number of entanglements in the wormlike micelle experiment and that in the simulation of monodisperse chains. It would be desirable to compare polydisperse predictions with wormlike micelle experiments since wormlike micelles have a broad length distribution. However, since the current polydisperse OSR prediction uses the Rolie-Double-Poly model for polymers, it exhibits a broad relaxation spectrum (i.e., many relaxation times), which is different from the single-mode Maxwell behavior in wormlike micelles in the fast-breaking regime. Thus, to compare with OSR experiments of wormlike micelles, we need to use a rheological model for wormlike micelles that incorporates stress relaxation due to chain breakage and recombination and includes the full exponential length distribution. Such a model has been published recently Peterson and Leal.[5] Comparison of OSR predictions using rheological models for wormlike micelles and WLM experiments will allow one to more directly distinguish effects of chain scission to the OSR moduli from other relaxation mechanisms that are present in regular polymers (e.g., reptation, retraction, convective constraint release).

For modeling the scattering of dilute polymers in flow, so far, we have only focused on linear polymers. To elucidate the effect of polymer architecture on the chain deformation and resistance to chain scission in flow, it is useful to extend the current model to other polymer architectures, such as branched and star polymers. Equilibrium models for such architectures already exist.[6] For predictions in flow, we propose either using Brownian Dynamics simulations of different polymer architectures to obtain the discretized probability distribution function of the polymer configuration that can be used directly in scattering calculations as shown in Chapter 6, or looking into methods to derive analytical expressions for the scattering intensity based on the gyration tensor components of chains with different architectures.

8.2.3 New experiments on wormlike micelles

In Chapter 5, we presented initial evidence for flow-enhanced scission of wormlike micelles based on steady state and time-resolved flow-SANS experiments. To further confirm the presence of flow-enhanced scission and explore other related phenomena, we propose the following set of experiments. With the scattering model that incorporates polydispersity that we described in the previous section, we can obtain the average chain length as a function of shear rate. By making measurements at the same Weissenberg number at different temperatures for the WLM sample, we can estimate the effective scission energy in flow. Specifically, according to the Cates model,[7] the average chain length has the following dependence on the scission energy at equilibrium:

$$\bar{L} \sim \phi^{1/2} \exp\left(\frac{E_{scis}}{k_B T}\right). \tag{8.2}$$

The effect of flow on the scission of wormlike micelles can be included as an additional term on the exponential, i.e., flow reduces the energy needed for scission. Thus, we have:

$$\bar{L}_{flow}(Wi) \sim \phi^{1/2} \exp\left(\frac{E_{scis} - E_{flow}(Wi)}{k_B T}\right) \sim \bar{L}_{eqm} \exp\left(-\frac{E_{flow}(Wi)}{k_B T}\right). \tag{8.3}$$

By plotting the ratio of the average chain length in flow and the average chain length at equilibrium, $\bar{L}_{flow}(Wi)/\bar{L}_{eqm}$, as a function of $1/T$, we can obtain $E_{flow}(Wi)$, the Weissenberg number dependent change in scission energy due to flow.

During the processing and end-use of wormlike micelles, wormlike micelles experience not only simple shear flow, but also extensional flow and complex flow. As discussed by Rothstein and Mohammadigoushki in their review article,[8] wormlike micelles in complex flow typically exhibit very interesting flow instabilities. Although many flow visualization experiments, rheology measurements, and simulation studies have been conducted for wormlike micelles in extensional flow and complex flow, there is a lack of direct microstructural measurements, such as small angle neutron scattering (SANS) and small angle x-ray scattering (SAXS). In particular, due to the often time-varying nature of the flow and the resulting instability, it is desirable to perform time-resolved SANS or SAXS measurements to elucidate the microscale response of micelles in complex flow. These new experiments can be analyzed using the framework we developed in this study, namely the parameterization of 2D scattering intensity and the connected-rod model. Such studies will be critical for answering whether it is possible to lump all microstructural factors into one critical threshold for the onset of instability for wormlike micelles in complex flows.[8]

In addition to the SANS technique discussed in this work, transmitted electron microscopy (TEM) is also a useful technique for measuring microstructures and is often complementary to SANS measurements. Traditionally, cryo-TEM was used for probing microstructures of wormlike micelles at equilibrium.[9,10] However, the sample needs to be frozen before the imaging in the microscope. More recently, liquid cell-TEM[11,12] has been developed and enables direct visualization of microstructures in a liquid sample as it is flowing through the field of view. Unlike SANS, liquid cell-TEM only allows viewing a few micelles at a time; therefore, it lacks the statistically averaged information that SANS offers. However, the direct visualization without the need to do inverse Fourier transform (like in SANS) makes liquid cell-TEM a potentially useful technique for studying the kinetics of WLM scission in flow.

Bibliography

[1] Murphy RP, Riedel ZW, Nakatani MA, et al. Capillary rheoSANS: measuring the rheology and nanostructure of complex fluids at high shear rates. *Soft Matter.* 2020; 16(27): 6285–6293.

[2] Dhakal S, Sureshkumar R. Uniaxial extension of surfactant micelles: counterion mediated chain stiffening and a mechanism of rupture by flow-induced energy redistribution. *ACS Macro Letters.* 2016; 5(1): 108–111.

[3] Sambasivam A, Sangwai AV, Sureshkumar R. Dynamics and scission of rodlike cationic surfactant micelles in shear flow. *Physical review letters.* 2015; 114(15): 158302.

[4] Peterson JD, Cates M. A full-chain tube-based constitutive model for living linear polymers. *Journal of Rheology.* 2020; 64(6): 1465–1496.

[5] Peterson JD, Gary Leal L. Predictions for flow-induced scission in well-entangled living polymers: The “living rolie-poly” model. *Journal of Rheology.* 2021; 65(5): 959–982.

[6] Higgins JS, Benoit HC. Polymers and neutron scattering. 1994.

[7] Cates M. Reptation of living polymers: dynamics of entangled polymers in the presence of reversible chain-scission reactions. *Macromolecules.* 1987; 20(9): 2289–2296.

[8] Rothstein JP, Mohammadigoushki H. Complex flows of viscoelastic wormlike micelle solutions. *Journal of Non-Newtonian Fluid Mechanics.* 2020: 104382.

[9] Kuperkar K, Abezgauz L, Danino D, et al. Viscoelastic micellar water/CTAB/NaNO3 solutions: rheology, SANS and cryo-TEM analysis. *Journal of colloid and interface science.* 2008; 323(2): 403–409.

[10] Helgeson ME, Hodgdon TK, Kaler EW, Wagner NJ. A systematic study of equilibrium structure, thermodynamics, and rheology of aqueous CTAB/NaNO3 wormlike micelles. *Journal of colloid and interface science.* 2010; 349(1): 1–12.

[11] He K, Shokuhfar T, Shahbazian-Yassar R. Imaging of soft materials using in situ liquid-cell transmission electron microscopy. *Journal of Physics: Condensed Matter.* 2019; 31(10): 103001.

[12] Pu S, Gong C, Robertson AW. Liquid cell transmission electron microscopy and its applications. *Royal Society open science.* 2020; 7(1): 191204.

Appendix A

Temperature and concentration dependence of wormlike micelle properties and elastic instability

A.1 Summary

In this Appendix chapter, we report rheology, flow-small angle neutron scattering, and flow visualization experiments that are supplemental to Chapter 5. In particular, we investigate the temperature dependence of wormlike micelle rheology, the scaling of alignment factor from SANS for samples at different concentrations and temperatures, and the possibility of elastic instability.

A.2 Methods

The preparation of wormlike micelles, procedures for rheological characterization, flow-small angle neutron scattering experiments, and the calculation of alignment factor from scattering are the same as those described in Chapter 5.

A.2.1 Flow Visualization

To investigate the possibility of elastic instability in wormlike micelles in the Taylor-Couette geometry, we modified the Anton-Paar Physica MCR300 setup, which was originally used for PTV measurements, to allow for visualization of the secondary flow. Specifically, a lamp was placed next to the rheometer to illuminate the side of the Taylor-Couette cell (Fig. A.1). The Taylor-Couette cell consisted of an outer stationary quartz cup with a radius $R_2 = 17.5$ mm and an inner moving anodized aluminum cylinder with a radius $R_1 = 17$ mm. In subsequent text, this geometry is referred to as ME34. The temperature of the Couette cell is controlled with a circulating water bath. The fluid was seeded with mica flakes (Iriodin 100 Silver Pearl from EMD Performance Materials, size 10-60 μm, density 2.8-3.0 g/cm^3). Because of the anisotropy in the shape of the mica flakes, if secondary flow (such as roll cell) develops, the fluid will show repeating bright and dark streaks. To delay rod climbing, a metal cap was placed on top of the shear cell with the bottom surface submerged in the fluid.

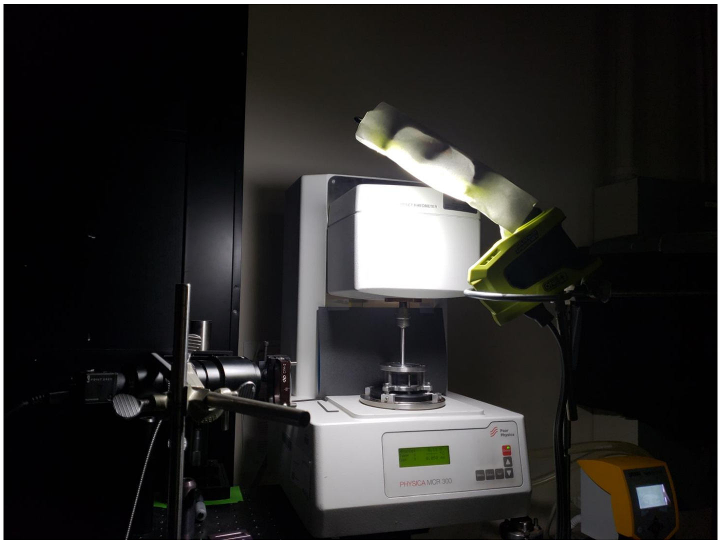

Figure A.1: Experimental setup for flow visualization.

We used a slow ramp of the shear rate. For example, for the 80 mM CTAB sample in Fig. A.2, the shear rate was ramped up from $0s^{-1}$ to $1500s^{-1}$ at a rate of $1s^{-1}$ per second. Images were taken at one image per second. Fig. A.2 outlines the procedures for image analysis in the ImageJ software. First, we crop a rectangle with a width of 10 pixels in each image at the same location (Fig. A.2(a) and (b)). Then we scale the cropped slice by 0.1 in the horizontal direction to make it 1 pixel-wide (Fig. A.2(c)). The intensity is the averaged value of the 10 pixels in the original slice. Next, we use the Montage function in the ImageJ software to stack up slices from each image as a function of time (Fig. A.2(d)). In the resulting image, the x-axis is time (or equivalently, the shear rate, since the shear rate is slowly ramped up in the experiment). Finally, if needed, we adjust the brightness and contrast of the montage image (Fig. A.2(e)).

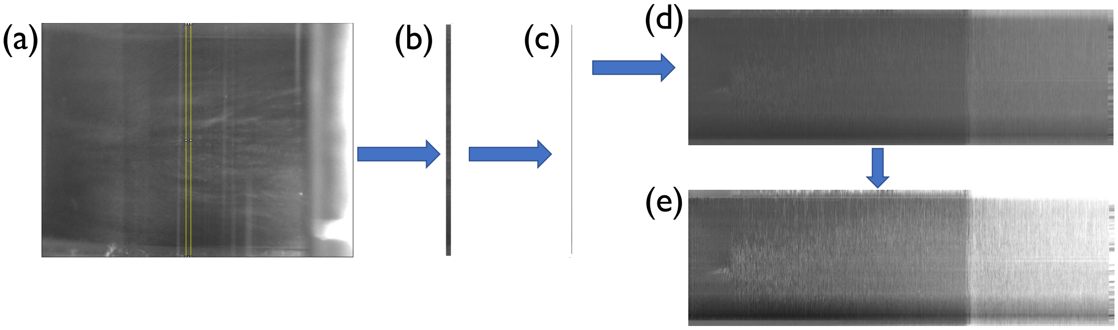

Figure A.2: Procedures for data analysis of flow visualization experiments. The images shown here are for the 80 mM CTAB sample.

A.3 Results

A.3.1 Temperature and concentration dependent rheology

In Chapter 5, we discussed the rheology of wormlike micelles at different concentrations at the same temperature (25 °C). Here, we are also interested in the temperature-dependence of the rheology for the sample with the highest concentration, 100 mM CTAB/300 mM $NaNO_3$. Shown in Fig. A.3(a) are linear viscoelastic measurements from 25 °C to 45 °C. Similar to the concentration-series data, the moduli have characteristic scaling in the low-frequency region: $G' \sim \omega^2$ and $G'' \sim \omega$. With increasing temperature, the moduli crossover shifts to higher frequencies, which indicates the relaxation time becomes shorter. Qualitatively speaking, increasing temperature has similar effect on the moduli at low frequency as decreasing concentration. Since the average length at equilibrium depends on both temperature and concentration: $\bar{L} \sim \phi^{1/2} \exp\left(E_a/2k_BT\right)$, increasing temperature and decreasing concentration both decrease the average length, which in turn affects the longest relaxation time. Different from the concentration series data, the storage moduli at different temperatures have nearly identical values for the plateau modulus (except for the highest temperature 45 °C). The temperature-independence of the plateau modulus has been observed in other WLM systems in the literature.[1] The authors suggested that the concentration-dependence and the temperature-independence of G_0 suggest that the structure of the samples is preserved throughout the concentration range studied under these conditions of shear and that only the density of effective elastic chains is varying. The moduli are also fitted to the single-mode Maxwell model and the fitting parameters are reported in Table A.1.

We also measured the nonlinear rheology of the 100 mM CTAB sample at different temperatures. Shown in Fig. A.3(b) is the viscosity (in filled symbols) and shear stress (in open symbols) as a function of shear rate. Similar to the concentration series, with increasing temperature (and decreasing concentration), the zero shear viscosity decreases, which is again a result of shorter micelles. However, a unique feature of the temperature-series result is the overlap of viscosity at intermediate to high shear rates for all the temperatures. In this shear rate range, the shear stresses at different temperatures are also almost overlapping and the slope of the stress increases with increasing temperature.

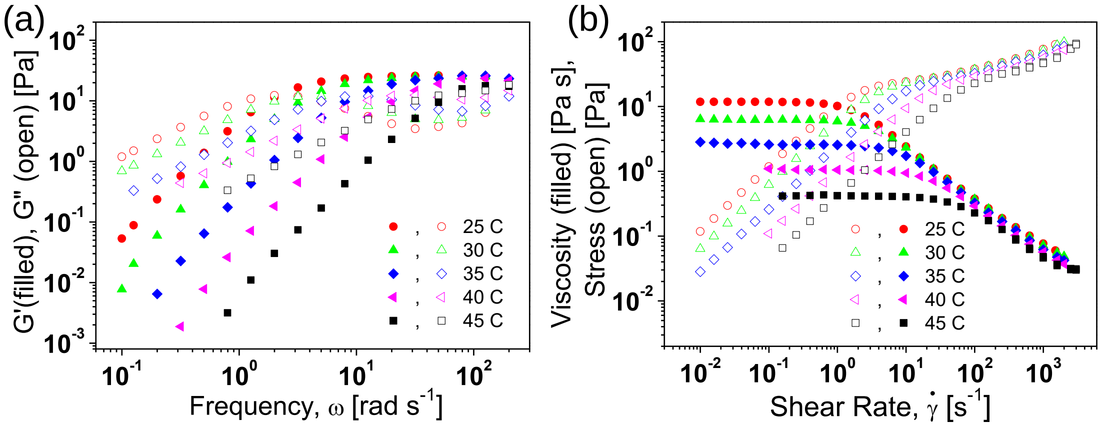

Figure A.3: Linear and nonlinear rheology of 100 mM CTAB wormlike micelles in D_2O at 25 °C-45 °C.

Table A.1: Parameters from single-mode Maxwell fits of the linear viscoelastic data of 100 mM CTAB wormlike micelles at 25 °C-45 °C.

CTAB	NANO$_3$	T	G_0	G''_{min}	τ_r	τ_{br}	τ_{rep}	N_e	η_∞
(mM)	(mM)	(°C)	(Pa)	(Pa)	(s)	(s)	(s)		(Pa s)
100	300	25	25.5	3.3	0.44	0.029	6.68	7.7	0.048
		30	25.0	4.6	0.24	0.022	2.55	5.5	0.050
		35	25.0	6.8	0.098	0.014	0.69	3.7	0.046
		40	24.1	10.5	0.041	0.010	0.17	2.3	0.045
		45	21.4	14.8	0.018	0.008	0.04	1.4	0.047

For the temperature series, the longest relaxation time follows an Arrhenius dependence on the temperature, as predicted by theory: $\tau \sim \exp(E_a/RT)$. The reptation time and breakage time also follow an Arrhenius dependence on the temperature.(Fig. A.4).

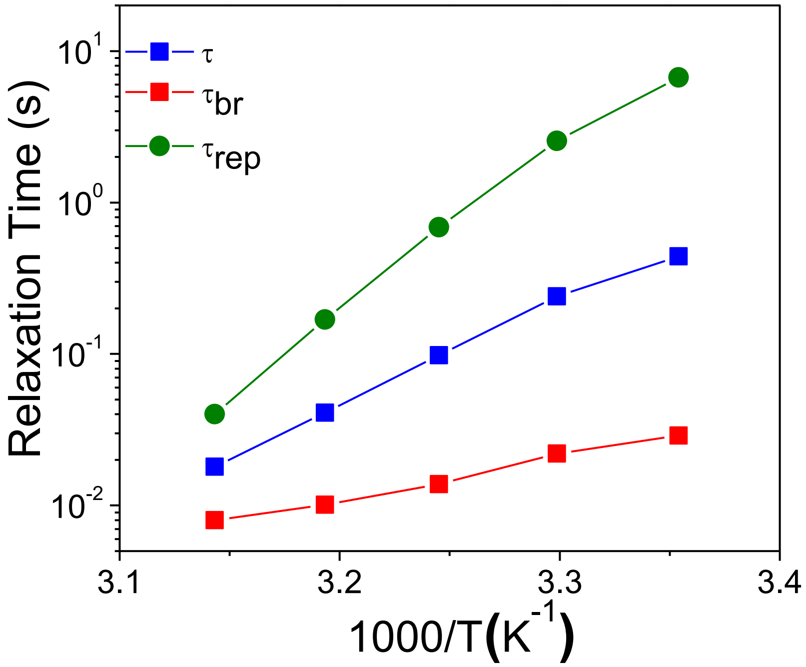

Figure A.4: Relaxation times identified from linear viscoelastic measurement as a function of inverse temperature.

We are also interested in finding out how the shape of the stress and viscosity curves change with concentration and temperature. Thus, we calculated the dimensionless stress by dividing the stress by the plateau modulus G_0. The longest relaxation time τ is used to obtain the Weissenberg number, a dimensionless shear rate $Wi = \tau\dot{\gamma}$, where $\dot{\gamma}$ is the applied shear rate. The dimensionless viscosity is calculated by dividing the dimensionless stress by Wi. The dimensionless stress and dimensionless viscosity are plotted as a function of Wi for the concentration series in Fig. A.5(a). The curves completely overlap on top of each other. The only small deviation occurs at the highest Wi for 60 mM CTAB due to inertial effects in the rheometer. The complete overlap of the dimensionless stress and viscosity suggests that the nonlinear dynamics of the WLM samples that are at the same temperature and with the same salt to surfactant ratio only depends on the equilibrium structure of the micelles (i.e., the average contour length and mesh size at equilibrium).

The same complete overlap of the dimensionless stress and dimensionless viscosity is not achieved for the temperature series. As shown in Fig. A.5(b), the overlap is only seen in the Newtonian region ($Wi < 1$). For $Wi > 1$, the slope of the shear stress increases with increasing temperature.

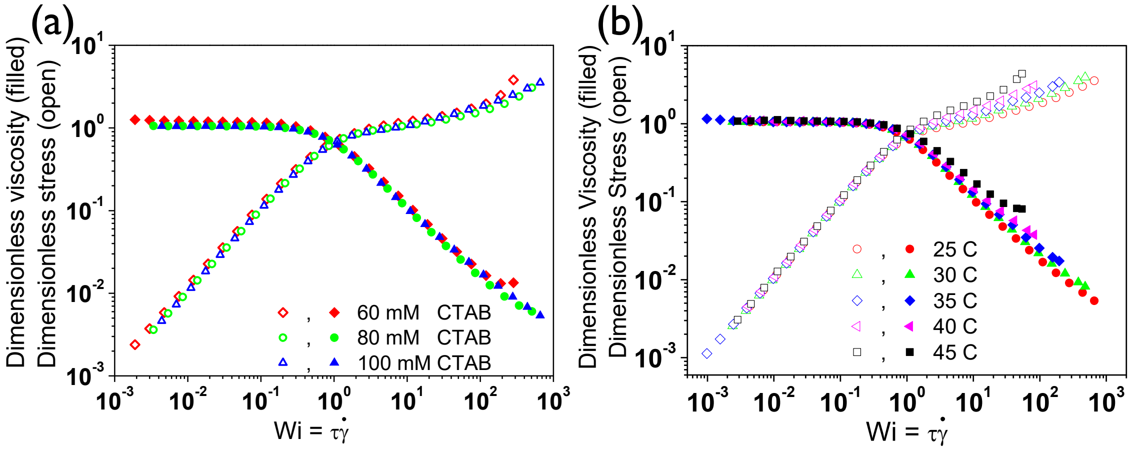

Figure A.5: Dimensionless shear stress and dimensionless viscosity as a function of dimensionless shear rate, Wi, for (a)60 mM CTAB, 80 mM CTAB, 100 mM CTAB in D_2O at 25 °C and (b) 100 mM CTAB at 25 °C-45 °C.

A.3.2 Scaling of the alignment factor

The alignment factor is used to quantify the degree of anisotropy from flow-SANS measurements. In Chapter 5, we presented the analysis of alignment factor for the 60 mM CTAB sample at 25 °C and examined its dependence on the shear rate and the scattering wave vector. Here we report a more in-depth analysis of the alignment factor as a function of shear rate for the concentration series and temperature series. In Fig. A.6(a), we plot alignment factor evaluated at $q = 0.025\text{Å}^{-1}$, which approximately corresponds to the inverse of the persistence length l_p. At a given shear rate, the 100 mM CTAB sample has the highest alignment factor and the 60 mM CTAB sample has the lowest alignment factor. With increasing shear rate, the alignment factor for all three samples first increases, then beyond a critical shear rate, the alignment factor decreases. For the 80 mM sample and the 100 mM sample, the alignment factor eventually reaches a plateau. The 60 mM sample is limited by the shear rate range available experimentally and the plateau is not observed.

Multiple causes can result in the decrease of the alignment factor with increasing shear rate. In Chapter 5, we discussed the possibility of flow-enhanced micellar scission. If micelles become shorter in flow, at a given shear rate, it becomes harder to align the micelles, thus the alignment factor can decrease. Additionally, previous flow visualization experiments on wormlike micelles have discussed the presence of elastic instability in wormlike micelles due to curved streamlines in the Taylor-Couette geometry.[2,3] In these experiments, the fluid is seeded with mica flakes. The elastic instability is signified by the appearance of roll cells that are stacked along the vorticity direction. We will examine the possibility of elastic instability in our wormlike micelle samples in the next section. When secondary flow starts to develop in the fluid, the orientation of the micelles become more randomized. As a result, the alignment factor decreases. Although the decrease in the alignment factor can also be caused by micellar scission, the coupling of the effects of the elastic instability and potential micellar scission makes it challenging to distinguish the contribution to the alignment factor from the two effects. Thus, for the subsequent analysis in this section, although we are plotting the A_f across the entire shear rate range investigated, we will only focus the analysis on the shear rate range before the alignment factor peak.

Based on the complete overlap of the dimensionless stress and dimensionless viscosity as a function Wi for the concentration series in Fig. A.5(a), we hypothesized plotting the alignment factor as a function of Wi may also completely overlap the results. However, as shown in Fig.A.6(b), although the alignment factor curves become more tightly grouped, there is still significant difference on the Wi-dependence. If we use the reptation time, instead of the longest relaxation time to nondimensionalize the shear rate, we achieve a complete overlap of the alignment factor results before the alignment factor peak for the concentration series. The alignment factor (as evaluated at $q = 0.025\text{Å}^{-1}$) describes the orientation on the segmental level. The shear stress is related to the deformation of the end-to-end vector, which is affected by stretch, orientation, and scission. The collapse of the dimensionless stress with the longest relaxation time $\tau = (\tau_{rep}\tau_{br})^{1/2}$ and the collapse of the alignment factor with the reptation time τ_{rep} suggests that on the segmental level, orientation is only affected by reptation (not scission), whereas on the level of the end-to-end of the chain, orientation and stretch are affected by both reptation and scission.

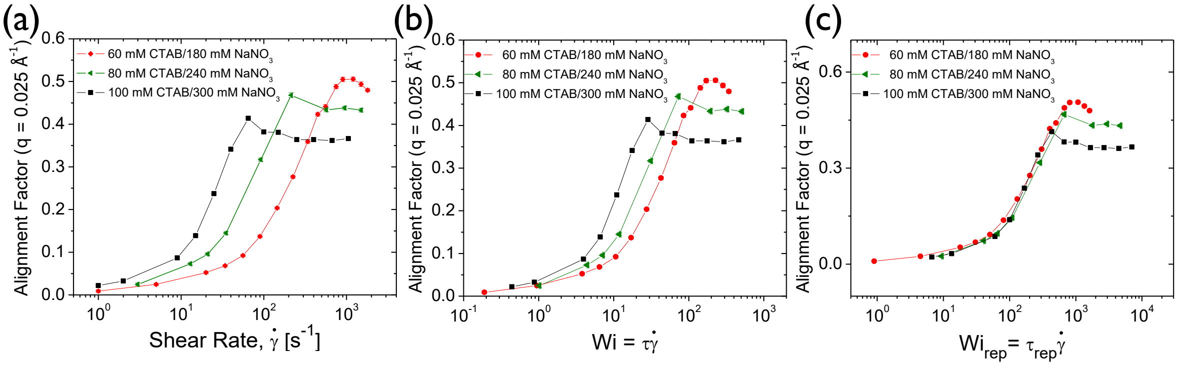

Figure A.6: Alignment factor at $q = 0.025$ Å^{-1} for 60 mM CTAB, 80 mM CTAB, and 100 mM CTAB as a function of (a) shear rate (b) dimensionless shear rate $Wi = \tau\,\dot{\gamma}$ (c) shear rate nondimensionalized by the reptation time $Wi_{rep} = \tau_{rep}\,\dot{\gamma}$

We also investigated the scaling of the alignment factor with different relaxation times for the temperature series (100 mM CTAB at 25 °C-45 °C). Plotted in Fig. A.7(a) are the alignment factors (at $q = 0.025$Å^{-1}) as a function of shear rate. For a given shear rate, the alignment factor decreases with increasing temperature. The leveling-off of the alignment factor at high shear rates is again possibly caused by secondary flows. The shape of the alignment factor at 45 °C is qualitatively different from the curves at lower temperatures. In particular, the slope for the 45 °C result is smaller. This is expected because at 45 °C, the micelles are so short that they are no longer entangled and no longer in the semi-dilute regime. The estimated number of entanglements is only 1.4 (See Table A.1). As was discussed earlier, in the semi-dilute region, the plateau modulus is expected to have very weak dependence on temperature and appear to be constant on the log-log plot. At temperatures below 45 °C, the plateau modulus is nearly temperature independent. However, at 45 °C, the plateau modulus decreases, which again suggests that the solution is no longer in the semi-dilute regime.

In Fig. A.7 (b), we plot the alignment factor as a function of Wi ($Wi = \tau\dot{\gamma}$). Interestingly, the alignment factor curves completely overlap both before and after the alignment factor peak (with the exception of 45 °C, because of the much shorter micelles). However, if we nondimensionalize the shear rate by the reptation time, we don't achieve an overlap (Fig. A.5 (c)). As was shown in Fig. A.5 (b), for the temperature series, without scaling by the relaxation time, the dimensional shear stress and viscosity have an overlap at high shear rates. The dimensionless shear stress and viscosity in the high shear rate region as a function of Wi have moderate temperature-dependence for the slope. The collapse of the alignment factor as a function of $Wi = \tau\dot{\gamma}$ suggests that the temperature-dependence of the micellar alignment at different shear rates is the same as the temperature-dependence of the longest relaxation time, which includes contributions from both reptation and scission.

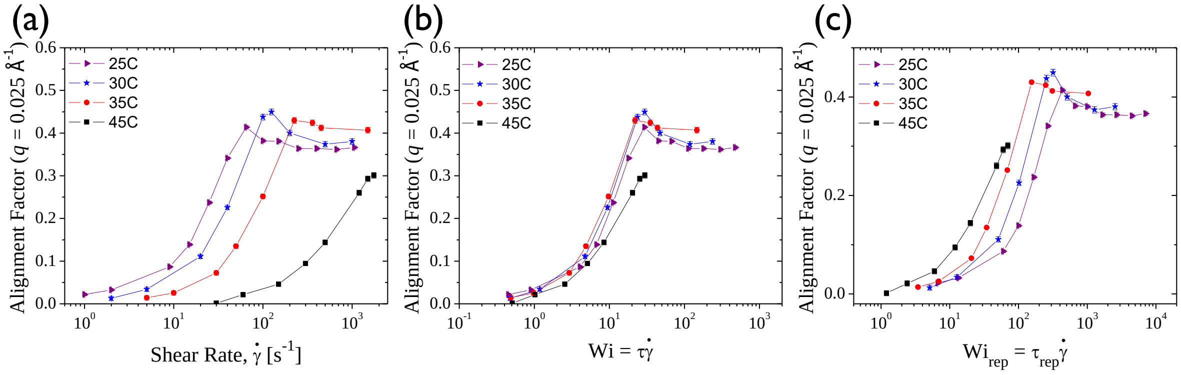

Figure A.7: Alignment factor at $q = 0.025$ Å^{-1} for 100 mM CTAB at temperatures 25 °C-45 °C as a function of (a) shear rate (b) dimensionless shear rate $Wi = \tau\,\dot{\gamma}$ (c) shear rate nondimensionalized by the reptation time $Wi_{rep} = \tau_{rep}\,\dot{\gamma}$

A.3.3 Characterizing the onset of elastic instability

Flow visualization experiments were conducted for 60 mM CTAB, 80 mM CTAB, and 100 mM CTAB at 25 °C. Additional experiments were also done at higher temperatures for 100 mM CTAB. In Fig. A.8, Fig. A.9, and Fig. A.10, panel (a) shows the montage image which consists of a slice of one pixel for each shear rate during the shear rate ramp. The arrows point to the start of important features in the secondary flow. For all three samples, at low shear rates, the flow is homogeneous and no roll cells are observed. At intermediate shear rates, bright streaks start to appear near the middle of the rotating cylinder, which eventually turn into secondary flows across the entire height of the cylinder. The shear rate at which full instability develops is indicated by the boldface label on top of the arrow. The panels below (a) in each figure are the images at each corresponding shear rate (except for $0s^{-1}$) before the images were cropped for making the montage.

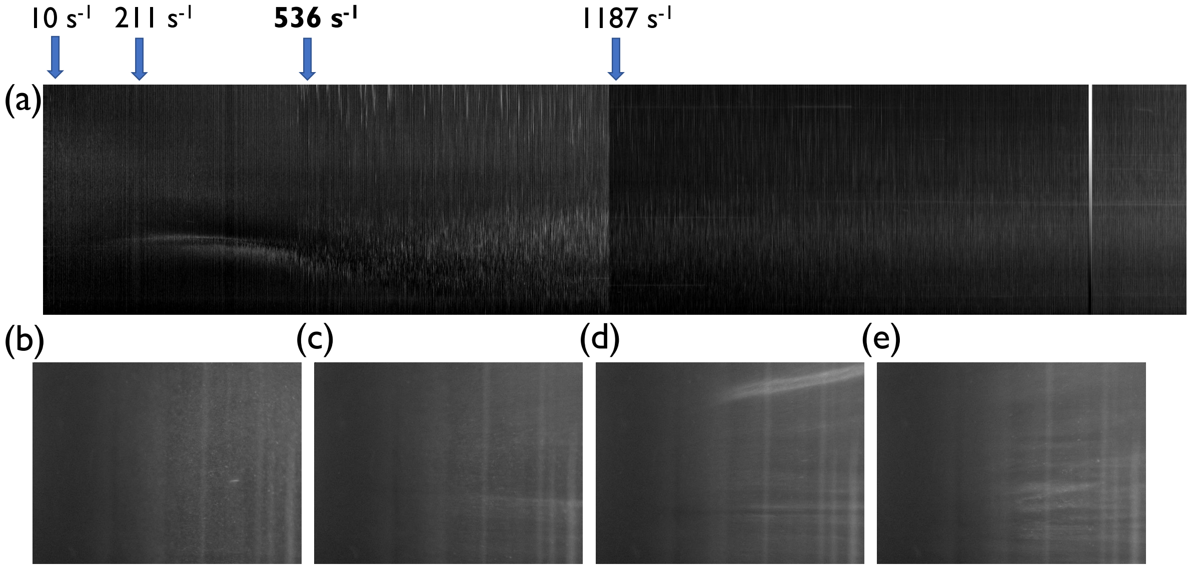

Figure A.8: Flow visualization of 60 mM CTAB wormlike micelles.

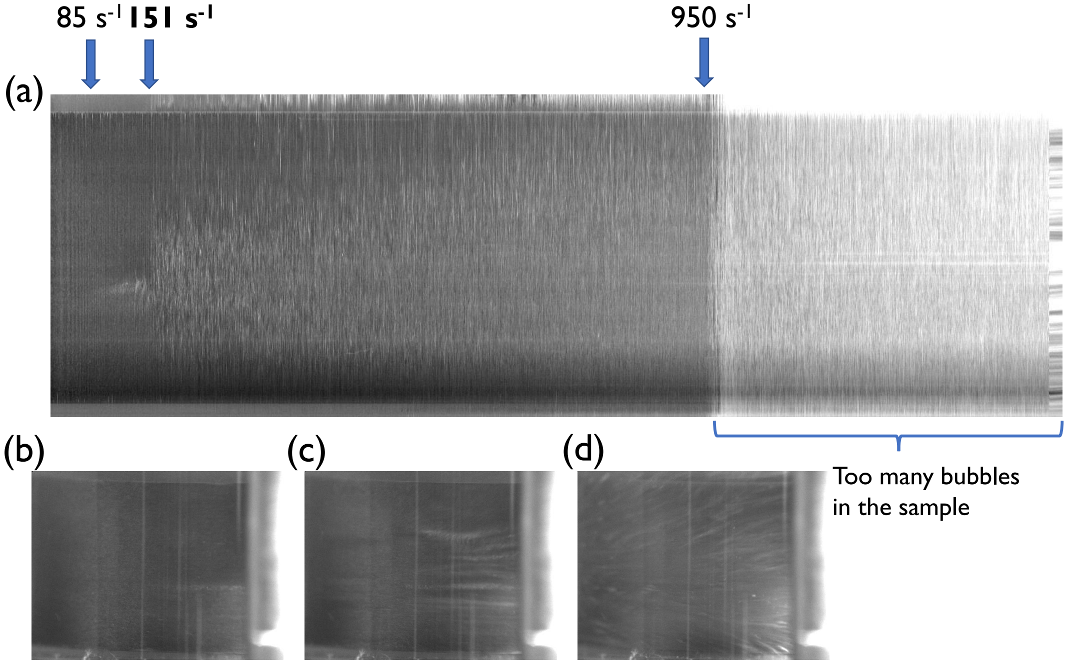

Figure A.9: Flow visualization of 80 mM CTAB wormlike micelles.

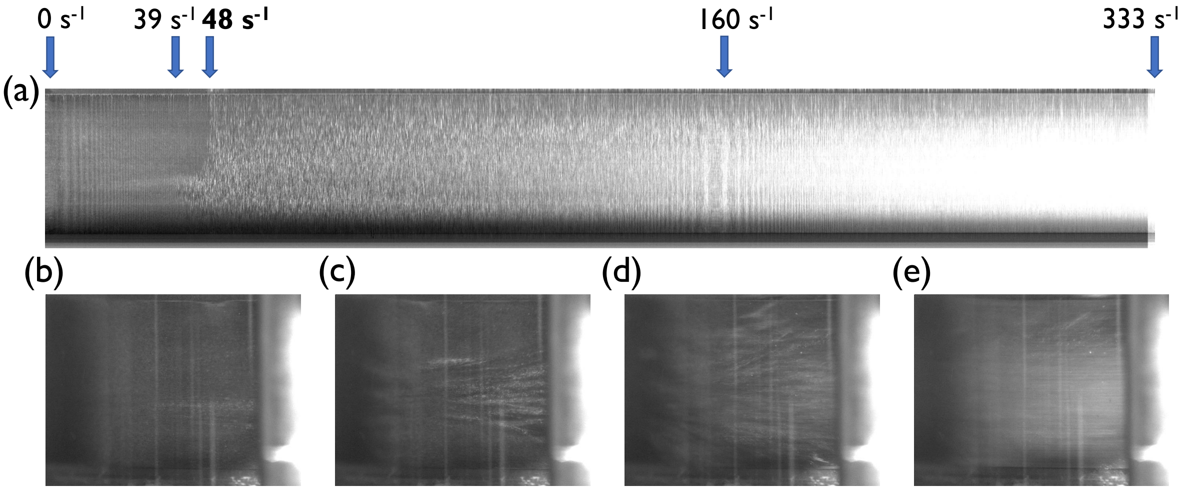

Figure A.10: Flow visualization of 100 mM CTAB wormlike micelles.

In Table. A.2, we summarize the shear rate and Wi corresponding to the peak in the alignment factor observed in the last section in the top half of the table. The bottom half of the table summarizes the shear rate corresponding to the observation of secondary flow across the entire Couette geometry in the flow visualization experiment in geometry ME34 and the scaled shear rate for the 1-2 shear cell in SANS experiment after accounting for differences in the curvature of the two flow geometries. The bottom row in the table indicates the expected Wi corresponding to the onset of elastic instability in the 1-2 shear cell. For all three samples, the Wi corresponding to elastic instability is smaller than the Wi at the peak of the alignment factor. In Table. A.3, we summarize the results for the 100 mM CTAB sample at different temperatures. The three rows each represent shear rate for alignment factor peak from SANS, Wi for alignment factor peak, and Wi for instability in the 1-2 shear cell, respectively. Again, the Wi corresponding to the elastic instability is smaller than the Wi at the peak of the alignment factor.

Table A.2: Summary of flow visualization results for concentration series (60 mM CTAB, 80 mM CTAB, 100 mM CTAB at 25 °C).

	60 mM CTAB	80 mM CTAB	100 mM CTAB
Shear rate for A_f peak (s^{-1})	1200	214	65
Relaxation time (s)	0.19	0.34	0.44
Wi for A_f peak	228	73	29
Shear rate for full instability in ME34	536	151	48
Scaled shear rate for 1-2 shear cell	464	130	41
Wi from ME34	102	51	21
Wi from 1-2 shear cell	88	44	18

Table A.3: Summary of flow visualization results for temperature series (100 mM CTAB at 25 °C-45 °C).

	25 °C	30 °C	35 °C
Shear rate for A_f peak (s^{-1})	65	125	360
Wi for A_f peak	29	30	35
Wi for instability in 1-2 shear cell	21	21	25

In Figure. A.11, we plot the alignment factor as a function of Wi (shear rate scaled by the longest relaxation time) for both the concentration series (a) and temperature series (b). The arrows represent the expected Wi for the onset of elastic instability based on flow visualization experiments. For all samples investigated, the elastic instability occurred at shear rates below than the peak of the alignment factor. Thus, the decrease in the alignment factor can be caused by the randomized orientation of the micelles due to the secondar flow.

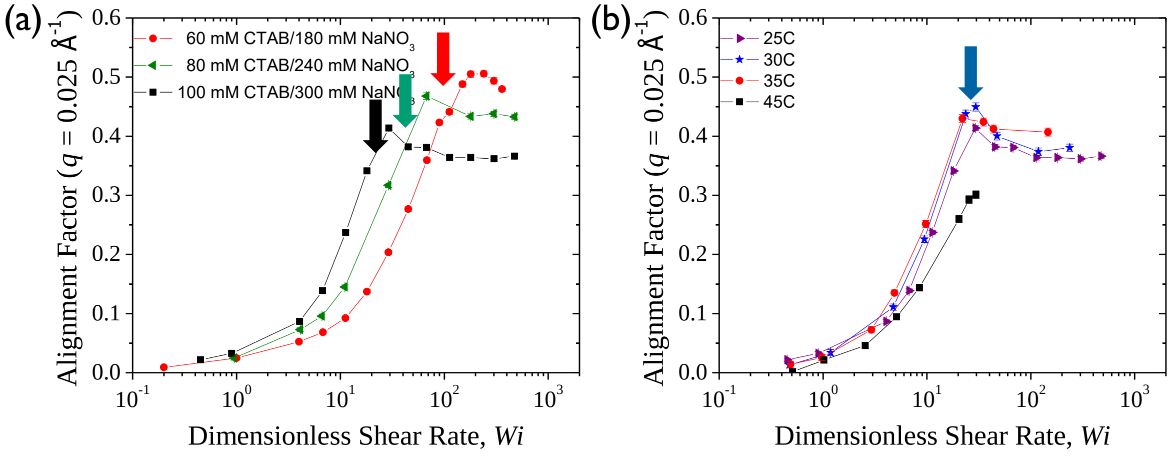

Figure A.11: Compare Wi for peak in alignment factor and the onset of elastic instability for (a) concentration series (b) temperature series. The shear rate is nondimensionalized by the longest relaxation time identified from linear viscoelastic measurements.

A.4 Conclusions and future directions

In this chapter, we discussed additional experiments that are supplementary to the experiments in Chapter 5. By conducting flow visualization experiments, we confirmed the presence of elastic instability in the wormlike micelle samples at high shear rates. For all samples investigated, the elastic instability occurs at shear rates just below the shear rates corresponding to the peak in the alignment factor from SANS. Although the decrease in the alignment factor can also be caused by a net shortening of micelles in flow, the coupling of the effects between the randomization of micelle orientation due to secondary flows and flow-enhanced scission makes the interpretation of the experimental results more challenging. To distinguish effects of micellar scission from secondary flows on the alignment factor, future studies should focus on quantifying the magnitude of the secondary flow relative to the main flow. This can be accomplished, for example, by seeding microbeads in the fluid along with mica flakes to image the trajectory of the beads in the roll cells in order to quantify the velocity in the secondary flow.

We also examined the temperature and concentration dependence of the wormlike rheology and alignment factor measured in SANS. Interestingly, although scaling the shear rate by the longest relaxation time completely overlaps the shear stress and viscosity for samples with different concentrations, the alignment factor results cannot be collapsed with the same scaling. Instead, scaling the shear rate by the reptation time completely collapses the alignment factor results. For the temperature series, the alignment factor at different temperatures (except for 45 °C) can be completely collapsed on the same curve when the shear rate is scaled by the longest relaxation time. The difference in the scaling of the temperature series and concentration series is potentially caused by the difference in the temperature-dependence and the concentration-dependence of the flow-enhanced scission. To test our hypotheses, future studies should use other surfactant and salt combinations for the wormlike micelles and study the rheology and flow-SANS for both the temperature series and concentration series to examine if the trends we observed in this study are general across different wormlike micelle systems.

Bibliography

[1] Alfaro J, Landázuri G, González-Álvarez A, et al. Phase and rheological behavior of the hexadecyl (trimethyl) azanium; 2-hydroxybenzoate/water system. *Journal of colloid and interface science.* 2010; 351(1): 171–179.

[2] Mohammadigoushki H, Muller SJ. Inertio-elastic instability in taylor-couette flow of a model wormlike micellar system. *Journal of Rheology.* 2017; 61(4): 683–696.

[3] Perge C, Fardin MA, Manneville S. Inertio-elastic instability of non shear-banding wormlike micelles. *Soft matter.* 2014; 10(10): 1450–1454.

Appendix B

Supplementary materials for modeling orthogonal superposition rheometry

This chapter is reproduced from:

Jiamin Zhang, Andres Jurzyk, Matthew E. Helgeson, and L. Gary Leal, "Modeling Orthogonal Superposition Rheometry to Probe Nonequilibrium Dynamics of Entangled Polymers", *Journal of Rheology*, **65(5)**, 983-998, 2021. *Featured article.* DOI: 10.1122/8.0000272,

with the permission of AIP publishing.

In this Appendix chapter, we include supplementary materials for Chapter 7 on modeling orthogonal superposition rheometry (OSR) to probe nonequilibrium dynamics of entangled polymers.

B.1 Method validation

B.1.1 Identification of the linear viscoelastic region

When conducting a linear viscoelastic measurement to obtain the storage and loss moduli of a material at equilibrium, one would usually do an amplitude sweep first to identify the range of strain amplitude in the linear viscoelastic region. Similarly, to choose a strain amplitude in the OSR simulation, we first calculated the storage and loss moduli at $\tilde{\omega} = 0.01$ with varying strain amplitudes γ_0 using the Rolie-Poly model (Fig. B.1 (a)). For $\gamma_0 \leq 0.1$, the storage and loss moduli are constant. At larger strain amplitudes, both the storage and loss moduli start decreasing with increasing strain amplitude. The region of constant moduli is the linear viscoelastic region. Since $\gamma_0 = 0.05$ is well inside this region, we chose 0.05 as the amplitude in the subsequent numerical calculations of the frequency-dependent moduli. Figure B.1 (b) shows the linear viscoelastic moduli and $\tan\delta$ as a function of the dimensionless frequency. The contribution of the Newtonian solvent is included in the calculation.

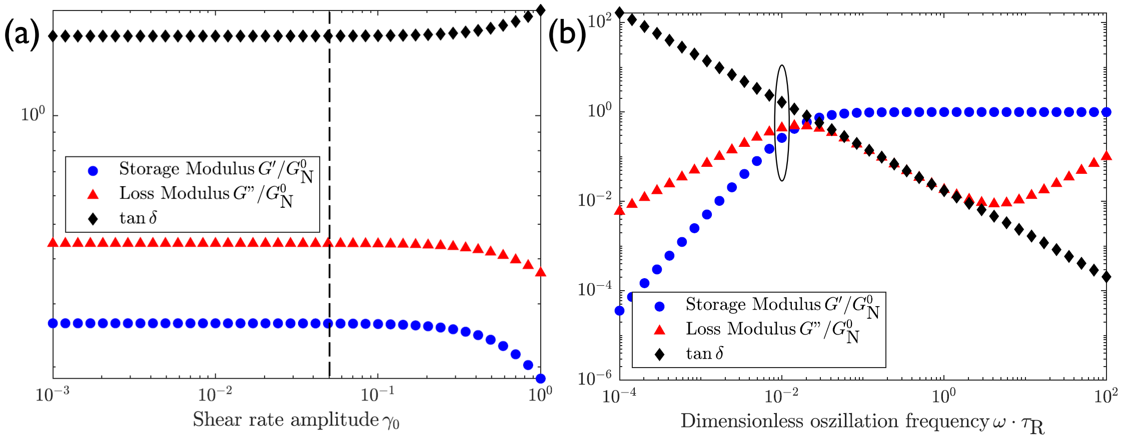

Figure B.1: (a) Amplitude sweep at frequency $\tilde{\omega} = 0.01$ to find the linear viscoelastic region. Dashed line corresponds to $\gamma_0 = 0.05$. (b) Simulation of linear viscoelastic measurement using the Rolie-Poly model at shear rate amplitude $\gamma_0 = 0.05$. Ellipse points to frequency $\tilde{\omega} = 0.01$.

B.1.2 Validation of numerical method

To verify that the numerical calculations are implemented correctly, we made two sets of comparisons. First, we compared the solution of the Rolie-Poly model in steady shear flow with Fig. 1 in the Rolie-Poly paper[1] to verify the equations of the model are implemented correctly (Figure B.2 (a)). Specifically, we compared the dimensionless shear stress $\sigma_{\mathrm{xy}}/G_N^0$ and the dimensionless first normal stress difference $\frac{N_1}{G_N^0} = \left(\sigma_{\mathrm{xx}} - \sigma_{\mathrm{yy}}\right)/G_N^0$ and found excellent agreement between our numerical results and the results in the Rolie-Poly paper. Second, we needed to check if the transient solver and calculations of the orthogonal superposition moduli are implemented correctly. To date, there has not been a study of orthogonal superposition using the Rolie-Poly model so we cannot make a direct comparison. However, the calculation methods do not depend on the specific model we use. So, we first did a test case of the numerical calculation using the Giesekus model and compared the numerical results to analytical results of the orthogonal superposition moduli from Kim *et al.*[2] The comparison of the storage moduli is shown in Figure B.2 (b) and the comparison of the loss moduli is shown in Figure B.2 (c). Again, we have excellent agreement between our numerical results and previous analytical results. By verifying the implementation of the Rolie-Poly model equations and the calculation method of the orthogonal superposition moduli separately, we confirmed that the numerical methods are accurate and can now proceed with the discussion of the numerical results as shown in the Results section of Chapter 7.

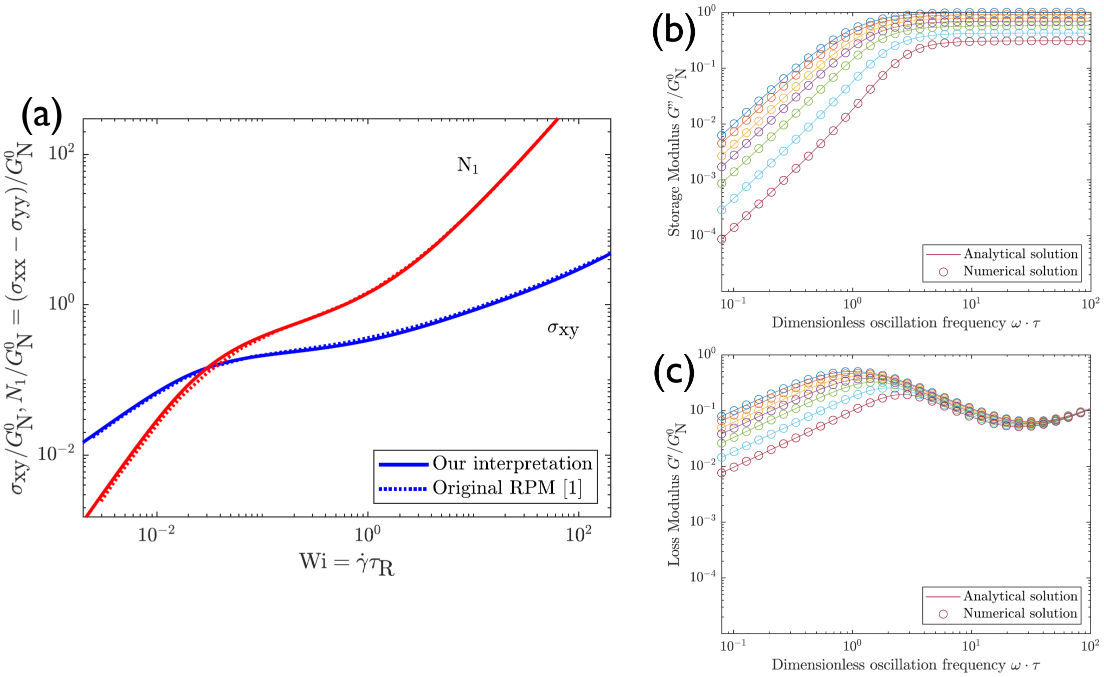

Figure B.2: (a) Comparison of steady shear results in this work and in the Rolie-Poly paper (b) and (c) Comparison of our numerical results for OSR moduli using the Giesekus model and the analytical results from Kim *et al.*[2]

B.1.3 Comparison of perturbation analysis and numerical calculation for monodisperse Rolie-Poly

We compared the numerical results of the monodisperse Rolie-Poly calculation and the analytical result from the perturbation analysis. As shown in Figure B.3 below, the two sets of results are indistinguishable. In fact, the maximum percent deviation of the perturbation result from the numerical result ($\%\ deviation = \frac{perturbation-numerical}{\text{numerical}} * 100\%$) for the storage moduli is only less than 0.2%. Thus, the assumption that the superposition is a small perturbation of the steady shear flow is valid. Similar agreement is found between numerical results and analytical results from the perturbation analysis for the loss moduli of the monodisperse case and for both the storage and loss moduli for the polydisperse case.

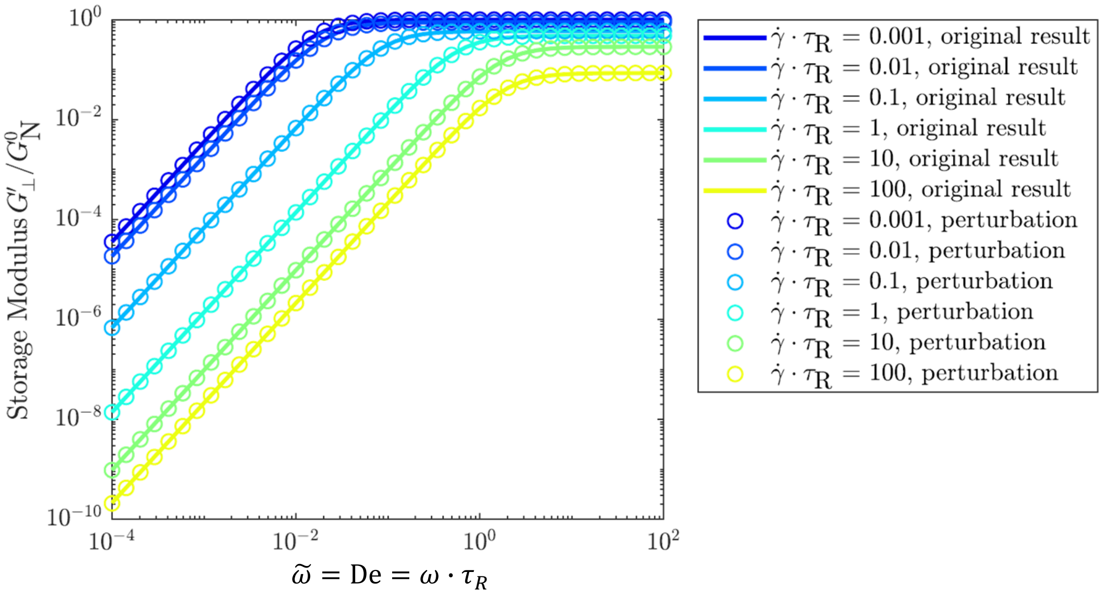

Figure B.3: Comparison of storage moduli prediction of numerical calculation (solid curves) and perturbation analysis (open circles) as a function of dimensionless frequency for dimensionless shear rate from 0.001 to 100. Predictions used the monodisperse Rolie-Poly model.

B.2 Additional predictions

B.2.1 Comparison of SRDP and RDP model predictions for bidisperse polymers

In the original work by Boudara *et al.*,[3] two versions of the model were presented for polydisperse entangled polymers, namely, the Rolie-Double-Poly (RDP) model and the Symmetric-Rolie-Double-Poly (SRDP) model. The two models primarily differ with regards to the symmetry (or asymmetry) of stress relaxation across entanglements between different types of chains. The RDP model is discussed in the Theory section of Chapter 7. Here we will briefly discuss the SRDP model. The SRDP model is developed by assuming that the microscopic picture of double reptation applies to all relevant nonlinear stress relaxation mechanisms. Specifically, the configuration of chain i at its point of entanglement with chain j, $\mathbf{A}_{\mathrm{ij}}$, always matches the configuration of chain j at its point of entanglement with chain i, $\mathbf{A}_{\mathrm{ji}}$. After doing a detailed comparison of SRDP and RDP models for a bimodal system (long chain and short chain), Boudara *et al.* concluded that the two models are in quantitative agreement to within ~10% for $|\boldsymbol{\kappa}|\,\tau_{s,L} < 1$, where $\boldsymbol{\kappa}$ is the velocity gradient tensor and $\tau_{s,L}$ is the stretch relaxation time of the long chain. Quantitative disagreement between the two models is most evident when short chains are stretching but not near full extension, $|\boldsymbol{\kappa}|\,\tau_{s,S} < 1$. However, even under these conditions, qualitative agreement is still quite good. In Chapter 7, we used the RDP model for all of the polydisperse calculations. We will now compare the SRDP and RDP models in the context of orthogonal superposition for bidisperse blends.

Shown in Figure B.4 are two representative sets of results for bidisperse blends: blend 1 ($Z_S = 3,\ Z_L = 60,\ \phi_S = 0.7,\ \phi_L = 0.3$) and blend 2 ($Z_S \sim 15.5,\ Z_L = 60, \phi_S = 0.9,\ \phi_L = 0.1$). Both blends have the same weight-average number of entanglements: $\overline{Z} = 20$. The shear rate and frequency are nondimensionalized by the Rouse time τ_R of the average chain. The two models only start to differ for $\dot{\gamma} \cdot \tau_R > 10$, when the long chain becomes significantly stretched. Since the qualitative trends for how OSR moduli shift with shear rate are the same for both models and the RDP model is more accurate, we will only discuss results for the RDP model in Chapter 7.

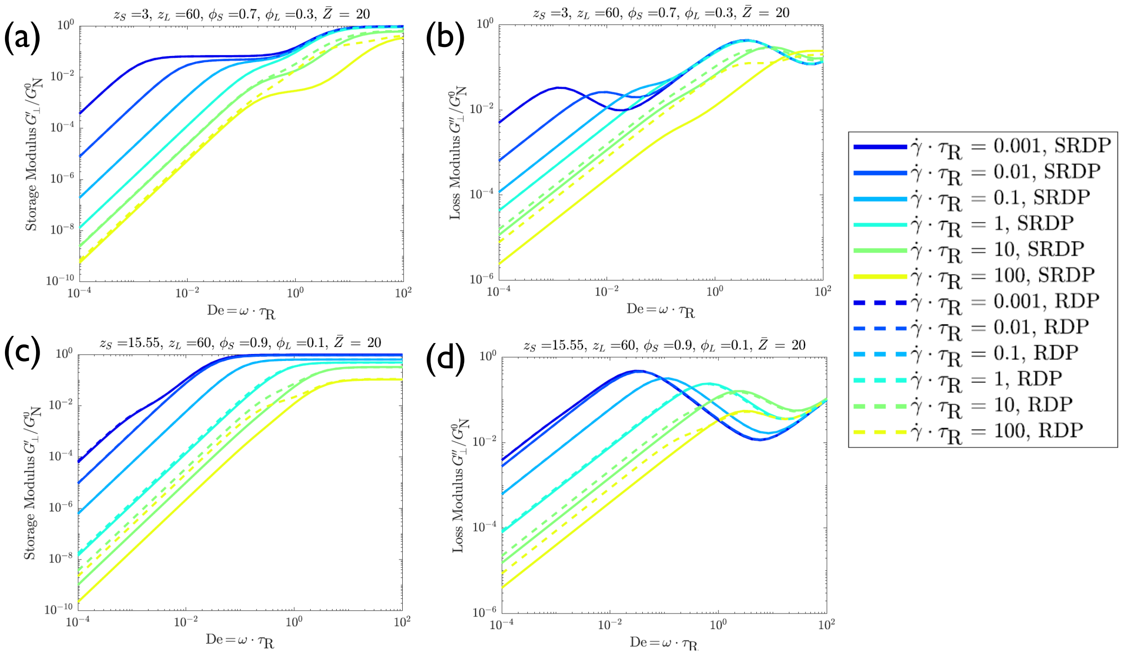

Figure B.4: Comparison of SRDP and RDP model predictions for two bimodal distributions with the same weight-average chain length: $\overline{Z} = 20$. Solid curves represent the SRDP model whereas dashed curves represent the RDP model. (a) $G'_\perp$ and (b) $G''_\perp$ for short chain length $Z_S = 3$, long chain length $Z_L = 60$, and volume fraction of short chain $\phi_S = 0.7$. The system is in region 4 of the Viovy diagram. (c) $G'_\perp$ and (d) $G''_\perp$ for short chain length $Z_S = 15.5$, long chain length $Z_L = 60$, volume fraction of short chain $\phi_S = 0.9$. The system is in region 3a of the Viovy diagram.

It is worth discussing to what extent the bimodal distribution changes the OSR moduli compared to the monodisperse case and determine to what extent the observations we made about OSR moduli of polymers with a lognormal distribution in Chapter 7 apply for a bimodal distribution. One distinctive feature of sharply peaked bimodal distribution is the presence of multiple crossovers and multiple plateaus in the equilibrium and low-Wi moduli for chains that differ significantly in length. In this case, the relaxation timescales for the two chains are well separated. The first plateau at low-frequency corresponds to the chain with longer length and the second plateau at higher-frequency corresponds to the chain with shorter length. In Figure B.5, (a) and (b) corresponds to $Wi = 0.001$ and $Wi = 100$ for the blend 1 shown in Figure B.4 ($Z_S = 3,\ Z_L = 60$). The moduli at

$Wi = 0.001$ has three crossovers whereas the moduli at $Wi = 100$ only has one crossover. (c) and (d) in Figure B.5 represents blend 2 shown in Figure B.4 ($Z_S = 15.55, Z_L = 60$). For both the highest and lowest Wi simulated, this bimodal distribution only has one crossover point because the chain lengths are closer together and the long chain has a smaller volume fraction.

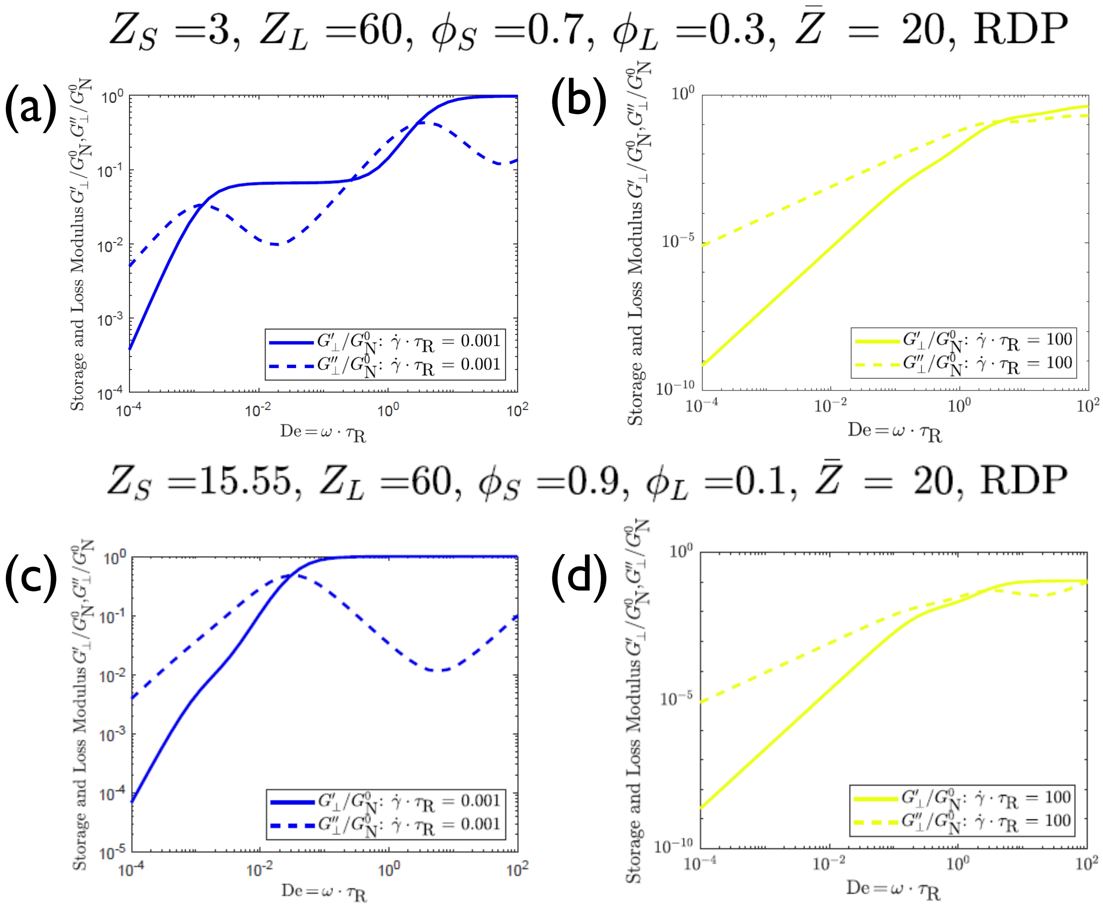

Figure B.5: Compare two different bimodal distributions (blend 1 and blend 2) at $Wi = 0.001$ and $Wi = 100$.

The derivation of the relationship between the high-frequency plateau value of $G'_\perp$ and the first normal stress difference N_1 also works for the bimodal distribution. If multiple plateaus exist at equilibrium, the derived relation is for the plateau at the highest frequencies since plateaus at lower frequencies will disappear with increasing Wi. For bimodal distribution with well-separated peaks (i.e., the long chain and short chain differ greatly in length), the $G'_{\perp}$ and $G''_{\perp}$ can have multiple crossovers instead of having a smooth transition to the plateau as in the log-normal distribution. Therefore, it is more difficult to develop a generalized representation for how the crossover moduli and crossover frequency depend on the polydispersity in the bi-modal distribution. For bimodal distributions with only one crossover in the moduli at equilibrium, the shifts in the location of the crossover follow similar trends as the lognormal distribution. The details of how the shape of the OSR moduli is modified for bimodal distribution relative to the monodisperse case depend on which region in the Viovy diagram the bimodal polymer belongs to. Shown in Figure B.6 are the quantitative comparisons between monodisperse results and blend 2 $(Z_S = 15.55, Z_L = 60, PDI = 1.2)$.

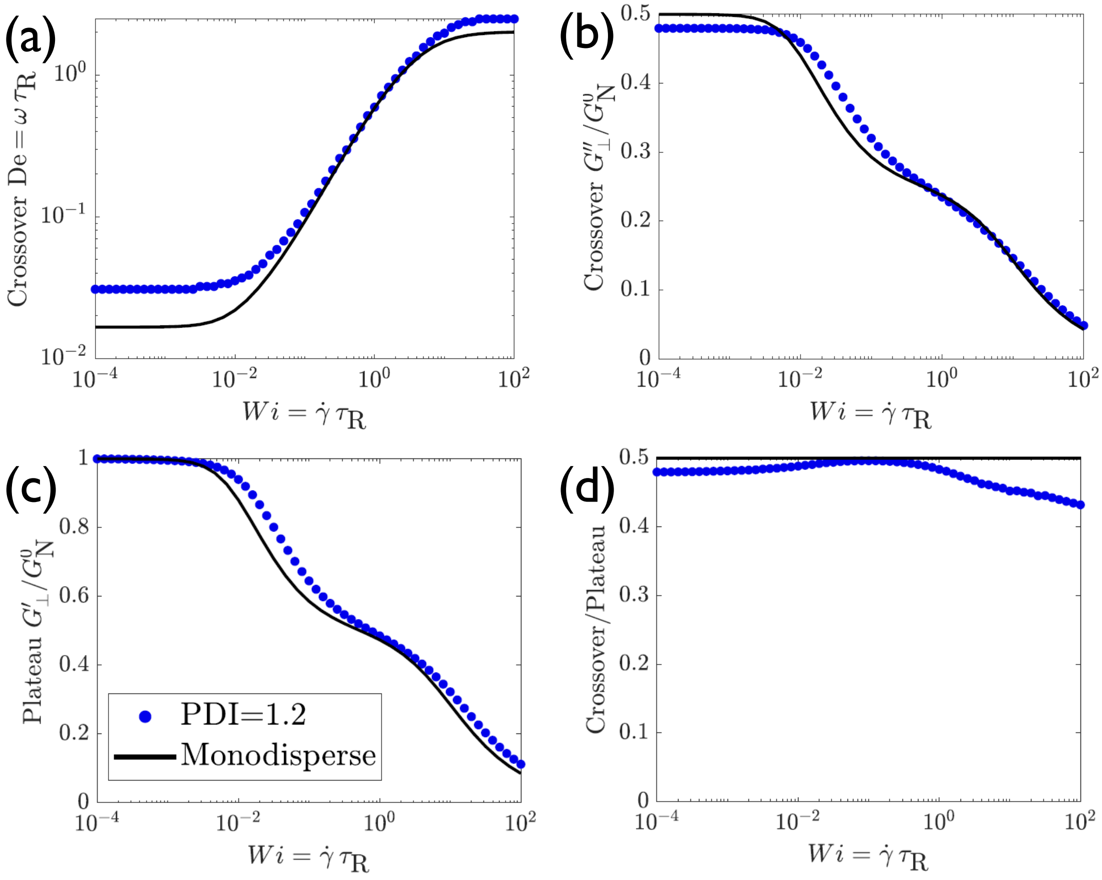

Figure B.6: Compare bimodal distribution with monodisperse results (Bimodal distribution: $Z_S = 15.55,\ Z_L = 60,\ \phi_S = 0.9, \phi_L = 0.1, \overline{Z} = 20, PDI = 1.2$).

B.2.2 Perturbation analysis on the DCR-CS model by Marrucci and Ianniruberto

To test the generality of our perturbation result (Eqn. 7.23 and Eqn. 7.24 in Chapter 7), we applied the same procedure to double-convection-reptation model with chain stretch (coupled DCR-CS model) by Marrucci and Ianniruberto.[4] This model was used by Unidad and Ianniruberto[5] to derive analytical expressions for the parallel superposition moduli. Because of the coupling between the main flow and the superposed flow in parallel superposition, the expressions for the superposition moduli are very complicated. In the previous work, the authors did not derive results for orthogonal superposition. Here, we will briefly introduce the main equations of the coupled DCR-CS model then present the results for orthogonal superposition from our perturbation analysis.

In the coupled DCR-CS model, time evolution of the polymer conformation tensor $\mathbf{A}$ is described as:

$$\frac{d\mathbf{A}}{dt} = \boldsymbol{\kappa} \cdot \mathbf{A} + \mathbf{A} \cdot \boldsymbol{\kappa}^T - \frac{1}{\tau}\left(\mathbf{A} - \frac{1}{3}\mathbf{I}\ \mathrm{tr}\mathbf{A}\right) - \frac{1}{3\tau_R}\left(\mathrm{tr}\mathbf{A} - 3\right)\mathbf{I} \tag{B.1}$$

where $\boldsymbol{\kappa}$ is the velocity gradient tensor, $\mathrm{tr}\mathbf{A}$ is the trace of $\mathbf{A}$, and $\mathbf{I}$ is the identity tensor. τ_R is the Rouse time and is taken to be a constant. The orientational time τ is believed to vary in fast flows, because of convective constraint release (CCR), and this is accounted for as follows:

$$\frac{1}{\tau} = \frac{2}{\tau_d} + \left(\frac{1}{\tau_R} - \frac{2}{\tau_d}\right)\frac{\beta_{\mathrm{CCR}}\left(\mathrm{tr}\mathbf{A} - 3\right)}{3 + \beta_{\mathrm{CCR}}\left(\mathrm{tr}\mathbf{A} - 3\right)} \tag{B.2}$$

β_{CCR} is a numerical parameter of order unity, measuring CCR effectiveness.

We can first plug expression for $\frac{1}{\tau}$ into Eqn. B.1 and take $\beta_{\mathrm{CCR}} = 1$, define $\lambda^2 = \frac{\mathrm{tr}\mathbf{A}}{3}$ then simplify to obtain:

$$\frac{d\mathbf{A}}{\mathrm{dt}} = \boldsymbol{\kappa} \cdot \mathbf{A} + \mathbf{A} \cdot \boldsymbol{\kappa}^T - \frac{1}{\tau_R}\mathbf{A} - \left(\frac{2}{\tau_d} - \frac{1}{\tau_R}\right)\frac{1}{\lambda^2}\mathbf{A} + \frac{2}{\tau_d}\mathbf{I} \tag{B.3}$$

We can conduct a perturbation analysis using the same procedure as outlined in the Theory section of Chapter 7 to obtain:

$$\frac{G'_{\perp}}{G_N^0} = \frac{A_{\mathrm{yy}}^{(0)}\tilde{\omega}^2}{B^2 + \tilde{\omega}^2} \tag{B.4}$$

$$\frac{G''_{\perp}}{G_N^0} = \frac{A_{\mathrm{yy}}^{(0)} B\tilde{\omega}}{B^2 + \tilde{\omega}^2} \tag{B.5}$$

Here we find that the expressions for $G'_{\perp}$ and $G''_{\perp}$ from the coupled DCR-CS model are identical to the expressions from the Rolie-Poly model (see Eqn. 7.23 and Eqn. 7.24 in Chapter 7). However, the expressions for $A_{\mathrm{yy}}^{(0)}$ and B are different between the two models. For the DCR-CS model, these are:

$$A_{yy}^0 = \frac{2/\theta}{\left(\frac{2}{\theta} - 1\right)\frac{1}{\lambda^{(0)2}} + 1}, \tag{B.6}$$

and

$$B = 1 + \left(\frac{2}{\theta} - 1\right)\frac{1}{\lambda^{(0)2}}. \tag{B.7}$$

Here, θ is the ratio of relaxation times, $\theta = \tau/\tau_R$ and $\lambda^{(0)}$ is the chain stretch caused by the steady shear flow.

B.2.3 Comparison of linear spring and Warner spring for the log-normal distribution

In Chapter 7, we used a linear spring law in both the Rolie-Poly calculations and the RDP calculations. Here, we will briefly comment on the effect of including a nonlinear spring law. We chose the Warner spring law: $f_E(\lambda_i) = (1 - \lambda_{\max}^{-2}) / (1 - \lambda_i^2 \lambda_{\max}^{-2})$, with $\lambda_{\max}$ the maximum stretch ratio. In an experimental system, the maximum stretching of the chain usually depends on the chemistry and on dilution, but it does not really affect the qualitative trends in the model predictions presented below. After including the nonlinear spring constant, the equations for the RDP model become:

$$\boldsymbol{\sigma} = G_N^0 \sum_{i=1}^{N} \phi_i f_E\left(\lambda_i\right) \mathbf{A_i} \tag{B.8}$$

$$\begin{aligned}\frac{\mathrm{d}\mathbf{A}_{\mathrm{ij}}}{\mathrm{d}t} =& \underbrace{\boldsymbol{\kappa}\cdot\mathbf{A}_{\mathrm{ij}} + \mathbf{A}_{\mathrm{ij}}\cdot\boldsymbol{\kappa}^{\mathrm{T}}}_{\text{convection}} - \frac{1}{2}\left(\underbrace{\frac{1}{\tau_{\mathrm{d,i}}}\left(\mathbf{A}_{\mathrm{ij}} - \mathbf{I}\right)}_{\text{reptation}} + \underbrace{\frac{\beta_{\mathrm{th}}}{\tau_{\mathrm{d,j}}}\left(\mathbf{A}_{\mathrm{ij}} - \mathbf{I}\right)}_{\text{constraint release}}\right) \\ &- \underbrace{\frac{2\left(1-\lambda_{\mathrm{i}}^{-1}\right)}{\tau_{\mathrm{R,i}}} f_E\left(\lambda_i\right)\mathbf{A}_{\mathrm{ij}}}_{\text{retraction}} - \underbrace{\beta_{\mathrm{CCR}}\frac{2\left(1-\lambda_{\mathrm{j}}^{-1}\right)}{\tau_{\mathrm{R,j}}} f_E\left(\lambda_j\right)\lambda_{\mathrm{i}}^{2\rho}\left(\mathbf{A}_{\mathrm{ij}} - \mathbf{I}\right)}_{\text{convective constraint release}}\end{aligned} \tag{B.9}$$

In Figure B.7 and Figure B.8 below, we make a comparison of the linear spring results and Warner spring results for lognormal distributions with varying degrees of polydispersity. We vary the maximum chain stretch for the two predictions: Figure B.7 is for $\lambda_{\max} = 10$ and Figure B.8 is for $\lambda_{\max} = 5$. Predictions using the Warner spring only start to differ significantly from predictions for the linear spring for $Wi > 10$ and $PDI \geq 2$. Here, the shear rate is nondimensionalized using the Rouse time for the average chain length. For $PDI = 5$, the longest chain in the discretized length distribution has $Z_L = 126$. Since the Rouse time scales as Z^2, for $Wi = \dot{\gamma}\cdot\tau_{R,\overline{Z}} = 10$, we have $\dot{\gamma}\cdot\tau_{R,Z_L} = \left(\frac{126}{20}\right)^2\cdot 10 = 400$. Therefore, the longest chains in the system become significantly stretched, i.e., λ_i for the longest chains approach $\lambda_{\max}$, making the spring constant $f_E\left(\lambda_i\right)$ become significantly larger than 1. Since the nonlinear spring constant appears in the expression for the polymeric stress (Eqn. B.8), at large Wi and high polydispersity, the stress can become much larger than the linear spring case. Thus, the plateau value of $G'_{\perp}$ shows the sharp increase for $PDI = 5$ and $Wi > 10$ (Fig. B.7 (c)). Changing the value of $\lambda_{\max}$ from 10 to 5 doesn't significantly change the Wi at which the Warner spring results start deviating from the linear spring result. The main effect of changing $\lambda_{\max}$ is to change the magnitude of the deviation. Since across most of the parameter space (spanning different shear rates and PDI) that is accessible experimentally, the predictions for linear and Warner spring are very similar and the Warner spring adds extra complication associated with an additional parameter $\lambda_{\max}$, we will only discuss results for the linear spring in Chapter 7.

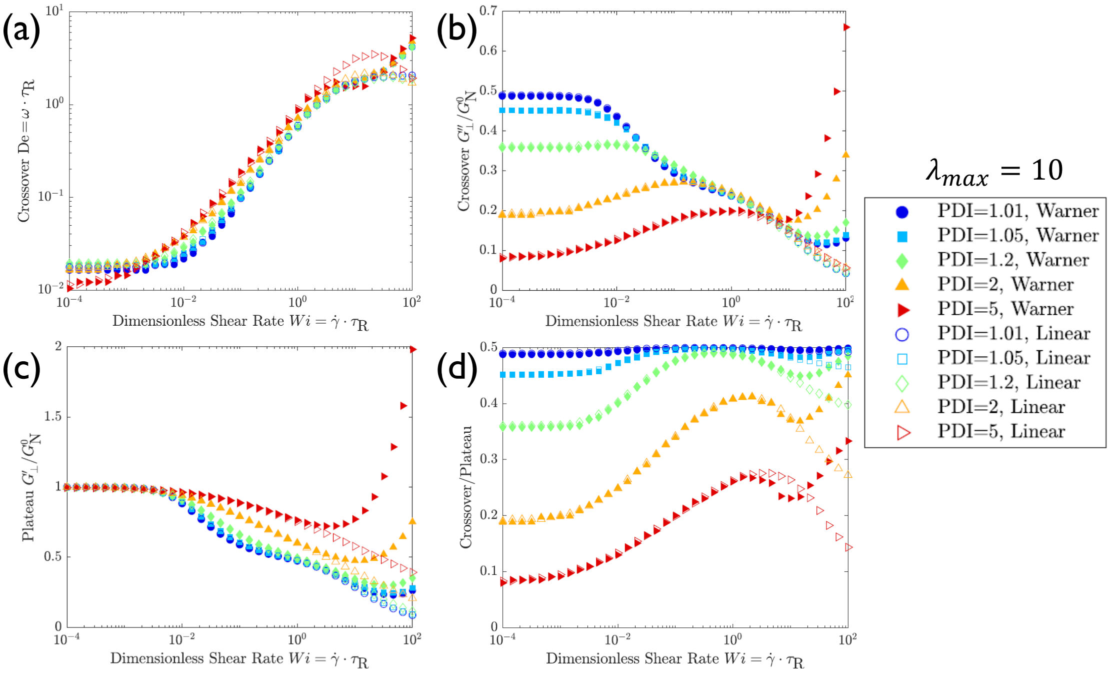

Figure B.7: Comparison of results from the perturbation analysis of the linear spring and numerical calculations of the Warner spring for log-normal distributions of varying degrees of polydispersity using the RDP model. Closed symbols represent the Warner spring with $\lambda_{\max} = 10$ and open symbols represent the linear spring; (a) crossover frequency, (b) moduli at crossover, (c) plateau modulus, (d) ratio of moduli at crossover and plateau.

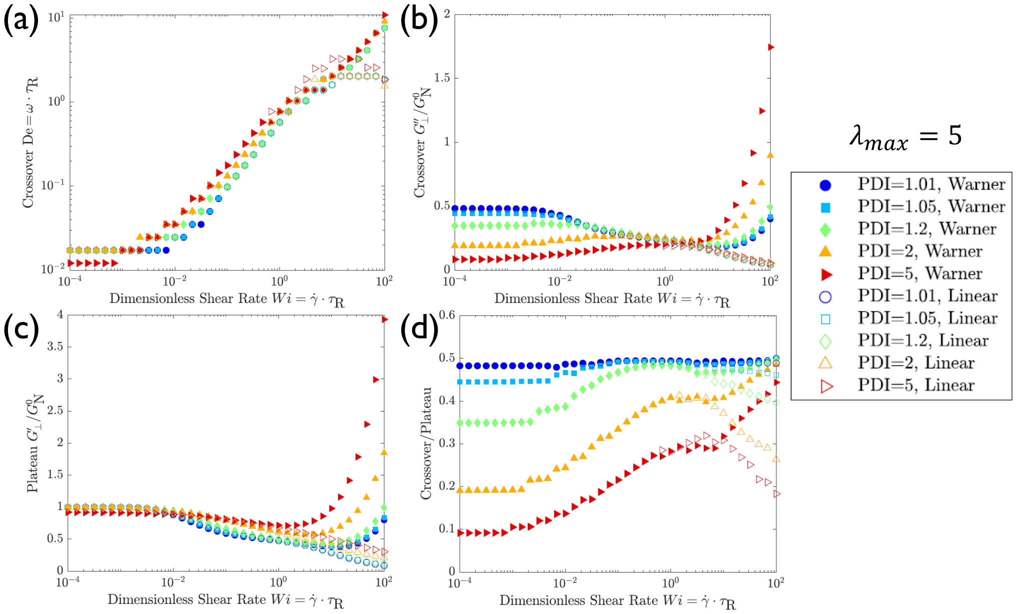

Figure B.8: Compare results from numerical calculations of the linear spring and the Warner spring for log-normal distributions of varying degrees of polydispersity using the RDP model. Closed symbols represent the Warner spring with $\lambda_{\text{max}} = 5$ and open symbols represent the linear spring. (a) crossover frequency, (b) moduli at crossover, (c) plateau modulus, (d) ratio of moduli at crossover and plateau.

B.2.4 Dependence of $\mathbf{A_i^{yy(0)}}$ on chain length $\mathbf{Z_i}$

To help explain the weakened softening of the plateau in the polydisperse case compared to the monodisperse case, as observed in Fig. 7.5 (c) and Fig. 7.6 (c) in Chapter 7, we plot in Fig. B.9 the yy-component of the configuration tensor $A_i^{yy(0)}$ using the monodisperse perturbation analysis for chains with lengths corresponding to the discretized log-normal distribution with $PDI = 2$. In the polydisperse calculation, the weight-averaged chain length is kept the same as the monodisperse case: i.e., $\overline{Z} = \sum_i^N \phi_i Z_i = 20$. The $A_i^{yy(0)}$ has a nonlinear dependence on the chain length Z_i. Thus, a weight-average of $A_i^{yy(0)}$ does not yield the same value as $A_{\text{yy}}^{(0)}$ for the monodisperse case of $Z = 20$.

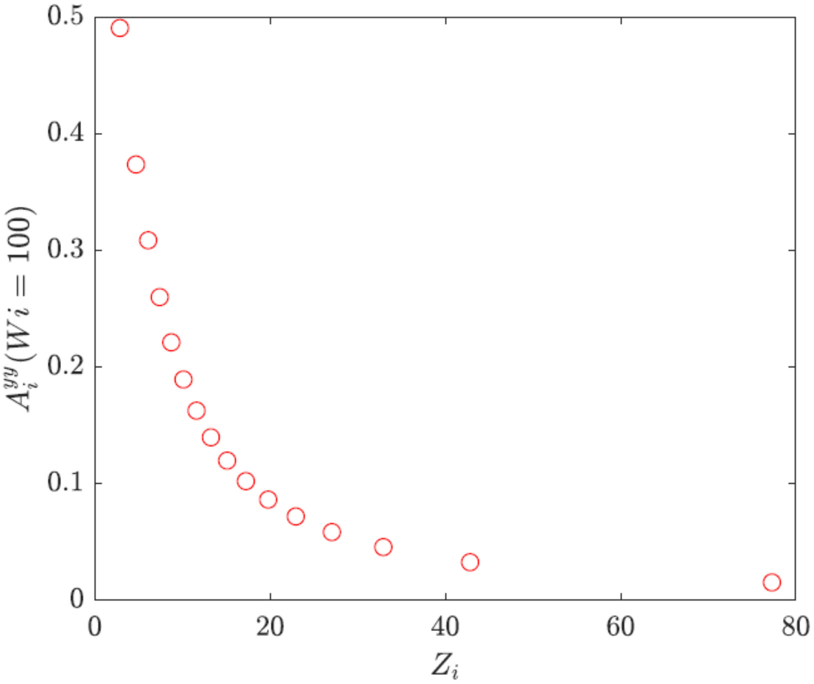

Figure B.9: Dependence of the yy-component of the configuration tensor $A_i^{yy(0)}$ on the chain length Z_i in the discretized distribution for a log-normal distribution with $PDI = 2$.

B.2.5 Derivation of the relationship between N_1 and OSR moduli

Here, we show the detailed derivation that led to Eqn. 7.31 in Chapter 7 for describing the relationship between the first normal stress difference and the OSR moduli. First, we can rearrange the equation for the xy-component of the conformation tensor, $A_{\mathrm{xy}}^{(0)}$, in the Rolie-Poly model to obtain an analytical expression for $A_{\mathrm{xy}}^{(0)}$ in steady shear:

$$\frac{dA_{\mathrm{xy}}^{(0)}}{dt} = 0 = A_{\mathrm{yy}}^{(0)} Wi + \left(-\frac{1}{\theta} - 2\left(1 - \frac{1}{\lambda^{(0)}}\right) - \frac{2\left(1 - \frac{1}{\lambda^{(0)}}\right)}{\lambda^{(0)}} \right) A_{\mathrm{xy}}^{(0)} \tag{B.10}$$

$$A_{\mathrm{xy}}^{(0)} = \frac{A_{\mathrm{yy}}^{(0)}\mathrm{Wi}}{\frac{1}{\theta} + 2\left(1 - \frac{1}{\lambda^{(0)}}\right) + \frac{2\left(1-\frac{1}{\lambda^{(0)}}\right)}{\lambda^{(0)}}} \tag{B.11}$$

Similarly, we can rearrange the equation for $A_{\mathrm{xx}}^{(0)}$ to get an analytical expression for $A_{\mathrm{xx}}^{(0)}$ in steady shear:

$$\frac{dA_{\mathrm{xx}}^{(0)}}{\mathrm{dt}} = 0 = 2A_{\mathrm{xy}}^{(0)}Wi + \left(-\frac{1}{\theta} - \frac{2\left(1 - \frac{1}{\lambda^{(0)}}\right)}{\lambda^{(0)}}\right)\left(A_{\mathrm{xx}}^{(0)} - 1\right) - 2\left(1 - \frac{1}{\lambda^{(0)}}\right)A_{\mathrm{xx}}^{(0)} \tag{B.12}$$

$$A_{\mathrm{xx}}^{(0)} = \frac{2A_{\mathrm{xy}}^{(0)}Wi + \frac{1}{\theta} + \frac{2\left(1-\frac{1}{\lambda^{(0)}}\right)}{\lambda^{(0)}}}{\frac{1}{\theta} + 2\left(1 - \frac{1}{\lambda^{(0)}}\right) + \frac{2\left(1-\frac{1}{\lambda^{(0)}}\right)}{\lambda^{(0)}}} \tag{B.13}$$

From the Theory section of the Chapter 7, we have:

$$A_{\mathrm{yy}}^{(0)} = \frac{\frac{1}{\theta} + \frac{2\left(1-\frac{1}{\lambda^{(0)}}\right)}{\lambda^{(0)}}}{\frac{1}{\theta} + 2\left(1 - \frac{1}{\lambda^{(0)}}\right) + \frac{2\left(1-\frac{1}{\lambda^{(0)}}\right)}{\lambda^{(0)}}} \tag{B.14}$$

Thus, we can calculate the first normal stress difference N_1:

$$\begin{aligned} N_1 &= G_N^0\left(A_{\mathrm{xx}}^{(0)} - A_{\mathrm{yy}}^{(0)}\right) \\ &= G_N^0\left(\frac{2A_{\mathrm{xy}}^{(0)}Wi + \frac{1}{\theta} + \frac{2\left(1-\frac{1}{\lambda^{(0)}}\right)}{\lambda^{(0)}}}{\frac{1}{\theta} + 2\left(1 - \frac{1}{\lambda^{(0)}}\right) + \frac{2\left(1-\frac{1}{\lambda^{(0)}}\right)}{\lambda^{(0)}}} - \frac{\frac{1}{\theta} + \frac{2\left(1-\frac{1}{\lambda^{(0)}}\right)}{\lambda^{(0)}}}{\frac{1}{\theta} + 2\left(1 - \frac{1}{\lambda^{(0)}}\right) + \frac{2\left(1-\frac{1}{\lambda^{(0)}}\right)}{\lambda^{(0)}}}\right) \\ &= G_N^0\left(\frac{2A_{\mathrm{xy}}^{(0)}\mathrm{Wi}}{\frac{1}{\theta} + 2\left(1 - \frac{1}{\lambda^{(0)}}\right) + \frac{2\left(1-\frac{1}{\lambda^{(0)}}\right)}{\lambda^{(0)}}}\right) \end{aligned} \tag{B.15}$$

We can substitute Eqn. B.11 into $A_{\mathrm{xy}}^{(0)}$ to obtain:

$$N_1 \;=\; 2G_N^0 A_{\mathrm{yy}}^{(0)} \left(\frac{\mathrm{Wi}}{\frac{1}{\theta} + 2\left(1 - \frac{1}{\lambda^{(0)}}\right) + \frac{2\left(1 - \frac{1}{\lambda^{(0)}}\right)}{\lambda^{(0)}}} \right)^2 \tag{B.16}$$

From Chapter 7, we have

$$B \;=\; \left(\frac{1}{\theta} + 2\left(1 - \frac{1}{\lambda^{(0)}}\right) + \frac{2\left(1 - \frac{1}{\lambda^{(0)}}\right)}{\lambda^{(0)}} \right). \tag{B.17}$$

So, we can simplify Eqn. B.16 to get:

$$N_1 = 2G_N^0 A_{\mathrm{yy}}^{(0)} \left(\frac{\mathrm{Wi}}{B} \right)^2, \tag{B.18}$$

which is Eqn. 7.31 in Chapter 7.

Bibliography

[1] Likhtman AE, Graham RS. Simple constitutive equation for linear polymer melts derived from molecular theory: Rolie–poly equation. *Journal of Non-Newtonian Fluid Mechanics.* 2003; 114(1): 1–12.

[2] Kim S, Mewis J, Clasen C, Vermant J. Superposition rheometry of a wormlike micellar fluid. *Rheologica Acta.* 2013; 52(8-9): 727–740.

[3] Boudara VA, Peterson JD, Leal LG, Read DJ. Nonlinear rheology of polydisperse blends of entangled linear polymers: Rolie-double-poly models. *Journal of Rheology.* 2019; 63(1): 71–91.

[4] Marrucci G, Ianniruberto G. Flow-induced orientation and stretching of entangled polymers. *Philosophical Transactions of the Royal Society of London. Series A: Mathematical, Physical and Engineering Sciences.* 2003; 361(1805): 677–688.

[5] Unidad HJ, Ianniruberto G. The role of convective constraint release in parallel superposition flows of nearly monodisperse entangled polymer solutions. *Rheologica Acta.* 2014; 53(2): 191–198.